

Abstract

Contents

1	Introduction	5
1.1	Overview	5
1.2	Transitional wall-bounded shear flows	8
1.2.1	Linear Stability Analysis	8
1.2.2	Nonlinear dynamical systems	12
1.2.3	Spatiotemporal transitional flows	15
1.3	Rayleigh-Bénard convection	18
1.4	Rayleigh-Bénard Poiseuille (RBP) flows	23
1.5	Thesis Outline	25
2	Numerical Methods	26
2.1	Method of weighted residuals	26
2.2	Galerkin Projection	28
2.3	Spectral/ <i>hp</i> element method	30
2.3.1	Domain partition	30
2.3.2	Standard Elements	30
2.3.3	Global assembly	32
2.3.4	Local basis expansions	34
2.3.5	Gaussian quadrature	37
2.3.6	Numerical differentiation	38
2.3.7	Example in 1D	39
2.4	Numerical techniques for solving the Navier-Stokes equations	41
2.4.1	Velocity Correction Scheme	41
2.4.2	Fourier spectral/ <i>hp</i> modes	43
2.4.3	Maintaining fluid flow through a channel	44
2.5	Stability analysis of the Navier-Stokes equations	48
2.5.1	Algorithms for linear stability analysis	48
2.5.2	Edge tracking	52
3	Transitional Rayleigh-Bénard Poiseuille flows	55
3.1	Objectives	55
3.2	Problem formulation	56

3.2.1	Governing equations	56
3.2.2	Numerical Methods	57
3.2.3	Parametric sweep of Ra - Re space	57
3.2.4	Linear Stability Analysis	57
3.3	Ra - Re phase space	59
3.3.1	Classification	59
3.3.2	Spatiotemporal intermittent rolls	60
3.3.3	Co-existence of convection rolls with turbulent bands	62
3.4	The role of longitudinal rolls	64
3.4.1	The thermally-assisted sustaining process (TASP) in a confined domain	64
3.4.2	Variation of Ra and Re on the thermally-assisted sustaining process in $\Gamma = \pi/2$	71
3.4.3	Extending to large domains, $\Gamma = 4\pi$	78
3.5	Conclusions	79
4	The state space structure of Spiral Defect Chaos	81
4.1	Objectives	81
4.2	Problem formulation	82
4.2.1	Rayleigh-Bénard convection (RBC)	82
4.2.2	Numerical method	83
4.2.3	Linear stability analysis of ISRs	83
4.3	Transient SDC and elementary states in minimal domain	84
4.4	Multiplicity of edge states	90
4.5	Unstable ideal straight rolls	97
4.5.1	Pathways leading to ISRs - heteroclinic orbits	98
4.5.2	Pathways leading to elementary states	101
4.5.3	A pathway to SDC in an extended domain $\Gamma = 4\pi$	104
4.6	Concluding remarks	104
5	Conclusions	116
A	Appendices	117
A.1	Non-dimensionalisation	117
A.2	Governing equations for Rayleigh-Bénard convection	117
A.3	Projection methods for Navier-Stokes equations	118
A.4	Simulation parameters for Ra - Re sweep	119
A.5	First- and second-order statistics of the buoyancy- and shear-driven regime	121
A.5.1	Buoyancy-driven regime	121
A.5.2	Shear-driven regime	121
A.6	Growth rates of primary instabilities	125
A.7	Verification of linear stability analysis	125
A.8	Other elementary states and ISRs	126

Chapter 1

Introduction

1.1 Overview

Fluid motions driven by buoyancy and frictional forces belongs to broad class of flows known as thermoconvective shear flows. These flows exhibit rich behaviour, and are of interest in both engineering and meteorology applications spanning across a broad range of length scales.

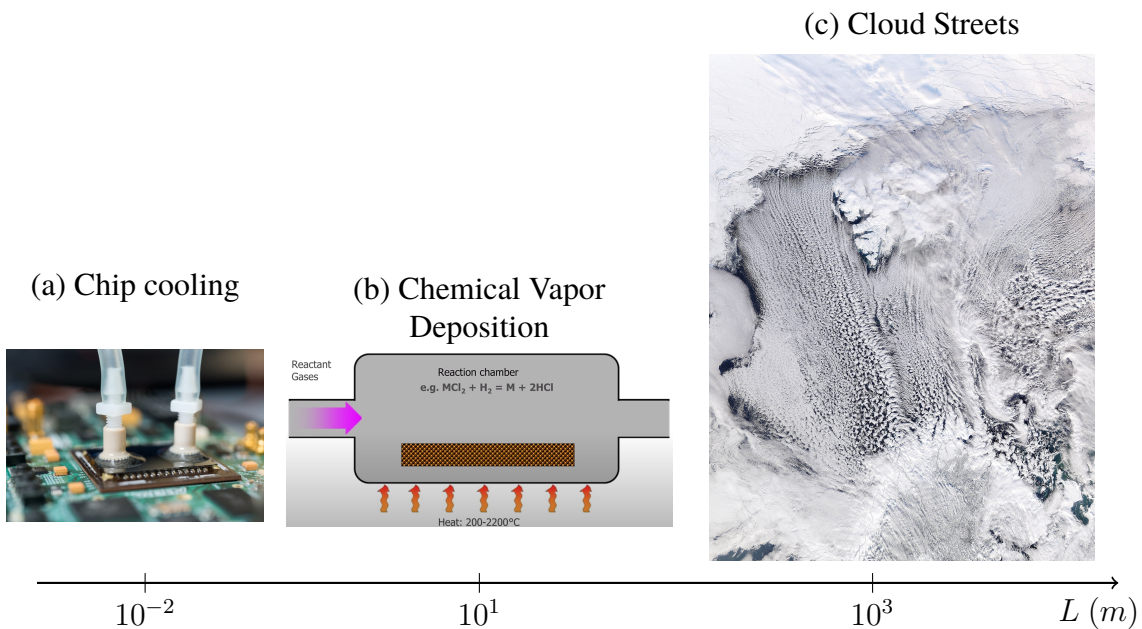


Figure 1.1: Thermoconvective shear flows driven by shear and buoyancy forces across length scales, $L \in [10^{-2} m, 10^3 m]$. Examples include (a) chip cooling, (b) chemical vapour deposition and (c) the formation of cloud streets.

At small scales, around $L \sim 10^{-2} m$, thermoconvective flows are relevant to the cooling of microprocessing chips. The fluid in such systems acting to dissipating heat, typically experiences shear and buoyancy forces from the confining walls, and heating. One of the major challenge in this industry is on increasing the density of transistors on a single chip, alluding to Moore's Law, which predicts the doubling of transistors on a single chip approximately every two years. However, one of the major limitations is the challenge of dissipating the excessive heat generated from the densely

packed transistors. Fluids, such as air, water or refrigerants, are often used to transport heat away from the components, and their fluid mechanical behaviour remains an open topic [Kennedy and Zebib, 1983, Ray and Srinivasan, 1992].

At intermediate length scales, $L \sim 1m$, the interaction between buoyancy and frictional forces is important in the fabrication of uniform thin films in chemical vapour deposition (CVD) [Evans and Greif, 1991, Jensen et al., 1991]. The CVD process typically involves a reactive gases carried by inert gases which flows through a channel with a heated substrate. Upon heating, the reactant gases react chemically on the substrate, depositing material and forming thin films, such as silicon layers. A key challenge in the CVD process is achieving a uniform deposition and maintaining sharp interfaces between layers. The interactions between shear and buoyancy forces often gives rise to boundary layers and thermoconvective rolls, which can disrupt uniform deposition, affecting film quality.

At larger length scales, $L \sim 10^3 m$, the thermoconvective shear flows can be observed in atmospheric flows such as the cloud streets over the Norwegian Sea. These parallel bands of cumulus clouds can stretch over hundreds of kilometres. They form when the relatively warmer sea surfaces heat up the colder air arriving from the North pole. As the colder air is heated, it rises upwards whilst carrying water vapour, condensing into visible clouds. This circulation is subsequently organised into parallel rotating parallel columns of air, forming distinct cloud streets.

The central focus of this thesis is on the investigation of fluid behaviour arising from the interaction between shear and buoyancy forces, a common thread among the examples discussed above. We note that by isolating our analysis to the interaction between shear and buoyancy forces, we might neglect other physical mechanisms such as phase change, chemical reactions and evaporation, which may be significant in the context of cooling microprocessors, chemical vapour deposition, and atmospheric boundary layers respectively [Vallis et al., 2019]. Nonetheless, the interaction between shear and buoyancy forces remains an open topic and will be the primary focus of this thesis, providing a foundation for future investigations that may include addition mechanisms.

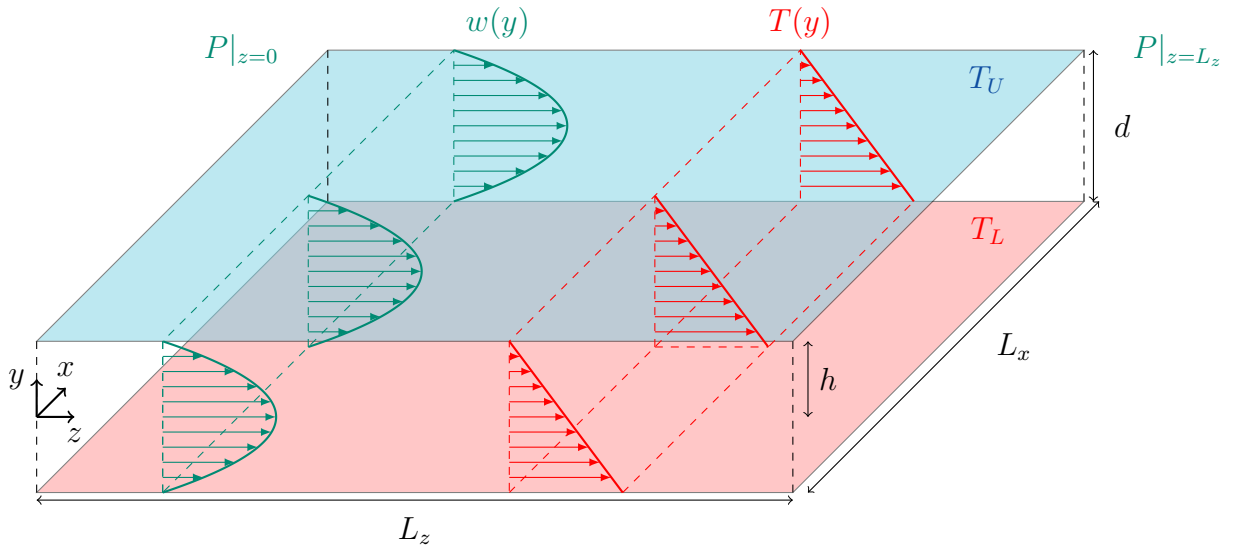


Figure 1.2: The Rayleigh-Bénard Poiseuille (RBP) flow configuration.

To consider this interaction, we consider an idealised setup, known as the Rayleigh-Bénard-

Poiseuille (RBP) flow. This RBP system describes the fluid motion confined between two infinitely extended parallel plates, heated from below and cooled from the top, with an additional pressure gradient driving the flow. The RBP configuration combines the two paradigmatic flow configurations; the classical Rayleigh-Bénard convection (RBC), driven purely by buoyancy, and plane Poiseuille flow (PPF), driven purely by shear. While the onset of convection in RBC, and the transition to subcritical shear-driven turbulence in PPF have been both extensively studied, the transitional regime in which both forces interact remains less understood. Understanding their transitional behaviour and their transport properties could have implications for the applications mentioned above.

The RBP configuration is illustrated in figure 1.1, where z, y, x refer to spatial coordinates denoting the streamwise, spanwise and wall normal directions. L_z, L_x, d and h corresponds to the length, span, depth and half-height of the domain respectively. We note that the RBP system is biperiodic along z and x , and are of equal size, $L = L_x = L_z$. The flow is driven by a pressure gradient along the streamwise z direction, $\Delta P = P|_{z=0} - P|_{z=L_z} < 0$, leading to a laminar Poiseuille flow, $w(y) = W_c(1 - y^2)$, where W_c is the laminar centerline velocity. We consider a fully developed flow, where the boundary layer from the top and the bottom wall meets at the midplane $y = 0$ and entrance effects are therefore neglected. Like the RBC system, the RBP system is unstably stratified. The temperature difference between the lower, T_L , and upper wall, T_U , is always positive, $\Delta T = T_L - T_U > 0$, leading to a stable linear conduction layer along the wall-normal direction, $T(y)$, if ΔT is kept sufficiently small. The behaviour of RBP flows is governed by four dimensionless parameters,

$$Re = W_c h / \nu, \quad Ra = \frac{\eta g d^3 \Delta T}{\nu \kappa}, \quad Pr = \frac{\kappa}{\nu}, \quad \Gamma = L/2d, \quad (1.1)$$

where Re, Ra, Pr, Γ refers to Reynolds, Rayleigh, Prandtl numbers and aspect ratio and η, g, ν, κ , are the thermal expansion coefficient, acceleration due to gravity, kinematic viscosity, thermal diffusivity, respectively.

In the absence of shear, $Re = 0$, the RBP configuration reduces to the classical Rayleigh-Bénard convection problem, bringing about buoyancy-driven convection for a sufficiently large unstable stratification. In the limiting case without unstable stratification, $Ra = 0$, the system reduces to the wall-bounded plane Poiseuille flow (PPF), where the transition towards subcritical shear-driven turbulence may be expected for a sufficiently large pressure gradient. We focus on the transitional regime, by investigating if buoyancy forces promote the transition to shear-driven turbulence and the effect of shear on convection in large domains.

We describe the structure of the introductory chapter as follows. We begin our discussion on the development of hydrodynamic stability theory of wall-bounded shear flows in §1.2. Theoretical frameworks used in the study of stability of flow such as linear modal/non-modal stability, nonlinear dynamical systems and the spatiotemporal character of transitional shear flows will be discussed. Throughout this discussion, we also highlight examples of PPF which is relevant to the RBP system. This followed by the developments of Rayleigh-Bénard convection (RBC) in §1.3, where theoretical concepts from §1.2 will be utilised. After which, we describe the developments of RBP flows §1.4, before concluding this chapter with an outline of the thesis in §1.5.

1.2 Transitional wall-bounded shear flows

Wall-bounded shear flows concerns the motion of the fluid flowing in parallel to walls, typically bounded by one or more walls. Near the wall, the fluid comes to rest due to the no-slip boundary condition, resulting in a velocity gradient perpendicular to the wall, giving rise to shear within the fluid - hence the term *wall-bounded shear flows*. Examples include the pressure-driven plane Poiseuille flow (channel flow), Hagen-Poiseuille flow (pipe flow), plane Couette flow and flat plate boundary layers. These geometrically simple configurations provides a convenient framework amenable to the mathematical analysis of fluid motion subjected to shear. Depending on the degree of shear, the fluid motion can be either laminar, where the fluid layers move in smooth parallel 'laminates', or turbulent, characterised by chaotic eddying motions. We also note that there is a transitional regime where both states can coexist discuss later. A central question is predicting the transition from the laminar regime to the turbulence.

The first investigation into this transition was conducted by [Reynolds \[1883\]](#). In his experimental setup, the flow speed through the pipe could be controlled by regulating the inlet pressure, while injecting dye to visualise the flow, as illustrated in figure 1.3(a). At low speeds, the fluid remained laminar, resulting to a single streak of steady dye in figure 1.3(b). As the speed increased, the dye begin to exhibit irregular 'sinuous' motions interspersed with laminar regions shown in figure 1.3(c). This is now referred to as the transitional/intermittent regime, alternating between the laminar and turbulent states. Beyond a critical speed, the dye breaks down entirely into chaotic 'eddies', mixing with the surrounding fluid and discolouring the flow with dye downstream in figure 1.3(d). This regime is now identified as turbulence.

Reynolds proposed that the threshold between the laminar, transitional and turbulent regimes could be characterised by a non-dimensional parameter, now referred to as the Reynolds number,

$$Re = UD/\nu, \quad (1.2)$$

where U is the centerline velocity in the pipe, D , the pipe diameter and ν , the kinematic viscosity. He observed that flow through the pipe remained 'stable' and laminar for $Re < 1900$, while it became 'unstable' and turbulent for $Re > 2000$ [[Reynolds, 1895](#)]. These findings introduced the concept of flow stability.

1.2.1 Linear Stability Analysis

Following Reynolds' experiment, interest towards the mathematical analysis of the stability of laminar flows grew in early 20st century. The mathematical approach typically begins by decomposing the velocity field, $\mathbf{u}(\mathbf{x}, t)$, into a laminar (base) state, $U(y)$, and the velocity perturbations, $\mathbf{u}'(\mathbf{x}, t)$, with pressure similarly decomposed as,

$$\mathbf{u}(\mathbf{x}) = U(y) + \mathbf{u}'(\mathbf{x}, t), \quad \text{and} \quad p(\mathbf{x}, t) = P(x) + p'(\mathbf{x}, t). \quad (1.3)$$

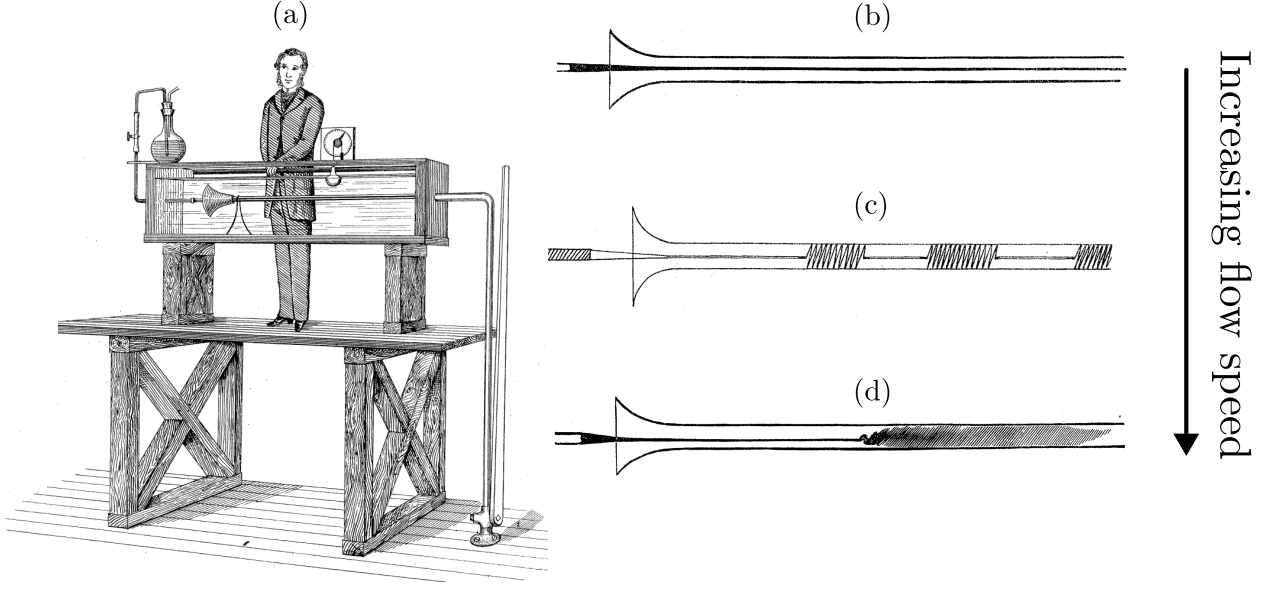


Figure 1.3: (a) Osbourne Reynolds pipe experiment with the dye injection apparatus, illustrating the (b) laminar flow, (c) intermittent regime and (d) turbulent flow as the flow speed is increased, taken from [Reynolds, 1883].

Substituting into the Navier-Stokes equations and linearising (neglecting nonlinear terms), we get,

$$\frac{\partial \mathbf{u}'}{\partial t} + (\mathbf{U} \cdot \nabla) \mathbf{u}' + (\mathbf{u}' \cdot \nabla) \mathbf{U} = -\nabla p' + \frac{1}{Re} \nabla^2 \mathbf{u}', \quad (1.4a)$$

$$\nabla \cdot \mathbf{u}' = 0, \quad (1.4b)$$

known as the linearised Navier-Stokes equations. This commonly followed by introducing a wavelike ansatz (mode) for the perturbations, and analysed by considering their behaviour independently, referred to as modal analysis in §1.2.1, or their coupled dynamics, referred to as non-modal analysis in §1.2.1.

Modal analysis

It is convenient to eliminate the pressure terms by reformulating equation (1.4) using the wall-normal perturbation velocity, v' , and wall-normal vorticity, $\eta' = \partial u'/\partial z - \partial w'/\partial x$, variables. Using (v, η) , we introduce a modal ansatz for them,

$$v'(\mathbf{x}, t) = \tilde{v}(y) e^{i(\alpha x + \beta z - \omega t)}, \quad \text{and} \quad \eta'(\mathbf{x}, t) = \tilde{\eta}(y) e^{i(\alpha x + \beta z - \omega t)}. \quad (1.5)$$

where α, β, ω denotes the streamwise and spanwise wavenumbers, and complex frequency (i.e. $\omega = \omega_r + i\omega_i$), respectively. Substituting this ansatz into linearised equations lead to the classical Orr-Sommerfeld and Squire equations [Orr, 1907, Sommerfeld, 1909, Squire, 1933, Schmid and

Henningson, 2001],

$$\begin{pmatrix} \mathcal{L}_{OS} & 0 \\ i\beta U' & \mathcal{L}_{SQ} \end{pmatrix} \begin{pmatrix} \tilde{v} \\ \tilde{\eta} \end{pmatrix} = i\omega \begin{pmatrix} k^2 - \mathcal{D}^2 & 0 \\ 0 & 1 \end{pmatrix} \begin{pmatrix} \tilde{v} \\ \tilde{\eta} \end{pmatrix}. \quad (1.6a)$$

with

$$\mathcal{L}_{OS} = i\alpha U(k^2 - \mathcal{D}^2) + i\alpha U'' + \frac{1}{Re}(k^2 - \mathcal{D}^2)^2, \quad \mathcal{L}_{SQ} = i\alpha U + \frac{1}{Re}(k^2 - \mathcal{D}^2). \quad (1.6b)$$

where $\mathcal{D} = d/dy$, $k^2 = \alpha^2 + \beta^2$ and U'' is the second derivative of $U(y)$. Equation (1.6a) is a generalised eigenvalue problem with eigenvalue $i\omega$, which determines the growth of perturbations.

The goal of modal stability analysis is to determine the critical Reynolds number Re_c , defined as the lowest value of Re , for all α and β in which $\Im[\omega] = 0$. For $Re > Re_c$, perturbations can grow exponentially, indicating instability. Squire's theorem states that for every unstable three-dimensional perturbation, there exist an unstable two-dimensional perturbation, with a lower Re_c [Squire, 1933]. This implies that the most linearly unstable perturbation of wall-bounded flows is two dimensional. Calculations by Tollmien [1928] and Schlichting [1933] for a flat-plate boundary layer flow yielded a critical Reynolds number based on streamwise distance x of $Re_{x,c} = Ux_c/\nu = 520$ [Schlichting and Gersten, 2017]. These two dimensional unstable eigenmodes are known as Tollmien-Schlichting (T.S) waves. In plane Poiseuillw flow, the critical Reynolds number is $Re_c = 5772.2$ with a critical wavenumber of $\alpha_c = 1.02$ [Orszag, 1971]. However, experiments reveal that transition to turbulence can occur at much lower Reynolds number, around, $Re \sim 1000 - 2000$ [Davies and White, 1928, Patel and Head, 1969, Dean, 1978, Iida and Nagano, 1998, Tsukahara et al., 2014a], highlighting a key limitation of modal analysis. Similar discrepancies are observed in plane Couette and pipe flows [Meseguer and Trefethen, 2003], where the laminar state is linearly stable for all Re , yet transition to turbulence occurs. Despite these limitations, modal analysis predicts instabilities in other flows such as Rayleigh-Bénard convection and Taylor-Couette flow [Chandrasekhar, 1968]. Further extensions of modal stability, including spatial instability analysis [Huerre and Monkewitz, 1990], and secondary instability [Orszag and Patera, 1983] are well established and are beyond the scope of this thesis.

Non-modal stability

One of a major limitations of modal analysis is that it treats each eigenmode independently. However, the interaction between decaying eigenmodes can lead to a transient growth, where perturbations amplify temporarily before decaying asymptotically. To demonstrate an example of transient growth, we consider a two-dimensional toy model governing the time-evolution of $\mathbf{q} = (v, \eta)^T$,

$$\frac{d}{dt} \begin{pmatrix} v \\ \eta \end{pmatrix} = \begin{pmatrix} -\frac{1}{Re} & -1 \\ 0 & -\frac{2}{Re} \end{pmatrix} \begin{pmatrix} v \\ \eta \end{pmatrix}, \quad (1.7)$$

where Re refers to the Reynolds number. The toy model has negative eigenvalues, $(\lambda_1, \lambda_2) = (-1/Re, -2/Re)$, indicating asymptotic decay. At $Re = 15$, the eigenvectors, $\mathbf{x}_1 = (1, 0)$, $\mathbf{x}_2 = (1, \frac{1}{\sqrt{Re^2+1}})$, are highly non-orthogonal, becoming almost parallel shown in figure 1.4(a). Notably, we become increasingly linearly dependent as $Re \rightarrow \infty$. For a particular initial condition, the energy

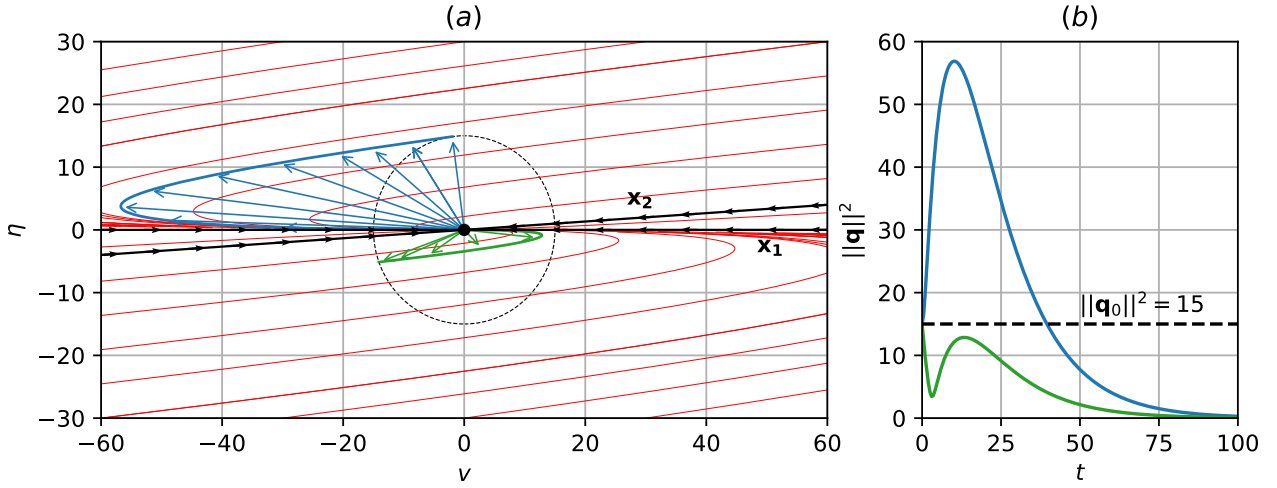


Figure 1.4: (a) The phase portrait of the toy model with $Re = 15$, where red lines are phase lines of the toy model. The blue trajectory lead to transient growth and the green trajectory do not (b) Time history of blue and green trajectory.

$\|q\|^2 = \sqrt{v^2 + \eta^2}$, is amplified four times before decaying in blue trajectory, shown in Figure 1.4(b). Yet for another choice of initial condition, the trajectory decays asymptotically as the green trajectory indicates. Despite decaying eigenmodes, the toy model highlights the significance of transient growth, which depends on the choice of initial condition.

The aim of non-modal stability analysis is find the initial conditions, $\tilde{\mathbf{q}}_0$, that leads to the maximum amplification, $G(\tau)$, over a time horizon τ . This is posed as an optimistaion problem,

$$G(\tau) = \max_{\tilde{\mathbf{q}}_0 \neq 0} \frac{\langle \tilde{\mathbf{q}}(\tau), \tilde{\mathbf{q}}(\tau) \rangle}{\langle \tilde{\mathbf{q}}_0, \tilde{\mathbf{q}}_0 \rangle}, \quad \text{s.t. } \langle \tilde{\mathbf{q}}_0, \tilde{\mathbf{q}}_0 \rangle = 1, \quad (1.8)$$

where, $\langle \cdot, \cdot \rangle$ denotes the inner-product,

$$\langle \mathbf{x}, \mathbf{y} \rangle = \int_{\Omega} \mathbf{x}^H \mathbf{y} \, d\Omega, \quad (1.9)$$

and \mathbf{x}^H refers to the complex conjugate transpose of \mathbf{x} . By considering the linearised operator of (1.6a), we can define a linear time invariant operator given as,

$$\tilde{\mathbf{q}}(\tau) = \mathcal{A}(\tau) \tilde{\mathbf{q}}_0, \quad (1.10)$$

which takes the solution from initial conditions, $\tilde{\mathbf{q}}_0$, to $\tilde{\mathbf{q}}(\tau)$ at time τ . Subtituting the expression above into equation (1.8),

$$G(\tau) = \max_{\tilde{\mathbf{q}}_0 \neq 0} \frac{\langle \mathcal{A}(\tau) \tilde{\mathbf{q}}_0, \mathcal{A}(\tau) \tilde{\mathbf{q}}_0 \rangle}{\langle \tilde{\mathbf{q}}_0, \tilde{\mathbf{q}}_0 \rangle} = \langle \tilde{\mathbf{q}}_0, \mathcal{A}^\dagger(\tau) \mathcal{A}(\tau) \tilde{\mathbf{q}}_0 \rangle = \lambda_{max}(\mathcal{A}(\tau)^\dagger \mathcal{A}(\tau)) \quad (1.11)$$

where \mathcal{A}^\dagger refers to the adjoint of $\mathcal{A}(t)$. The maximum amplification factor $\max G(t)$ is the largest

eigenvalue of $\mathcal{A}^\dagger(\tau)\mathcal{A}(\tau)$. The eigenvalue problem is given as,

$$\mathcal{A}^\dagger(t)\mathcal{A}(t)\tilde{\mathbf{q}}_0 = \lambda\tilde{\mathbf{q}}_0, \quad (1.12)$$

where $\tilde{\mathbf{q}}_0$ refers to the eigenvector denoting the optimal initial condition. For a detailed derivation of the optimal initial conditions or forcing, the reader is referred to [Butler and Farrell, 1992, Schmid, 2007]. An alternative method of computing the optimal transient growth is by analysing the pseudospectral of linear operators discussed in [Trefethen, 1997], but is outside the scope of this thesis.

Both two-, and three-dimensional non-modal analyses reveal mechanisms for transient growth. In two-dimensions, the optimal initial conditions are in the form of near wall vortices tilted upstream, which amplifies transiently via the Orr-mechanism [Orr, 1907, Farrell, 1988, Reddy et al., 1993]. In three-dimensions, streamwise vortices are optimal, leading to the the amplification of streamwise streaks via the lift-up effect [Ellingsen and Palm, 1975, Reddy and Henningson, 1993]. Notably, the spacing of these streaks analysed using non-modal analysis at higher Reynolds number has been consistently reported to occur around 100 wall units [Del Álamo and Jiménez, 2006, Pujals et al., 2009, Hwang and Cossu, 2010], which supports experimental observations of streak spacing in turbulent boundary layers [Kline et al., 1967, Smith and Metzler, 1983]. The main results from non-modal analysis is that three dimensional perturbations can lead to strong transient growth at subcritical Reynolds numbers, contradicting the two dimensional TS waves from modal analysis. Both modal and non-modal mechanisms highlight important insights into the linear mechanisms which might be responsible for the transition from laminar to turbulent flows.

1.2.2 Nonlinear dynamical systems

In the previous section, we have examined the laminar to turbulent transition using linear frameworks. However, the the transition process is ultimately described by the nonlinear Navier-Stokes equations, which motivates the development and adoption of mathematical frameworks beyond linear methbods.

In the context of shear flow turbulence, there has been a growing interesting in adopting techniques from nonlinear dynamical systems, interpreting turbulence as a chaotic trajectories which evolves within a finite-dimensional phase space. This phase space refers to a set of solutions satisfying the Navier-Stokes equations, conjectured to be infinite dimensional by Hopf [1948]. Hopf [1948] further conjectured that within the infinite dimension phase space lie a finite dimensional manifold, whose properties depended on viscosity. For large viscosities (i.e. low Re), this finite dimensional space corresponds to a single point, the laminar state. This point may become unstable at a certain critical Reynolds number, bifurcating to form new manifolds, as viscosity is decreased (i.e. Re is increased) further, potentially leading to chaos. The set of such manifolds is referred to *inertial manifolds*, and its existence under certain properties has been established [Foias et al., 1988]. A implication of this is that the transition to turbulence could be viewed as successive bifurcations from the laminar state, govern by a single control parameter (i.e. the Reynolds numnber), generalised by the so called *routes to chaos* scenarios.

Landau [1944] proposed that the transition to turbulence may occur through a sequence of Hopf

bifurcations, each introducing a new incommensurate frequency, resulting in quasi-periodic motions on a high-dimensional torus. However, this model did not capture the essential ingredients of turbulence, such as sensitivity of initial conditions and mixing [John et al., 1993]. Ruelle and Takens [1971] later show that a *strange attractor* exhibit key features of chaos can emerge after three successive Hopf bifurcations from a stationary state, referred to as the *Ruelle-Takens* route to chaos. This scenario has been observed in Taylor-Couette flow [Gollub and Swinney, 1975], and Rayleigh-Bénard convection [Swinney and Gollub, 1978]. Other routes to chaos scenarios, such as periodic-doubling [Feigenbaum, 1979], and intermittency Manneville and Pomeau [1979] scenarios have been proposed. For a review of these routes to chaos scenarios, the reader is referred to John et al. [1993]. Nonetheless, the transition to turbulence is subcritical in shear flow configurations, meaning that the route of chaos scenarios do not necessarily apply through bifurcations from the laminar state.

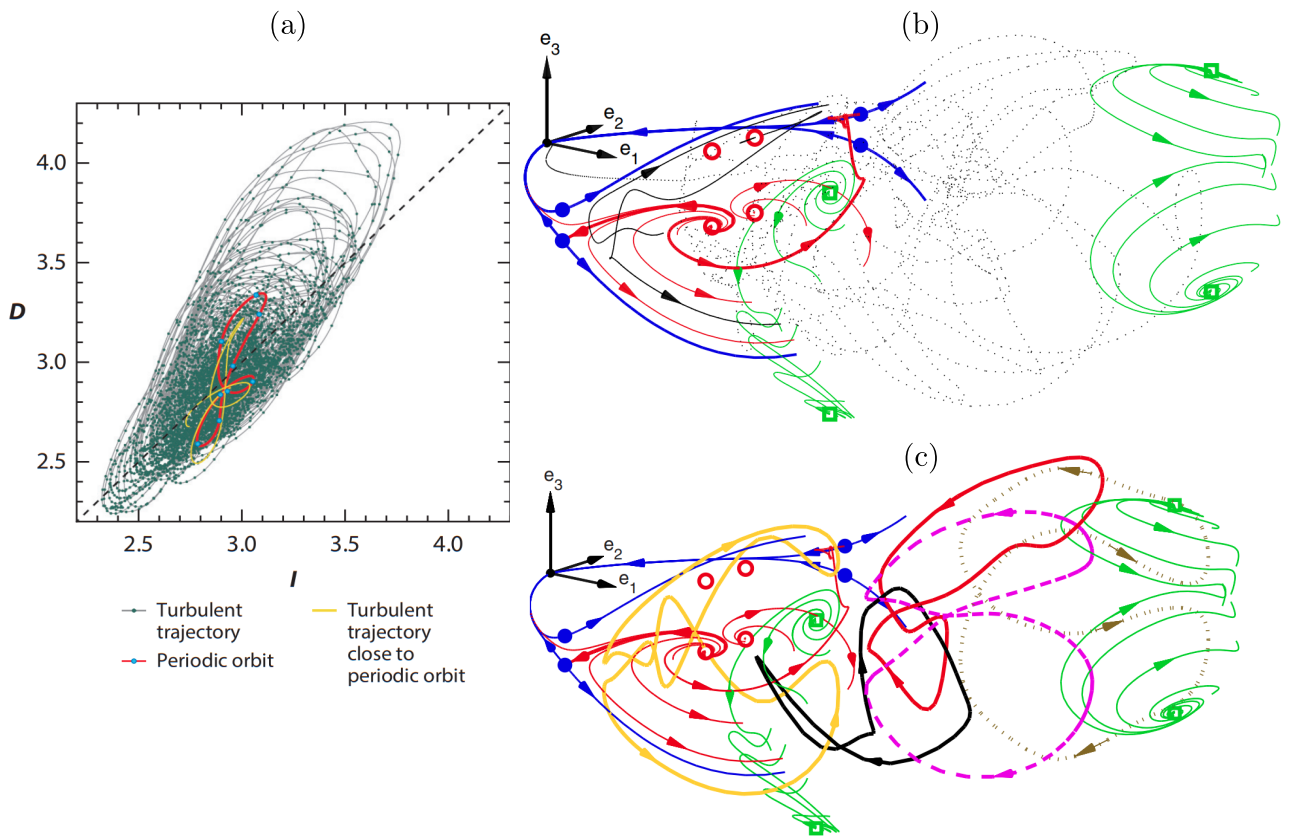


Figure 1.5: (a) Chaotic trajectories of turbulence of plane Couette flow at $Re = 400$, approaching the an unstable periodic orbit (red) highlighted as yellow, adopted from Kawahara and Kida [2001]. (b) State space organisation of turbulence trajectories (black dots) confined around equilibria (circles, dots and squares) and their unstable manifolds (solid lines), heteroclinic connections between them are shown in red. The coordinate system is centered on the laminar state, using a linear combination of the upper branch invariant state. (c) State space projection of five periodic orbits (coloured solid lines), embedded within the same space where turbulence evolves in (b), adopted from [Cvitanović and Gibson, 2010].

A major development came with the identification of a pair of non-trivial, unstable equilibrium states in plane Couette flow [Nagata, 1990]. This pair referred to as the *lower* and *upper* branches, emerging from a saddle node bifurcation which is disconnected from the stable laminar state. The

lower branch lies closer to the laminar state, while the *upper* branch resides further away in state space. Later, a travelling-wave solution in plane Couette flow also later found by the same author [Nagata, 1997]. A family of equilibrium and travelling-wave solutions was found later for plane Couette and plane Poiseuille flows under different boundary conditions (i.e. stress-free, slip and no-slip) were identified by [Waleffe, 2001, 2003], sometimes referred to as *exact coherent states*. Additional equilibria and travelling-wave solutions were identified by Gibson et al. [2008, 2009], along with their heteroclinic connections between them [Halcrow et al., 2009]. In the context of pipe flow, multiple travelling-wave solutions have also been reported [Faisst and Eckhardt, 2003, Wedin and Kerswell, 2004, Kerswell and Tutty, 2007, Wang et al., 2007, Duguet et al., 2008, Pringle et al., 2009]. The set of equilibria, and travelling waves, shows good agreement with the statistical quantities (e.g. mean and fluctuations) with direct numerical simulations. However, since they are equilibria, and travelling-waves (relative equilibria), they do not capture the temporal dynamics of turbulence such as the *self-sustaining process* (SSP) [Hamilton et al., 1995]. While these unstable solutions demonstrate good agreements with results from DNS such as the spanwise length scales, and mean and fluctuations, they do not capture the dynamical processes.

The next breakthrough was on the identification of time-dependent invariant solutions in the form of periodic orbits. Kawahara and Kida [2001] computed a pair of periodic orbits in plane Couette, with one exhibiting a single regeneration cycle similar to the SSP while the other exhibits mild modulation of streaks. These periodic orbits are connected via heteroclinic trajectories. In plane Poiseuille flow, Toh and Itano [2003] also identified periodic orbits displaying bursting behaviour. Using a Newton–Krylov iteration with a hook-step modification, Viswanath [2007] computed multiply relative periodic orbits. These studies conceptualise that the chaotic trajectories of turbulence as being embedded within a set of unstable periodic orbits, evolving along their unstable manifolds [Viswanath, 2007, Gibson et al., 2008, 2009, Halcrow et al., 2009, Graham and Floryan, 2021]. An example is shown in figure 1.5, where the chaotic trajectories in figure 1.5(b), reside within the same state space as the periodic orbits, enclosed by equilibria and their heteroclinic connections shown in figure 1.5(c). The set of equilibria, travelling waves and their relative counterparts, are referred to as *invariant solutions* offering a building block description of turbulence. However, they do not provide insight into the transition process, since these solutions already reside in the turbulent attractor.

The transition to turbulence in canonical shear flow configurations are typically subcritical, emerging from the invariant solutions described above, accompanied by an underlying stable laminar state. A consequence of this is that the laminar and turbulent states form a bistable attractors in phase space. The laminar and turbulent states coexist as stable attractors, with a boundary—known as the *edge*, separating their respective basins of attraction. Attractors that sit along this edge have been identified and found to possess a saddle-like structure, attracting trajectories within the edge and repelling them toward either the laminar or turbulent state, known as *edge states*. The algorithm to identify such states, known as edge tracking, was first employed in pipe flow experiments Schneider et al. [2007], where the it chaotic. Time-averaging of this chaotic attractor revealed a close resemblance to the unstable lower branch travelling-wave solutions, suggesting that the edge separating basin of attraction between the laminar and turbulent states consist of the lower branch solutions and their symmetries [Duguet

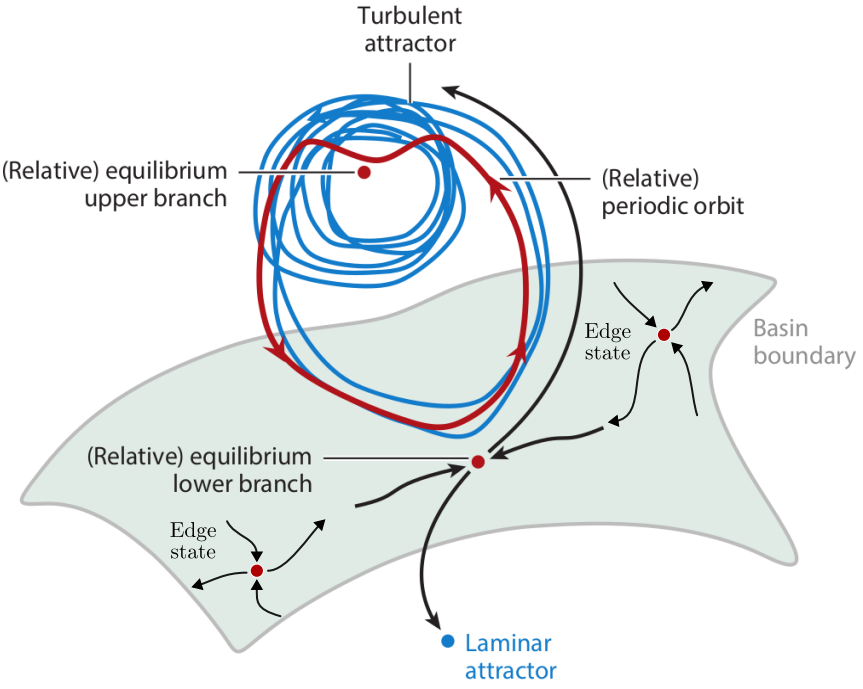


Figure 1.6: A graphical representation of the edge (grey surface) separating the basin of boundary of the laminar and turbulent attractor, consisting of attractors, known as edge states, adapted from [Graham and Floryan \[2021\]](#).

[et al., 2008, Pringle et al., 2009](#)]. As Reynolds number increases, the edge and the turbulent attractor moves apart [[Schneider and Eckhardt, 2009](#)]. In the context of pipe flows, it was recognised that the edge consists of a set of unstable travelling-wave solutions connected to the lower branch. A graphical representation of the edge, and edge states, separating the laminar the turbulent states is shown in figure 1.6. Near the onset of subcritical turbulence, turbulence appear to be transient, decaying towards the laminar solution after a finite lifetime [[Bottin et al., 1998, Faisst and Eckhardt, 2004, Hof et al., 2006](#)] This may be interpreted as the turbulent attractor colliding with the lower branch solution (i.e. the edge) through a *boundary crisis* [[Lai and Tél, 2011](#)], where the chaotic attractor becomes *leaky*, providing an avenue for the solution trajectory towards relaminarisation [[Kreilos and Eckhardt, 2012, Zammert and Eckhardt, 2015](#)].

1.2.3 Spatiotemporal transitional flows

This section describes the inherent spatiotemporal structure of subcritical turbulence near the onset commonly reported in large extended domains. In this regime, turbulence is characterised by the coexistence of turbulent and laminar structures. Examples of such are found in canonical shear flow systems such as plane Couette flows [[Prigent et al., 2003, Barkley and Tuckerman, 2005, 2007, Tuckerman and Barkley, 2011, Duguet et al., 2010, Reetz et al., 2019](#)], Taylor-Couette flows [[Prigent and Dauchot, 2002, Prigent et al., 2003](#)], pipe flows [[Avila et al., 2010, 2011, Song et al., 2017, Avila et al., 2023](#)] and plane Poiseuille flows [[Tsukahara et al., 2014a,c, Tuckerman et al., 2014, Tsukahara et al., 2014b, Gomé et al., 2020, Paranjape, 2019, Paranjape et al., 2020, 2023](#)].

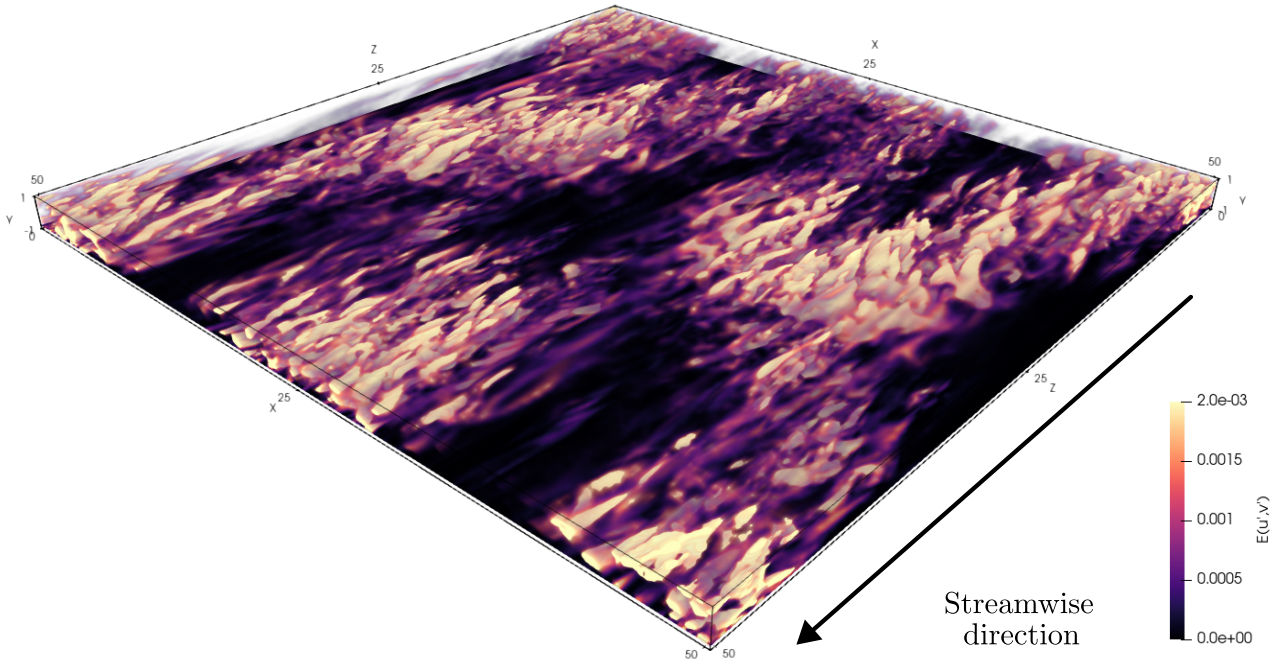


Figure 1.7: A snapshot of turbulent-laminar bands at $Re = 1400$ in a large domain $L/d = 8\pi$, depicting its spatiotemporal intermittent nature. Isovolumetric renderings are based on the spanwise, u' , and wall-normal, v' , perturbation kinetic energy, $E(u', v') = 1/2(u'^2 + v'^2)$, where the perturbation velocities are defined about the laminar state $\mathbf{u}'(\mathbf{x}, t) = \mathbf{u}(\mathbf{x}, t) - U_{lam}(y)$.

We will focus on the plane Poiseuille flow configuration, where the spatiotemporal intermittent patterns are referred to as oblique turbulent-laminar bands illustrated in figure 1.7 at $Re = 1400$ for $L/h = 16\pi$. The bright and dark regions highlight coexisting spatially localised turbulent and laminar regions. These turbulent-laminar bands occur over a range of Reynolds numbers, and its precise range is likely dependent on the domain's aspect ratio [Tsukahara et al., 2014b, Tuckerman et al., 2014, Paranjape et al., 2023]. Near the upper Re threshold of this regime, the domain is fully engulfed by developed turbulent regions, referred to uniform, featureless turbulence appearing at $Re = 1800$ in figure 1.7(a). As Re decreases towards $Re = 1050$, spatiotemporal turbulent and laminar structures known as turbulent-laminar bands persist in between $Re \in [1050, 1600]$ shown in figures 1.8(b-f). In particular, these turbulent-laminar bands appear to have a preferred inclined angle, between $20^\circ \sim 30^\circ$, with streamwise wavelengths of $\sim 60h$, and spanwise wavelengths of $\sim 20h - 30h$ [Tsukahara et al., 2014b]. Kashyap et al. [2022] considered the linear response of the fluctuating turbulent field, and showed that the preferred band angle emerges near 23.2° . In the minimal band unit (MBU) studies of plane Poiseuille flows, the turbulent bands convect at about $\sim 1\%$ of the bulk velocity, propagating either upstream or downstream, depending on Re [Tuckerman et al., 2014, Gomé et al., 2020]. Notably, the spanwise lengths of the bands are much wider than the half-heights and depends on Re , appearing

at $\lambda_z \sim 20h$ $Re \gtrsim 1400$ and $\lambda_z \sim 40h$ for $Re \lesssim 1100$. Interestingly, the bands alternate between both spanwise lengths between the Re range, merging and splitting continuously [Tuckerman et al., 2014], reminiscent of a puff splitting in pipe flows [Avila et al., 2011]. An example of this could be observed in $Re = 1050$, where the band appears to alternate between different spanwise wavelengths in figure 1.8(f). As Re falls below a certain Re threshold, turbulent bands spontaneously decay and relaminarises [Tuckerman et al., 2014, Gomé et al., 2020]. An example is shown in figure 1.8(g).

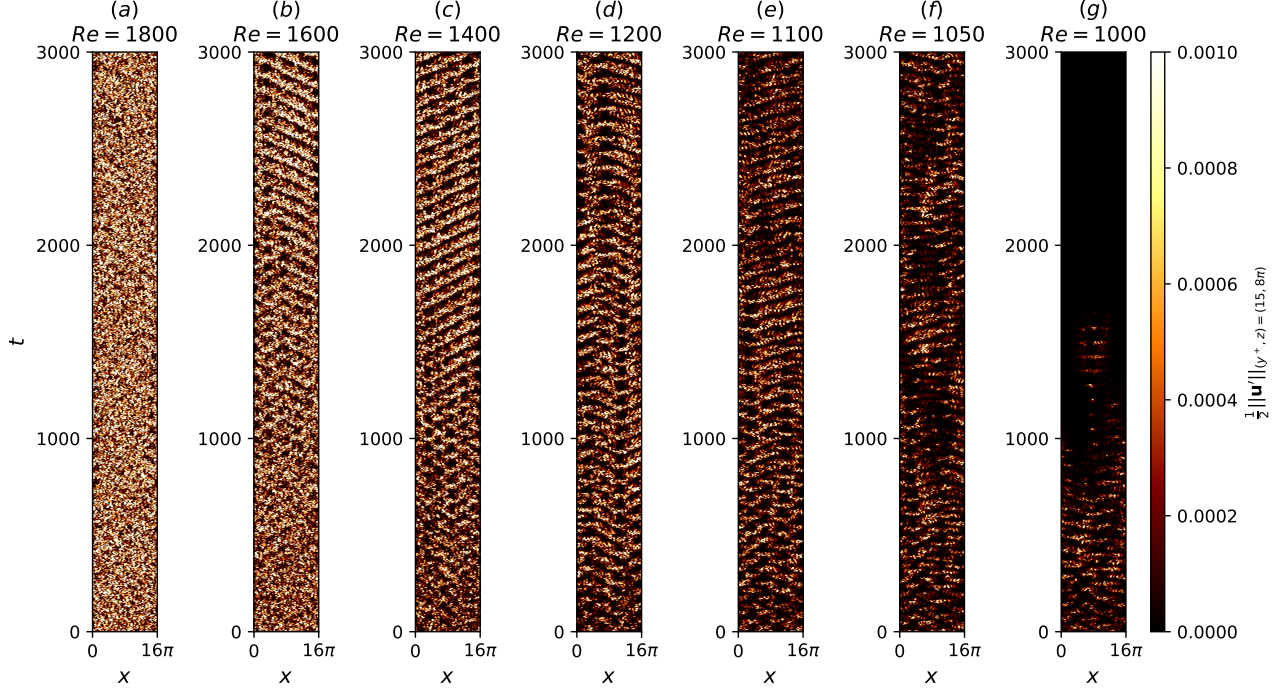


Figure 1.8: Turbulent-laminar bands for $t \in [0, 3000]$ in large domains $(L_x, L_z) = (16\pi, 16\pi)$ at (a) $Re = 1800$, (b) $Re = 1600$, (c) $Re = 1400$, (d) $Re = 1200$, (e) $Re = 1100$, (f) $Re = 1050$, (g) $Re = 1000$.

Gomé et al. [2020] computed the probability distributions for turbulent-laminar band decay, $P(\Delta t^d)$, where Δt^d is the time until decay. A key insight is that the probability distributions of turbulent band decay mimics a memoryless Poisson process,

$$P(\Delta t^d) = \exp(-\Delta t^d/\tau^d(Re)), \quad (1.13)$$

where $\tau^d(Re)$ refers to the mean lifetime for decay as a function of Re . Similarly, the band splitting process also follows a Poisson process

$$P(\Delta t^s) = \exp(-\Delta t^s/\tau^s(Re)), \quad (1.14)$$

with $\tau^s(Re)$ the mean splitting lifetime. Both τ^d and τ^s exhibit superexponential dependence on Re ,

$$\tau^{d,s} = \exp(\exp(Re)), \quad (1.15)$$

This is shown in figure 1.9, with a crossover point at $Re_{cross} \approx 965$, where both decay and splitting

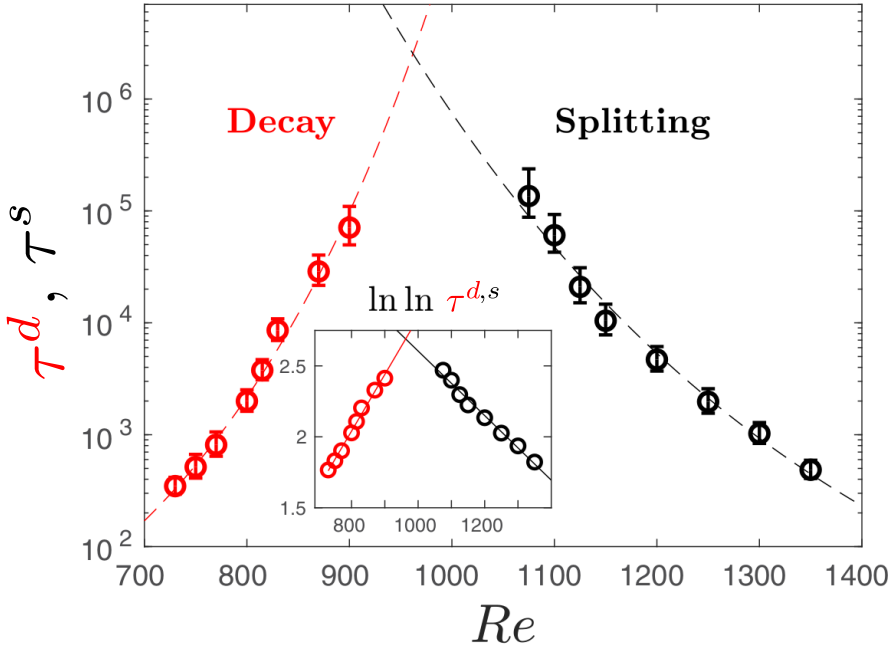


Figure 1.9: The mean decay times (red), τ^d , and mean splitting times (black), τ^s , as a function of Reynolds number, leading to a crossover point at $Re_{cross} \approx 965$, adapted from [Gomé et al., 2020].

becomes equally probable. This crossover point is considered as the critical Reynolds number for the onset of turbulent bands.

While there has been progress made towards our understanding of infinitely periodic turbulent-laminar bands in MBUs, recent studies of isolated (non-periodic) turbulent bands (ITBs) reveal different behaviour. Notably, ITBs persist at Reynolds number below Re_{cross} at $Re = 700$ for durations exceeding $t = 10000$, exceeding the mean decay lifetime in figure 1.9. The ITBs are characterised by streak generating head and a diffusive upstream tail. [Xiong et al., 2015, Tao et al., 2018, Shimizu and Manneville, 2019, Xiao and Song, 2020]. We conclude our discussion on transitional wall-bounded shear flows.

1.3 Rayleigh-Bénard convection

Rayleigh-Bénard convection (RBC) is a paradigmatic fluid configuration describing the motion of the fluid confined between two infinite-parallel plates heated from below and cooled from the top. As the bottom plate is heated, the bottom layer fluid becomes more buoyant and tends to rise, while the colder top fluid layer becomes relatively less buoyant and tends to sink, leading to an overturning of layers. Viscous forces between neighbouring fluid parcels act to resist the motion. As buoyancy overcomes these viscous forces, the fluid layers overturn, resulting in the initiation of buoyancy-driven convection, the physical mechanism underpinning RBC.

One of the earliest experimental studies dedicated to buoyancy-driven convection was conducted by Henri Bénard [Bénard, 1901], who observed the formation of hexagonal convection cells above a certain temperature threshold ΔT . These hexagonal patterns are referred to as Bénard cells are illustrated in figure 1.10(a) (adapted from [Koschmieder and Pallas, 1974]). Subsequently, Rayleigh

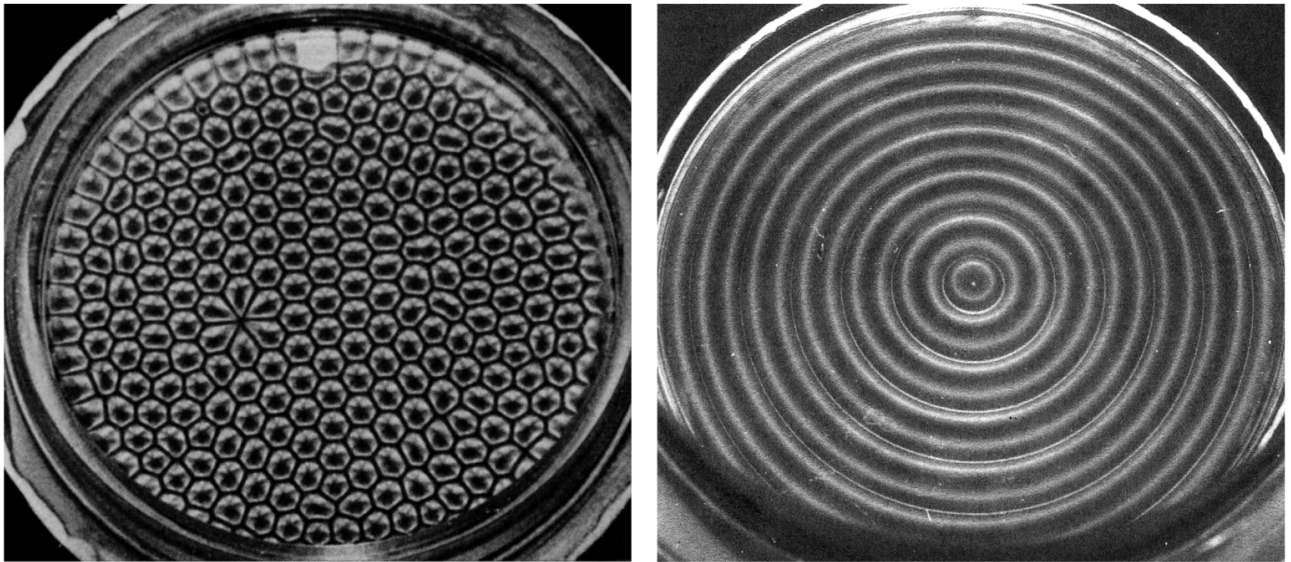


Figure 1.10: (a) Surface tension driven convection leading to the onset of hexagonal Bénard cells in a thin layer of silicone oil, heated from below and cooled by ambient air. A diamond defect appears, likely caused by plate imperfections. (b) Buoyancy driven convection in rigid plates, resulting to concentric convection rolls at 2.9 times the critical Rayleigh number. Both experiments were performed by Koschmieder and Pallas [1974], and the convection patterns were illuminated by aluminum powder, where the dark and bright regions refer to vertical and horizontal motions resepctively. These higher resolution images were taken from [Van Dyke and Van Dyke, 1982].

[1916] carried out one of first linear stability analyses of buoyancy-driven convection, predicting the onset of convection at a critical Rayleigh number of $Ra_c = 657.5$. However, Rayleigh's analysis assumed an idealised free-free boundary conditions, which differed from the rigid-free setup of Bénard's experiment. The linear stability analysis for rigid-free configuration was later performed by Jeffreys [1928] yielding a higher critical Rayleigh number of $Ra_c = 1058$. In the rigid-rigid configuration, the critical Rayleigh number increases further to $Ra_c = 1708$ [Pellew and Southwell, 1940]. The Rayleigh number in Bénard's original experiment contradicted results from linear stability analysis as it was found to be 300 to 1500 smaller than Ra_c for the free-free and rigid-free cases respectively [Wesfreid, 2017]. This contradiction, not recognised by Bénard at the time, lies in the significant role of surface tension in thin fluid layers exposed to air, now known as Bénard-Maragoni (BM) convection [Block, 1956, Cloot and Lebon, 1984, ?, Wesfreid, 2017]. In BM convection, fluid motion is primarily driven by surface tension gradients due to variations of temperature, forming hexagonal cells, as in figure 1.10(a). The preference for hexagonal cells in BM convection was later confirmed based on weakly nonlinear stability analysis [Cloot and Lebon, 1984]. As the fluid layer becomes thicker, surface-tension effects diminish and buoyancy-driven convection becomes dominant. Similarly, placing a rigid lid on top of a thin fluid layer suppresses surface-tension effects, resulting in buoyancy-driven convection. The preferred convection patterns based on weakly nonlinear stability analysis are the two-dimensional parallel rolls, now referred to as ideal straight rolls (ISRs) [Schlüter et al., 1965, Bodenschatz et al., 2000]. In circular ontainers, the ISRs conform to the geometry of the boundaries, forming concentric convection rolls illustrated in figure 1.10(b). Interestingly, hexgaonal

cells have been observed in buoyancy-driven flows of non-Boussinesq fluids [Hoard et al., 1970, Bodenschatz et al., 2000]. In this thesis, I will consider the RBP setup (and RBC in chapter 4) with rigid-rigid boundary conditions with for which the critical Rayleigh number is $Ra_c = 1708$. Notably, the corresponding critical wavelength is $q_c = 3.12/d$ (or $\lambda_c \approx 2d$), suggesting that distance separating the plates, d , dictates the length of a single roll, $l_{roll} = \lambda_c/2 \approx d$.

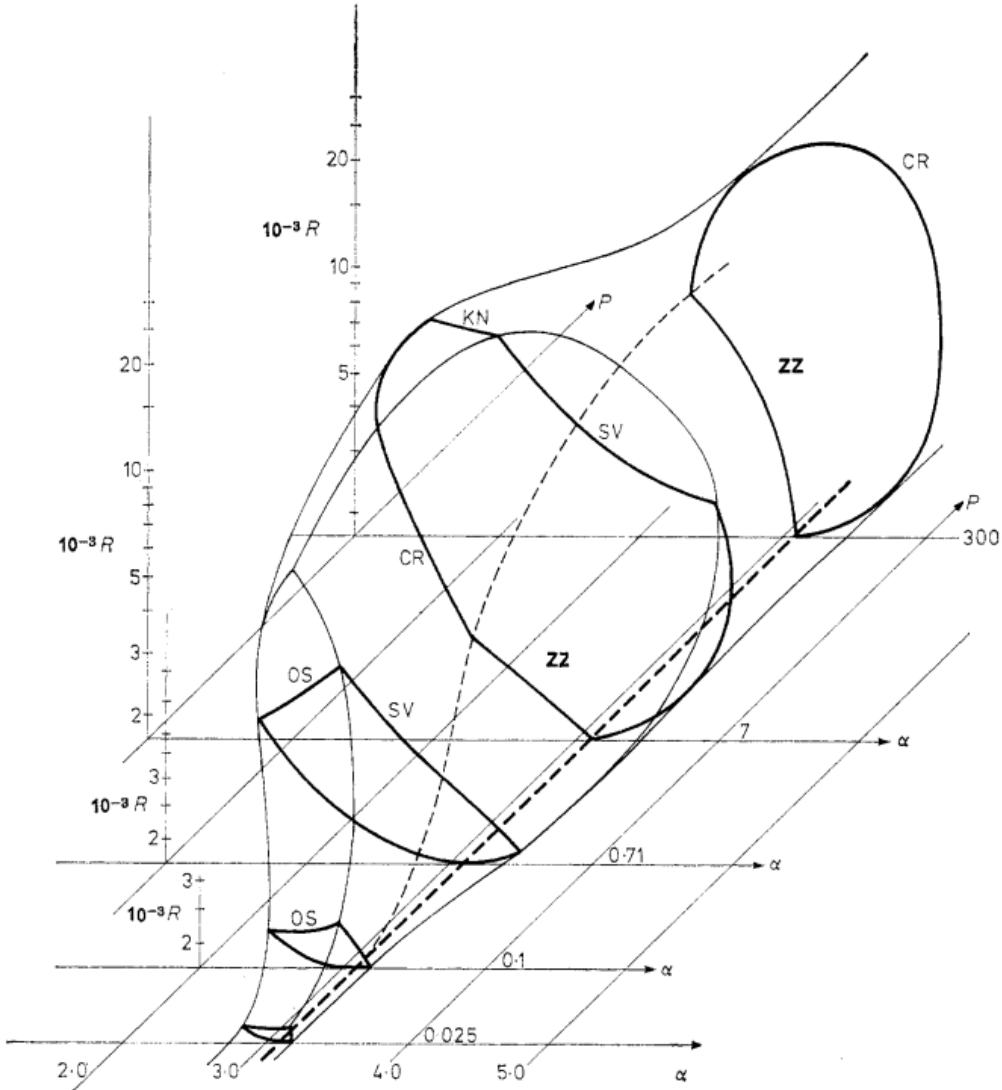


Figure 1.11: The Busse balloon describes the stability boundaries of ISRs in a $\varepsilon - q$ space. For larger wavenumbers, the instability mechanism is described by the skewed-varicose (SV) instability. For smaller wavenumbers, the instability mechanism is described by the Eckhaus instability. For large ε , the instability is described by the onset of oscillatory instability. Busse balloon digitised from [Plapp, 1997] for $Pr \approx 1$.

As mentioned earlier, stationary ISRs near q_c emerge just above Ra_c , based on weakly nonlinear stability analysis. [Eckhaus, 1965, Schlüter et al., 1965]. However, this prediction contradicted by the emergence of time-dependent oscillatory ISRs in experiments [Rossby, 1969, Willis and Deardorff, 1970] at $Ra = 9200$ (or roughly five times Ra_c), where weakly nonlinear stability becomes inapplicable far from threshold. To address this, a direct secondary stability analysis was employed to study the stability of ISRs further from Ra_c , based on Galerkin truncation [Busse, 1972]. One of the key results

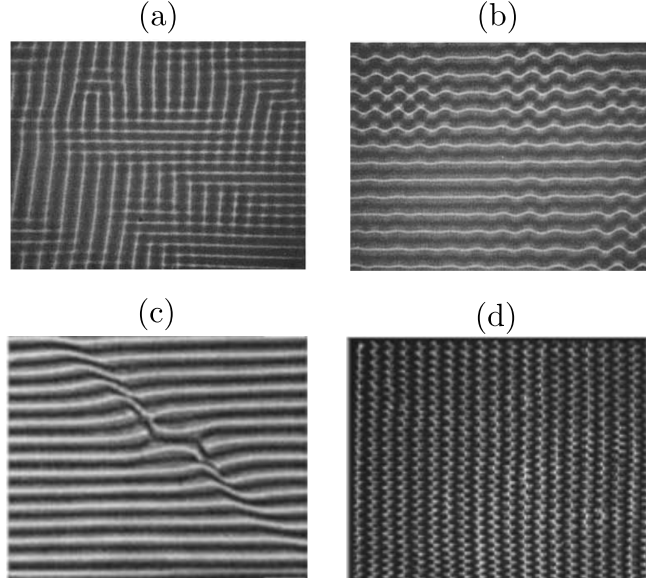


Figure 1.12: ISRs experiencing (a) cross-roll instability at $Ra = 3000, Pr = 100$ and (b) zig-zag instability at $Ra = 3600, Pr = 100$ [Busse and Whitehead, 1971]. (c) Skew-varicosed instability at $Ra = 5568, Pr = 1$ [Plapp, 1997], and (d) oscillatory instability at $Ra = 10384, Pr = 1$ [Cakmur et al., 1997a].

from this analysis is the Busse balloon, which describes the stability boundaries of ISRs as a function of Ra and Pr , and roll wavenumber, α , shown figure 1.11 [Busse, 1978]. The boundaries of the Busse balloon are described by a range of secondary instabilities, each arising from different physical mechanisms [Busse, 1978]. At large Prandtl numbers, $Pr = O(10^2)$, the zig-zag (ZZ) and cross-roll (CR) instabilities delimits the balloon for small and large roll wavenumbers. The zig-zag instabilities cause zig-zag undulations while the CR instabilities generates rolls orthogonal to the underlying ISR structure, effectively increasing or decreasing the roll wavenumber respectively [Busse and Whitehead, 1971]. Examples of these instabilities at $Pr = 100$ are illustrated in figure 1.12(a,b).

At moderate Prandtl numbers, $Pr = O(1)$, the Busse balloon is bounded by the skewed varicosed (SV) for high roll wavenumbers and the oscillatory (OS) instability at large Ra . The skewed-varicosed (SV) instability leads to roll-pinching where pinched rolls merged into a single roll, reducing roll wavenumber while the oscillatory instability leads to the onset of an oscillatory ISRs. Examples of the respective instabilities at $Pr = 1$ are shown in figure 1.12(c,d). At higher wavenumbers, the skewed varicose (SV) instability becomes relevant at intermediate Prandtl numbers, characterised by roll pinching and merging that effectively reduces the roll wavenumber. Finally, the Eckhaus instability (not shown), related to the symmetry of the system, appears close to the Ra_c , leading a disturbance parallel to the underlying rolls which either creates or destroy rolls such that the resultant roll wavenumber adheres to the stability boundaries [Lowe and Gollub, 1985]. Near $Pr = 1$, the Eckhaus instability coincides with the crossroll instability (figure 6 from Bodenschatz et al. [2000], adapted from Plapp [1997].)

In this thesis, we focus on fluids with $Pr = 1$, where secondary instabilities such as skewed-varicose, Eckhaus and cross-roll instabilities typically arise. While the stability boundaries of the Busse balloon have been experimentally verified [Busse and Whitehead, 1971, Croquette, 1989a,

[Plapp, 1997], accurately predicting the wavenumber of ideal straight rolls (ISRs) remain difficult due to hysteresis and the existence of multiple stable ISRs of different roll wavenumbers. As Ra continuously increases, ISRs with wavenumbers outside the Busse Balloon undergo the secondary instabilities (described above) that drive their wavenumbers back to the stable boundaries. The hysteretic behaviour highlights that the roll wavenumber of the ISRs is strongly dependent on the system's history [Bodenschatz et al., 2000].

It is worth noting that the ISRs are the exception rather than the rule in RBC [Croquette, 1989b]. A range of non-ISR states, such as squares, travelling or stationary target patterns, giant rotating spirals, and oscillatory convection, have been observed over the years [Le Gal et al., 1985, Croquette, 1989a, Plapp, 1997, Hof et al., 1999, Rüdiger and Feudel, 2000, Borońska and Tuckerman, 2010a,b]. For example, Hof et al. [1999] identified eight stationary and two oscillatory state in cylindrical RBC with small aspect ratios at the same Rayleigh number. These results were later verified in numerical simulations and bifurcation analysis, reveal up to twelve stable branches near the onset ($Ra \leq 2500$) and the potential for hundreds more as Ra increases [Ma et al., 2006, Borońska and Tuckerman, 2010a,b].

In larger domains ($\Gamma \geq 28$), giant rotating spirals were found and have been investigated [Plapp and Bodenschatz, 1996, Plapp et al., 1998]. Experimental and numerical studies of RBC with varying sidewall boundary conditions (i.e. thermally insulating, conducting and no-slip) [Tuckerman and Barkley, 1988, Siggers, 2003, Paul et al., 2003, Bouillé et al., 2022], non-Boussinesq convection [Bodenschatz et al., 1992], and rotational effects [Hu et al., 1997] were investigated, where multiple states were also reported. In inclined RBC, Reetz and Schneider [2020], Reetz et al. [2020] identified up to sixteen stable and unstable invariant states, along with heteroclinic orbits connecting them. These findings indicate that RBC support a rich variety of coexisting stable states beyond ISRs, resulting to a system with multiple stable states above the critical Rayleigh number. To complicate matters further, RBC also exhibits spatiotemporal chaotic states.

In the late 1990s, convection rolls exhibiting spatio-temporal chaotic behaviour known as spiral defect chaos (SDC) were observed within the same stability boundaries where ISRs were expected [Morris et al., 1993, Hu et al., 1993, Decker et al., 1994, Hu et al., 1995, Morris et al., 1996, Cakmur et al., 1997a, Ahlers, Egolf et al., 1998, 2000, Chiam et al., 2003, Vitral et al., 2020]. Notably, ISRs emerge with carefully prepared initial conditions while uncontrolled initial conditions lead to SDC. It is now well established that SDC exists as intrinsic attractor of RBC, independent of sidewall conditions Morris et al. [1996], forming a bistable system with ISRs [Cakmur et al., 1997a] across a range of Ra at $Pr = 1$ illustrated in figure 1.13. However, this bistability appears to be Prandtl number dependent. At $Pr = 4$, the SDC appears to be transient decaying towards ISRs over long periods [Bajaj et al., 1997]. SDC has also been replicated in numerical simulations using two-dimensional Swift-Hohenberg equations [Swift and Hohenberg, 1977, Xi et al., 1993, Xi and Gunton, 1995, Schmitz et al., 2002, Karimi et al., 2011]. The critical Rayleigh number for the onset of SDC, Ra_s , depends on the domain's aspect ratio, and Prandtl number [Hu et al., 1995, Bajaj et al., 1997, Cakmur et al., 1997b, Bodenschatz et al., 2000]. SDC has been primarily reported in large aspect ratio domains ($\Gamma \gtrsim 20$), suggesting a minimal domain size for SDC to occur [Bodenschatz et al.,

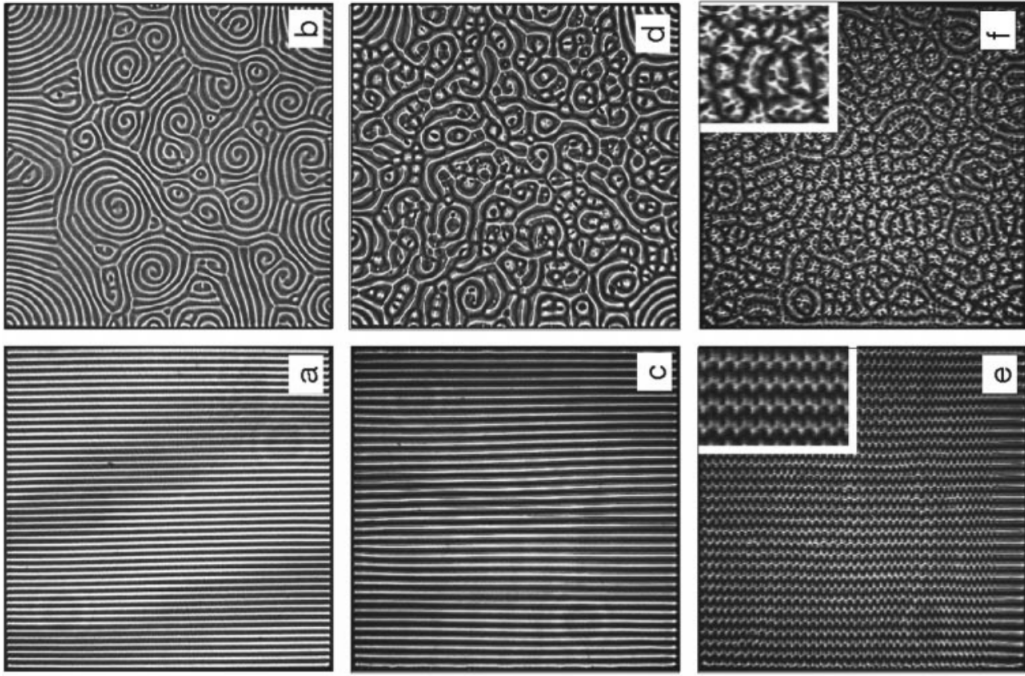


Figure 1.13: The coexistence of spiral defect chaos (SDC, top row) and ideal straight rolls (ISRs, bottom row) at (a,b) $Ra = 3279$, (c,d) $Ra = 6832$ and (e,f) $Ra = 10384$. The domain size is $\Gamma = 50$ and $Pr = 1$, adapted from Cakmur et al. [1997a].

2000]. Furthermore, the leading Lyapunov exponents of SDC decreases as Γ [Egolf et al., 2000, Paul et al., 2007]. To better characterise SDC, several studies have investigated its spatial-temporal properties, such as the averaged roll-curvature Hu et al. [1995], probability distribution of spirals Ecke et al. [1995], Liu and Ahlers [1996] and correlation length-/time-scales [Morris et al., 1993, 1996, Cakmur et al., 1997b]. Specifically, the correlation length-scales were found to grow exponentially with [Morris et al., 1993, 1996, Cakmur et al., 1997b], suggesting that transition from ISRs to SDC resembles a phase transition. Similar spatiotemporal chaotic behaviour has been observed in other pattern-formation systems, including rotating RBC Hu et al. [1997], dielectric barrier discharge Dong et al. [2005] and advection diffusion reaction systems Affan and Friedrich [2014].

1.4 Rayleigh-Bénard Poiseuille (RBP) flows

This section describes the development of Rayleigh-Bénard Poiseuille (RBP) flows, integrating key findings from both plane Poiseuille flow (PPF) and Rayleigh-Bénard convection (RBC) systems discussed in § 1.2 and § 1.3 respectively. The neutral stability curves in the Rayleigh-Bénard Poiseuille (RBP) comprising of both plane Poisueuille flow (PPF) and Rayleigh-Béanrd convection (RBC) systems, are bounded by the onset of Tollmien-Schlichting waves at $Re_c = 5772.22$ [Orszag, 1971], and by the onset of convection rolls at $Ra_c = 1708$ [Pellew and Southwell, 1940], respectively. In RBP systems, the imposed mean Poiseuille flow in the RBP system breaks the rotational symmetry of the convection rolls, categorising them based on their orientation to the mean flow direction, namely: longitudinal, transverse and oblique rolls. These primary instabilities were first investigated by Gage and Reid [1968] in an infinitely extended layer. For longitudinal rolls, the linearised system

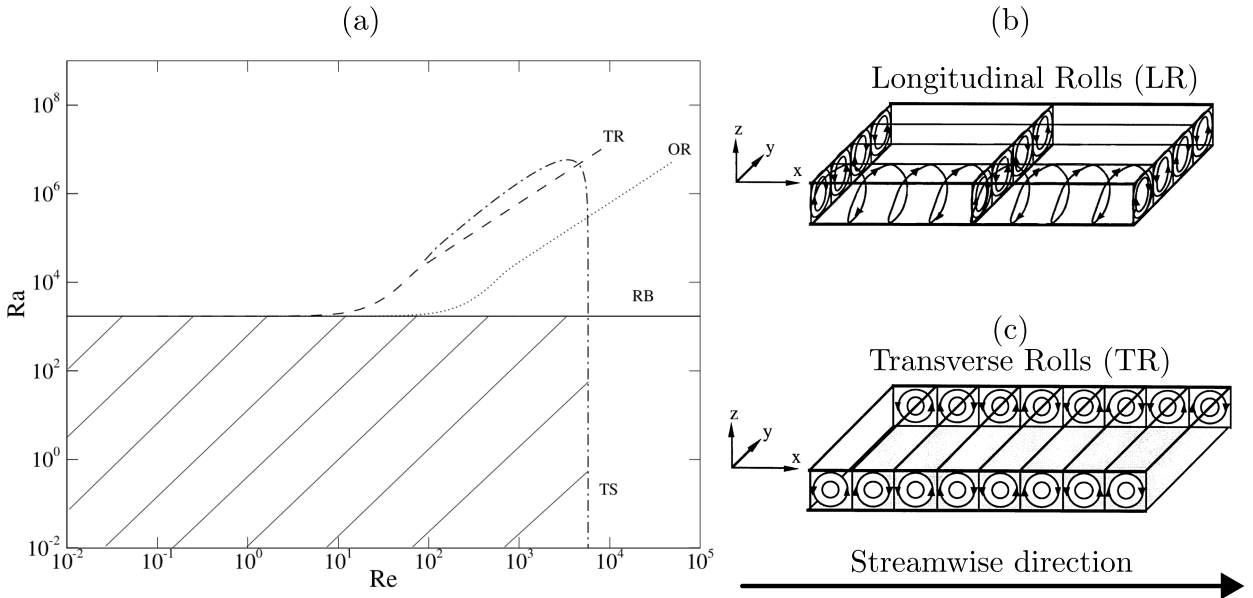


Figure 1.14: (a) Neutral stability curves of longitudinal rolls (LR), oblique rolls (OR), transverse rolls (TR) and Tollmien-Schlichting (TS) waves, adapted from John Soundar Jerome et al. [2012]. The shaded area refers to damped perturbations. Sketch of (b) longitudinal and (c) transverse rolls, adapted from Kelly [1994].

reduces to the classical RBC problem. Thus, the critical Rayleigh number remains unchanged at $Ra_{\parallel} = Ra_c = 1708.8$ with a critical wavenumber, $\alpha_{\parallel} = \alpha_c = 3.13$, independent of Reynolds number Re and Prandtl number Pr [Pellew and Southwell, 1940, Kelly, 1994]. In contrast, the critical Rayleigh number for the onset of transverse rolls increases with Re , dependent on Pr [Gage and Reid, 1968, Müller et al., 1992, Nicolas et al., 1997]. The critical Rayleigh number for the onset of oblique rolls can be derived using by applying a Squire transformation [Squire, 1933] to transverse roll system. For a given Ra , the corresponding critical Re for the onset of oblique rolls is higher than that for transverse rolls [Gage and Reid, 1968]. The neutral stability curves for the three different rolls are illustrated in figure 1.14.

Experimental studies in channels with large transverse aspect ratios (i.e. span-to-depth) showed the onset of longitudinal rolls [Akiyama et al., 1971, Ostrach and Kamotani, 1975, Fukui et al., 1983], while transverse rolls are more prevalent in narrower channels [Luijkx et al., 1981, Ouazzani et al., 1989, 1990]. Linear stability analysis of longitudinal rolls for finite channels confirms that Ra_{\parallel} remains fairly independent for transverse aspect ratios greater than five, and increases quickly below that. Hence, for small Re , critical Rayleigh number of transverse rolls is smaller than that of longitudinal rolls, $Ra_{\perp} < Ra_{\parallel}$, giving rise to transverse rolls [Nicolas et al., 2000]. However, temporal linear stability analysis could not explain the observations by Ouazzani et al. [1990], where the laminar Poiseuille flow persisted in the same parameter space where transverse rolls were expected. This discrepancy was resolved by Müller et al. [1992], who showed that transverse rolls may be convectively or absolutely unstable, with the transition boundary aligning with the experimental data. Later, Carrière and Monkewitz [1999] showed that demonstrated that longitudinal rolls are always convectively unstable. Nonmodal stability analysis of subcritical RBP by John Soundar Jerome et al. [2012] revealed that the

optimal transient growth is primarily dominated by streamwise rollers similar to those of PPF [Reddy and Henningson, 1993], with a spanwise wavenumber of $\beta_{opt} \approx 2.05$. The maximum amplification factor, G_{max} increases modestly with Ra , and the critical wavenumber approaches α_{\parallel} , indicative of longitudinal rolls.

For $Re > 0$ in infinite domains, the longitudinal rolls emerge as the dominant primary instability [Gage and Reid, 1968], and their secondary stability was analysed by [Clever and Busse, 1991]. They identified a time-dependent, wavy instability near $Re \sim 100$, giving rise to tertiary solutions in the form of wavy rolls. These wavy rolls have been observed experimentally and were found to be convectively unstable [Pabiou et al., 2003, 2005, Nicolas et al., 2010]. Clever and Busse [1991] also hypothesised that the wavy rolls are less efficient at transporting heating than longitudinal rolls for the same Ra , which was later confirmed numerically [Nicolas et al., 2012]. The influence of finite transverse aspect ratios on the onset of wavy rolls have also been studied [Xin et al., 2006, Nicolas et al., 2010], where the critical Ra was found to be approximately 1.5 times higher than in infinite domains Clever and Busse [1991]. Furthermore, the effect of external excitation has been explored, showing that increased excitation amplitude can reduce the development length required for wavy roll formation [Nicolas et al., 2010, 2012]. In the turbulent regime, shear driven turbulence has been shown to enhance heat transport in RBP flows [Scagliarini et al., 2014, 2015, Pirozzoli et al., 2017]. Extensions of the RBP configuration, such as flows over wavy walls or with sinusoidal thermal forcing have been investigated, potentially offering a reduction in drag and enhancing heat transport [Hossain et al., 2012, Hossain and Floryan, 2016, 2020]. For a comprehensive overview of RBP flows, the reader is referred to the reviews by Kelly [1994] and Nicolas [2002].

1.5 Thesis Outline

In this thesis, I am particularly focused on the transition behaviour of fluid flow in RBP systems by conducting direct numerical simulations and linear stability analysis. In particular, the onset of instabilities does not necessarily lead to turbulence, and are neither laminar nor turbulent, as we shall see later. For the sake of terminology, the transitional regimes can be loosely referred to as regimes that are neither laminar nor turbulent. There had been significant progress in our understanding of the instabilities of Rayleigh-Bénard convection and plane Poiseuille flows, their combined effects are not known. The motivation of this thesis is primarily academic, which explores the bridge between RBC and PPF.

The thesis is structured into the follows: §1 provides the background of this thesis, with relevant literature review. §2 presents the numerical methods, which includes the spectral/ hp element method, algorithms for solving the Navier-Stokes equations, linear stability analysis and edge tracking. §3 first presents a $Ra - Re$ phase space of the flow structures in RBP flows with a particular focus on the role of longitudinal rolls in sustaining turbulence as we introduce the *thermally-assisted sustaining process*. §?? presents the state space organisation of the bistability between spiral defect chaos and ideal straight rolls at $Ra = 2903$. We finally conclude this thesis, and present possible avenues of future work in §??.

Chapter 2

Numerical Methods

We will discuss the fundamentals of numerical methods relevant to solving the Navier-Stokes equations. We begin the discussion of the weighted of residuals (§2.1) and the spatial discretisation using spectral/*hp* element methods in one dimension (§2.3). This is followed by techniques for solving the Navier-Stokes equations (§2.4), introducing the velocity-correction scheme, enforcing a constant flow rate and the quasi-3D approach for semi-homogeneous domains. This chapter concludes with numerical techniques for the stability analysis of the Navier-Stokes equations (§2.5), including eigenvalue computation and edge tracking.

2.1 Method of weighted residuals

Spatial discretisation errors, or residuals, arises as one seeks an approximate solution to some partial differential equation (PDE). The method of weighted residual provides a generic mathematical framework in which constraints on the residual could be applied flexibly, defining the spatial discretisation scheme and its convergence properties. In summary, we approximate the solution of PDE by considering a finite expansion of a suitable basis, to which its coefficients are sought after by minimising the inner product between the PDE and a test (or weight) function. To demonstrate this, we consider a linear partial differential equation as,

$$\mathbf{L}[u(x)] = 0, \quad x \in \Omega, \tag{2.1}$$

where \mathbf{L} refers to a linear spatial differential operator subjected to some boundary conditions within the domain, Ω , while $u(x)$ refers to the exact solution of \mathbf{L} . Examples of PDEs with linear spatial differential operators include the Laplace equation, $\nabla^2 u = 0$, Poisson equation, $\nabla^2 u = f$, and the Helmholtz equation, $\nabla^2 u + \lambda u = f$. We suppose that the exact solution $u(x)$ can be approximated (discretised) by N finite number of basis (or expansion) functions, $\Phi(x)$.

$$u(x) \approx u^\delta(x) = \sum_{i=0}^{N-1} \hat{u}_i \Phi_i(x), \tag{2.2}$$

where $u^\delta(x)$ refers to the approximate solution of $u(x)$, consisting of a linear combination of the product between the i^{th} basis coefficient, \hat{u}_i , and the i^{th} global basis expansion, $\Phi_i(x)$, defined within Ω . Since $u^\delta(x)$ is an approximate solution of equation (2.5), we expect a residual (or ‘error’) between the exact solution, $u(x)$, and $u^\delta(x)$,

$$\mathbf{L}[u^\delta(x)] = R[u^\delta(x)], \quad (2.3)$$

where $R[u^\delta(x)]$ refers to the residual which depends on the approximate solution $u^\delta(x)$ and varying within Ω . In other words, equation (2.5) might not be satisfied everywhere in Ω . We need to place restrictions on the residual, such that it the residual approaches zero, $R \rightarrow 0$, and the approximate solution approaches the exact solution, $u^\delta(x) \rightarrow u(x)$. The method of residuals places a restriction on the residual by applying an inner product between the governing equation, and N test (or weight) functions, $v_j(x)$, and setting it to zero,

$$(v_j(x), R[u^\delta(x)]) = 0, \quad j = 0, \dots, N - 1. \quad (2.4)$$

Definition 2.1.1 (Inner product). The inner product between two functions $f(x)$ and $g(x)$ is,

$$(f, g) = \int_{\Omega} f(x)g(x)dx.$$

By setting equation (2.4) to zero, it becomes a system of N ordinary differential equations, where the N basis coefficients, \hat{u}_i . The choice of test function defines the projection methods, and examples of projection methods are shown in table 2.1. We emphasise that the method of weighted residuals merely describes the projection method, but does not specify the type of basis expansions, as we will discuss later in §2.3. The choice of projection method coupled with suitable basis expansions will have different solution convergence properties. A particular interest is on how quickly the residual vanishes as the number of basis expansions increases. For instance, by considering the Galerkin method coupled with Fourier expansions, one can expect exponential convergence, desirable for an efficient representation of turbulent dynamics.

Weight functions	Projection method
$v_j(x) = \delta(x - x_j)$	Collocation
$v_j(x) = \begin{cases} 1 & \text{if } x \in \Omega_j \\ 0 & \text{if } x \notin \Omega_j \end{cases}$	Finite-Volume
$v_j(x) = \phi_j$	Galerkin
$v_j(x) = \frac{\partial R}{\partial \hat{u}_j}$	Least-squares

Table 2.1: Examples of weight functions and projection methods

2.2 Galerkin Projection

The Galerkin projection remains a standard projection method in the context of the finite element method, where the test functions, $v(x)$, are chosen to be lie in the same functional space as the global basis functions, $\Phi(x)$. To demostrate the Galerkin projection method, we consider that the differential operator earlier in equation (2.1) as a 1D Helmholtz equation,

$$\mathbf{L}[u(x)] \equiv \frac{\partial^2 u(x)}{\partial x^2} - \lambda u(x) - f(x) = 0, \quad x \in \Omega := [0, l] \quad (2.5a)$$

$$u(0) = g_D, \quad \left. \frac{\partial u}{\partial x} \right|_{x=l} = g_N. \quad (2.5b)$$

where λ is a real positive constant, $f(x)$ is a forcing function, and Ω refers to the spatial domain bounded between 0 and l . To ensure that problem is well posed, Dirichlet and Neumann boundary conditions, g_D and g_N , are imposed at $x = 0$ and $x = l$ respectively. Equation 2.5 is commonly referred to as the strong or classical form.

The subsequent step in Galerkin projection methods is take the inner product of the equation (2.5) with a test function, $v(x)$, that satisfies the homogeneous Dirichlet boundary conditions by definition, i.e. $v(0) = 0$, and setting the inner product to zero,

$$(v(x), \mathbf{L}[u(x)]) = \int_0^l v \left[\frac{\partial^2 u(x)}{\partial x^2} - \lambda u(x) + f(x) \right] dx = 0. \quad (2.6)$$

This step is equivalent to applying the method of weighted residuals (§2.1), where $u(x)$ could refer to the approximate solution, $u^\delta(x)$. Next, we perform integration by parts,

$$\underbrace{\int_0^l \frac{\partial v}{\partial x} \frac{\partial u}{\partial x} dx}_{a(v,u)} + \underbrace{\int_0^l \lambda v u dx}_{f(v)} = \underbrace{\int_0^l v f dx}_{f(v)} + \left[v \frac{\partial u}{\partial x} \right]_0^l. \quad (2.7)$$

This equation is typically referred to as the weak ¹ form of equation (2.5). In compact notation, we define the bilinear and linear forms as,

$$a(v, u) = f(v), \quad (2.8a)$$

where $a(v, u)$ and $f(v)$ are typically referred to as the strain energy and forcing function in structural mechanics, required to remain finite. To ensure this, we restrict the choice of solutions $u(x)$ to lie in the solution space, \mathcal{U} , defined as

$$\mathcal{U} := \{u \mid u \in H^1(\Omega), u(0) = g_D\}, \quad (2.9)$$

¹The notions of the *weak* and *strong* are refers to the smoothness (regularity) required of admissible solutions. In the weak formulation, the highest derivative involved is up to first-order, so the solution space is H^1 . This space is generally larger than that of the strong formulation, which required $u \in H^2(\Omega)$. Since $H^2(\Omega) \subset H^1(\Omega)$ the weak formulation imposeds a ‘less stringent’ constraint of the solution space of admissible functions.

where $u \in H^1$ refers to functions of u belonging to Sobolev space of order 1, and satisfying the Dirichlet condition, $u(0) = g_D$, at $x = 0$.

Definition 2.2.1 (Sobolev space). We define Sobolev space of order $n \geq 1$ on Ω ,

$$H^n(\Omega) = \{u \mid u \in L_2(\Omega), D^\alpha u \in L_2(\Omega), \forall \alpha : \alpha \leq n\},$$

where $D^\alpha u$ refers to derivatives up to order α and $L_2(\Omega)$ refers to functions that are square integrable.

Definition 2.2.2 (L_2 space). The space $L_2(\Omega)$ refers to functions that are square integrable,

$$(u, u)_{L_2} = \int_{\Omega} |u(x)|^2 d\Omega < \infty. \quad (2.10)$$

We consider admissible functions up to the first derivatives, the highest order derivative in the weak formulation of equation (2.6). Similarly, the space of test functions, \mathcal{V} , is defined as,

$$\mathcal{V} := \{v \mid v \in H^1, v(0) = 0\}, \quad (2.11)$$

where $v \in H^1$ are refer to test functions belonging to the Sobolev the space of order 1, and is defined to be zero, $v(0) = 0$ on Dirichlet boundary condition, $x = 0$. The generalised weak form is therefore finding $u(x) \in \mathcal{U}$, such that

$$a(v, u) = f(v), \quad \forall v \in \mathcal{V}. \quad (2.12)$$

At this point, equation (2.12) is infinite dimension as the function spaces, \mathcal{U} and \mathcal{V} , contain infinitely many functions. To obtain an approximate solution, $u^\delta(x)$, we restrict ourselves to finite dimensional subspaces, $\mathcal{U}^\delta \subset \mathcal{U}$, and $\mathcal{V}^\delta \subset \mathcal{V}$. The problem is then to find $u^\delta \in \mathcal{U}^\delta$, such that

$$a(v^\delta, u^\delta) = f(v^\delta), \quad v^\delta \in \mathcal{V}^\delta. \quad (2.13)$$

Here, the subspaces $u^\delta \in \mathcal{U}^\delta$ and $v^\delta \in \mathcal{V}^\delta$ are not the same, compare equations (2.9) and (2.11), necessary for the standard Galerkin projection procedure where they should lie in the same subspace. To ensure that they belong to the same space, we lift the solution u^δ into two parts,

$$u^\delta = u^{\mathcal{H}} + u^{\mathcal{D}}. \quad (2.14)$$

where $u^{\mathcal{H}} \in \mathcal{V}^\delta$ satisfies the homogeneous Dirichlet condition (e.g. is zero on Dirichlet boundaries), belonging to the same subsapce as $v^\delta \in \mathcal{V}^\delta$, while $u^{\mathcal{D}} \in \mathcal{U}^\delta$ satisfies the Dirichlet boundary conditions $u^{\mathcal{D}}(0) = g_D$. Hence, the standard Galerkin projection method is to search for the homogeneous solution, $u^{\mathcal{H}} \in \mathcal{V}^\delta$, such that,

$$a(v^\delta, u^{\mathcal{H}}) = f(v^\delta) - a(v^\delta, u^{\mathcal{D}}). \quad (2.15)$$

This concludes the classical Galerkin formulation. Under certain assumptions of a , a solution is guaranteed under the Lax-Milgram theorem [Lax and Milgram, 1955].

2.3 Spectral/ hp element method

We have described the procedure for approximating a solution of a PDE using the classical Galerkin projection technique. However, the spatial discretisation scheme, related to the choice of basis (and test) functions, remains undiscussed. In this section, we discuss the spectral/ hp element method [Patera, 1984], where the solution is partitioned into a set of non-overlapping finite elements of size h , consisting of a linear combination of continuous orthogonal polynomial functions up to order P . It leverages the geometric flexibility of classical finite-element methods, allowing for the representation of complex engineering geometries, and the exponential (spectral) convergence properties of classical spectral methods, where the solution error decreases exponentially. Suppose we consider $P + 1$ linearly independent polynomials spanning the polynomial space of \mathcal{P}_P , the error of a smooth solution with element size of h and polynomial order P has the property of [Karniadakis and Sherwin, 2005],

$$\|u(x) - u^\delta(x)\| \leq Ch^P \|u(x)\| \approx O(h^P). \quad (2.16)$$

where C is some constant. Equation 2.16 implies that the error decreases linearly with h , and exponentially with P . This section is organised into domain partition, standard elements, assembly process, modal and nodal expansion functions, numerical integration and differentiation, concluding with an example in 1D.

2.3.1 Domain partition

The first step concerns the partitioning the domain into a set of (finite) elemental regions. We consider an example in one dimension within Ω , and partition it into a set of N_{el} elements, where Ω^e , refers to the elemental partitions with $1 \geq e \geq N_{el}$, such that they meet at their boundaries and do not overlap,

$$\Omega = \bigcup_{e=1}^{N_{el}} \Omega^e, \quad \text{where } \bigcap_{e=1}^{N_{el}} \Omega^e = \emptyset \quad (2.17)$$

where the e^{th} element is defined as,

$$\Omega^e = \{x \mid x_{e-1} \geq x \geq x_e\}. \quad (2.18)$$

Each element can be represented by a linear combination of orthogonal basis expansions. The basis expansions can be either modal or nodal expansions, as we shall see later.

2.3.2 Standard Elements

In general, we expect to work with non-uniform elements that may have arbitrarily shapes, making the definition of basis expansions potentially unwieldy. To simplify the formulation, it is convenient to define a *standard* element,

$$\Omega_{st} = \{\xi \mid -1 \geq \xi \geq 1\}, \quad (2.19)$$

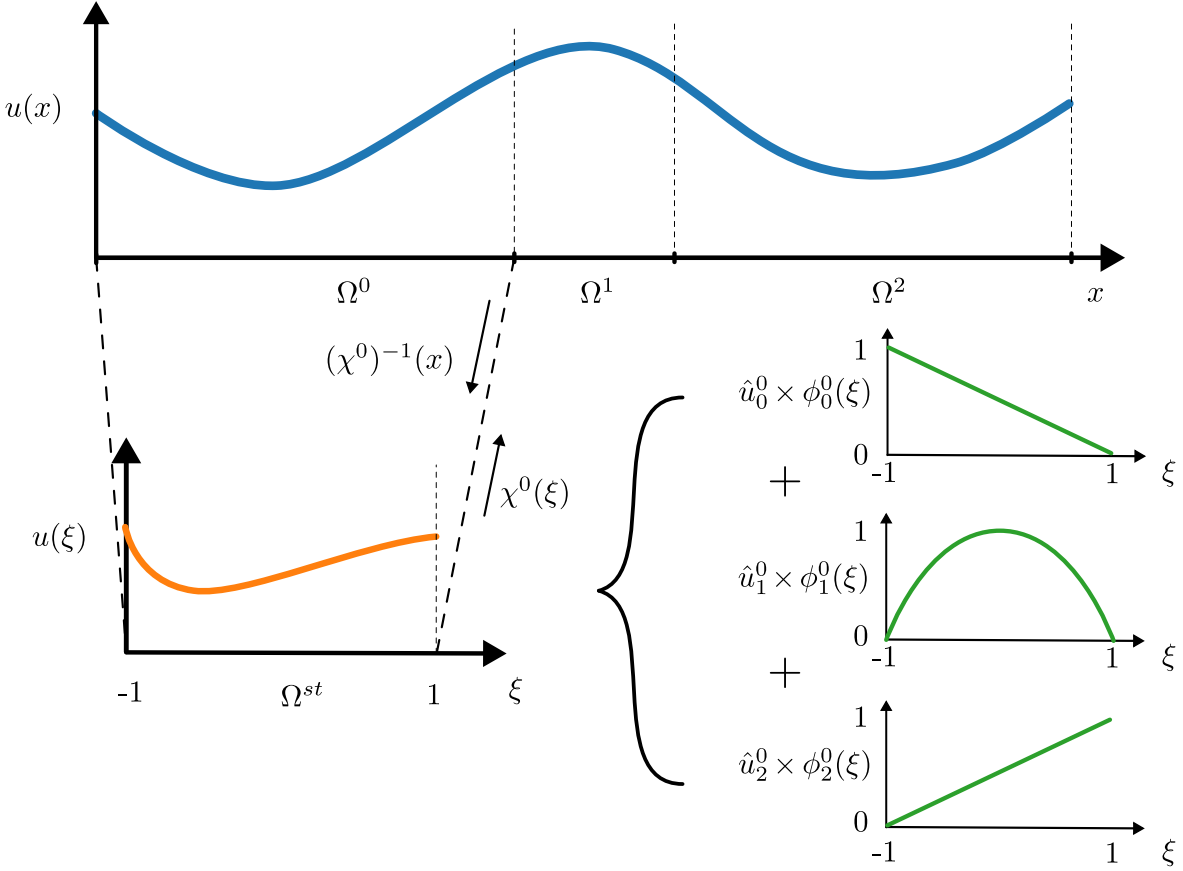


Figure 2.1: A spectral/ hp element representation of $u(x)$, consisting of three non-overlapping finite elements, each containing a linear combination of local expansion bases of up to $P = 2$.

where Ω_{st} refers to the standard element defined in local coordinates, $\xi \in [-1, 1]$. Within this standard element, the formulation of basis expansions, as well as differential and integration operations, can be carried out in the local coordinate system ξ , before mapping the solution back to the global domain, x . We can map the standard element into any arbitrary global coordinates based on a linear mapping $\chi^e : \Omega_{st} \rightarrow \Omega$,

$$x = \chi^e(\xi) = \frac{1 - \xi}{2}x_e + \frac{1 + \xi}{2}x_{e+1}, \quad \xi \in \Omega_{st} \quad (2.20)$$

which has an analytical inverse, $(\chi^e)^{-1}(x)$,

$$\xi = (\chi^e)^{-1}(x) = 2 \frac{x - x_{e-1}}{x_e - x_{e-1}} - 1, \quad x \in \Omega^e. \quad (2.21)$$

For illustration purposes, we consider that the standard element can be represented by three local basis expansions of polynomial order of up to $P = 2$,

$$\phi_0^e(\xi) = \frac{1 - \xi}{2}, \quad \phi_1^e(\xi) = (1 + \xi)(1 - \xi), \quad \phi_2^e(\xi) = \frac{1 + \xi}{2}, \quad (2.22)$$

where ϕ_0^e, ϕ_2^e and ϕ_1^e refers to the linear and quadratic local basis expansions of the e^{th} element. These local basis expansions is illustrated in figure 2.1. We note that the formulations of local basis

expansion here is merely an example. In practice, the local basis expansions are usually chosen to have orthogonality properties under a certain inner product. The approximate solution is now represented as,

$$u^\delta(x) = \sum_{e=0}^{N_{el}-1} \sum_{i=0}^P \hat{u}_i^e \phi_i^e(\chi^e(\xi)). \quad (2.23)$$

where \hat{u}_i^e refers to the local expansion basis coefficients. The approximate solution, $u^\delta(x)$, now lie within the solution space \mathcal{U}^δ defined as,

$$\mathcal{U}^\delta := \{u^\delta \mid u^\delta \in H^1, u^\delta(\chi^e(\xi)) \in \phi_i^e(\xi), \forall i : 0 \leq i \leq P, \forall e : 0 \leq e \leq N_{el}\} \quad (2.24)$$

2.3.3 Global assembly

In this section, we introduce the concept of global assembly (or direct stiffness summation) which relates the global basis expansions (equation (2.2)), $\Phi_i(x)$, to the local basis expansions (equation (2.23)), $\phi_i^e(x)$, where the solution can be approximated using either formulation,

$$u^\delta(x) = \sum_{i=0}^{N-1} \hat{u}_i \Phi_i(x) = \sum_{e=0}^{N_{el}-1} \sum_{i=0}^P \hat{u}_i^e \phi_i^e(\chi^e(\xi)). \quad (2.25)$$

In general, we can represent the global and local basis coefficients each as a column vector,

$$\hat{\mathbf{u}}_g = \begin{pmatrix} \hat{u}_0 \\ \vdots \\ \hat{u}_N \end{pmatrix}, \quad \hat{\mathbf{u}}_l = \begin{pmatrix} \hat{\mathbf{u}}^0 \\ \vdots \\ \hat{\mathbf{u}}^{N_{el}-1} \end{pmatrix}, \quad (2.26)$$

where $\hat{\mathbf{u}}^e = (\hat{u}_0^e, \dots, \hat{u}_P^e)^T$, $\hat{\mathbf{u}}_g \in \mathbb{R}^N$, $\hat{\mathbf{u}}_l \in \mathbb{R}^{N_{loc}}$ and $N_{loc} = N_{el}(P + 1)$. As there can be more global degrees of freedom than local degrees of freedom, $N > N_{loc}$, we need to impose some conditions on the local expansion coefficients. One of the common approach is to enforce C^0 continuity across elemental boundaries, referred to as the continuous Galerkin projection. Following the definition of local basis expansions in equation (2.22), this condition can be supplemented using,

$$\hat{u}_P^{e-1} = \hat{u}_0^e. \quad (2.27)$$

The graphical representation of this condition enforcing C^0 continuity between the element boundaries for three finite elements with $P = 2$ local basis expansions, and the relationship between global and local basis coefficients are shown in figure 2.2. We can relate the global and local basis coefficients with an assembly matrix, $\mathbf{A} \in \mathbb{R}^{N_{loc} \times N}$,

$$\hat{\mathbf{u}}_l = \mathbf{A} \hat{\mathbf{u}}_g. \quad (2.28)$$

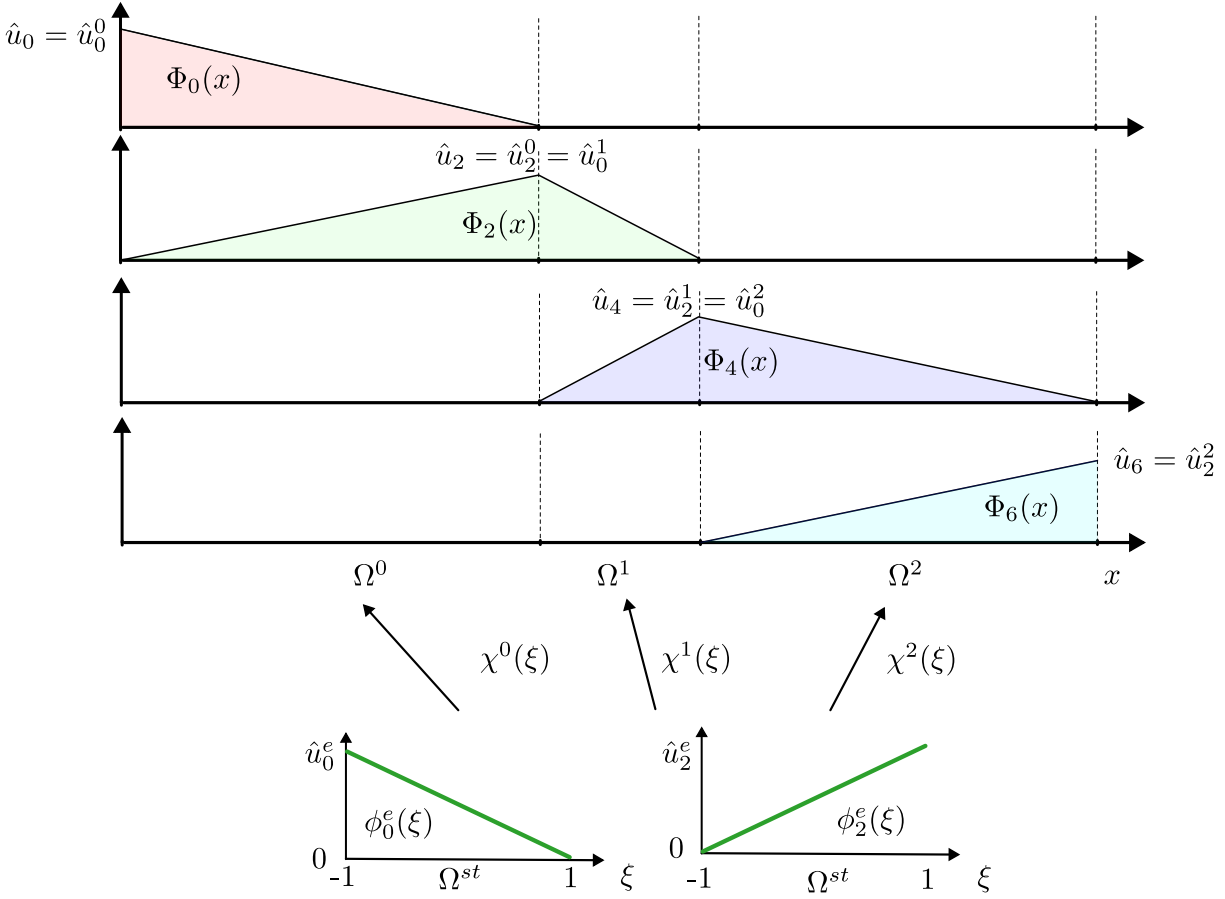


Figure 2.2: A graphical representation of C^0 across elemental boundaries and the relationship between local basis coefficients, u_0^e , u_2^e , and global basis expansions, u_i .

In the case for $P = 2$ and three finite elements as in the case of figures 2.1 and 2.2, the assembly matrix and the vectors of global and local basis coefficients are given as,

$$\hat{\mathbf{u}}_l = \begin{pmatrix} \hat{u}_0^0 \\ \hat{u}_1^0 \\ \hat{u}_2^0 \\ \hat{u}_0^1 \\ \hat{u}_1^1 \\ \hat{u}_2^1 \\ \hat{u}_0^2 \\ \hat{u}_1^2 \\ \hat{u}_2^2 \end{pmatrix}, \quad \mathbf{A} = \begin{pmatrix} 1 & 0 & 0 & 0 & 0 & 0 & 0 \\ 0 & 1 & 0 & 0 & 0 & 0 & 0 \\ 0 & 0 & 1 & 0 & 0 & 0 & 0 \\ 0 & 0 & 1 & 0 & 0 & 0 & 0 \\ 0 & 0 & 0 & 1 & 0 & 0 & 0 \\ 0 & 0 & 0 & 0 & 1 & 0 & 0 \\ 0 & 0 & 0 & 0 & 1 & 0 & 0 \\ 0 & 0 & 0 & 0 & 0 & 1 & 0 \\ 0 & 0 & 0 & 0 & 0 & 0 & 1 \end{pmatrix}, \quad \hat{\mathbf{u}}_g = \begin{pmatrix} \hat{u}_0 \\ \hat{u}_1 \\ \hat{u}_3 \\ \hat{u}_4 \\ \hat{u}_5 \\ \hat{u}_6 \end{pmatrix}, \quad (2.29)$$

The assembly matrix \mathbf{A} ‘scatters’ the global degrees of freedom to local degrees of freedom, while the transpose of it, \mathbf{A}^T , performs the reverse, referred to as global assembly. For example, we wish to perform integration in the domain Ω ,

$$\mathbf{I}_g[j] = (\Phi_j(x), u^\delta(x)), \quad (2.30)$$

where $\mathbf{I}_g \in \mathbb{R}^N$ refers to a vector containing the integral between $\Phi_i(x)$ and $u^\delta(x)$. This is related to first performing integration using local expansion basis within standard elements, and then assembling using \mathbf{A}^T ,

$$\mathbf{I}_g = \mathbf{A}^T \mathbf{I}_l, \quad (2.31a)$$

where,

$$\mathbf{I}_g = \begin{bmatrix} \mathbf{I}_0 \\ \vdots \\ \mathbf{I}_{N_g-1} \end{bmatrix}, \quad \mathbf{I}_l = \begin{bmatrix} \mathbf{I}^0 \\ \vdots \\ \mathbf{I}^{N_{el}-1} \end{bmatrix}, \quad \text{with} \quad \mathbf{I}^e = \begin{bmatrix} \int_{-1}^1 \phi_0^e(\xi) u(\chi^e) \frac{d\chi^e}{d\xi} d\xi \\ \vdots \\ \int_{-1}^1 \phi_{P-1}^e(\xi) u(\chi^e) \frac{d\chi^e}{d\xi} d\xi \end{bmatrix}, \quad (2.31b)$$

and $\mathbf{I}_l \in \mathbb{R}^{N_{loc}}$ refer to the vector of integration operations performed within a standard element. In the spectral/ hp element approach, we perform integration and differentiation using local basis expansions within a standard element. After doing so, we assemble the local operations from the standard element to the global domain by using \mathbf{A}^T , as we shall show later using a 1D example. We note that the structure of assembly matrix is generally sparse, where the entries either contain 0, 1 or -1 in multidimensional formulation. Therefore, the assembly matrix is not constructed in practice, and a mapping array is used instead.

2.3.4 Local basis expansions

The choice of local basis expansions, $\phi_i^e(\xi)$, concerns the representation of the solution, and the convergence properties of the numerical solver, in particular, the condition number of the mass and laplacian matrices. In general, the local basis expansions can be classified into two groups, either *modal* or *nodal* expansions.

Modal expansions

Modal expansions, or hierarchical expansions, describes a set of expansion basis where an expansion set (\mathcal{X}_{P-1}^δ) of order $P - 1$, is contained within a set (\mathcal{X}_P^δ) of order P , e.g. $\mathcal{X}_{P-1}^\delta \subset \mathcal{X}_P^\delta$. An example of modal expansions are the Jacobi polynomials, $P_p^{\alpha,\beta}(x)$, representing a family of solutions to the Sturm-Liouville problem within, $x \in [-1, 1]$. The Jacobi polynomials become symmetric for $\alpha = \beta$, referred to ultraspheric polynomials. Special cases of ultraspheric polynomials are the Legendre polynomials, $\alpha = \beta = 1$, and the Chebyshev polynomials, $\alpha = \beta = 1/2$. Within the Nektar++ framework, we utilise the *modified* basis, constructed using on the Jacobi polynomials and modified (hence its name) by linear expansions given as,

$$\phi_p(\xi) \rightarrow \psi_p(\xi) = \begin{cases} \frac{1-\xi}{2} & \text{for } p = 0 \\ \left(\frac{1-\xi}{2}\right) \left(\frac{1+\xi}{2}\right) P_{p-1}^{1,1}(\xi) & \text{for } 0 < p < P \\ \frac{1+\xi}{2} & \text{for } p = P, \end{cases} \quad (2.32)$$

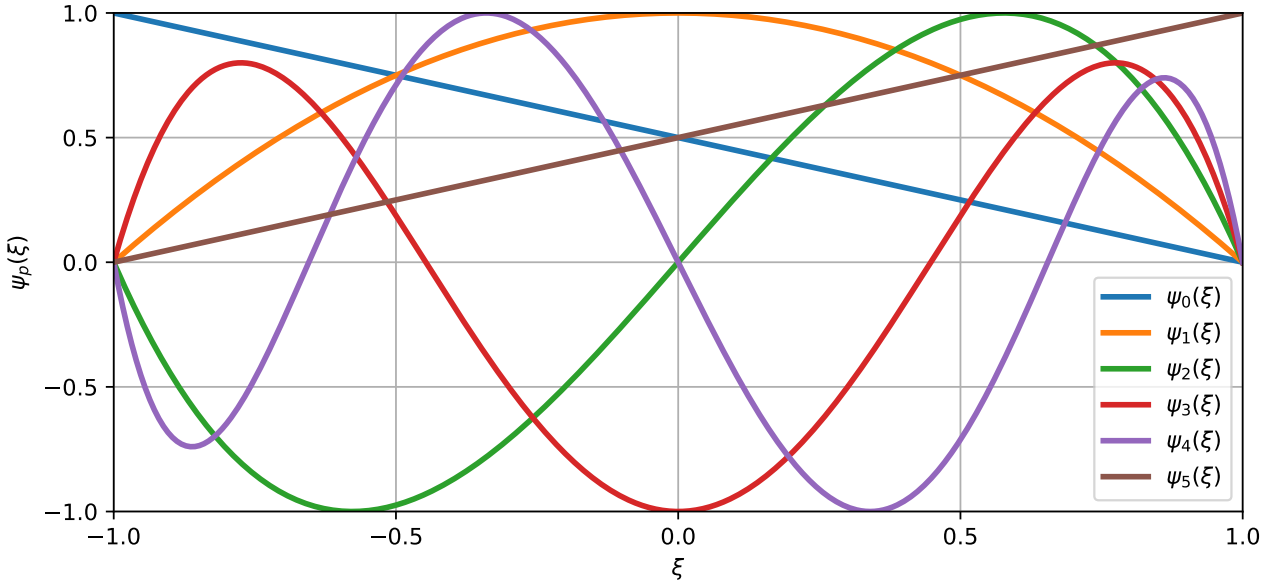


Figure 2.3: The modified basis for up to $P = 5$ normalised to $-1 \leq \psi_p \leq 1$.

We note that $\phi_p(\xi)$ refers to a general local expansion basis while $\psi_p(\xi)$ to definition of the modified basis. The one-dimensional expansion modes of the modified basis of up to $P = 5$ is shown in figure 2.3. The linear modes, corresponding to $p = 0$ and $p = P$, are the only expansions which has a magnitude of at the boundaries, referred to as boundary modes. The modified basis for $0 < p < P$, are clearly hierarchical, and have non-zero values except at the boundaries, referred to as interior/bubble modes.

Nodal expansions

Nodal expansions are basis expansions that are non-hierarchical, $\mathcal{X}_{P-1}^\delta \not\subset \mathcal{X}_P^\delta$. An example of nodal expansions are the Lagrange polynomials,

$$\phi_p(\xi) \rightarrow h_p(\xi) = \frac{\prod_{q=0, q \neq p}^P (\xi - \xi_q)}{\prod_{q=0, q \neq p}^P (\xi_p - \xi_q)} \quad (2.33)$$

The Lagrange polynomials, $h_p(\xi)$, are particular attractive as it has a unit value at discrete nodal values, ξ_q , and zero everywhere else, $h_p(\xi_q) = \delta_{pq}$, which implies that

$$u^\delta(\xi_q) = \sum_{p=0}^P \hat{u}_p h_p(\xi_q) = \sum_{p=0}^P \hat{u}_p \delta_{pq} = \hat{u}_q, \quad (2.34)$$

where the Lagrange coefficient \hat{u}_q is the same as the value evaluated at the node ξ_q . The nodal values, ξ_q , are based on the Gauss-Lobatto-Legendre (GLL) points which will be defined later in §2.3.5. Figure 2.4 presents Lagrange expansions evaluated along the GLL points.

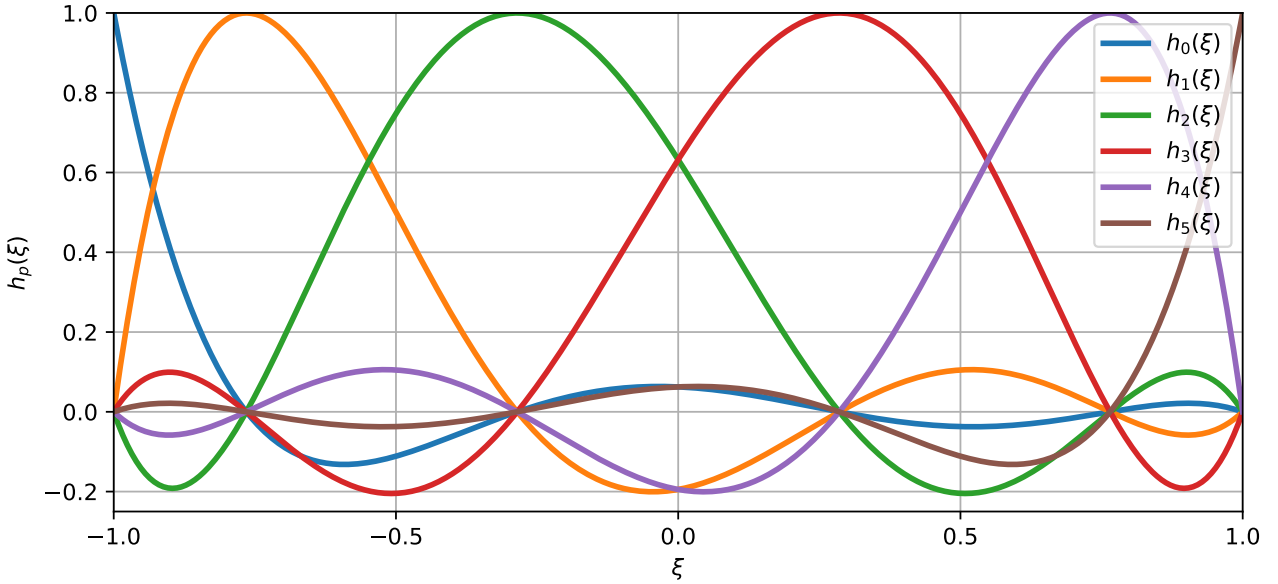


Figure 2.4: Lagrange polynomials for $P = 5$ with nodal values along GLL points.

Multi-dimensional expansions

We have introduced modal and nodal expansions in one dimension, and its extension to multi-dimensions bases can be generalised using a tensorial expansion of the local expansion bases. The standard element in a two dimensional quadrilateral, \mathcal{Q}^2 , and a three dimensional hexahedral \mathcal{H}^3 , are given as,

$$\mathcal{Q}^2 = \{-1 \leq \xi_1, \xi_2 \leq 1\}, \quad \mathcal{H}^3 = \{-1 \leq \xi_1, \xi_2, \xi_3 \leq 1\} \quad (2.35)$$

where ξ_1, ξ_2, ξ_3 refers to the local coordinates in multi-dimensions. Thus, the multi-dimensional expansion bases for quadrilaterals and hexadrals using modified bases are simply a tensor product of the one dimensional modified bases,

$$\phi_{pq}(\xi_1, \xi_2) = \psi_q(\xi_1)\psi_q(\xi_2), \quad \text{and} \quad \phi_{pqr}(\xi_1, \xi_2, \xi_3) = \psi_q(\xi_1)\psi_q(\xi_2)\psi_r(\xi_3). \quad (2.36)$$

An example of the modal tensorial bases, for $p = q = 4$ in a standard quadrilateral element is shown in figure 2.5. While we have discussed the tensorial the expansions for regular domains such as the standard quadrilateral and hexahedral elements, the extensions for simplex domains such as triangles, tetrahedrals, prisms and pyramids commonly used to represent complex geometries, are less straightforward. The challenge for simplexes is that the local coordinates, ξ_1, ξ_2, ξ_3 , become dependent where a direct tensorial expansion becomes unwieldy. Instead, a collapsed coordinate system is introduced, providing a transformation from a standard simplex element to a standard regular element. In this thesis, we utilise quadrilateral elements. The reader is referred to [Karniadakis and Sherwin \[2005\]](#) for more details about the multi-dimensional formulation of regular and simplex elements.

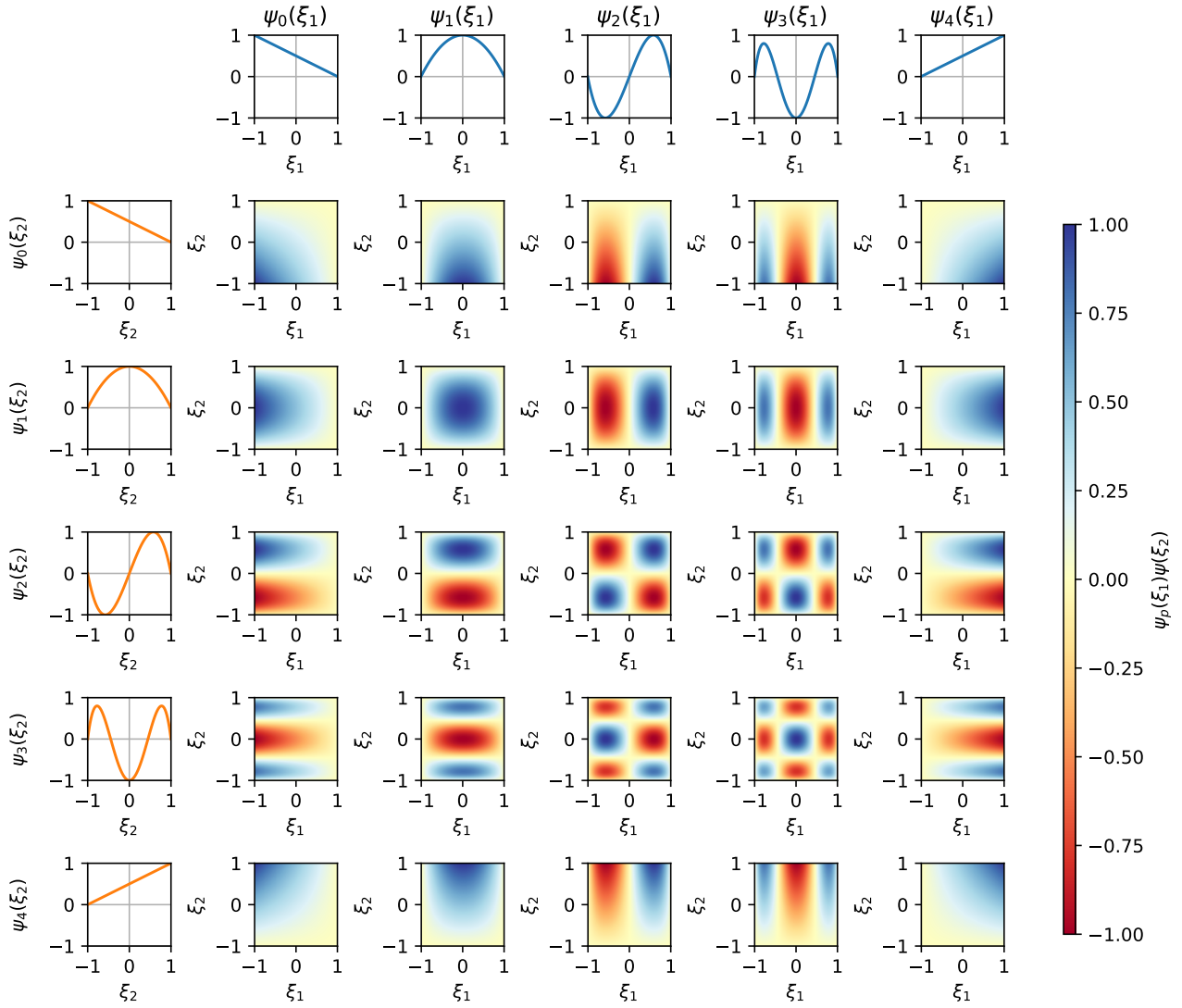


Figure 2.5: Two dimensional modified basis with $p = q = 4$ in a standard quadrilateral, $-1 \leq \xi_1, \xi_2 \leq 1$. The modified bases are normalised to $-1 \leq \phi_{pq} \leq 1$.

2.3.5 Gaussian quadrature

In the Galerkin formulation, we perform integration between basis functions routinely, and an efficient numerical technique is sought after. Suppose we want to approximate the integral of a function, $u(\xi)$, in a standard element numerically given as,

$$\int_{-1}^1 u(\xi) \, d\xi = \sum_{i=0}^{Q-1} w_i u(\xi_i) + R(u). \quad (2.37)$$

The premise is determine the optimal number of quadrature points, Q , integration weights, w_i , and zeros, ξ_i , in which the integral error, $R(u)$, can be minimised. If $u(\xi)$ is of polynomial order of P , we may expect that we require at least $P + 1$ equispaced points to represent $u(\xi)$ sufficiently. Using Gaussian quadrature rules, we can approximate an integral of a function of order P , with far fewer than $P + 1$ points with specific integration weights and zeros. In general, Gaussian quadrature rules

can be grouped into three categories: Gauss, Gauss-Radau and Gauss-Lobatto quadrature. The main difference between the three categories are on the inclusion of the end points. Gauss quadrature rule evaluates the integral without the end points $\xi = \pm 1$. Gauss-Radau quadrature rule either select one of the end points, typically at $\xi = -1$. Gauss-Lobatto quadrature rule consider both end points. We will only focus on describing the Gauss-Lobatto quadrature rules and the zeros of Jacobi polynomials known as the Gauss-Lobatto-Jacobi quadrature rules given as,

$$\xi_i^{\alpha,\beta} = \begin{cases} -1 & i = 0, \\ \xi_{i-1,Q-2}^{\alpha+1,\beta+1} & i = 1, \dots, Q-2, \\ 1, & i = Q-1, \end{cases} \quad (2.38a)$$

$$w_i^{\alpha,\beta} = \begin{cases} (\beta + 1)C_{0,Q-2}^{\alpha,\beta}, & i = 0, \\ C_{i,Q-2}^{\alpha,\beta}, & i = 1, \dots, Q-2, \\ (\alpha + 1)C_{Q-1,Q-2}^{\alpha,\beta}, & i = Q-1, \end{cases} \quad (2.38b)$$

$$C_{i,Q-2}^{\alpha,\beta} = \frac{2^{\alpha+\beta+1}\Gamma(\alpha+Q)\Gamma(\beta+Q)}{(Q-1)(Q-1)!\Gamma(\alpha+\beta+Q+1)[P_{Q-1}^{\alpha,\beta}(\xi_i)]^2} \quad (2.38c)$$

where $w_i^{\alpha,\beta}$, $\xi_i^{\alpha,\beta}$ are the zeros (or sometimes referred to as quadrature points) and weights of the Gauss-Lobatto-Jacobi quadrature rules, and Γ refers to the Gamma function. For $\alpha = \beta = 0$, the quadrature points is known as the Gauss-Lobatto-Legendre (GLL) points, typically employed for Lagrange polynomials. By evaluating the integral using the zeros and integrations weights defined above, we can obtain an exact integral of the function $u(\xi)$, of polynomial order P , with at least $Q \geq (P+3)/2$ quadrature points.

2.3.6 Numerical differentiation

In the same fashion as Gaussian quadrature rules, we want to evaluate the derivative of a function, $u^\delta(\xi)$ numerically. Suppose that we want to differentiate in x using local coordinates given as,

$$\frac{du^\delta(\xi)}{dx} = \frac{du^\delta(\xi)}{d\xi} \frac{d\xi}{dx} = \sum_{p=0}^P \hat{u}_p \frac{d\phi_p(\xi)}{d\xi} \frac{d\xi}{dx}, \quad (2.39)$$

where $d\xi/dx$ is the jacobian. The main step in involves evaluating the derivative of the local expansion bases, $d\phi_p(\xi)/d\xi$, referred to as collocation differentiation as differentiation is performed in physical space. Suppose that we express the solution of polynomial order P with modified polynomials, $\phi_p(\xi) \rightarrow \psi_p(\xi)$, through a set of $Q \geq P+1$ quadrature points, the derivative in discrete local coordinates is expressed as,

$$\left. \frac{du^\delta(\xi)}{d\xi} \right|_{\xi=\xi_i} = \sum_{j=0}^{Q-1} \hat{u}_j \left. \frac{d\psi_j(\xi)}{d\xi} \right|_{\xi=\xi_i} = \sum_{j=0}^{Q-1} D_{ij} \hat{u}_j, \quad (2.40)$$

where D_{ij} refers to the differential matrix containing values of the derivative of the basis at discrete quadrature points given as,

$$D_{ij} = \frac{dh_j(\xi)}{d\xi} \Big|_{\xi=\xi_i}, \quad (2.41)$$

which is often pre-computed. To differentiate a function, $u(\xi)$, we typically need to construct the differential matrices, and the general representation of the differential matrix is,

$$D_{ij} = \begin{cases} \frac{p'_Q(\xi_i)}{p'_Q(\xi_j)} \frac{1}{\xi_i - \xi_j}, & i \neq j, \\ \frac{p''_Q(\xi_i)}{2p'_Q(\xi_i)}, & i = j. \end{cases} \quad (2.42)$$

where $p'_Q(\xi_i), p''_Q(\xi_i)$ refers to the first and second differentiative of Jacobi polynomials evaluated at the quadrature points ξ_i .

2.3.7 Example in 1D

We have outlined the basic formulation of spectral/ hp element methods in a single dimension. To conclude the section on spectral/ hp element methods, we will describe its solution procedure, converting the weak form of the Helmholtz equation into a system of linear equations, and introduce the mass and laplacian matrices. Starting from the weak form,

$$\underbrace{\lambda \int_{-1}^1 v^\delta u^H d\xi}_{\mathbf{M}^e \hat{\mathbf{u}}^e} + \underbrace{\int_{-1}^1 \frac{\partial v^\delta}{\partial \xi} \frac{\partial u^H}{\partial \xi} d\xi}_{\mathbf{L}^e \hat{\mathbf{u}}^e} = \underbrace{\int_{-1}^1 v^\delta f d\xi}_{\hat{\mathbf{f}}^e} - \underbrace{\int_{-1}^1 \frac{\partial v^\delta}{\partial \xi} \frac{\partial u^D}{\partial \xi} d\xi}_{\mathbf{L}^0} + v(l)g_N, \quad (2.43)$$

we wish to seek the solution $u^H(\xi)$. Recall that the solution space of $u^H(\xi)$ and $v^\delta(\xi)$ are the same, following the standard Galerkin projection procedure. Suppose they can be discretised by spectral/ hp elements with e elements and local basis expansions of up to polynomial order P ,

$$u^H(\xi) = \sum_{i=0}^P \hat{u}_i^e \phi_i^e(\xi), \quad v^\delta(\xi) = \sum_{i=0}^P \hat{v}_i^e \phi_i^e(\xi). \quad (2.44)$$

Substituting into equation (2.43) and evaluating the first term on the left hand side through a set of Q quadrature points.

$$\begin{aligned} \int_{-1}^1 \sum_{i=0}^P \hat{v}_i^e \phi_i^e(\xi) \sum_{i=0}^P \hat{u}_i^e \phi_i^e(\xi) d\xi &= \sum_{q=0}^{Q-1} \left[\sum_{i=0}^P \hat{v}_i^e \phi_i^e(\xi_q) \sum_{i=0}^P \hat{u}_i^e \phi_i^e(\xi_q) \right] w_q^e \\ &= (\hat{\mathbf{v}}^e)^T (\mathbf{B}^e)^T \mathbf{W}^e \mathbf{B}^e \hat{\mathbf{u}}^e \\ &= \hat{\mathbf{v}}^T \mathbf{M}^e \hat{\mathbf{u}}^e \end{aligned} \quad (2.45)$$

where $\mathbf{M}^e = (\mathbf{B}^e)^T \mathbf{W} \mathbf{B}^e \in \mathbb{R}^{(P+1) \times (P+1)}$ refers to the elemental mass matrix, while $\mathbf{B}^e \in \mathbb{R}^{Q \times (P+1)}$ refers to the elemental basis matrix, and $\mathbf{W}^e \in \mathbb{R}^{Q \times Q}$, the elemental weight matrix, a diagonal matrix

consisting of discrete integration weights along Q quadrature points.

$$\mathbf{B}^e = \begin{bmatrix} \phi_0(\xi_0) & \cdots & \phi_P(\xi_0) \\ \vdots & \ddots & \vdots \\ \phi_0(\xi_Q) & \cdots & \phi_P(\xi_Q) \end{bmatrix}, \quad \mathbf{W}^e = \begin{bmatrix} w_0^e & & 0 \\ & \ddots & \\ 0 & & w_{Q-1}^e \end{bmatrix} \quad (2.46)$$

Next, we move onto the second term on the left hand side,

$$\begin{aligned} \int_{-1}^1 \sum_{i=0}^P \hat{v}_i^e \frac{d\phi_i^e}{d\xi} \sum_{i=0}^P \hat{u}_i^e \frac{d\phi_i^e}{d\xi} d\xi &= \sum_{q=0}^Q \left[\sum_{i=0}^P \hat{v}_i^e D_{qi}^e \phi_i^e(\xi_q) \sum_{i=0}^P \hat{u}_i^e D_{qi}^e \phi_i^e(\xi_q) \right] w_q^e \\ &= \hat{\mathbf{v}}^T (\mathbf{B}^e)^T (\mathbf{D}^e)^T \mathbf{W}^e \mathbf{D}^e \mathbf{B}^e \hat{\mathbf{u}}^e \\ &= \hat{\mathbf{v}}^T \mathbf{L}^e \hat{\mathbf{u}}^e \end{aligned} \quad (2.47)$$

where $\mathbf{L}^e = (\mathbf{B}^e)^T (\mathbf{D}^e)^T \mathbf{W}^e \mathbf{D}^e \mathbf{B}^e \in \mathbb{R}^{(P+1) \times (P+1)}$ refers to the elemental Laplacian matrix while $\mathbf{D}^e \in \mathbb{R}^{Q \times (P+1)}$ refers to the differential matrix defined in equation (2.42). Moving onto the first term on the right hand side,

$$\begin{aligned} \int_{-1}^1 \sum_{i=0}^P \hat{v}_i^e \phi_i^e(\xi) f^e(\xi) d\xi &= \sum_{q=0}^Q \sum_{i=0}^P \hat{v}_i^e \phi_i^e(\xi_q) f^e(\xi_q) w_q^e, \\ &= \hat{\mathbf{v}}^T (\mathbf{B}^e)^T \mathbf{W}^e \mathbf{f}^e \\ &= \hat{\mathbf{v}}^T \hat{\mathbf{f}}^e, \end{aligned} \quad (2.48)$$

where $\hat{\mathbf{f}}^e$, is referred to the elemental forcing vector. As we bolt the elemental laplacian, mass matrices, and forcing vector, the system of linear equations within a standard element is given as,

$$[\lambda \mathbf{M}^e + \mathbf{L}^e] \hat{\mathbf{u}}^e = \hat{\mathbf{f}}^e. \quad (2.49)$$

We note that the boundary conditions have been omitted. To include the boundary conditions, we consider the full system of linear of equations consisting of e number of elements,

$$\lambda \underbrace{\begin{bmatrix} \mathbf{M}^0 + \mathbf{L}^0 & \mathbf{0} \\ \mathbf{0} & \ddots \\ \mathbf{0} & \mathbf{M}^{N_{el}-1} + \mathbf{L}^{N_{el}-1} \end{bmatrix}}_{\mathbf{M}_l + \mathbf{L}_l} \underbrace{\begin{bmatrix} \hat{\mathbf{u}}^0 \\ \vdots \\ \hat{\mathbf{u}}^{N_{el}-1} \end{bmatrix}}_{\hat{\mathbf{u}}_l} = \underbrace{\begin{bmatrix} \hat{\mathbf{f}}^0 \\ \vdots \\ \hat{\mathbf{f}}^{N_{el}-1} \end{bmatrix}}_{\hat{\mathbf{f}}_l} + \underbrace{\begin{bmatrix} \mathbf{L}^0 g_D \\ \vdots \\ \mathbf{0} \end{bmatrix}}_{\mathbf{g}_D} + \underbrace{\begin{bmatrix} \mathbf{0} \\ \vdots \\ g_N \end{bmatrix}}_{\mathbf{g}_N}, \quad (2.50)$$

where $\mathbf{M}_l \in \mathbb{R}^{N_{el}(P+1) \times N_{el}(P+1)}$, $\mathbf{L}_l \in \mathbb{R}^{N_{el}(P+1) \times N_{el}(P+1)}$, $\hat{\mathbf{u}}_l \in \mathbb{R}^{N_{el}(P+1)}$ refers to the local mass matrix, local laplacian matrix and the vector of local expansion coefficients. On the right hand side, $\hat{\mathbf{f}}_l \in \mathbb{R}^{N_{el}(P+1)}$, $\mathbf{g}_D^{N_{el}(P+1)}$, $\mathbf{g}_N^{N_{el}(P+1)}$ refers local forcing vector, Dirichlet and Neumann boundary conditions in vector form. Lastly, to ensure that the solution remains C^0 continuous across the elemental

boundaries, we perform the assembly process by using the assemble matrices (see §2.3.3),

$$\lambda \mathbf{A}^T (\mathbf{M}_l + \mathbf{L}_l) \mathbf{A} \hat{\mathbf{u}}_g = \mathbf{A}^T (\hat{\mathbf{f}}^l + \mathbf{g}_D + \mathbf{g}_N), \quad (2.51)$$

and obtain the solution for $\hat{\mathbf{u}}_g$.

2.4 Numerical techniques for solving the Navier-Stokes equations

2.4.1 Velocity Correction Scheme

The spatial discretisation of the Helmholtz operator and its numerical solution procedure has been discussed using the spectral/ hp element methods. Here, we describe the numerical methods that is used to solve the Navier-Stokes equations given as,

$$\frac{\partial \mathbf{u}}{\partial t} + (\mathbf{u} \cdot \nabla) \mathbf{u} = -\nabla p + \nu \nabla^2 \mathbf{u} + \mathbf{f} \quad (2.52a)$$

$$\nabla \cdot \mathbf{u} = 0, \quad (2.52b)$$

with boundary conditions,

$$\mathbf{u} = 0, \quad \text{on } \partial\Omega. \quad (2.52c)$$

Here, the primitive variables are velocity and pressure (\mathbf{u}, p) and we assumed unit density, $\rho = 1$, with the kinematic viscosity appearing as the control parameter. The time evolution of velocity is explicit expressed in equation (2.52a), but does not appear for the pressure, which is coupled to the velocity field, enforcing the incompressibility condition. Several strategies exist for addressing the coupled velocity-pressure fields by

1. Solving the coupled system such as the Uzawa algorithm,
2. Splitting methods,
3. Change of coordinates (e.g. vorticity-streamfunction approach).

We adopt splitting methods, which solves the of the Navier-Stokes equation by splitting them into ‘subequations’, and solving them sequentially. These methods, belonging to the broader family of projection methods introduced by Chorin [1967] and Témam [1969], and can be further classified into pressure-correction or velocity-correction schemes. This thesis employs the use of the high-order velocity-correction scheme introduced by Karniadakis et al. [1991]. We rewrite the incompressible Navier-Stokes equations in semi-discrete form with using linear and nonlinear operators as,

$$\frac{\partial \mathbf{u}}{\partial t} = \mathbf{N}(\mathbf{u}) - \nabla p + \nu \mathbf{L}(\mathbf{u}), \quad (2.53a)$$

$$\nabla \cdot \mathbf{u} = 0, \quad (2.53b)$$

with boundary conditions,

$$\mathbf{u}|_{\Omega} = 0, \quad \mathbf{u}(t = 0) = \mathbf{u}_0. \quad (2.53c)$$

The nonlinear, \mathbf{N} , linear, \mathbf{L} , operators are obtained from a suitable spatial-discretisation method such as the spectral/ hp element method. The nonlinear and linear operators are defined as,

$$\mathbf{N}(\mathbf{u}) \equiv -(\mathbf{u} \cdot \nabla)\mathbf{u} = -\frac{1}{2}[(\mathbf{u} \cdot \nabla)\mathbf{u} + \nabla \cdot (\mathbf{u}\mathbf{u})], \quad \mathbf{L}(\mathbf{u}) \equiv \nabla^2\mathbf{u}, \quad (2.54)$$

We note that the nonlinear terms are written in the skew-symmetric to minimise aliasing errors [Karniadakis et al., 1991]. To advance the velocity at time step, \mathbf{u}^n , to the next time step, \mathbf{u}^{n+1} , we integrate equation (2.53) over a time step Δt ,

$$\mathbf{u}^{n+1} - \mathbf{u}^n = \underbrace{\int_{t_n}^{t_{n+1}} \mathbf{N}(\mathbf{u}) dt}_{\Delta t \sum_{q=0}^{J_e-1} \beta_q \mathbf{N}(\mathbf{u}^{n-q})} - \underbrace{\int_{t_n}^{t_{n+1}} \nabla p dt}_{\Delta t \nabla \bar{p}^{n+1}} + \nu \underbrace{\int_{t_n}^{t_{n+1}} \mathbf{L}(\mathbf{u}) dt}_{\Delta t \sum_{q=0}^{J_i-1} \gamma_q \mathbf{L}(\mathbf{u}^{n+1-q})}. \quad (2.55)$$

The velocity correction scheme evaluates the underbraced terms in three successive independently from left to right independently, effectively ‘splitting’ equation (2.53) from this point onwards. The first step we perform is to extrapolate the advection velocities, by approximating the nonlinear terms using an explicit scheme such as the Adams-Bashforth family of J_e order,

$$\frac{\hat{\mathbf{u}} - \sum_{q=0}^{J_e-1} \alpha_q \mathbf{u}^{n-q}}{\Delta t} = \sum_{q=0}^{J_e-1} \beta_q \mathbf{N}(\mathbf{u}^{n-q}), \quad (2.56)$$

where $\hat{\mathbf{u}}$ is denotes the primary intermediate velocity field desired and α_e, β_e refers to the time integration coefficients for a prescribe J_e -th order, described later. After evaluting $\hat{\mathbf{u}}$, we move onto the second term in equation (2.55), which defines the pressure at time step $n + 1$ as,

$$\frac{\hat{\mathbf{u}} - \hat{\mathbf{u}}}{\Delta t} = -\nabla p^{n+1}. \quad (2.57)$$

$\hat{\mathbf{u}}$ denotes as the secondary intermediate velocity. In this single equation, we seek to obtain two unknown solutions, $\hat{\mathbf{u}}$ and p^{n+1} , which is ill-posed, and seek to impose certain restrictions. The splitting method assumes that the secondary intermediate velocity is divergence free, $\nabla \cdot \hat{\mathbf{u}} = 0$, and satisfies the Dirichlet boundary conditions normal to the boundary, $\hat{\mathbf{u}} \cdot \mathbf{n} = \mathbf{u}|_{\Omega} \cdot \mathbf{n}$. By considering the assumptions above and the divergence of equation (2.57), we obtain the pressure Poisson equation with the primary intermediate velocity acting as the forcing term,

$$\nabla^2 p^{n+1} = \nabla \cdot \left(\frac{\hat{\mathbf{u}}}{\Delta t} \right) \quad (2.58a)$$

and boundary conditions,

$$\frac{\partial p^{n+1}}{\partial n} = \mathbf{n} \cdot \left(\frac{\hat{\mathbf{u}} - \hat{\mathbf{u}}}{\Delta t} \right). \quad (2.58b)$$

While the pressure boundary condition (2.58b) is straightforward to evaluate, it is sensitive to large splitting errors [Karniadakis et al., 1991]. To overcome this, we consider a high-order boundary condition of pressure, obtained by taking the normal dot product of equation (2.53),

$$\frac{\partial p^{n+1}}{\partial t} = - \sum_{q=0}^{J_e-1} \beta_q \left[\frac{1}{\Delta t} \mathbf{u}^{n-q} + \nu [\nabla \times (\nabla \times \mathbf{u}^{n-q})] + (\mathbf{u}^{n-q} \cdot \nabla) \mathbf{u}^{n-q} \right] \cdot \mathbf{n}. \quad (2.59)$$

Notably, the linear operator is expressed as $\mathbf{L}(\mathbf{u}) = \nabla(\nabla \cdot \mathbf{u}) - \nabla \times (\nabla \times \mathbf{u})$, favouring numerical stability [Orszag et al., 1986, Karniadakis et al., 1991]. J_e is the order the explicit scheme as in equation (2.56). After solving for the pressure Poisson equation, the secondary intermediate velocity could be subsequently obtained using equation (2.57). After which, we can move onto the final substep in equation (2.55), by solving a Helmholtz equation for \mathbf{u}^{n+1} ,

$$\frac{\gamma_0 \mathbf{u}^{n+1} - \hat{\mathbf{u}}}{\Delta t} = \nu \sum_{q=0}^{J_i-1} \gamma_q \mathbf{L}(\mathbf{u}^{n+1-q}), \quad (2.60)$$

where the linear terms are treated based similar to the family of Adams-Moulton implicit scheme and J_i, γ_q denotes the order of the scheme and time integration coefficients, completing the velocity correction scheme. The time integration coefficients are determined from stiffly stable schemes shown in table 2.2, an improvement from the Adams-family schemes [Karniadakis et al., 1991]. The high

Coefficients	1^{st} order	2^{nd} order	3^{rd} order
γ_0	1	3/2	11/6
α_0	1	2	3
α_1	0	-1/2	-3/2
α_2	0	0	1/3
β_0	1	2	3
β_1	0	-1	-3
β_2	0	0	1

Table 2.2: Integration coefficient of stiffly stable schemes from Karniadakis et al. [1991].

order velocity correction scheme and be summarised in a three step process of the following,

$$\mathbf{u}^n \xrightarrow{\mathbf{N}(\mathbf{u}^n)} \hat{\mathbf{u}} \xrightarrow{\nabla^2 p} \hat{\mathbf{u}} \xrightarrow{\mathbf{L}(\hat{\mathbf{u}})} \mathbf{u}^{n+1},$$

evolving the velocity fields at time step n to $n + 1$.

2.4.2 Fourier spectral/ hp modes

Fourier-Chebyshev-Fourier type discretisation have been recognised as preferred method for performing direct numerical simulations (DNS) of transitional or turbulent channel flows [Kim et al., 1987] owing to its efficient representation of the inhomogeneous wall-normal directions and the homogeneous streamwise and spanwise directions, using Chebyshev and Fourier expansions respectively.

The Fourier spectral/ hp element method draws on this approach, where the homogeneous and

the inhomogeneous directions are represented by the Fourier expansions and spectral/ hp elements respectively. This approach has been commonly referred to as the Quasi-3D or (2.5D) approach, allowing for the representation of two inhomogeneous directions. For example, in the turbulent channel flows with riblets, the Fourier expansions are used to represent the periodic streamwise, while the spectral/ hp elements are used to discretise the wall-normal direction. In the analysis of three-dimensional wakes of cylinders where the Fourier expansions are treated in the spanwise directions. In this thesis, we routinely use the the Quasi-3D approach, consisting of the 2D spectral/ hp elements with 1D Fourier expansions are used to discretise the cross stream plane and streamwise flow respectively. The velocity and pressure in the spectral/ hp plane is described by two dimensional modified bases with Fourier expansions,

$$\begin{bmatrix} \mathbf{u}^\delta(x, y, z, t) \\ p^\delta(x, y, z, t) \end{bmatrix} = \sum_{k=0}^{N_z-1} \sum_{p=0}^P \sum_{q=0}^P \psi_p(x) \psi_q(y) e^{ik\beta z} \begin{bmatrix} \hat{\mathbf{u}}_{p,q,k}(t) \\ \hat{p}_{p,q,k}(t) \end{bmatrix} = \sum_{k=0}^{N_z-1} e^{ik\beta z} \begin{bmatrix} \tilde{\mathbf{u}}_k(x, y, t) \\ \tilde{p}_k(x, y, t) \end{bmatrix} \quad (2.61)$$

where $\beta = \frac{2\pi}{L_z}$ is the spanwise wavenumber, L_z the spanwise length, N_z the number of Fourier expansions. Substituting equation 2.61 into the Navier-Stokes equations and taking the Fourier transform (equivalently to the Galerkin projection with respect to Fourier expansion as a test function) yields a system of N_z decoupled equations, amenable for parallel processing,

$$\frac{\partial \tilde{\mathbf{u}}_k}{\partial t} = -\tilde{\nabla}_k \tilde{p}_k + \nu(\nabla_{x,y}^2 - k^2 \beta^2) \tilde{\mathbf{u}}_k - [\widehat{(\mathbf{u} \cdot \nabla) \mathbf{u}}]_k \quad (2.62a)$$

$$-k\beta \tilde{\nabla} \cdot \tilde{\mathbf{u}}_k = 0, \quad k = 0, \dots, N_z - 1 \quad (2.62b)$$

where, $\tilde{\nabla}_k = (\frac{\partial}{\partial x}, \frac{\partial}{\partial y}, ik\beta)$, $\nabla_{x,y}^2 = (\frac{\partial^2}{\partial x^2}, \frac{\partial^2}{\partial y^2})$ and $[(\widehat{\mathbf{u} \cdot \nabla}) \mathbf{u}]_k$ refers to the Fourier-transformed of the k^{th} nonlinear term.

2.4.3 Maintaining fluid flow through a channel

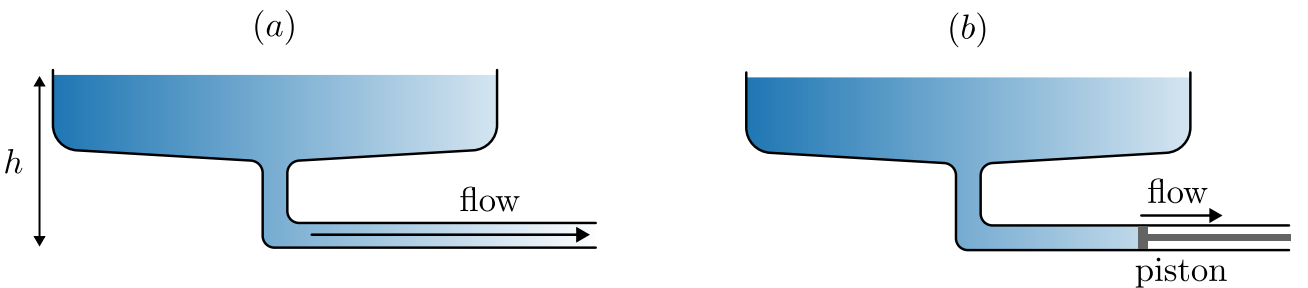


Figure 2.6: (a) Flow rate driven by a pressure gradient from an reservoir elevated by h . (b) Flow driven by a piston at a constant flow rate.

In general, there are two approaches to drive a fluid flow through a channel, either by maintaining a constant pressure drop, or a constant volumetric flux (flow rate). This difference is illustrated in figure 2.6, whereby the flow through the channel is driven by a constant pressure drop from an elevated

reservoir of constant height h in figure 2.6(a), while a piston moves at a constant speed rightwards, drawing fluid through the channel at a constant volumetric flux in figure 2.6(b).

Constant pressure via body-forcing

As we prescribe the homogeneous direction along the streamwise directions, a pressure drop cannot be prescribe directly. Instead, we substitute the constant pressure drop with a constant body force $\mathbf{f} = f_x \hat{\mathbf{e}}_x$ in the streamwise direction,

$$\frac{\partial u}{\partial t} + (u \cdot \nabla)u = -\nabla p + \nu \nabla^2 u + f_x, \quad (2.63)$$

The central question now becomes what is the magnitude of body force required a laminar or turbulent flow. To begin this discussion, we assume that we can decompose our flow variables into a mean and a fluctuating component,

$$u(x, y, t) = U(y) + u'(x, y, t), \quad (2.64)$$

where $U(y) = \langle u \rangle$ refers to the averaged velocity and $\langle \cdot \rangle = \frac{1}{TL_x L_z} \int \cdot dz dx dt$ refers to the temporal and span-averaged operator. The fluctuating component is defined with an average of 0, i.e. $\langle u' \rangle = 0$. Next, we substitute this decomposition into equation (2.63), and perform the averaging operation,

$$\begin{aligned} & \left\langle \frac{\partial(U + u')}{\partial t} + (U + u') \frac{\partial(U + u')}{\partial x} + (V + v') \frac{\partial(V + v')}{\partial y} \right. \\ & \left. = -\frac{\partial(P + p')}{\partial x} + \nu \nabla^2(U + u') + F_x + f'_x \right\rangle. \end{aligned} \quad (2.65)$$

For a statistically stationary turbulent (or laminar) channel flow with periodic streamwise boundary conditions, we can make the following assumptions:

1. stationary flow $\frac{\partial U}{\partial t} = 0$,
2. fully-developed in x , $\frac{\partial}{\partial x} \rightarrow 0$,
3. $\frac{\partial V}{\partial y} = 0$, as a consequence of continuity and the no-slip boundary condition.
4. $\langle u', v', w', p' \rangle = 0$, based on the definition of fluctuations,
5. $\frac{\partial p}{\partial x} = 0$ due to the enforced periodicity in x .

Applying the assumptions above, the mean momentum equations simplify into,

$$\langle F_x \rangle = \left\langle \frac{\partial(u'v')}{\partial y} \right\rangle - \nu \frac{\partial U^2}{\partial y^2}, \quad (2.66)$$

where the body force on the left-hand side balances the sum of Reynolds stresses and viscous diffusion on the right-hand side. Next, we integrate the expression from $y \in [-1, 1]$,

$$2F_x = [\langle u'v' \rangle]_{y=-1}^{y=1} + \nu \left[\frac{\partial U}{\partial y} \Big|_{y=1} - \frac{\partial U}{\partial y} \Big|_{y=-1} \right]. \quad (2.67)$$

The wall shear stress is defined by $\tau_w = \nu \frac{\partial U}{\partial y} \Big|_{y=1}$ (ρ is assumed to be 1), and it is antisymmetric about the channel centreline, $\nu \frac{\partial U}{\partial y} \Big|_{y=1} = -\nu \frac{\partial U}{\partial y} \Big|_{y=-1}$. Due to the no-slip condition, the Reynolds shear stresses is zero, i.e. $[u'v'] \Big|_{y=-1,1} = 0$. Hence, the expression above simplifies to,

$$\tau_w = F_x. \quad (2.68)$$

In other words, the body force F_x is balanced by the wall shear stress (drag), τ_w , along the channel walls. In the case of laminar flow, τ_w can be determined analytically, and the body force required for sustaining a laminar flow for a velocity profile of $u(y) = 1 - y^2$, is $F_x = -2\nu$. However, to determine the wall shear stress (and hence the magnitude of body force) is not as straightforward task for transitional or turbulent channel flow as there isn't an analytical expression for τ_w and its dependence on Reynolds number. Instead, we can only rely on empirical relations of turbulent channel flow between the skin friction coefficient, $c_f = \tau_w / \frac{1}{2} \rho U_c^2$ and Reynolds number Re_c from [Dean \[1978\]](#).

$$c_f = 0.00302 Re_c^{-1/4}, \quad (2.69)$$

where Re_c is the Reynolds number based on the laminar centerline velocity. Similarly, the skin

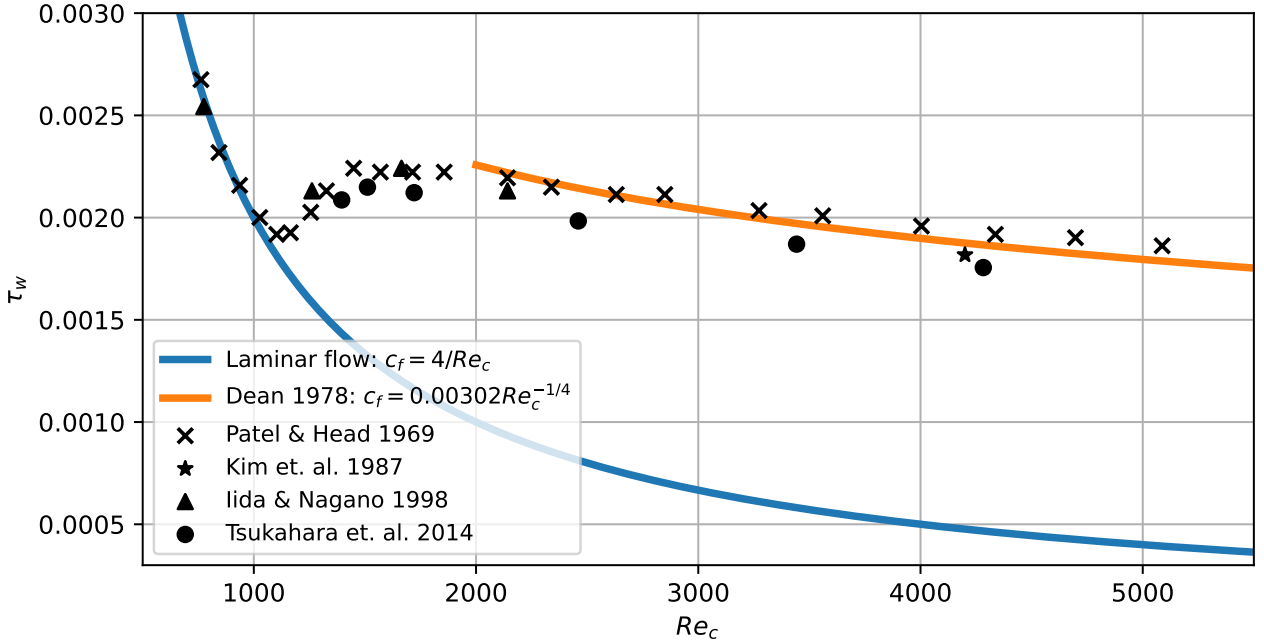


Figure 2.7: τ_w against Re_c using skin friction coefficients from [Dean \[1978\]](#) with $\rho = U_c = 1$. Experimental scatter points from [[Patel and Head, 1969](#), [Kim et al., 1987](#), [Iida and Nagano, 1998](#), [Tsukahara et al., 2014a](#)].

friction coefficient for the case of laminar flow is $c_f = 4/Re_c$ [Dean, 1978]. Figure 2.7 illustrates the relationship between τ_w and Re_c of channel flow using empirical relationship from Dean [1978] (here $\rho = U_c = 1$) and experimental data from Patel and Head [1969], Kim et al. [1987], Iida and Nagano [1998], Tsukahara et al. [2014a]. While the empirical relation for laminar flow, $Re_c \lesssim 1000$ and turbulent flow $Re_c \gtrsim 2000$ appears reasonably robust, the wall shear stress in the transitional region is lacking therefore, the body forcing approach is not preferred.

Constant volumetric flux

An alternative approach is to enforce a constant volumetric flux, illustrated using the piston method in figure 2.6(b). We employ the efficient Green's function approach introduced by Chu and Karniadakis [1993], and outline its solution procedure. The volumetric flux is defined as,

$$Q(\mathbf{u}) = \frac{1}{2\mu(R)} \int_R \mathbf{u} \cdot d\mathbf{s}, \quad (2.70)$$

where $Q(\cdot)$ refer to the flow rate operator through the surface R with surface area of $\mu(R)$. The idea is to append a correction velocity, \mathbf{u}_{corr} , to the velocity field at time step n , \mathbf{u}^n , such that the corrected solution, $\bar{\mathbf{u}}^n = \mathbf{u}^n + \mathbf{u}_{corr}$, has the desired volumetric flux $\bar{Q} = Q(\bar{\mathbf{u}}^n)$. While adding two solutions together is straightforward, the resultant velocity field may not directly satisfy the Navier-Stokes equations. Fortunately, we can leverage the velocity correction scheme which (in general) evaluates the nonlinear advection terms followed by a linear terms (pressure and dissipation). This process is summarised as,

$$\begin{cases} \frac{\partial \mathbf{u}}{\partial t} = \mathbf{N}(\mathbf{u}) \\ \mathbf{u}(\mathbf{x}, 0) = \mathbf{u}^n \end{cases} \xrightarrow{\hat{\mathbf{u}}(\mathbf{x}, \Delta t)} \begin{cases} \frac{\partial \mathbf{u}}{\partial t} = -\nabla p + \nu \mathbf{L}(\mathbf{u}) \\ \mathbf{u}(\mathbf{x}, 0) = \hat{\mathbf{u}}(\mathbf{x}, \Delta t), \end{cases} \quad (2.71)$$

where $\mathbf{u}(\mathbf{x}, 0) = \mathbf{u}^n$ and $\hat{\mathbf{u}}(\mathbf{x}, \Delta t)$ refer to the initial condition for the nonlinear advection terms, and the intermediate velocity, the initial condition for the linear terms, respectively. Since the second step correspond to solving the linear Stokes equation, any solution of the linear Stokes (such as \mathbf{u}_{corr}) added to the final solution will still satisfy the linear Stokes equations - a property of linear differential equations. We consider the linear Stokes equation governing the evolution of the correction velocity,

$$\frac{\partial \mathbf{u}_{corr}}{\partial t} = -\nabla p_{corr} + \nu \mathbf{L}(\mathbf{u}_{corr}) + \alpha^n \hat{\mathbf{e}}_x, \quad (2.72)$$

where α^n is the undetermined magnitude of body force at time step n in the streamwise direction, $\hat{\mathbf{e}}_x$, required to maintain the desired flow rate $\bar{Q} = Q(\mathbf{u}^n) + Q(\mathbf{u}_{corr})$. Since \mathbf{u}_{corr} is appended to \mathbf{u}^n , the initial condition for \mathbf{u}_{corr} must be $\mathbf{u}_{corr}(\mathbf{x}, 0) = 0$, so that \mathbf{u}^n remains compatible with the initial conditions in equation (2.71). Since α^n is undetermined, we normalise the equation with respect to α^n , yielding the linear Stokes equations with unit forcing,

$$\frac{\partial \mathbf{v}}{\partial t} = -\nabla \hat{p} + \nu \mathbf{L}(\mathbf{v}) + \hat{\mathbf{e}}_x, \quad \mathbf{v}(\mathbf{x}, 0) = \mathbf{0}, \quad (2.73)$$

where $\mathbf{v} = \mathbf{u}_{corr}/\alpha^n$ and $\hat{p} = p_{corr}/\alpha^n$. The corrected velocity field becomes

$$\bar{\mathbf{u}} = \mathbf{u} + \alpha^n \mathbf{v}^1, \quad (2.74)$$

where \mathbf{v}^1 is solution field obtained by solving equation (2.73) in the first time step. To match the target volumetric flux, \bar{Q} , we need to scale α^n such that,

$$\bar{Q} = Q(\bar{\mathbf{u}}^n) = Q(\mathbf{u}^n) + Q(\alpha^n \mathbf{v}^1). \quad (2.75)$$

which gives,

$$\alpha^n = \frac{\bar{Q} - Q(\mathbf{u}^n)}{Q(\mathbf{v}^1)}, \quad (2.76)$$

evaluated at every time step n . The Green's function approach is computationally efficient as we only need to compute \mathbf{v}^1 and $Q(\mathbf{v}^1)$ once during the first time step and reuse it for subsequent time steps. The process of adding the correction velocity at the end of velocity correction scheme can be summarised in the procedure as follows,

$$\mathbf{u}^n \xrightarrow{\mathbf{N}(\mathbf{u}^n)} \hat{\mathbf{u}} \xrightarrow{\nabla^2 p} \hat{\mathbf{u}} \xrightarrow{\mathbf{L}(\hat{\mathbf{u}})} \mathbf{u}^{n+1} \xrightarrow{\alpha^{n+1} \mathbf{v}^1} \bar{\mathbf{u}}^{n+1}.$$

2.5 Stability analysis of the Navier-Stokes equations

2.5.1 Algorithms for linear stability analysis

In this section, we present a general overview of the numerical procedure for linear stability analysis. Linear stability analysis examines the stability of a base flow by considering the evolution of infinitesimal perturbations. These perturbations in general, may either grow or decay exponentially, indicating whether the base flow is linearly unstable or stable respectively. In §1.2, we introduced linear stability analysis in the context of wall-bounded shear flows leading to the Orr-Sommerfeld equations, where the base flows depend on a single inhomogeneous and two homogeneous directions, commonly referred to as local² stability analysis. For example, the laminar Poiseuille flow, $U(y) = 1 - y^2$ and the laminar Couette flow $U(y) = y$, $y \in [-1, 1]$. For some flows such as boundary layers, wakes and jets, their base flows are not strictly parallel. By considering a weak dependence on the stream and spanwise directions, their stability are described by the parabolised stability equations [Herbert, 1997]. When the base flow depends on two spatially inhomogeneous directions, $U(x, y)$, or three spatially inhomogeneous directions, $U(x, y, z)$, the analysis of such states are commonly referred to as biglobal or triglobal stability analysis, respectively [Theofilis, 2003]. If the base flow is time-dependent, such as in the secondary instability of cylinder flows, we use Floquet stability analysis [Henderson and Barkley, 1996].

In this section, we consider a time-independent base flow and consider a generic decomposition

²Referring to being spatially local in the context of ‘real’ flows which are typically inhomogeneous in all directions

of the velocity field in three spatial dimensions,

$$\mathbf{u}(\mathbf{x}, t) = \mathbf{U}(\mathbf{x}) + \mathbf{u}'(\mathbf{x}, t), \quad (2.77)$$

where $\mathbf{U}(\mathbf{x})$, $\mathbf{u}'(\mathbf{x}, t)$ refers to the base flow and perturbations. Substituting this into the Navier-Stokes equations and linearising,

$$\frac{\partial \mathbf{u}'}{\partial t} = -(\mathbf{U} \cdot \nabla) \mathbf{u}' - (\mathbf{u}' \cdot \nabla) \mathbf{U} - \nabla p' + \frac{1}{Re} \nabla^2 \mathbf{u}', \quad (2.78a)$$

$$\nabla \cdot \mathbf{u}' = 0. \quad (2.78b)$$

This can be rewritten in as,

$$\frac{\partial}{\partial t} \mathbf{q}' = \mathcal{L} \mathbf{q}', \quad \mathcal{L} = \begin{bmatrix} -(\mathbf{U} \cdot \nabla) - (\nabla \mathbf{U}) + \frac{1}{Re} \nabla^2 & -\nabla \\ \nabla \cdot & 0 \end{bmatrix}, \quad (2.79)$$

where \mathcal{L} refer to the linearised operator and, $\mathbf{q}' = (\mathbf{u}', p')^T$. Assuming an initial perturbation, $\mathbf{q}'(\mathbf{x}, t = 0) = \mathbf{q}_0$, its evolution to time T is given by,

$$\mathbf{q}(\mathbf{x}', T) = \mathcal{A}(T, Re) \mathbf{q}_0, \quad \text{where } \mathcal{A}(T, Re) = \exp(\mathcal{L}T). \quad (2.80)$$

We assume that the perturbations can be represented as a normal mode,

$$\mathbf{q}'(\mathbf{x}, t) = \tilde{\mathbf{q}}(\mathbf{x}) \exp(\lambda t) + \text{c.c} \quad (2.81)$$

where $\lambda_j, \tilde{\mathbf{q}}_j(x)$ refer to the j^{th} eigenvalue and eigenmode, and c.c refers to the complex conjugate. Substituting the normal mode into equation (2.80), we obtain an eigenvalue problem,

$$\mathcal{A}(T, Re) \tilde{\mathbf{q}}_j = \mu_j \tilde{\mathbf{q}}_j, \quad \mu_j = \exp(\lambda_j T). \quad (2.82)$$

where μ_j refers to the eigenvalue of $\mathcal{A} = \exp(\mathcal{L}T)$, and we typically set $T = 1$ [Barkley et al., 2008]. The real component of the eigenvalues determine the stability of the base flow, which can be either,

1. Unstable: $\Re(\lambda) > 0$,
2. Stable: $\Re(\lambda) < 0$,
3. Neutral: $\Re(\lambda) = 0$.

This concludes the mathematical overview of linear stabiltiy analysis, and the challenge lies in the computing the eigenpairs of \mathcal{A} efficiently. For large matrices, $\mathcal{A} \in \mathbb{R}^{M \times M}$ (assuming it is real here for simplicity), direct eigenvalue solvers such as the QR algorithm costing $O(M^3)$ might be computationally infeasible. Another concern is that we are typically only interested in the most dangerous (leading) eigenvalues of largest real parts, and not the full spectrum. Lastly, we do not have access to \mathcal{A} in a time stepping based code.

Power Iteration Method

A simple method in computing the dominant eigenpair is the power iteration method,

Definition 2.5.1 (Power iteration). Given a diagonalisable matrix $\mathbf{A} \in \mathbb{R}^{n \times n}$ and a non-zero vector \mathbf{x}_0 , the sequence of matrix vector products between them (we neglect normalisation here),

$$\mathbf{A}\mathbf{x}_0, \mathbf{A}^2\mathbf{x}_0, \mathbf{A}^3\mathbf{x}_0, \dots, \mathbf{A}^k\mathbf{x}_0. \quad (2.83)$$

approaches the eigenvector of \mathbf{A} with the largest magnitude. i.e. $\tilde{\mathbf{x}}_1 = \lim_{k \rightarrow \infty} \mathbf{A}^k \mathbf{x}_0$. The dominant eigenvalue, λ_1 , can be computed using the Rayleigh quotient, $\lambda_1 = \frac{\tilde{\mathbf{x}}_1^T \mathbf{A} \tilde{\mathbf{x}}_1}{\tilde{\mathbf{x}}_1^T \tilde{\mathbf{x}}_1}$.

Arnoldi Method

We typically require two to four eigenpairs with the largest real parts. To compute more than one eigenpair, we utilise the Arnoldi method [Arnoldi, 1951], belonging to a class of Krylov subspace iterative methods, for performing a Hessenberg reduction.

Definition 2.5.2 (Krylov Subspaces). Given a matrix $\mathbf{A} \in \mathbb{R}^{n \times n}$ and a non-zero vector $\mathbf{x}_0 \in \mathbb{R}^n$, the k^{th} -Krylov subspace, $\mathcal{K}_n(\mathbf{A}, \mathbf{x}_0, k)$ is defined by,

$$\mathcal{K}_n(\mathbf{A}, \mathbf{x}_0, k) = \text{span}\{\mathbf{x}_0, \mathbf{A}\mathbf{x}_0, \mathbf{A}^2\mathbf{x}_0, \mathbf{A}^3\mathbf{x}_0, \dots, \mathbf{A}^{k-1}\mathbf{x}_0\}. \quad (2.84)$$

Definition 2.5.3 (Hessenberg reduction). The Hessenberg reduction is a matrix decomposition technique commonly used for the computing eigenpairs of matrices. Given a unsymmetric matrix $\mathbf{A} \in \mathbb{R}^{N \times N}$ (we assume that \mathbf{A} is real for simplicity), we seek a decomposition of the form,

$$\mathbf{A} = \mathbf{Q}\mathbf{H}\mathbf{Q}^T, \quad (2.85)$$

where,

- $\mathbf{H} \in \mathbb{R}^{N \times N}$ is an upper Hessenberg matrix (i.e. $a_{i,j} = 0$ for $i > j + 1$)
- $\mathbf{Q} \in \mathbb{R}^{N \times N}$ is an orthonormal matrix (i.e. $\mathbf{Q}^{-1} = \mathbf{Q}^T$), whose columns $\mathbf{q}_1, \dots, \mathbf{q}_N$, form an orthonormal basis.

The Hessenberg reduction shows that \mathbf{A} and \mathbf{H} are similar matrices, which have the same eigenvalues. If $\mathbf{Ax} = \lambda\mathbf{x}$, using $\mathbf{Q}^T = \mathbf{Q}^{-1}$ and multiplying (2.85) by \mathbf{x} ,

$$\mathbf{Ax} = \mathbf{Q}\mathbf{H}\mathbf{Q}^{-1}\mathbf{x} \Rightarrow \lambda\mathbf{x} = \mathbf{Q}\mathbf{H}\mathbf{Q}^{-1}\mathbf{x} \Rightarrow \lambda\mathbf{Q}^{-1}\mathbf{x} = \mathbf{H}\mathbf{Q}^{-1}\mathbf{x} \Rightarrow \lambda\mathbf{y} = \mathbf{Hy}. \quad (2.86)$$

Hence, $\lambda(\mathbf{A}) = \lambda(\mathbf{H})$, and their eigenvectors are related by $\mathbf{x} = \mathbf{Q}\mathbf{y}$.

The Arnoldi method generates a sequences of vectors $[\mathbf{u}_0, \mathbf{Au}_0, \dots, \mathbf{A}^{k-1}\mathbf{u}_0]$ that spans the k -dimensional Krylov subspace. These vectors, are known as Arnoldi vectors [Golub and Van Loan, 2013], and are used to construct an orthogonal matrix via the Gram-Schmidt process, $\mathbf{Q} = [\mathbf{q}_1, \mathbf{q}_2, \dots, \mathbf{q}_k] \in$

$\mathbb{R}^{M \times K}$. This is equivalent to performing a partial Hessenberg reduction of $\mathcal{A} = \mathbf{Q}\mathbf{H}\mathbf{Q}^T$, where the eigenvalues of $\mathcal{A} \in \mathbb{R}^{N \times N}$ can be approximated by a smaller Hessenberg matrix $\mathbf{H} \in \mathbb{R}^{k \times k}$, suitable for a direct eigenvalue computation using the QR algorithm. The k -step Arnoldi factorisation of \mathcal{A} gives,

$$\mathcal{A}\mathbf{Q}_k = \mathbf{Q}_k\mathbf{H}_k + \mathbf{r}_k\mathbf{e}_k^T, \quad (2.87)$$

where $\mathbf{H} \in \mathbb{R}^{k \times k}$ refers to the upper Hessenberg matrix, $\mathbf{e}_k = [0, \dots, 0, 1] \in \mathbb{R}^k$, and $\mathbf{r}_k \in \mathbb{R}^N$ is a residual vector. If $\mathbf{x} = \mathbf{Q}_k\mathbf{y}$, and $\mathbf{H}\mathbf{y} = \lambda\mathbf{y}$ then,

$$(\mathcal{A} - \mathbf{I}\lambda)\mathbf{x} = (\mathbf{e}_k^T\mathbf{y})\mathbf{r}_k. \quad (2.88)$$

In other words, the residual vector difference between the approximation of $\lambda(\mathcal{A})$, using $\lambda(\mathbf{H})$. If $\|\mathbf{r}_k\| = 0$, then $\lambda(\mathbf{H}) \subseteq \lambda(\mathcal{A})$.

We now present the Arnoldi method by generating k Arnoldi vectors,

$$\mathbf{T}_k = [\mathbf{u}_0, \mathbf{u}_1, \dots, \mathbf{u}_{k-1}] = \left[\mathbf{u}_0, \frac{\mathcal{A}(T, Re)\mathbf{u}_0}{\alpha_1}, \frac{\mathcal{A}(T, Re)\mathbf{u}_1}{\alpha_2}, \dots, \frac{\mathcal{A}(T, Re)\mathbf{u}_{k-1}}{\alpha_k} \right], \quad (2.89)$$

where α_j is scaled such that $\|\mathbf{u}_j\| = 1$. Following [Barkley et al., 2008], the projection of \mathcal{A} onto the Krylov subspace is given as,

$$\mathcal{A}\mathbf{T}_k = \mathbf{T}_{k+1}D_k^{(k+1)}, \quad (2.90)$$

where $D_k^{(k+1)} \in \mathbb{R}^{(k+1) \times k}$ is a shifted diagonal matrix with entries $D_{ij} = \alpha_i \delta_{i,j+1}$. We assume that \mathbf{T}_k and \mathbf{T}_{k+1} admit QR decompositions,

$$\mathcal{A}\mathbf{Q}_k\mathbf{R}_k = \mathbf{Q}_{k+1}\mathbf{R}_{k+1}\mathbf{D}_k^{(k+1)}, \quad (2.91)$$

where $\mathbf{Q}_k \in \mathbb{R}^{N \times k}$, $\mathbf{R}_k \in \mathbb{R}^{k \times k}$ and $\mathbf{Q}_{k+1}, \mathbf{R}_{k+1}$ are similarly defined. The upper Hessenberg matrix $\mathbf{H}_k^{(k+1)} \in \mathbb{R}^{(k+1) \times k}$ is defined as,

$$\mathbf{H}_k^{(k+1)} = \mathbf{R}_{k+1}\mathbf{D}_k^{(k+1)}\mathbf{R}_k^{-1}, \quad (2.92)$$

in which the last row of $\mathbf{H}_k^{(k+1)}$ only contains a single non-zero entry, $h^* = h_{k,k-1}$. By substituting the definition of the upper Hessenberg matrix and separating the last row of $\mathbf{H}_k^{(k+1)}$ we obtain,

$$\mathcal{A}\mathbf{Q}_k = \mathbf{Q}_k\mathbf{H}_k + h^*\mathbf{q}_k\mathbf{e}_k^T. \quad (2.93)$$

Equation (2.93) describes the projection of \mathcal{A} onto the Krylov subspace spanned by orthonormal bases \mathbf{Q}_k , yielding a smaller \mathbf{H}_k matrix. The accuracy of this approximation is dictated by the magnitude of the residual term, $h^*\mathbf{q}_k\mathbf{e}_k^T$. Assuming that \mathbf{H}_k is diagonalisable as $\mathbf{H}_k = \Psi_k \Lambda_k \Psi_k^{-1}$, we multiply equation (2.93) by Ψ_k ,

$$\mathcal{A}\mathbf{Q}_k\Psi_k = \mathbf{Q}_k\Psi_k\Psi_k^{-1}\mathbf{H}_k\Psi_k + h^*\mathbf{q}_k\mathbf{e}_k^T\Psi_k. \quad (2.94)$$

Simplifying the expression above we get,

$$\mathcal{A}\mathbf{V}_k = \mathbf{V}_k\Lambda_k + h^*\mathbf{q}_k\mathbf{e}_k^T\boldsymbol{\Psi}_k, \quad (2.95)$$

where Λ_k contains the k eigenvalues and $\mathbf{V}_k = \mathbf{Q}_k\boldsymbol{\Psi}_k$ the eigenvectors of \mathcal{A} . The error in approximating the j^{th} eigenpair is given by,

$$\varepsilon_j = \|\mathcal{A}\mathbf{v}_j - \lambda_j\mathbf{v}_j\| = \|h^*\mathbf{q}_k\mathbf{e}_k^T\psi_j\| = |h^*|\mathbf{v}_j[k-1]|, \quad (2.96)$$

where $\mathbf{v}_j[k-1]$ is the last component of the eigenvector \mathbf{v}_j .

Lastly, we are generally interested in obtaining the eigenpairs with the the largest real part. We introduce exponential power method [Tuckerman and Barkley, 2000], which is naturally considered by time stepping an initial perturbation \mathbf{q}'_0 from $t = 0$ to T ,

$$\mathbf{q}'(T) = \exp(\mathcal{L}T)\mathbf{q}'_0 = \mathcal{A}(T)\mathbf{q}'_0. \quad (2.97)$$

The dominant eigenvalues, μ , of \mathcal{A} obtained from the Arnoldi method described above, which correspond to the eigenvalue of the largest real part λ , of \mathcal{L} by $\mu = \exp(\lambda T)$, where T is typically set to 1. For further details on this algorithm, the reader is referred to Barkley et al. [2008] for more details.

In summary, the algorithm described above have been implemented in Nektar++, referred to as the ‘modified’ Arnoldi algorithm, which modifies the existing time-stepper code with a wrapper function that generates Arnoldi vectors and solves the Hessenberg matrix using the subroutine dgeev from LAPACK (Linear Algebra PACKage, [Anderson et al., 1999]). The modified Arnoldi algorithm has been verified against using a separate implementation based on the third-party package ARPACK (ARnoldi PACKage [Lehoucq et al., 1998]) [Rocco, 2014].

2.5.2 Edge tracking

In the section, we consider the dynamical system interpretation of transition, where the laminar state is separated by the turbulent state by an edge, referred to the edge of chaos. Along this edge, there could be attractors, sometimes in the form of travelling-waves, tori, and high-order invariant sets, known as the edge states. For the edge tracking, we use the bisection method [Skufca et al., 2006, Schneider et al., 2007, Khapko et al., 2016], with an initial condition given by

$$\mathbf{x}_0 = \chi\mathbf{x}_L + (1-\chi)\mathbf{x}_T \quad (2.98)$$

where \mathbf{x}_0 refers to an initial condition consisting of a weighted sum, $\chi \in [0, 1]$, between a laminar state, \mathbf{x}_L , and a turbulent state, \mathbf{x}_T . Since the laminar and turbulent state forms a bistable system, there could be (at least) one critical value of $\chi \in [0, 1]$, where the trajectory walks along the ‘edge’ between the turbulent and laminar state without decaying to either states. To find this χ_c , we perform n successive bisections between χ_L^n, χ_T^n , the upper and lower bounds such that the trajectory relaminaris or become turbulent respectively, where χ^n is updated by $\chi^n = \frac{1}{2}(\chi_L^n + \chi_T^n)$ At every n^{th} bisection,

it involves a stopping criteria, a tolerance based on the deviation of an observable (e.g. wall shear stresses) away from the initial condition. Then, a direct numerical simulation is reinitialised with an initial condition given by equation (2.98) For every successive bisection, the difference between two trajectories, $\Delta\chi^n = \chi_L^n - \chi_T^n$, decays like $\Delta\chi^n \sim 0.5^n$, and is related to the Lyapunov exponent of the edge

$$\Delta\chi \approx C \exp(\mu_e t) \quad (2.99)$$

where μ_e, C refers to the Lyapunov exponent of the edge and a constant. In practice, we consider $n = 10, 20$ and for $n = 10$, the solution along the edge is converged. After we determine the critical χ_c , we repeat the bisections step by replacing the laminar state, \mathbf{x}_L , and the turbulent state \mathbf{x}_T , which the solution trajectory with χ_L and χ_T , that has been terminated after exceeded the threshold. We refer this repetition as the number of ‘outer’ bisections, while the bisection for χ^n is referred to ‘inner bisections’ After a certain number of ‘outer’ bisections, the trajectory may converge towards an attractor, which may exist in a form of travelling-waves, periodic orbits or a chaotic attractor. This attractor sits along the edge is referred to as the edge state, a saddle acting as a separatrix between the turbulent and laminar attractor. We describe the algorithm of edge tracking in algorithm 2.5.2

Algorithm 1 Algorithm for edge tracking between a turbulent and laminar state

```
1: Initialise maxInBisects, maxOutBisects           ▷ Maximum inner and outer bisections
2: Initialise tol                                     ▷ Tolerance for stopping criteria (e.g., wall-shear stress)
3: outBisects ← 0
4: while outBisects < maxOutBisects do
5:   if outBisects == 0 then
6:      $\mathbf{x}_L, \mathbf{x}_T \leftarrow \text{input}()$                       ▷ Initial laminar and turbulent states
7:   end if
8:    $\chi_L \leftarrow 0, \chi_T \leftarrow 1, \chi \leftarrow \frac{1}{2}(\chi_L + \chi_T)$       ▷ Initialise bisection coefficients
9:    $\mathbf{x}_0 \leftarrow \chi \mathbf{x}_T + (1 - \chi) \mathbf{x}_L$                          ▷ Initialise initial condition
10:  inBisects ← 0
11:  while inBisects < maxInBisects do
12:    k ← 0,  $\Delta \leftarrow 10^6$ 
13:    while  $\Delta > \text{tol}$  do
14:       $\mathbf{x}_{k+1} \leftarrow \text{TimeIntegrate}(\mathbf{x}_k)$ 
15:       $\Delta \leftarrow |\mathbf{x}_{k+1} - \mathbf{x}_0|$                                 ▷ Deviation from initial condition
16:      k ← k + 1
17:    end while
18:    if isTurbulent( $\mathbf{x}_k$ ) then                                         ▷ Check if terminal state is turbulent
19:       $\chi_L \leftarrow \chi$                                               ▷  $\mathbf{x}_L$  gets larger weight
20:      if inBisects == maxInBisects - 1 then
21:         $\mathbf{x}_T \leftarrow \mathbf{x}_k$                                          ▷ Save turbulent-leaning initial condition
22:        break
23:      end if
24:    else
25:       $\chi_T \leftarrow \chi$ 
26:      if inBisects == maxInBisects - 1 then
27:         $\mathbf{x}_L \leftarrow \mathbf{x}_k$                                          ▷ Save laminar-leaning initial condition
28:        break
29:      end if
30:    end if
31:     $\chi \leftarrow \frac{1}{2}(\chi_L + \chi_T)$ 
32:     $\mathbf{x}_0 \leftarrow \chi \mathbf{x}_L + (1 - \chi) \mathbf{x}_T$                   ▷ Update initial conditions
33:    inBisects++
34:  end while
35:  outBisects++
36: end while
```

Chapter 3

Transitional Rayleigh-Bénard Poiseuille flows

In this chapter, we investigate the transitional flow regimes arising from the interaction between buoyancy and shear in Rayleigh-Bénard Poiseuille (RBP) flows within large domains. The transition boundaries between the bistable system consisting of spiral defect chaos (SDC) and ideal straight rolls (ISRs) in Rayleigh-Bénard convection (see §1.3), and subcritical turbulence in plane Poiseuille flows (see §1.2) are not known.

Using Nektar++, a spectral/ hp element package, we conduct direct numerical simulations over a range of Rayleigh numbers, $Ra \in [0, 10000]$, Reynolds numbers, $Re \in [0, 2000]$ and unit Prandtl number, we identify five distinct regimes: (1) bistable SDC & ISRs, (2) ISRs, (3) wavy rolls, (4) intermittent rolls, and (5) shear-driven turbulence. The newly identified intermittent rolls state, features longitudinal rolls that spontaneously decay towards the laminar state. In the transitional shear-driven turbulent regime, longitudinal rolls may coexist with turbulent-laminar bands. The role of longitudinal rolls in transitional RBP flows is apparent, and we examine the unstable manifold of longitudinal rolls in a confined domain, integrating along which led to transient turbulence, decaying towards the laminar state before regenerating into longitudinal rolls again, sustaining transient turbulence. Near the intermittent roll regime, a periodic orbit emerges between the longitudinal rolls and the laminar state within a confined domain. Above a certain Re threshold, the unstable longitudinal rolls provide an intermediate pathway for the transition from the laminar state to turbulence. Finally, we provide a state space sketch of the dynamical processes, emphasising the role of longitudinal rolls in transitional RBP in confined domains, and discuss connections to the large domains.

3.1 Objectives

While the linear stability characteristics of laminar RBP flows have been well studied (see §1.4), the transition to shear-driven turbulence remains and the related nonlinear dynamics remain largely unexplored.

As the first step towards understanding the transition in RBP flows, the main objective of this chapter is to perform exploratory direct numerical simulations (DNS) of transitional RBP flows while investigating the impact of Re on the bistability between SDC and ISRs in RBC as well as the influence of Ra on turbulent-laminar bands in PPF. For this purpose, we consider a relatively wide range of

parameter space given by $Ra \in [0, 10000]$ and $Re \in [0, 2000]$ at $Pr = 1$ in both large and confined domains ($\Gamma = 4\pi, \pi/2$, in particular). Given that this study is largely exploratory, we will focus on identifying different flow regimes and providing key insights into their dynamical processes. Due to the large parameter space, we do not intend to perform an extensive bifurcation analysis that involves the computation and analysis of the invariant solutions, which could be computationally very costly, especially in a large domains.

The chapter is organised as follows: in §3.2, we describe the problem formulation, governing equations, the numerical methods and setup. In §3.3, we present the Ra - Re phase space, identifying five distinct regimes and their coarse-grained transition boundaries. We also show a new ‘intermittent roll’ regime and discuss the coexistence of longitudinal rolls with turbulent-laminar bands, highlighting the role of longitudinal rolls in transitional RBP flows. In §3.4, we perform a numerical experiment, in which simulations are performed along the unstable manifolds of longitudinal rolls in a confined domain, $\Gamma = \pi/2$. We will see that this reveals some dynamical connections between shear-driven turbulence, longitudinal rolls, and the laminar state and subsequently discuss their relevance to the larger domain. Finally, we conclude in §3.5, and provide some perspectives for future work.

3.2 Problem formulation

3.2.1 Governing equations

The motion of fluid flow in an RBP system (see §1.1), is governed by the non-dimensionalised Navier-Stokes equations with Boussinesq approximation,

$$\frac{\partial \mathbf{u}}{\partial t} + (\mathbf{u} \cdot \nabla) \mathbf{u} = -\nabla p + \frac{1}{Re} \nabla^2 \mathbf{u} + \frac{Ra}{8PrRe^2} \theta \mathbf{j}, \quad (3.1a)$$

$$\frac{\partial \theta}{\partial t} + (\mathbf{u} \cdot \nabla) \theta = \frac{1}{RePr} \nabla^2 \theta, \quad (3.1b)$$

$$\nabla \cdot \mathbf{u} = 0, \quad (3.1c)$$

with the following boundary conditions at the wall,

$$\mathbf{u}|_{y=\pm h} = 0, \quad \theta|_{y=-h} = 1, \quad \theta|_{y=h} = 0, \quad (3.2)$$

and periodic boundary conditions in the planar x and z directions. $\mathbf{u}(\mathbf{x}, t)$ denotes the non-dimensionalised velocity scaled by the laminar centreline velocity, W_c , i.e. $W_{lam}(y) = W_c(1 - y^2)$. $\mathbf{x} = (x, y, z)$ and t denote the non-dimensionalised spatial and temporal coordinates scaled by the half-height, h and the advective time scale, W_c/h , where x, y, z refers to the spanwise, wall-normal and streamwise directions, respectively. p refers to the non-dimensionalised pressure scaled by ρW_c^2 , and $\theta (\equiv (T - T_U)/\Delta T)$ refers to the non-dimensionalised temperature with T being the absolute temperature. \mathbf{j} denotes the unit vector in the y -direction.

We note that the rescaled $Ra/8$ term in the momentum forcing terms is equivalent to the Rayleigh number scaled based on the half-depth, h , whereas Ra is scaled based on depth, d , as in classical RBC. The Rayleigh number, Ra , Reynolds number Re and Prandtl number, Pr are defined in §1.1. We set $Pr = 1$ in this study. For $Re = 0$, the Rayleigh-Bénard convection problem, we note that the equation (3.1) becomes singular. In such cases, we solve the non-dimensionalised incompressible Navier-Stokes equations based on thermal length, velocity and temporal scales given in §4.

3.2.2 Numerical Methods

The governing equations are solved numerically using Nektar++, an open-source spectral/ hp -element package [Cantwell et al., 2015, Moxey et al., 2020]. The computational mesh consists of 2D quadrilateral elements in the $x - y$ plane generated using Gmsh [Geuzaine and Remacle, 2009] and then imported into Nektar++ using Nekmesh [Green et al., 2024]. The spatial domain is discretised based on the quasi-3D approach, employing spectral/ hp elements in the $x - y$ plane and Fourier expansions in the z (see §2.4.2). We emphasise that the streamwise direction is in z . The discretised equations are solved using a velocity correction scheme, based on a second-order stiffly splitting scheme, where the nonlinear advection and forcing terms are treated explicitly, while the pressure and diffusion terms are treated implicitly (see §2.4.1). The 3/2 and polynomial de-aliasing rule for the Fourier expansions and spectral/ hp elements are applied during the evaluation of the nonlinear advection terms. To drive the flow, we also enforce a constant volumetric flux (see §2.4.3).

3.2.3 Parametric sweep of Ra - Re space

We consider fifty-two numerical simulations at $Re = 0, 0.1, 1, 10, 100, 500, 750, 1000, 1050, 2000$, and $Ra = 0, 2000, 3000, 5000, 8000, 10000$ at $Pr = 1$ with a large aspect ratio of $\Gamma = 4\pi$. Their spatial and temporal numerical resolutions and time-integration horizon, T , are described in the Appendix A.4. The initial conditions of all cases are sampled from a statistically stationary solution. Laminar solutions are obtained for $Ra = 0$, $Re \leq 1000$, with the given set of parameters and are omitted from the analysis. For all the cases considered here, we maintain the same spatial resolution except $Re = 2000$, where the number of Fourier expansions was doubled. The temporal resolution between the numerical simulations differs due to time scales arising from the different flow physics, as we shall see later. We have also considered a mesh independence study for the end case of $Ra = 10000$, $Re = 2000$, where doubling the number of Fourier modes or increasing the polynomial order by 1 led to a $< 1\%$ change in near-wall transport properties defined by the Nusselt number, $Nu = -\langle d\theta/dy_{y=-1} \rangle_{x,z} d/\Delta T$, and shear, $\langle dw/dy|_{y=-1} \rangle_{x,z}$, on the lower wall, where $\langle \cdot \rangle_{x,z} = 1/(L_x L_z) \int_{z,x} \cdot dx dz$ refer to the plane-averaged operator.

3.2.4 Linear Stability Analysis

In §3.4, we will perform numerical experiments where small disturbances are added along the unstable manifolds of longitudinal rolls. This is rooted in linear stability methods discussed earlier in §1.2,

and its numerical technique is presented in §2.5.1. To determine the unstable manifolds, we consider a small disturbance about the longitudinal roll state,

$$\mathbf{u}(\mathbf{x}, t) = \mathbf{u}_{LR}(\mathbf{x}) + \hat{\mathbf{u}}(\mathbf{x}, t), \quad (3.3a)$$

$$\theta(\mathbf{x}, t) = \theta_{LR}(\mathbf{x}) + \hat{\theta}(\mathbf{x}, t), \quad (3.3b)$$

$$p(\mathbf{x}, t) = p_{LR}(\mathbf{x}) + \hat{p}(\mathbf{x}, t), \quad (3.3c)$$

where $\mathbf{q} = [\mathbf{u}, \theta, p]^T$, $\mathbf{q}_{LR} = [\mathbf{u}_{LR}, \theta_{LR}, p_{LR}]^T$ and $\hat{\mathbf{q}} = [\hat{\mathbf{u}}, \hat{\theta}, \hat{p}]^T$ refers to the solution vector, the longitudinal state and the disturbances respectively. We substitute equation (3.3) into (3.1) and neglect the nonlinear terms, leading to the linearised equations,

$$\frac{\partial \hat{\mathbf{q}}}{\partial t} = \mathcal{A}(\mathbf{q}_{LR}; Re, Ra, Pr)\hat{\mathbf{q}}, \quad (3.4a)$$

where

$$\mathcal{A}(\mathbf{q}_{LR}; Re, Ra, Pr) = \begin{pmatrix} -(\mathbf{u}_{LR} \cdot \nabla) - (\nabla \mathbf{u}_{LR} \cdot) + 1/Re \nabla^2 & \frac{Ra}{8Re^2Pr} \hat{\mathbf{j}} & -\nabla \\ -(\nabla \theta_{LR} \cdot) & -(\mathbf{u}_{LR} \cdot \nabla) + \nabla^2 & 0 \\ \nabla \cdot & 0 & 0 \end{pmatrix}. \quad (3.4b)$$

Consider that the longitudinal rolls are invariant along the z -direction, which are also assumed to be periodic in x -direction, and the following form of normal-mode solution can be considered,

$$\hat{\mathbf{q}}(\mathbf{x}, t) = \check{\mathbf{q}}(x, y)e^{i(\alpha x + \beta z) + \lambda t} + \text{c.c}, \quad (3.5)$$

where λ , α and β are the complex frequency, the spanwise wavenumber (or the Floquet exponent), and the stream wavenumber, respectively. Using the periodic nature of $\check{\mathbf{q}}(x, y)$ in the x -direction, (3.5) can also be written as

$$\hat{\mathbf{q}}(\mathbf{x}, t) = \left[\sum_{n=-\infty}^{\infty} \check{\mathbf{q}}_n(y) e^{i \frac{2\pi}{L_x} (n+\epsilon)x} \right] e^{i\beta z + \lambda t} + \text{c.c}, \quad (3.6)$$

where $\epsilon (= \alpha L_x / (2\pi))$ is the Floquet detuning parameter with $0 \leq \epsilon \leq 1/2$. In this study, we will only consider the identification of the unstable manifolds of longitudinal rolls in a fixed computational domain; therefore, the fundamental mode, $\epsilon = 0$, is of sole interest. Substituting equation (3.6) into (3.4) result to a discretised eigenvalue problem with the eigenvalue λ . The wavenumber β , is restricted to discrete values of $\beta = 2\pi m / L_z$, and m is a positive integer for the given computational domain. The resulting eigenvalue problems are solved using an iterative Arnoldi algorithm based on time-stepping schemes implemented in Nektar++ (see §2.5.1).

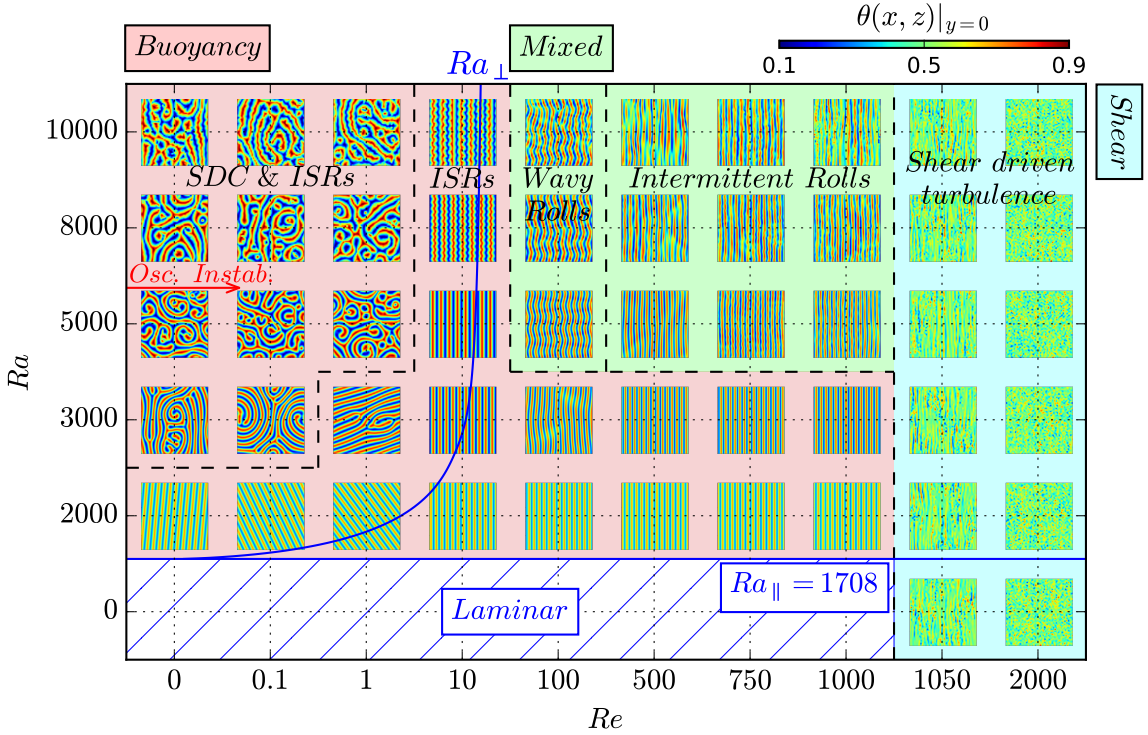


Figure 3.1: The $Ra - Re$ phase space illustrates the terminal midplane temperature snapshots, $\theta(x, z)|_{y=0}$ for $Re \in [0, 2000]$ and $Ra \in [0, 10000]$, classified into five distinct regimes: (1) SDC & ISRs, (2) ISRs, (3) wavy rolls, (4) intermittent rolls and (5) shear-driven turbulence. The blue solid curves refer to primary neutral curves of the longitudinal and transverse rolls Ra_{\parallel} , Ra_{\perp} . The red curve refers to secondary oscillatory instability of ISRs at $Re = 0$ [Bodenschatz et al., 2000]. Shades of red, green and blue indicate their dominant mechanism, whether driven by buoyancy or shear (or mixed). The plot is not to scale.

3.3 Ra - Re phase space

3.3.1 Classification

We present the results obtained from the DNS of transitional RBP flows, focusing on the parameter space defined by Rayleigh numbers in the range $Ra \in [0, 10000]$, and Reynolds numbers in the range of $Re \in [0, 2000]$ (see Appendix A.4 for the full details). At the two end points of the Re -spectrum considered (i.e. $Re = 0, 2000$), SDC and subcritical shear-driven turbulence appear. Figure 3.1 shows the snapshots of the midplane temperature, $\theta(x, z)|_{y=0}$, of different flow regimes on the Ra - Re phase space. The solid blue curves represents to the neutral stability boundaries for the longitudinal and transverse rolls as $Ra_{\parallel} = 1708$ and $Ra_{\perp} = f(Re)$, respectively [Gage and Reid, 1968]. In the absence of shear at $Re = 0$, these curves merge into the classical critical RBC instability at $Ra_c = 1708$, as ISRs become rotationally invariant about the wall-normal axis. Furthermore, a red arrow roughly indicates the secondary neutral stability boundary, marking the onset of oscillatory instabilities of ISRs within $5000 < Ra < 8000$ at $Re = 0$ [Clever and Busse, 1974]. We note that the phase diagram in figure 3.1 is not plotted to scale precisely but serves as a conceptual reference to distinguish between different flow states.

In this Ra - Re phase space, we categorise the flow behaviour into five distinct regimes: (1)

bistability between SDC and ISRs (SDC & ISRs), (2) ideal straight rolls (ISRs), (3) wavy rolls, (4) intermittent rolls, and (5) shear-driven turbulence. The categories are defined based on common flow structures (patterns), and/or dynamical characteristics, ranging from equilibrium solutions to intermittent and chaotic dynamics. Furthermore, we classify these states based on their first and second-order statistical properties, where they appear independent of Re in the buoyancy-dominated regime (shaded in red), and Ra in the shear-dominated regime (shaded in blue), discussed in Appendix A.5. In the mixed regime shaded in green, both Ra and Re are important.

Given that the buoyancy-dominated regime is relatively well studied in RBC systems [Bodenschatz et al., 2000], we will only provide a brief description of the simulation results in this regime. In the buoyancy-dominated regime, the flow structures are predominantly organised by convection rolls, such as SDC, transverse, oblique, longitudinal rolls (and ISRs with no mean flow), or oscillatory rolls. The bistability between SDC and ISRs is preserved for $Ra \geq 3000$ at $Re = 0.1$, and $Re = 1$ for $Ra \geq 5000$. This points towards the existence of Re , at which SDC disappears, say Re_s , Re_s appears to depend on Ra , as demarcated by the black dashed lines on the left side of figure 3.1. However, computing this Re_s -threshold is beyond the scope of this thesis.

Notably, a transverse roll with a ‘hooked-like’ defect is observed at $Re = 1$, $Ra = 3000$, reminiscent of the multiple ‘non-ISR’ states in RBC (see references in §1.3). At $Re = 10$, SDC disappears and longitudinal rolls appear. As Re is increased further to 1000, the longitudinal rolls emerge as the preferred solution at $Ra = 2000, 3000$. Notably, the non-dimensionalised spanwise wavenumber of these longitudinal rolls is approximately $\alpha d \approx 1.65$, which happens to lie outside of the stability boundaries of the Busse balloon in RBC [Busse, 1978]. This suggests that the stability boundaries of the longitudinal rolls may expand as Re increases.

As Re approaches 100, the longitudinal rolls undergo a secondary wavy instability [Clever and Busse, 1991, Pabiou et al., 2005, Nicolas et al., 2010], leading to the emergence of wavy longitudinal rolls depicted in figure 3.1. The wavelength of the streamwise waviness and the spanwise periodic longitudinal roll appear to be approximately three intervals of streamwise length, $\Lambda_z \sim L_z/3$, and twelve intervals of spanwise length, $\Lambda_x \sim L_x/12$, respectively. The ratio between the wavelength of streamwise waviness and spanwise roll is about ~ 4 , around the ballpark reported by Clever and Busse [1991].

3.3.2 Spatiotemporal intermittent rolls

As Re approaches $Re = 500$, the wavy rolls disappear. Instead, a new regime, referred to as intermittent rolls, is observed. In this regime, the longitudinal rolls remain as the dominant convection structure, interspersed with a spatio-temporal intermittent breakdown towards the laminar state. For $Ra = 8000$, $Re = 500$, this behaviour is illustrated with figure 3.2(a), where the temporal oscillations of the plane-averaged shear rate on the lower wall, $\langle dw/dy|_{y=-1} \rangle_{x,z}$, and the Nusselt number, Nu . We note that the plane-averaged shear rate and Nusselt number for the laminar state is at 2 and 1 respectively.

The spatio-temporal intermittent breakdown of the longitudinal rolls towards the laminar state is observed in figure 3.2(b), where the bright and dark regions in the space-time plot of near-wall spanwise

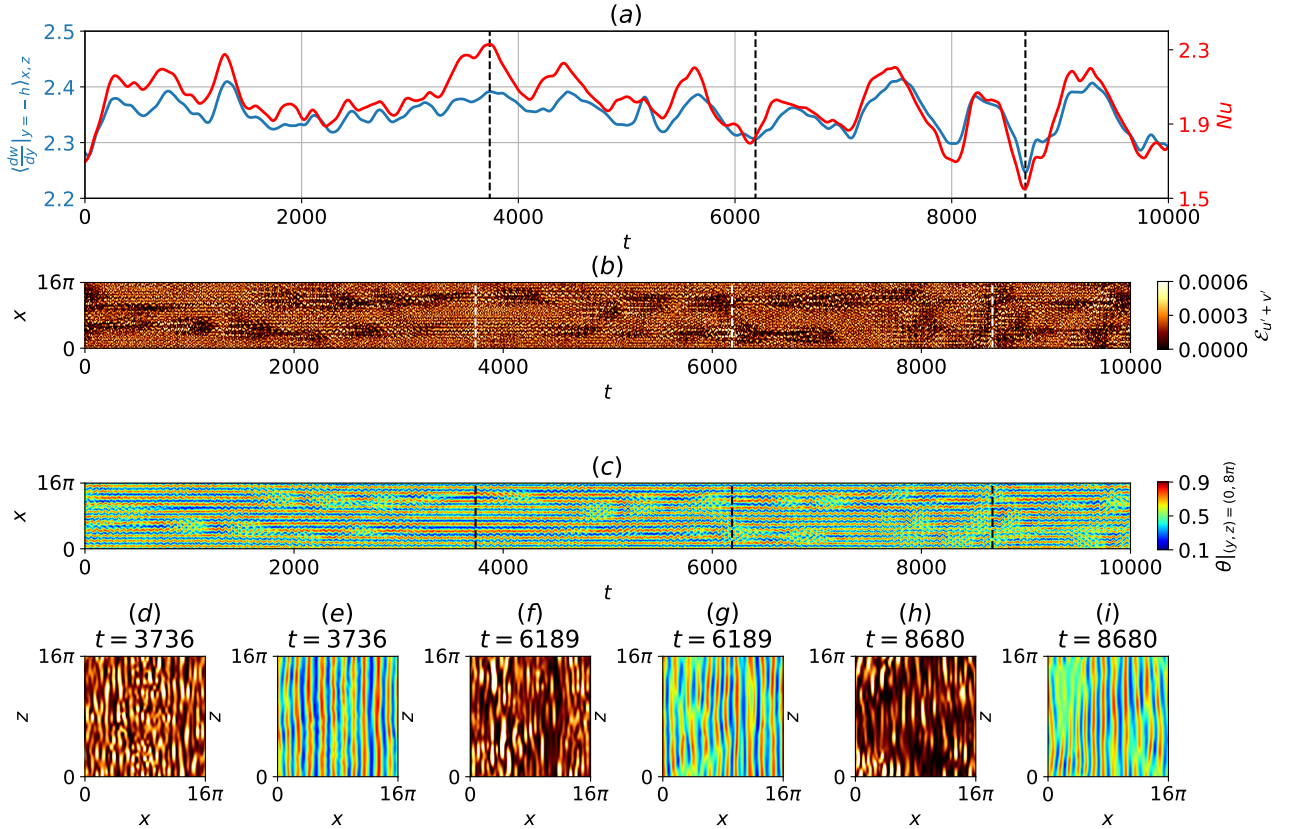


Figure 3.2: The intermittent rolls regime at $Ra = 8000$, $Re = 500$, $t \in [0, 10000]$. (a) The time history of shear on the lower wall and the Nusselt number. Space-time ($x-t$) plots of (b) the near-wall wall-normal and spanwise perturbation kinetic energy and (c) midplane temperature space-time plot, and with the corresponding near-wall and midplane temporal planar snapshots at (d,e) $t = 3736$, (f,g) $t = 6189$, and (h,i) $t = 8680$.

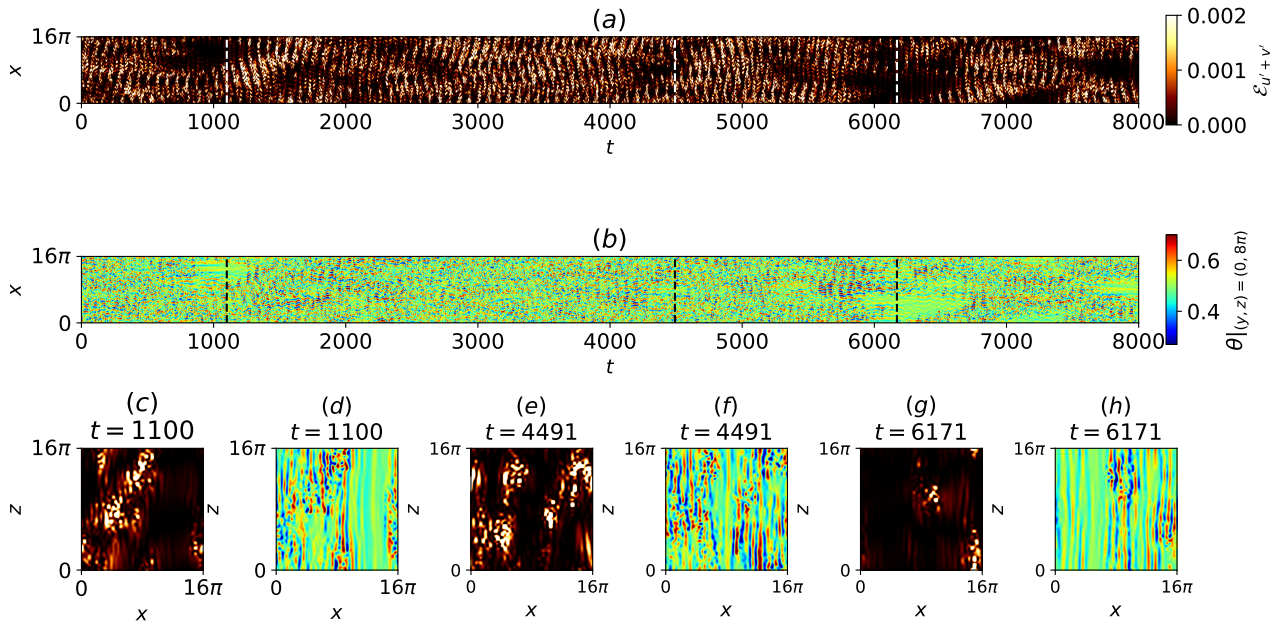


Figure 3.3: Shear-driven turbulence regime at $Ra = 0, Re = 1050, t \in [0, 8000]$. Spacetime plots of (a) near-wall wall-normal and spanwise perturbation kinetic energy, (b) midplane temperature spacetime plot, and near-wall and midplane temporal planar snapshots at (c,d) $t = 1100$, (e,f) $t = 4491$, and (g,h) $t = 6171$, highlighting a prolonged laminar patch.

and wall-normal perturbation kinetic energy, $\mathcal{E}_{u'+v'} = 1/2 \left[u'|_{(y^+, z)=(15, 8\pi)}^2 + v'|_{(y^+, z)=(15, 8\pi)}^2 \right]$ (where $\mathbf{u}' = \mathbf{u} - W_{lam}(y)$, $y^+ = u_\tau y_0 / \nu$, $u_\tau = \sqrt{\langle \gamma/h \rangle_t}$, $y_0 = h - y = 0.44$, refer to perturbation velocities, dimensionless height, frictional velocity, wall-normal height respectively), highlight the presence of longitudinal rolls and spatially-localised laminar states. A similar observation is made with the spacetime plot of midplane temperature, $\theta|_{(y,z)=(0,8\pi)}$, in figure 3.2(c), where the elongated red/blue contours correspond to up-/down-welling regions of longitudinal rolls, and the green regions indicate spatially-localised laminar states. The two near-wall transport properties, such as the wall shear and the Nusselt number, exhibit strong correlations. For example, both peak at $t = 3736$, revealing to a spatially coherent longitudinal roll structure in figure 3.2(d,e). There are also dips observed at $t = 6189$ and $t = 8680$, indicative of the spatially local breakdown towards the laminar state, as shown in figures 3.2(f,g) and 3.2(h,i) respectively. In summary, the longitudinal rolls enhance heat and momentum transfer towards the wall, but they appear to be intermittently disrupted by the breakdown towards the laminar state. To better understand this behaviour, we later consider investigating the temporal dynamics in a confined domain, $\Gamma = \pi/2$, where the spatial intermittency is artificially suppressed (see §3.4.2).

3.3.3 Co-existence of convection rolls with turbulent bands

As Re approaches $Re = 1050$, shear-driven turbulence emerges as spatio-temporal intermittent turbulent-laminar bands, where turbulent and laminar regions can co-exist (see references in §1.2). In the absence of buoyancy ($Ra = 0$), these bands emerge clearly, as shown in figure 3.3. The

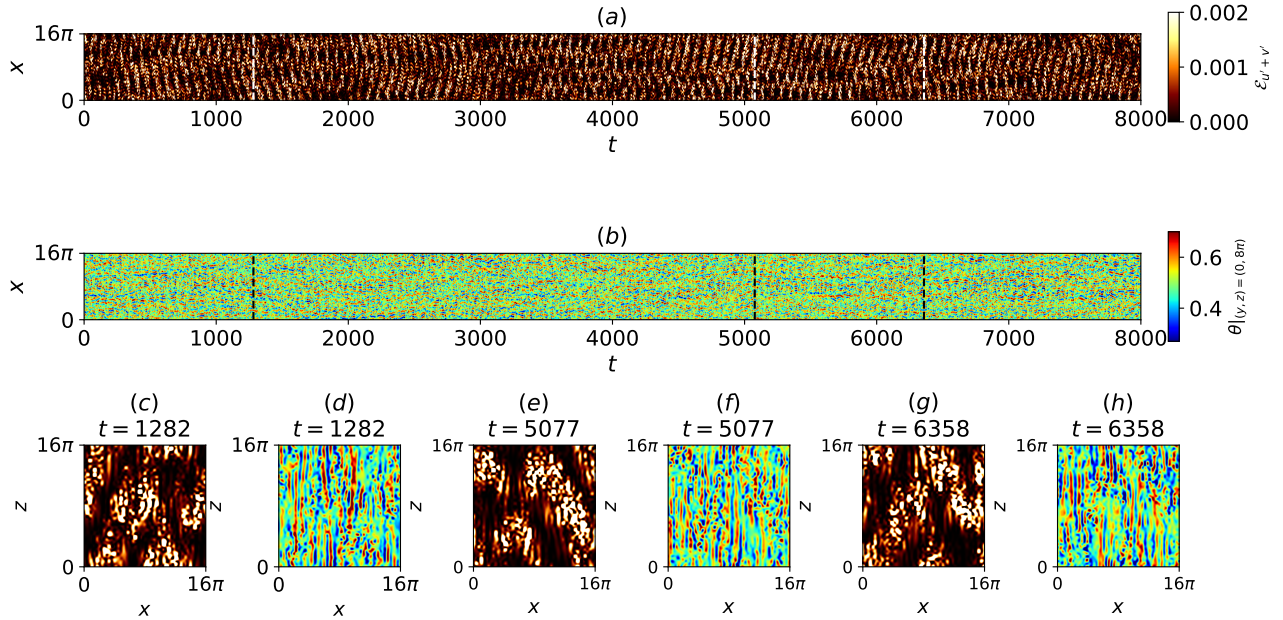


Figure 3.4: Shear-driven turbulence regime at $Ra = 100000$, $Re = 1050$, $t \in [0, 8000]$. Spacetime plots of (a) near-wall wall-normal and spanwise perturbation kinetic energy, (b) midplane temperature spacetime plot, and their corresponding near-wall and midplane temporal $x - z$ planar snapshots at (c,d) $t = 1282$, (e,f) $t = 5077$, and (g,h) $t = 6358$, highlighting the coexistence of longitudinal rolls and turbulent bands.

spacetime plot of the near-wall wall-normal and spanwise perturbation kinetic energy, $\mathcal{E}_{u'+v'}$, in figure 3.3(a) highlights this coexistence, where the turbulent and laminar regions are indicated by dark and bright areas, respectively. In particular, a period of prolonged laminar state is observed at $t = 1100, 4491, 6171$, represented by localised green regions in the space-time plot of midplane temperature, $\theta|_{(y,z)=(0,8\pi)}$, in figure 3.3(b). The prolonged laminar states are also evident in the near-wall and midplane temporal snapshots of figures 3.3(c-h), shown as large pockets of dark and green regions that fill approximately half of the spatial domain. Next, we consider the influence of buoyancy on the turbulent-laminar bands and compare cases at $Ra = 0$ and $Ra = 10000$ at $Re = 1050$. At $Ra = 10000$, the key features of the turbulent-laminar bands depicted as alternate dark and bright bands are also seen in the space-time plot of near-wall wall-normal and spanwise perturbation kinetic energy, $\mathcal{E}_{u'+v'}$, in figure 3.4(a). However, some important differences emerge compared to case in $Ra = 0$. In particular, the midplane temperature snapshots, $\theta|_{(y,z)=(0,8\pi)}$, at $t = 1282, 5077, 6358$ in figures 3.4(d,f,g) reveal some localised regions of streamwise-aligned red and blue contour stripes, indicating the presence of longitudinal rolls, which are absent in $Ra = 0$. These longitudinal roll regions are typically located next to neighbouring turbulent (bright) regions in the near-wall perturbation kinetic energy snapshots in figures 3.4(c,e,g), suggesting that longitudinal rolls coexist with turbulent patches at $Ra = 10000$. However, we caution that although they are relatively weak, similar red and blue contour stripes are also observed at $Ra = 0$, where longitudinal rolls are not expected, shown in figure 3.3(f). In this case, these weak elongated red and blue contour stripes are likely to be near-wall streaks. Nonetheless, turbulence occurs more spatially intermittently at $Ra = 0$, containing prolonged pockets of laminar regions, while the turbulent regions at $Ra = 10000$

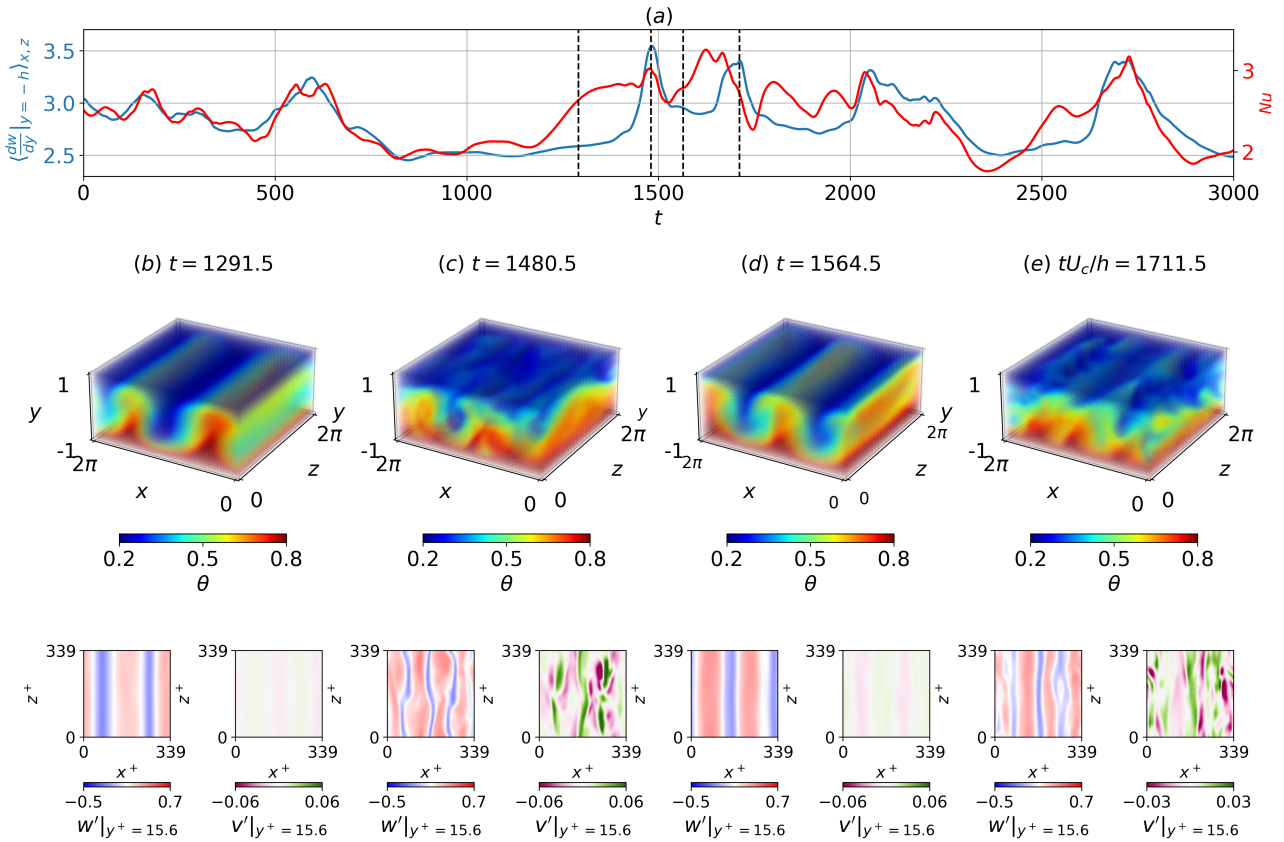


Figure 3.5: Intermittent dynamics in a confined domain at $Ra = 10000$, $Re = 1050$, $t \in [0, 3000]$, $\Gamma = \pi/2$. The time history of the (a) Nusselt number and shear. Temporal snapshots of volumetric temperature, planar near-wall streamwise and spanwise perturbations at (b) $t = 1291.5$, (c) $t = 1480.5$, (d) $t = 1564.5$, (e) $t = 1711.5$. Longitudinal rolls and transient turbulence are observed at (b,d) and (c,e), respectively.

appear more visibly consistently (compare figures 3.3(a) with 3.4(a)). In other words, the presence of longitudinal rolls may promote turbulence locally, and we will investigate this issue further in §3.4 as we consider a confined domain.

3.4 The role of longitudinal rolls

3.4.1 The thermally-assisted sustaining process (TASP) in a confined domain

Given the spatio-temporal complexities observed in §3.3, we consider simulations confined to a confined domain defined by $\Gamma = \pi/2$, where the longitudinal rolls and localised turbulence could be viewed as spatially isolated. We start from a numerical simulation at $Ra = 10000$ and $Re = 1050$, in $\Gamma = \pi/2$, integrated in time for $t \in [0, 3000]$. The initial condition has been sampled from a statistically stationary turbulent field at $Ra = 10000$ and $Re = 2000$, which is then slowly lowered to $Re = 1050$. The time history for $t \in [0, 3000]$ of the two near-wall transport properties, the Nusselt number, and the shear rate, is presented in figure 3.5, together with the snapshots of the temperature, $\theta(x)$, and the near-wall stream- and spanwise perturbation velocities, $w'|_{y^+=15.6}, v'|_{y^+=15.6}$. In this confined domain,

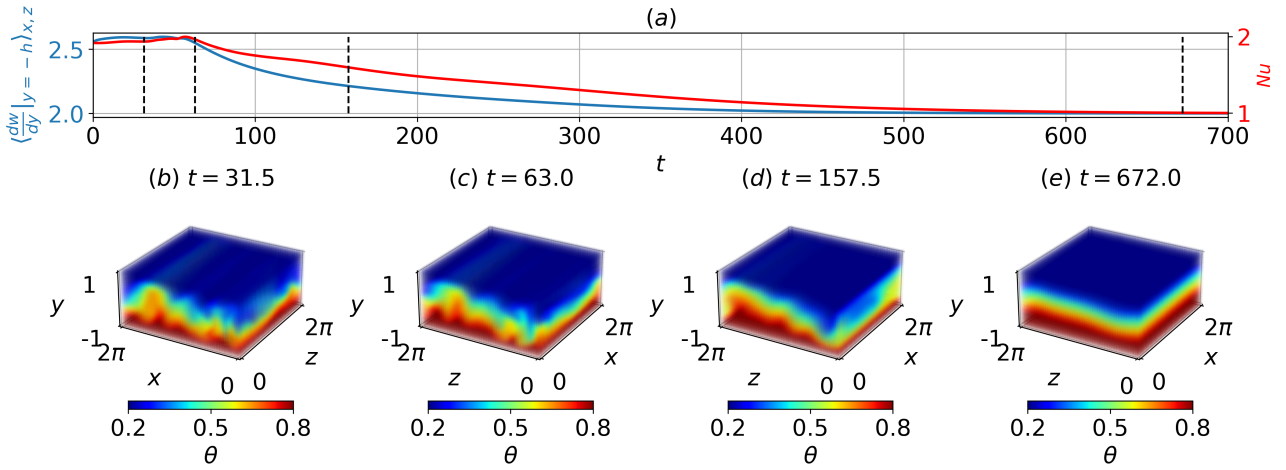


Figure 3.6: Relaminarisation in a confined domain at $Ra = 0$, $Re = 1050$, $t \in [0, 3000]$, $\Gamma = \pi/2$. The time history of the (a) Nusselt number and shear. Temporal snapshots of volumetric temperature at (b) $t = 31.5$, (c) $t = 63$, (d) $t = 157.5$, (e) $t = 672$.

the dynamics of the system exhibits temporal intermittency, where the solution trajectory appears to wander between the longitudinal rolls and highly disorganized chaotic flow fields, characterised by low- and high-near-wall transport properties, respectively. The turbulent dynamics mentioned here refer to chaotic trajectories (see §1.2) marked by a disordered volumetric temperature field and high near-wall transport quantities.

Starting from a longitudinal roll state of spanwise wavenumber of $\alpha d = 4$ at $t = 1291.5$ in figure 3.5(b), the solution erupts into a highly disorganized turbulent state at $t = 1480.5$, marked by a disordered temperature field in figure 3.5(c). During this breakdown, the near-wall snapshots of streamwise perturbation velocity, $w'|_{y+=15}$, and wall-normal perturbation velocity, $v'|_{y+=15}$, illustrated in the bottom panels of figures 3.5(c), reveal three pairs of high- and low-speed streaks, each with an average spanwise wavelength of $\Lambda_x^+ \approx 339/3 = 113$ (where $\Lambda_x^+ = u_\tau \Lambda_x / \nu$ refers to non-dimensionalised wavelength), close to the mean streak spacing ($\Lambda^+ \sim 100$) commonly reported in shear flow turbulence [Kline et al., 1967, Smith and Metzler, 1983, Kim et al., 1987, Hamilton et al., 1995]. These streaks appear to be meandering, negatively correlated with wall-normal perturbation velocities, reminiscent of a streak breakdown process [Hamilton et al., 1995], or a bursting event [?], where high- and low-speed streaks are brought close to and away from the wall, respectively, enhancing near-wall transport quantities. Indeed, this is reflected in large increments in the Nusselt number and wall shear rate of roughly 40% at $t = 1480.5$ in figure 3.5(a). Subsequently, the solution trajectory returns to a longitudinal roll state at $t = 1564.5$, before erupting into turbulence at $t = 1711.5$ (see figures 3.5(d,e) respectively). This suggests that the turbulence has a finite lifetime, occurring transiently before decaying towards the laminar state at $Re = 1050$ [Hof et al., 2006, Schneider et al., 2007], which is linearly unstable, leading to the onset of longitudinal rolls where transient turbulence could be re-excited again.

To test this hypothesis, we consider a numerical simulation at $Ra = 0$, $Re = 1050$, in $\Gamma = \pi/2$, where longitudinal rolls cannot appear. The initial condition is taken from a stationary turbulent

solution at $Ra = 0$, $Re = 2000$, which is then slowly lowered to $Re = 1050$, and then integrated in time for $t \in [0, 700]$. The time history of the Nusselt number, Nu , and the wall shear rate is reported in figure 3.6, together with the temperature snapshots, $\theta(\mathbf{x})$ at selected times. An initial turbulent flow field decays towards decays towards the laminar solution in $t \in [0, 700]$ within the confined domain. Comparing the results between $Ra = 0$ and $Ra = 10000$, we propose that the longitudinal rolls at $Ra = 10000$ could provide a transition mechanism to transient turbulence, which could be sustained indefinitely.

Next, we investigate the impact of longitudinal rolls on this proposed mechanism at different Ra . We perform four numerical simulations with an initial condition taken from $Ra = 10000$ and $Re = 1050$, at $t = 850.5$ (before the onset of longitudinal rolls, see figure 3.5), which is lowered instantaneously to $Ra = 8000, 5000, 3000, 2000$ respectively. The initial conditions are time-integrated further to $t \in [850.5, 5000]$, and the time history of the wall shear rate, $\langle dw/dy|_{y=-h} \rangle_{x,z}$, and the temperature volumetric temporal snapshots, $\theta(\mathbf{x})$, of these experiments of Ra -quenching are presented in figure 3.7. The time history of shear is visibly intermittent for $Ra = 8000, 5000$, depicted as the orange and green trajectories in figure 3.7(a), similar to $Ra = 10000$. At $Ra = 8000, 5000$, the longitudinal rolls emerge approximately at $t = 1312.5$ (see figures 3.7(d,f)), before erupting into turbulence at $t = 1743$ and $t = 3570$ in figures 3.7(e,g) respectively. This is then accompanied by a large spike in the wall shear rate before dipping briefly in figure 3.7(a). As Ra is lowered further to $Ra = 3000, 2000$, the transients begin to decay into a longitudinal state from $t = 850.5$ to $t = 1312.5$, which remains asymptotically stable until $t = 4200$, represented as the red and purple trajectories of figures 3.7(i,k) respectively. This suggests that the longitudinal rolls are likely be linearly unstable for $Ra = 8000, 5000$, leading to turbulence, while remaining stable for $Ra = 3000, 2000$. In particular, the longitudinal rolls state at $Ra = 5000$ remained saturated for a longer period $t \in [1500, 3400]$ (green curve of figure 3.7), indicating that the growth rate of the linear instability is smaller than that of $Ra = 8000$. We note that the longitudinal rolls in figure 3.7 have a spanwise wavenumber of $\alpha d = 4$, which corresponds to the wavenumber of the dominant primary instability (see Appendix A.6), indicating that it is the most preferred wavenumber within the confined domain.

To understand the stability characteristics of the longitudinal rolls, we perform a linear stability analysis about the longitudinal roll state ($\alpha d = 4$), at $Ra = 10000, 8000, 5000, 3000, 2000$. The details of linear stability analysis are described in §3.2.4, where λ and $\hat{s}_\beta e^{i\beta z}$ refer to the eigenvalue and eigenmode. The longitudinal roll (base) states, \mathbf{q}_{LR} , are obtained by time integrating an initial condition consisting of the laminar (conduction) state, superimposed by the primary eigenmode, $\alpha d = 4$, at $Ra = 10000, 8000, 5000, 3000, 2000$, in a two-dimensional $x - y$ plane, suppressing any three-dimensional perturbations numerically. The growth rates as a function of discrete streamwise wavenumbers, $2 \leq \beta d \leq 5$, are presented in figure 3.8. We note that the admissible streamwise wavenumbers within $\Gamma = \pi/2$ are $\beta d = m$, where m is a positive even integer, $m = 2, 4, \dots$, and $\beta d = 3, 5$ are included for completeness. The longitudinal rolls are linearly unstable for $Ra \geq 5000$, while they remain stable for $Ra \leq 3000$, which confirms our hypothesis earlier. In particular, the growth rates between $Ra = 5000$ and $Ra = 10000$ differ by an order of magnitude, which could explain the prolonged period of saturation in the green curve of figure 3.7(a,b). The dominant

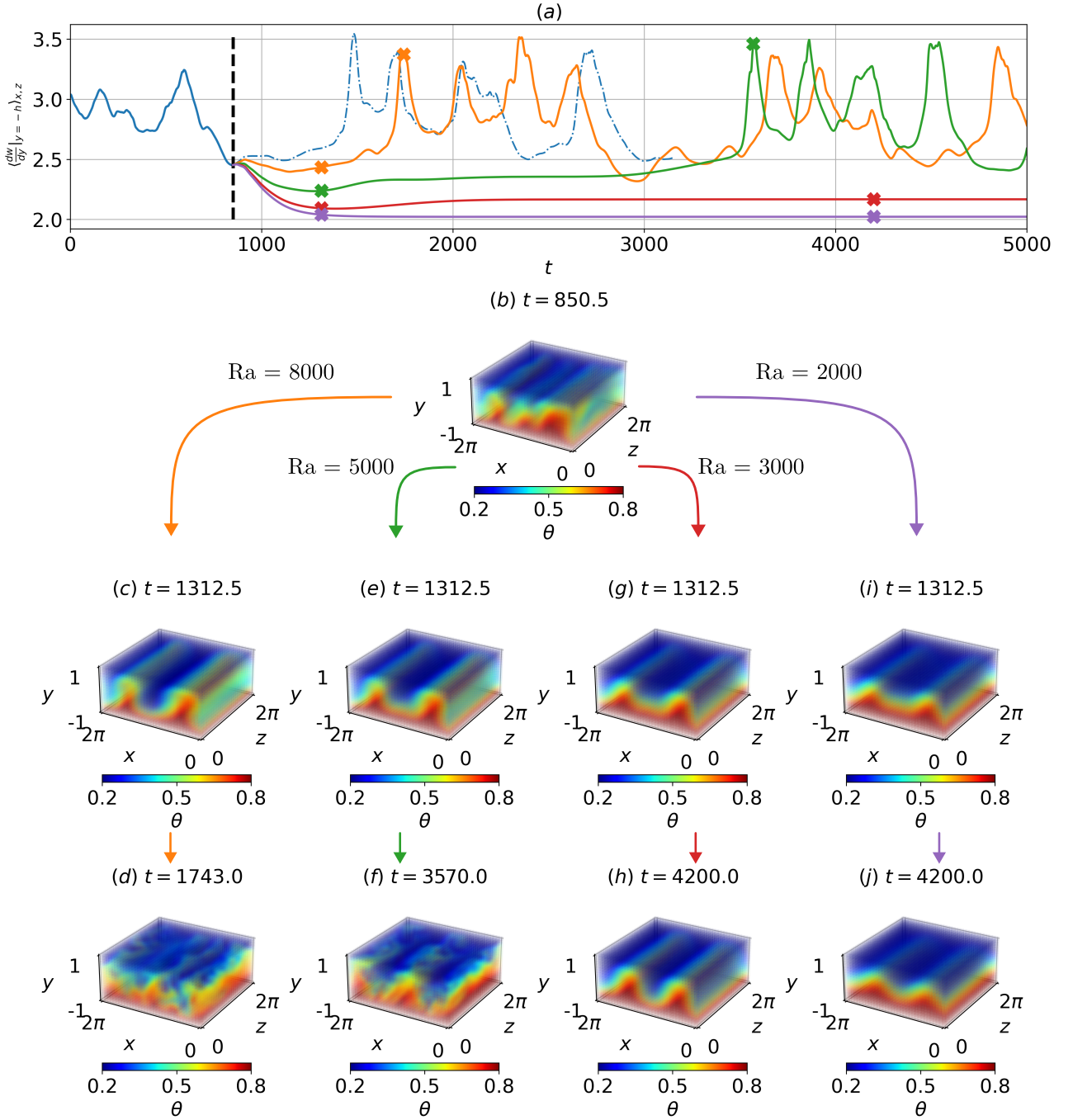


Figure 3.7: Ra -quenching experiments for $Ra = 8000, 5000, 3000, 2000$, $Re = 1050$, $\Gamma = \pi/2$, $t \in [850.5, 5000]$. The time history of (a) shear and (b) volumetric temperature snapshots of the initial condition at $t = 850.5$. Volumetric temperature snapshots for $Ra = 8000$ at (c,d) $t = 1312.5, 1743$, and $Ra = 5000$ at (e,f) $t = 1312.5, 3570$, revealing a longitudinal roll and a turbulent state, respectively. Stable longitudinal rolls emerge for $Ra = 3000$ at (g,h) $t = 1312.5, 4200$, and $Ra = 2000$ at (j,k) $t = 1312.5, 4200$.

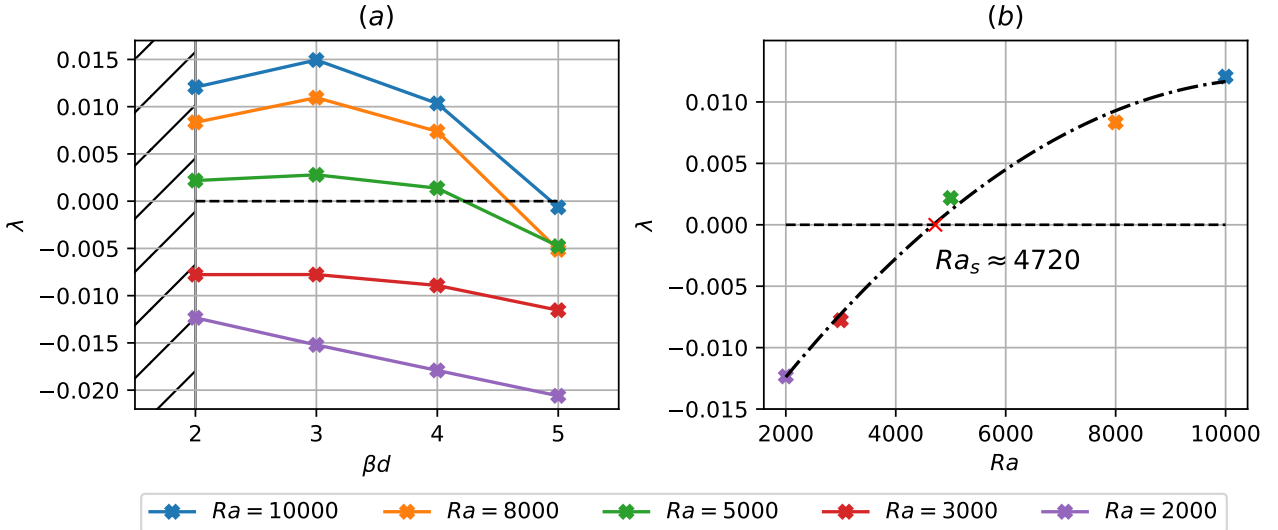


Figure 3.8: The growth rates of infinitesimal perturbations linearised about longitudinal rolls, \mathbf{q}_{LR} , of spanwise wavenumber of $\alpha d = 4$, against (a) streamwise wavenumber λ , and (b) Ra for $\beta d = 1$. The hatches in (a) refer to wavenumbers smaller than those admissible in $\Gamma = \pi/2$. The dash-dotted line in (b) is a standard quadratic regression yielding $Ra_s \approx 4720$.

secondary instability of longitudinal rolls in $\Gamma = \pi/2$ has a streamwise wavenumber of $\beta d = 2$. Using a standard quadratic regression, the critical Rayleigh number for disturbances with $\beta d = 2$ is approximately $Ra_s \approx 4720$, presented in figure 3.8(b).

Following this, we examine the dominant unstable manifold ($\beta d = 2$) of the longitudinal rolls, by considering an initial condition,

$$\mathbf{q}_0(\mathbf{x}, t = 0) = \mathbf{q}_{LR}(x, y) + \hat{\mathbf{q}}_\beta(x, y)e^{i\beta z}, \quad (3.7)$$

which is prescribed to equation (3.1). Here, $\hat{\mathbf{q}}_\beta e^{i\beta dz}$ is an eigenmode for the streamwise wavenumber βd , and its amplitude of which was scaled such that its total energy is defined by,

$$\delta = \frac{1}{V} \int_{\Omega} \hat{\mathbf{u}}(\mathbf{x})^T \hat{\mathbf{u}}(\mathbf{x}) + \frac{Ra}{8Re^2Pr} \hat{\theta}(\mathbf{x})^2 d\Omega \approx O(10^{-3}) \quad (3.8)$$

is considered. We have also considered that $\delta = 10^{-2}, 10^{-4}$, but $\delta = 10^{-3}$ was found to be sufficiently small enough to ensure linear growth, while large enough to be computationally practical. WHAT DO YOU MEAN BY COMPUTATIONALLY PRACTICAL.

The initial condition is time-integrated for $t \in [0, 8000]$, and its time history of the near wall transport properties, the space-time plot of midplane temperature, $\theta|_{(y,z)=(0,\pi)}$, are presented in figure 3.9, with snapshots of temperature, $\theta(\mathbf{x})$, and near-wall streamwise and spanwise perturbation velocities snapshots, $w'|_{y^+=15}, v'|_{y^+=15}$ at some selected times. The intermittent trajectory is visually apparent, oscillating between the longitudinal rolls and transient turbulence over four cycles for $t = [0, 8000]$: for example, the regions of low and high near-wall transport quantities in figure 3.9(a) correspond well to the organised and disorganised longitudinal rolls in figure 3.9(b), respectively. The snapshots

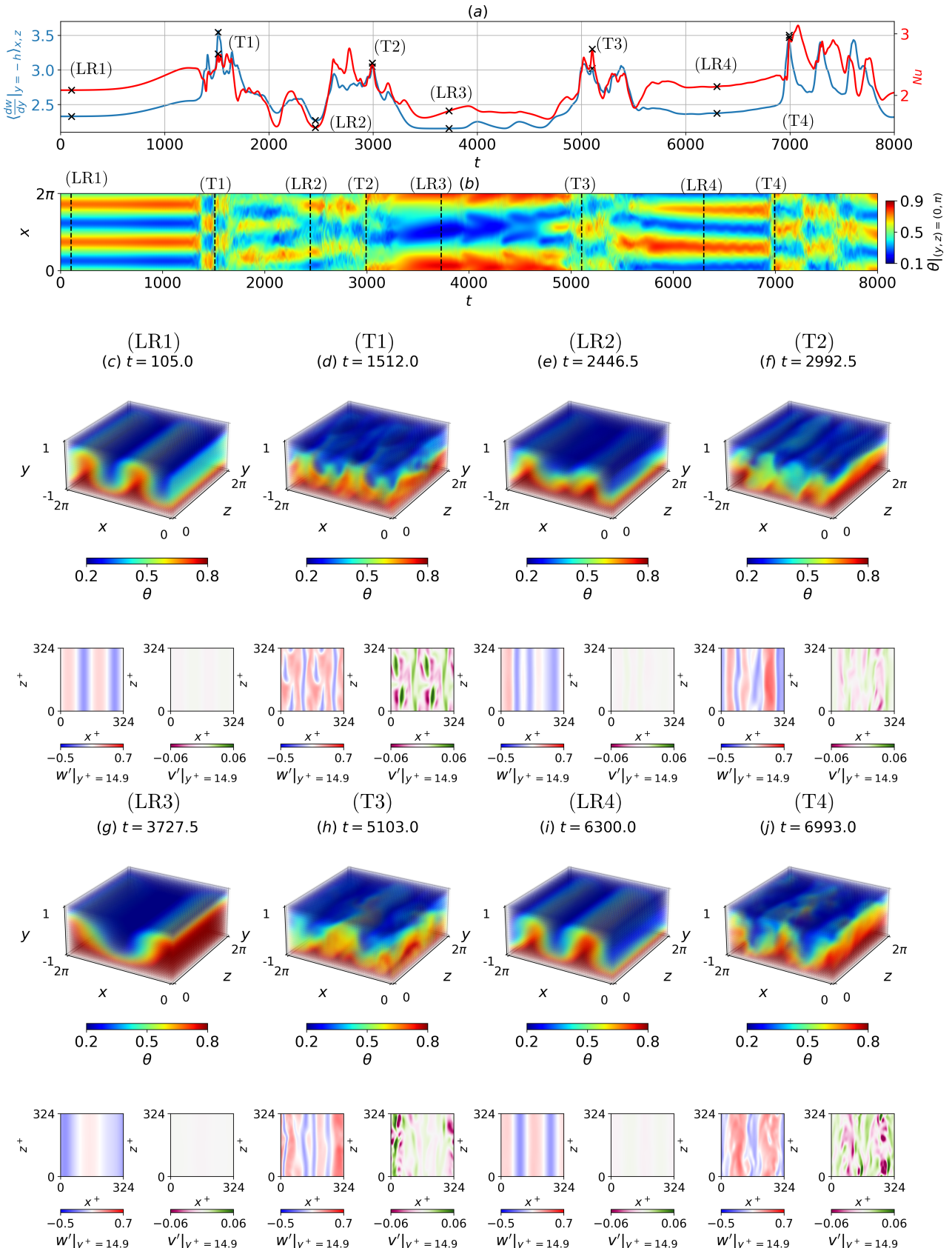


Figure 3.9: Time integration along the dominant unstable manifold, $\beta d = 2$, of the longitudinal rolls at $Ra = 5000$, $Re = 1050$, $\Gamma = \pi/2$ for $t \in [0, 8000]$. Time history of the (a) Nusselt number and wall shear rate, and (b) midplane temperature spacetime plot. This system oscillates between the longitudinal rolls ($LR1 - 4$) and turbulence ($T1 - 4$) over four intervals. Snapshots of volumetric temperature and near-wall streamwise and spanwise velocity perturbations at (b) $t = 105$, (c) $t = 1512$, (d) $t = 2446.5$, (e) $t = 2992.5$, (f) $t = 3727.5$, (g) $t = 5103$, (h) $t = 6300$, (i) $t = 6993$.

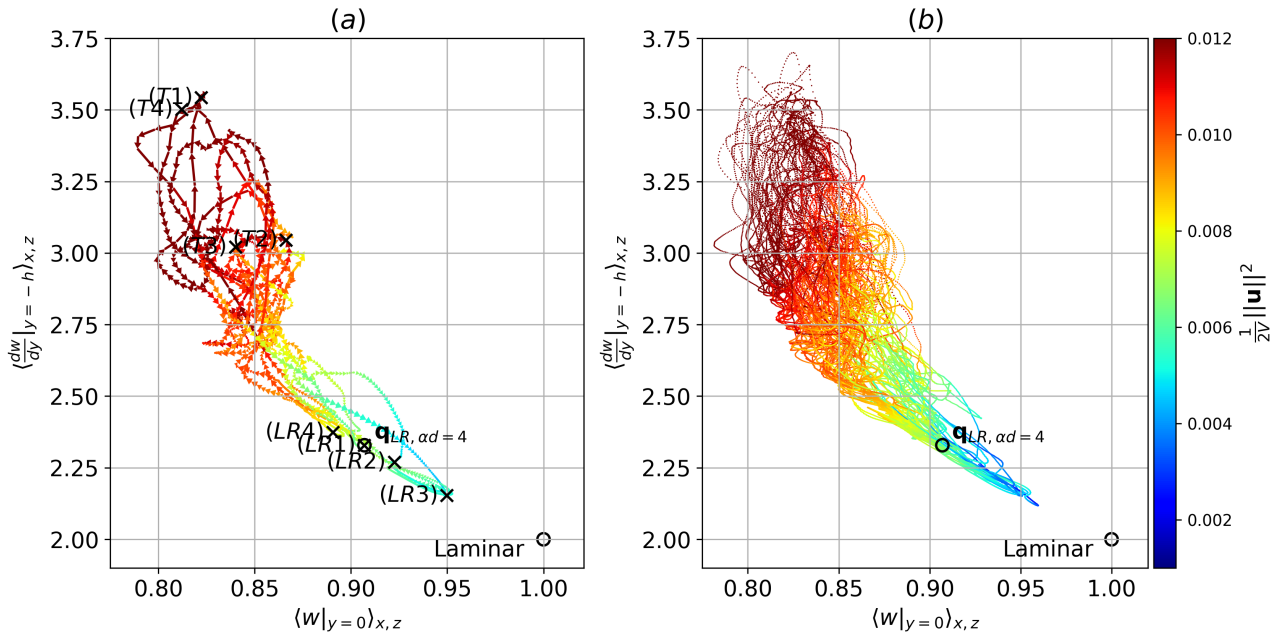


Figure 3.10: State space projection based on the planar averaged centerline velocity and shear, coloured by the volume normalised perturbation kinetic energy at $Ra = 5000$, $Re = 1050$, $\Gamma = \pi/2$, (a) $t \in [0, 800]$, (b) $t \in [0, 68750]$. The open black circles represent the unstable equilibria of longitudinal rolls and the laminar state. Note that the black-crosses, labelled by (T1-4) and (LR1-4), refer to temporal snapshots in figure 3.9, not equilibria solutions.

of figure 3.9 illustrate the volumetric temperature field, planar near-wall streamwise and wall-normal perturbations, resembling the longitudinal rolls ($LR1 - 4$), and transient turbulent states ($T1 - 4$). As the solution emerges from the unstable manifold of the longitudinal roll state, ($LR1$) in figure 3.9(c), the trajectory erupts into turbulence at $t = 1512$, marked by a disordered volumetric temperature field with high- and low-speed streaks in snapshot ($T1$) in figure 3.9(c). These high- and low-speed streaks are negatively correlated in space, with wall-normal perturbation velocities in figure 3.9(d), reminiscent of sweeps and ejection events commonly found in wall-bounded shear flows [Wallace et al., 1972, Willmarth and Lu, 1972]. Turbulence occurs transiently, and the solution decays towards a longitudinal roll-like state at $t = 2446.5$, shown by snapshot ($LR2$) in figure 3.9(e), forming a single cycle. The intermittent cycle repeats over three subsequent intervals, where the transient turbulent state and longitudinal rolls emerge at $t = 2992.5, 5103, 6993$, and $t = 3727.5, 6300$, as shown in the snapshots ($T2, 3, 4$) and ($LR3, 4$) in figures 3.9(f,h,j) and 3.9(g,i), respectively.

Lastly, we show that the dominant unstable manifold of the longitudinal rolls is connected to a transient turbulent state. Interestingly, a ‘single’ longitudinal roll with $\alpha d = 2$ emerges sometimes, shown as snapshot ($LR3$). This suggests that other unstable manifolds may well be linked to the transition to transient turbulence.

To better visualise the temporal dynamics in figure 3.9 with better clarity, we project the solution trajectory onto the space composed of two state observables: planar averaged centerline velocity, $\langle w|_{y=0} \rangle_{x,z}$, shear, $\langle dw/dy|_{y=-h} \rangle_{x,z}$ coloured by the volume-averaged perturbation kinetic energy, $1/(2V)\|\mathbf{u}'\|^2$, in figure 3.10, where $\|\mathbf{u}'\|^2 = \int_{\Omega} \mathbf{u}'^H \mathbf{u}' dV$ with Ω being the flow domain. These

observables are chosen because they are found to distinguish well the regions of turbulent states, longitudinal roll states, and the laminar state that reside around $(0.82, 3.2)$, $(0.90, 2.32)$ and at $(1, 2)$, respectively. Indeed, the temporal snapshots of $(T1 - 4)$ appear around the representative location of turbulent states, $(0.82, 3.2)$, and the snapshots of $(LR1 - 4)$ and an equilibrium related to the longitudinal roll state with the spanwise wavenumber $\alpha d = 4$ (denoted by $\mathbf{q}_{LR,\alpha d=4}$) are seen around $(0.90, 2.32)$.

The solution trajectory emerges from the unstable manifold of the longitudinal roll state, $\mathbf{q}_{LR,\alpha d=4}$, evolving towards turbulent states around $(0.85, 3.2)$, characterised by high wall shear rate. At this Re , the turbulence is transient in a confined domain, occurring with a finite lifetime, eventually decaying towards the laminar state [Hof et al., 2006, Schneider et al., 2007]. As the solution trajectory approaches the laminar solution $(1, 2)$, it abruptly reverses towards the longitudinal roll state near $(0.95, 2.15)$, $(LR3)$ due to the buoyancy-driven linear instability of the laminar base state in RBP flow. Subsequently, the solution trajectory could depart along the unstable manifold of the longitudinal rolls again, leading to the onset of turbulence, where the cycle repeats.

To see if this cycle could be sustained indefinitely, we consider a longer time horizon, $t \in [0, 68750]$, illustrated in figure 3.10(b). The solution trajectory wanders between the ‘cloud’ of chaotic transient turbulence at the top left corner (in red), and longitudinal roll and laminar states (in blue) in the bottom right, forming a basin of attraction between the unstable longitudinal rolls, transient turbulence, and the unstable laminar base state. This basin of attraction is likely established above a critical Ra as the longitudinal rolls become linearly unstable (i.e. $Ra \gtrsim Ra_s \approx 4720$, see figure 3.8(b)), and the instability of the longitudinal rolls provides an intermediate pathway towards transient turbulence, which could be regenerated again - a ‘self-sustaining’ dynamical process. We refer to this process as the *thermally-assisted sustaining process (TASP)*, inspired by the self-sustaining process (SSP) from turbulent shear flows [Hamilton et al., 1995].

3.4.2 Variation of Ra and Re on the thermally-assisted sustaining process in $\Gamma = \pi/2$

In this section, we further explore the behaviour of the *TASP* as Re and Ra are varied. We consider eight different cases at $Ra = 8000, 4000$ and $Re = 600, 700, 1000, 1400$. The results of these eight cases, where longitudinal rolls are unstable at $Ra = 8000$ or stable at $Ra = 4000$, are shown in figure 3.11, depicting the space-time plot of midplane temperature, $\theta|_{y=0}(x, t)$, time history of the Nusselt number, Nu , and the wall shear rate, $\langle dw/dy|_{y=-h} \rangle_{x,z}$ and the state space portrait using the planar-averaged centerline velocity, $\langle w|_{y=0} \rangle_{x,z}$, the wall shear rate, coloured by the volume normalised perturbation kinetic energy, $\frac{1}{2V} \|\mathbf{u}'\|^2$. For all cases, except $Ra = 4000$, $Re = 1000$ and $Re = 1400$, their initial conditions are prepared from the laminar state, superimposed by a random noise based on a Gaussian distribution with zero mean and unit variance, scaled to a total energy of $\delta = 10^{-3}$ (see (3.8) for the definition). For the exceptional cases at $Ra = 4000$, $Re = 1000$ and $Re = 1400$, where subcritical turbulence and stable longitudinal rolls are expected, their initial conditions are obtained by gradually lowering Re from a statistically stationary turbulent solution at $Re = 2000$.

We first consider $Re = 1000$ (figures 3.11(c,g).) At $Ra = 8000$ (figure 3.11(c)), the trajectory

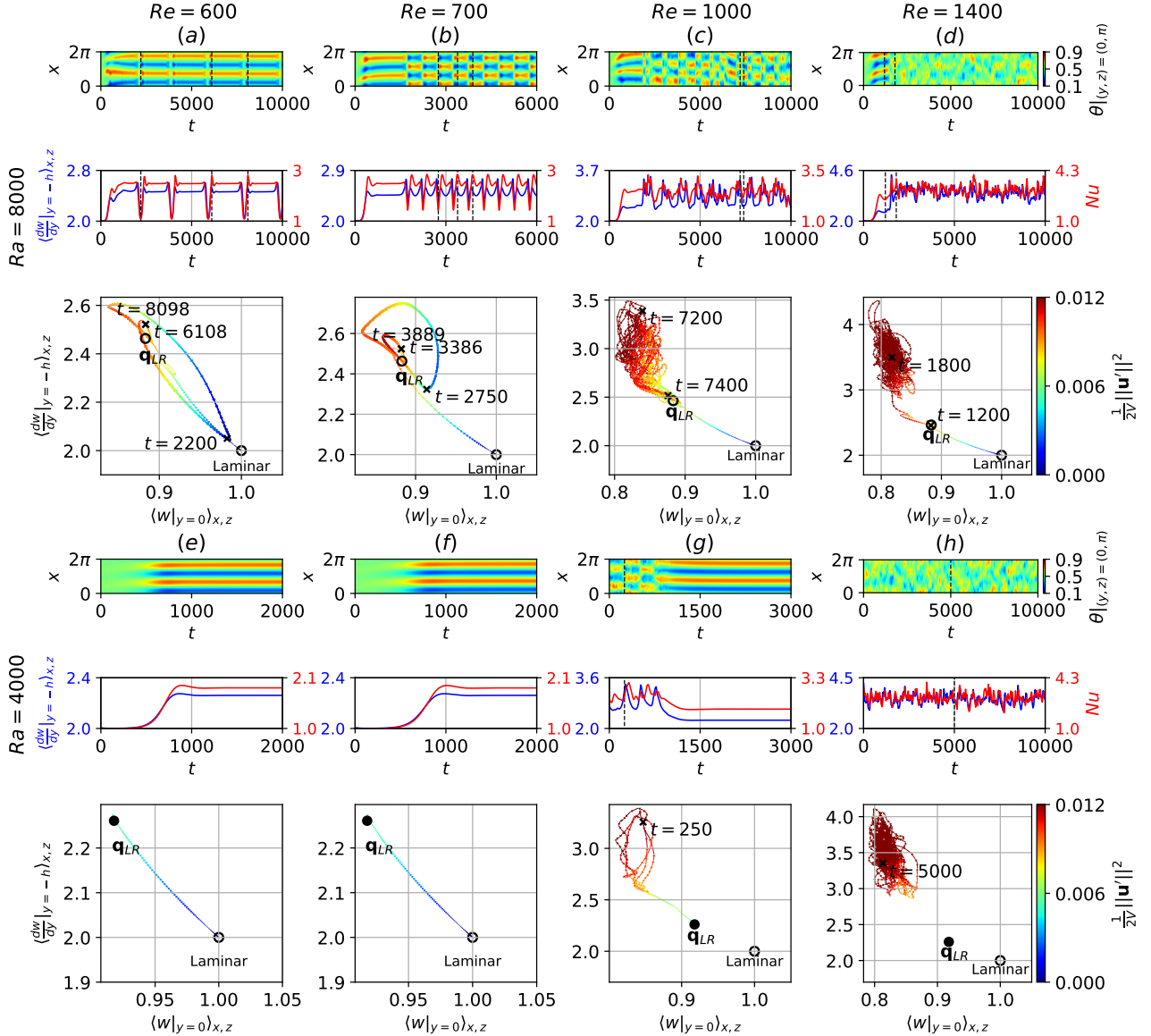


Figure 3.11: The behaviour of the unstable and stable longitudinal rolls at $Ra = 8000, 4000$ for (a,e) $Re = 600$, (b,f) $Re = 700$, (c,g) $Re = 1000$ and (d,h) $Re = 1400$ within $\Gamma = \pi/2$. Each parameter regime consist of three panels from the top to bottom, depicting the midplane temperature spacetime plot, $\theta|_{(y,z)=(0,\pi)}$, time history of the Nusselt number and shear, and state space projection based on the planar averaged centerline velocity and shear, coloured by the volume normalised perturbation kinetic energy.

visits the transient turbulence regime near $t = 7200$, which decays towards the longitudinal roll state, \mathbf{q}_{LR} ($\beta d = 4$), at $t = 7400$, which could be regenerated again, consistent with the TASP in §3.4.1. As Ra is lowered to 4000 (figure 3.11(g)), the solution trajectory decays towards the longitudinal roll state, \mathbf{q}_{LR} , where the TASP disappears. In this case, the longitudinal rolls are linearly stable, confirming our hypothesis earlier that the TASP is only established when longitudinal rolls become linearly unstable above a certain Ra -threshold (i.e $Ra \gtrsim Ra_s \approx 4720$).

At $Re = 1400$, $Ra = 4000$, the solution trajectory remains within the turbulent ‘cloud’ near $(0.8, 3.8)$ for $t \in [0, 10000]$, as illustrated in figure 3.11(h). This suggests that turbulence might be sustained indefinitely, although we have not investigated whether the turbulent chaotic saddle at $Re = 1000$ truly transitioned into a chaotic attractor at $Re = 1400$. As Ra is increased to 8000, the solution trajectory originating from the laminar state, evolves towards the unstable longitudinal roll state, \mathbf{q}_{LR} at $t = 1550$, transitioning into sustained turbulence at $t = 1800$. Therefore, in this case, the linearly unstable longitudinal rolls serve as an intermediate transitional pathway between the laminar base state and subcritical turbulence, whereas at $Ra = 4000$, a bistability between stable longitudinal rolls (not shown) and turbulence is established.

Next, we examine the behaviour of TASP as Re decreases towards the intermittent regime at $Re = 600, 700$, where a periodic orbit emerges between the longitudinal roll and the laminar state. At $Re = 600$, $Ra = 8000$ in figure 3.11(a), the solution trajectory initially evolves towards the longitudinal roll state, \mathbf{q}_{LR} , which is linearly unstable and breaks down towards the laminar state at $t = 2200$. This breakdown is evidenced by the trajectory’s proximity to the laminar state in state space and the presence of a narrow green patch in the midplane temperature spacetime plot. The longitudinal roll state is regenerated again, forming a periodic orbit with a period of $T_{\text{period}} = 8098 - 6108 = 1990$, oscillating between the longitudinal roll and laminar state over five intervals within $t \in [0, 10000]$. As Re increases slightly to 700, the periodic orbit persists over a shorter period of $T_{\text{period}} = 3889 - 3386 = 503$. A notable difference is observed in the regenerated longitudinal rolls, which is continuously translated by $L_x/2$ in the x -direction. Additionally, as Re increases from 600 to 700, the trajectory moves further away from the laminar state during breakdown, suggesting an increasing attraction towards the longitudinal roll state, \mathbf{q}_{LR} (compare $t = 2200$ in figure 3.11(a) and $t = 2750$ in figure 3.11(b)). When Ra is lowered to $Ra = 4000$, the periodic orbit disappears and the trajectory stabilises into the longitudinal roll state, \mathbf{q}_{LR} , at $Re = 600, 700$.

To summarise the dynamical processes identified in figure 3.11, we present a state space sketch of it in figure 4.21. At $Ra = 8000$, $Re = 600$ and $Re = 700$, the longitudinal rolls become linearly unstable, breaking down to the laminar state before being regenerated, forming a periodic orbit illustrated enclosed by black dotted paths in figures 4.21(a,b). For $Re = 700$, the regenerated longitudinal roll is continuously translated by $L_x/2$, suggesting a possible merger of two periodic orbits into one as sketched in figure 3.11(b). Future bifurcation studies are required to establish this, providing an avenue for future work. As Ra is lowered to $Ra = 4000$, the laminar state stabilises into the longitudinal rolls in figure 4.21(e). However, the flow in this regime may contain some invariant solutions [?], denoted as saddle points here. Integrating along the unstable manifold of longitudinal roll states at $Ra = 8000$, $Re = 1000$ leads to transient turbulence, which eventually decays to the laminar

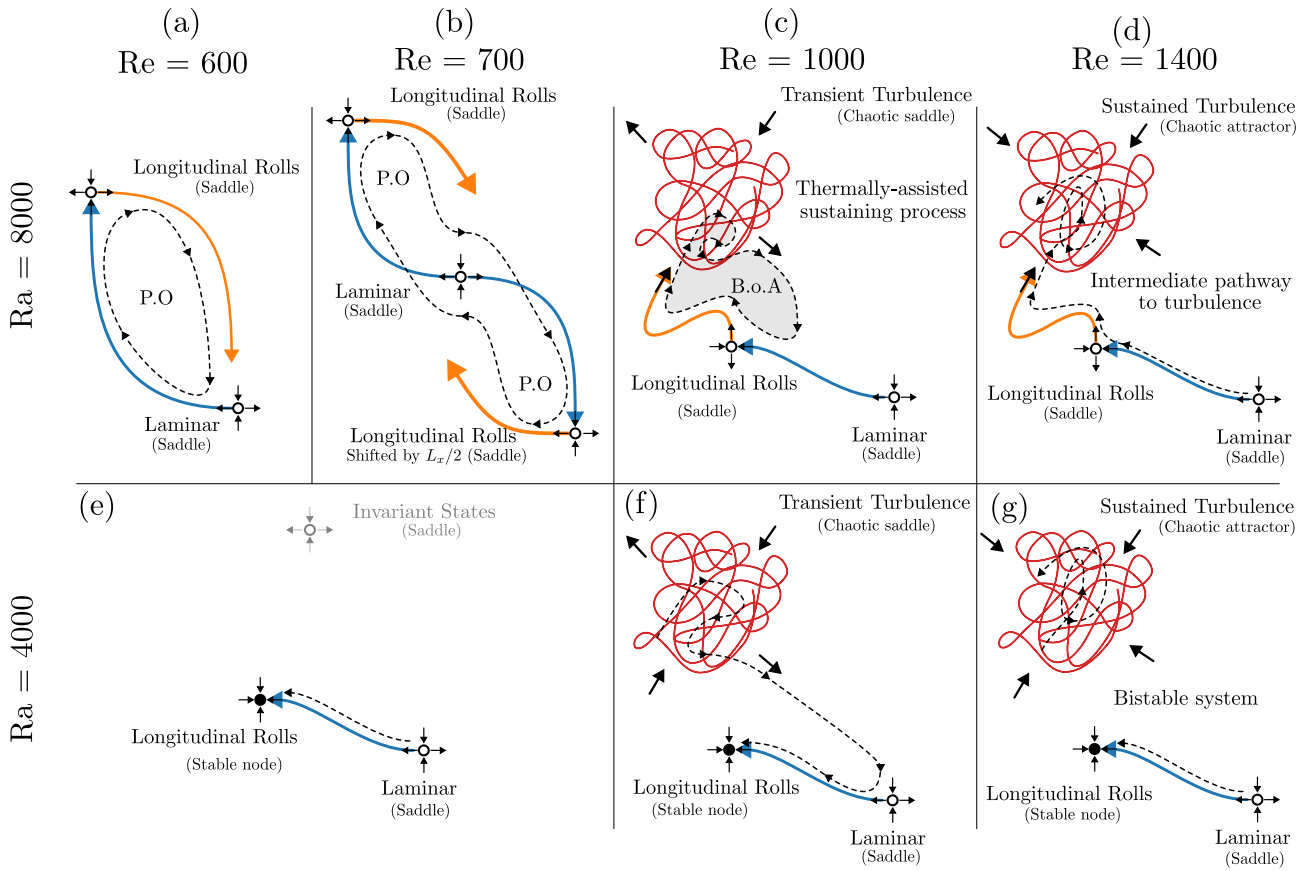


Figure 3.12: A state space sketch of figure 3.11 at $Ra = 8000$, (a) $Re = 600$, (b) $Re = 700$, (c) $Re = 1000$, (d) $Re = 1400$ and $Ra = 4000$ at (e) $Re = 600, 700$, (f) $Re = 1000$, (g) $Re = 1400$. The longitudinal roll is linearly unstable (saddle) at $Ra = 8000$, and is stable at $Ra = 4000$, whereas the laminar state is always linearly unstable (saddle). The blue and orange solid arrows refer to the unstable manifold of longitudinal rolls and the laminar state. The red solid lines denote the chaotic trajectories of turbulence, likely forming a chaotic saddle at $Re = 1000$ and a chaotic attractor at $Re = 1400$. The black-dashed trajectories refer to possible solution trajectories, forming a periodic orbit (P.O.) at $Ra = 8000$, $Re = 600, 700$, and a basin of attraction (B.o.A.) at $Ra = 8000$, $Re = 1000$. We note that invariant states could exist at $Ra = 4000$, $Re = 600, 700$, labelled as a saddle here [?].

state before regenerating the longitudinal rolls again, forming the *TASP* in figure 4.21(c). In contrast, at $Ra = 4000$, $Re = 1000$, the longitudinal rolls become linearly stable, eliminating the intermediate (orange) pathway towards turbulence. Therefore, the transient turbulence stabilises into longitudinal rolls, as shown with the black-dashed trajectory in figure 4.21(f). For $Ra = 8000$, $Re = 1400$, the linearly unstable longitudinal rolls provide an intermediate pathway towards turbulence from the laminar state, as sketched in figure 4.21(d), breaking the bistability between the laminar state and subcritical turbulence seen at $Ra = 4000$ in figure 4.21(g). This behaviour resembles the nature of subcritical turbulence in shear-driven flow, highlighting the contribution of unstable longitudinal rolls towards the transition to turbulence within $\Gamma = \pi/2$.

We have examined the dynamics of unstable longitudinal rolls as the Reynolds number, Re , and the Rayleigh number, Ra , are varied, identifying three key dynamical processes: (1) periodic orbits between longitudinal rolls and the laminar state (figure 4.21(a,b)), (2) the *TASP*, where transient turbulence can be sustained (figure 4.21(c)) and (3) an intermediate transitional pathway towards sustained turbulence (figure 4.21(d)). To establish a connection between these processes and refine their transitional boundaries, we conduct a further parametric study on $Ra \in [4000, 10000]$ and $Re \in [600, 1400]$ within $\Gamma = \pi/2$. Figure 3.13 presents the midplane temperature spacetime plot alongside the time history of wall shear rate, $\langle dw/dy|_{y=-h} \rangle_{x,z}$ and the Nusselt number, Nu . For all simulations, the initial conditions are prepared from the laminar state, superimposed with a random noise based on a Gaussian distribution with zero mean and unit variance, scaled to a total energy of $\delta = 10^{-3}$ (see definition in (3.8)). Due to the subcritical nature of turbulence and the expected stable longitudinal rolls, exceptions are made for $Ra = 4000$, $Re \in [900, 1400]$, where initial conditions are taken from gradually lowering Re from a statistically stationary turbulent state at $Re = 2000$, $Ra = 4000$. The *thermally-assisted sustaining process* is highlighted in green for $Ra \in [5000, 10000]$ and $Re \in [900, 1200]$, where temporally intermittent shear and Nusselt number fluctuations are observed, accompanied by a mixture of organised and disorganised flow structures in the temperature spacetime plots. In this regime, longitudinal rolls provide an intermediate pathway towards transient turbulence, which appears linearly unstable for $Ra \geq 5000$. For $Ra < 5000$, transient turbulence decays into stable longitudinal rolls, as observed at $Ra = 4000$, $Re \in [900, 1200]$ labelled as 'transient turbulence'. Periodic orbits between longitudinal rolls and the laminar state occur for $Ra \in [6000, 10000]$ and $Re \in [600, 800]$, establishing above a critical $Ra - Re$ threshold, below which solutions stabilise into longitudinal rolls shaded in red. Around $Re = 800$, we note that the periodic orbit becomes increasingly quasi-periodic, likely related to the *TASP* near $Re \sim 900$. Although longitudinal rolls are linearly stable at $Ra = 4000$, $Re = 1400$ (not shown), turbulence is sustained at least for a sufficiently long time, shaded blue at $Re = 1400$. In this case, a bistable system forms between longitudinal rolls and turbulence at $Ra = 4000$, while the longitudinal rolls provide an intermediate pathway towards turbulence for $Ra \geq 5000$. Figure 3.13 underscores the role of unstable longitudinal rolls in transitional RBP flows within confined domains.

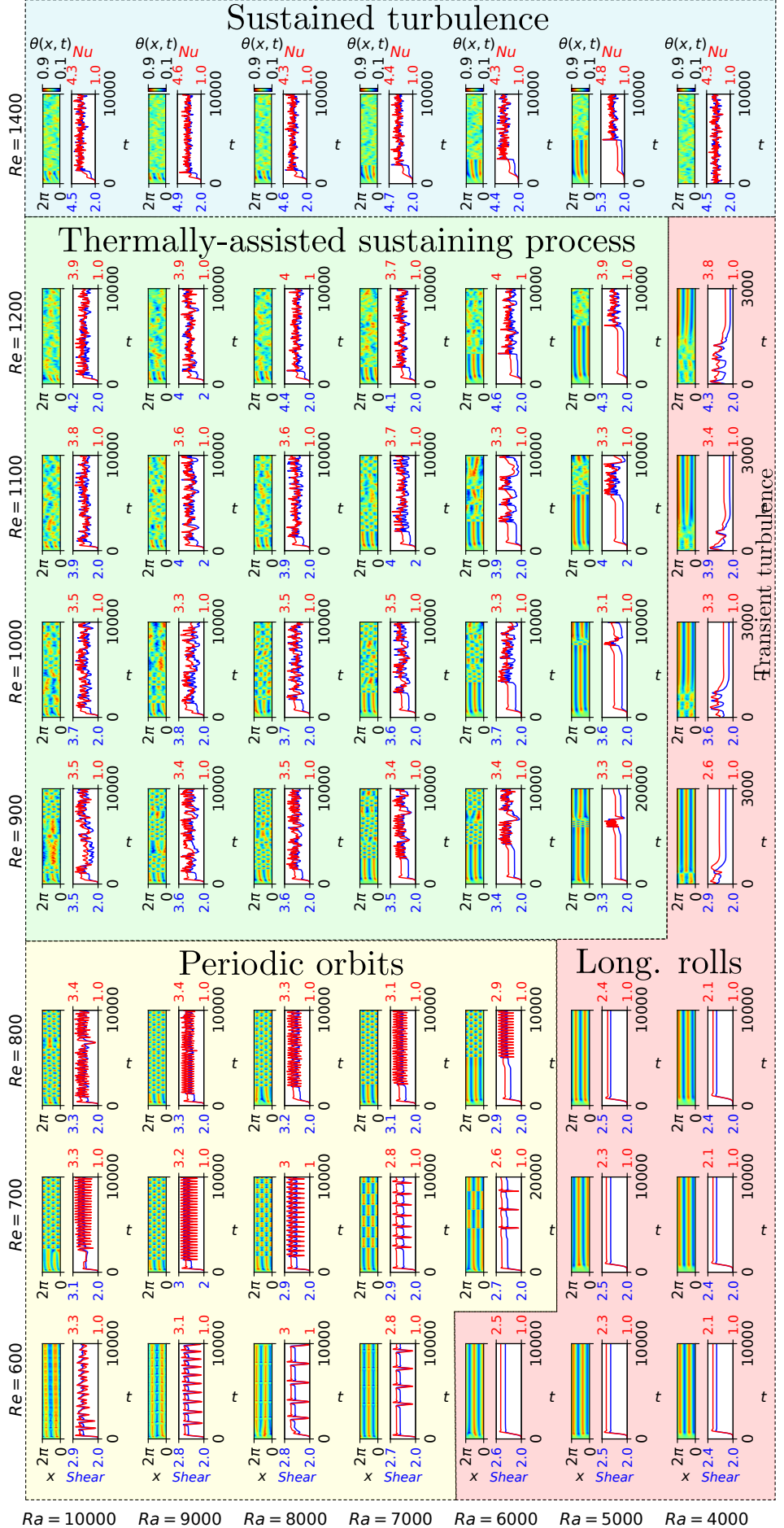


Figure 3.13: The temperature spacetime plots and time history of shear and the Nusselt number for $Ra \in [5000, 10000]$, $Re \in [600, 1400]$ within $\Gamma = \pi/2$. Unstable longitudinal rolls lead to the onset of (1) periodic orbits (yellow), (2) the *thermally-assisted sustaining process* (green), and (3) sustained turbulence (blue), occurring beyond an $Ra - Re$ boundary, below which longitudinal rolls remain stable (red).⁷⁶

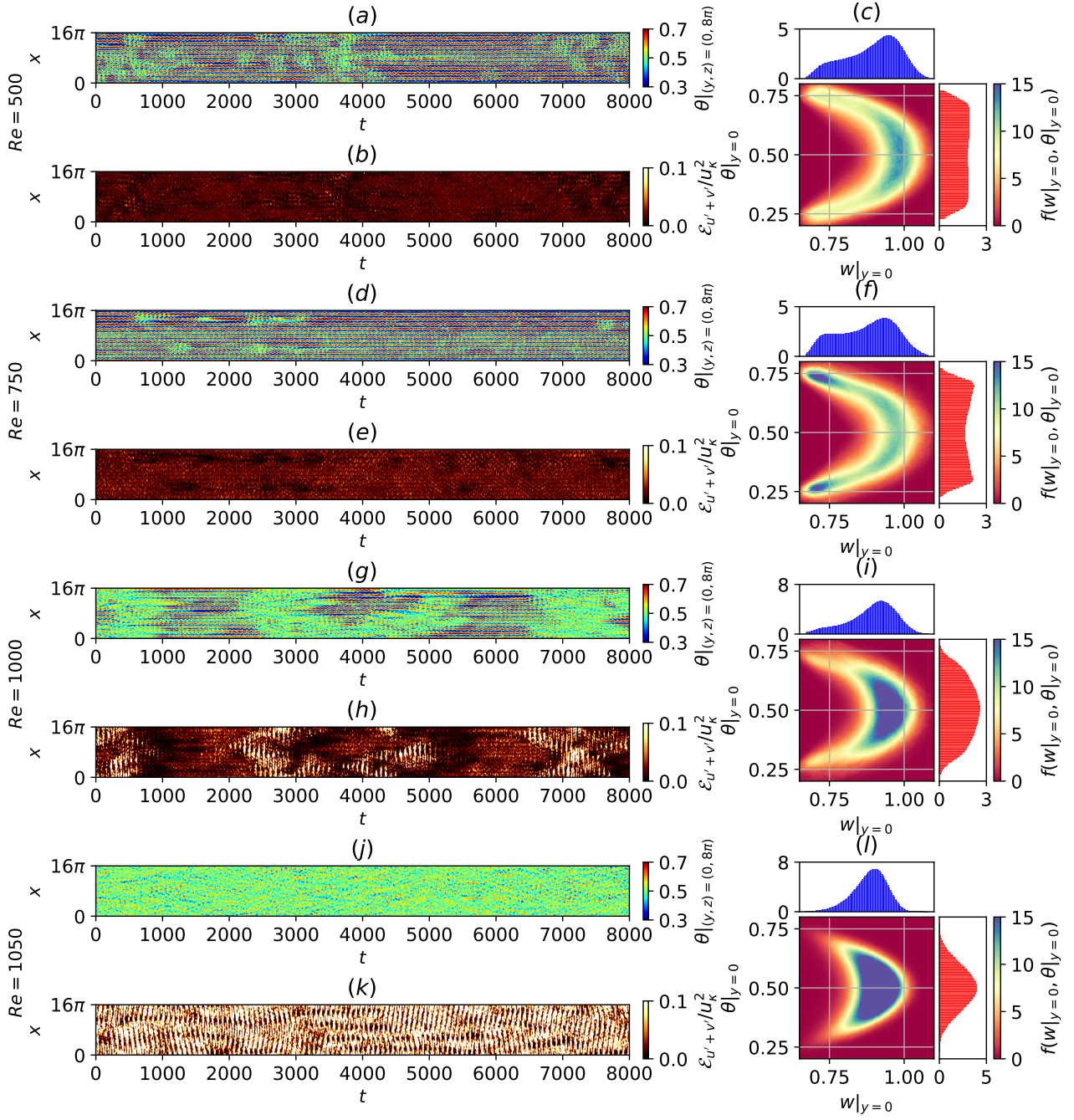


Figure 3.14: The midplane temperature spacetime plot, and near-wall wall-normal and spanwise perturbation kinetic energy by normalised by thermal velocity scale, u_κ , and the probability density functions based on planar-averaged centerline velocity and the midplane temperature at $Ra = 10000$, (a,b,c) $Re = 500$, (d,e,f) $Re = 750$, (g,h,i) $Re = 1000$, (j,k,l) $Re = 1050$.

3.4.3 Extending to large domains, $\Gamma = 4\pi$.

In this section, we return to the simulation results in the large domain $\Gamma = 4\pi$, and try to establish the relevance of the local dynamical process identified in the confined domain, $\Gamma = \pi/2$. It should be mentioned that, by doing so, the discussion in this section does not fully account for the spatial interactions between the flow structures. However, we will see that many important flow features can be well explained based on the simulation results from the confined domain. The understanding of the full spatio-temporal dynamics is deemed to be a formidable task at this point and is beyond the scope of this study. Here, we will focus on $Ra = 500, 750, 1000, 1050$ for $Ra = 10000$ presented in figure 3.14, illustrating their space-time plots of the midplane temperature, $\theta|_{(y,z)=(0,8\pi)}$, and near-wall wall-normal and spanwise perturbation kinetic energy, $\mathcal{E}_{w'+v'}$, at $y^+ = 15$. Furthermore, to statistically characterise the flow structures, we calculate the joint probability distribution function using the velocity and temperature in the midplane, $f(w|_{y=0}, \theta|_{y=0})$. At $Ra = 10000$, $Re = 500$, the breakdown of longitudinal rolls towards the laminar state is observed, highlighted by spatially-localised green spots in the midplane temperature plots, and dark regions in the near-wall perturbation kinetic energy spacetime plot near $t = 500, 3800$ in figure 3.14(a,b) respectively. As Re increases from 500 to 750, the breakdown towards the laminar state remains visually apparent. The spatio-temporal dynamics between longitudinal rolls and the laminar state observed in the large domain in this regime are reminiscent of the stable periodic orbits identified between them in a confined domain, although the dynamics in the large domain is much more complex due to the spatial interactions between different flow structures. There is a noticeable decrease in the number of green and dark regions between figures 3.14(a,b) and (d,e), suggesting fewer laminar events at $Re = 750$. Indeed, this difference is further reflected in their PDFs, where the probability of laminar events, at $(w|_{y=0}, \theta|_{y=0}) = (1, 0)$, depicted as the ‘head’ of the ‘arc-shaped’ PDF decreasing from $Re = 500$ (figure 3.14(c)) to $Re = 750$ (figure 3.14(f)). This suggests fewer laminar state events and more occurrences of the longitudinal roll state. It is also consistent with the result from the confined domain case, where the solution trajectory becomes increasingly attracted towards the longitudinal roll state from $Re = 600$ and $Re = 700$ at $Ra = 8000$ (figures 3.11(a,b)).

At $Re = 1000$, we observe the coexistence of the laminar state, the longitudinal rolls, and turbulence appearing as can be seen from the dark, bright and very bright regions in the near-wall wall-normal and spanwise perturbation velocities, in figure 3.14(h). Starting at $t = 2000$, the longitudinal rolls that appear as elongated red/blue contour strips in figure 3.14(g) erupt into turbulence at $t = 2500$, appearing as very bright spots in figure 3.14(h). Turbulence is transient, decaying towards the laminar state at $t = 3000$, as indicated by the dark patches in figure 3.14(h). By $t = 4000$, longitudinal rolls are regenerated, appearing as red/blue elongated contour strips in figure 3.14(g). This process resembles TASP in a confined domain (figure 4.21(c)), suggesting that a similar process may be present in the large domain.

As Re approaches $Re = 1050$, turbulence appears more uniformly in space and time as seen in figure 3.14(k,h). The increase in turbulent events is reflected by the PDFs, where a ‘D’-shaped PDF absent in $Re = 750$, gradually increases in intensity from $Re = 1000$ to $Re = 1050$. The lack of prolonged laminar spots, previously identified for $Ra = 0$ (figure 3.3, highlights the role of

longitudinal rolls in providing an intermediate pathway from laminar to turbulent state, identified in a confined domain (figure 3.11(d)).

3.5 Conclusions

We conclude by summarising the key findings of transitional RBP flow from figure 3.1, where we have identified five different regimes and their rough transition boundaries. First, we have examined the bistability between SDC and ISRs in RBP flows, which persists up to $Re = 1$, beyond which only ISR solutions are observed. The critical Re_s at which SDC disappears appears to depend on Re and remains an avenue for future study. At $Re = 10$, the wavenumber of the stable ISRs adheres to the stability boundaries of the Busse balloon, and we observe longitudinal rolls as well as oscillatory longitudinal rolls, expected from the secondary instabilities of RBC [Clever and Busse, 1974]. The wavy rolls appear at $Re = 100$ and $Ra \geq 5000$ [Clever and Busse, 1991, Pabiou et al., 2005, ?], but disappear for $Re \geq 500$, where a new regime referred to as intermittent rolls emerges. This regime is characterised by the spatio-temporal intermittent breakdown of longitudinal rolls towards the laminar state, before being regenerated again. Similarly to the wavy rolls regime, intermittent rolls only appear above a Ra -threshold, $Ra \geq 5000$ (see figure 3.1), below which longitudinal rolls persist. As Re approaches the shear-driven turbulent regime ($Re \gtrsim 1000$), we observe the coexistence of longitudinal rolls with neighbouring turbulent bands at $Ra = 10000$, indicating a role played by the longitudinal rolls in transitional RBP flow.

To investigate the role of longitudinal rolls in transitional RBP flow around $Re = 1000$, we have considered a confined domain, $\Gamma = \pi/2$, where spatial intermittency can be artificially suppressed. Integrating along the unstable manifold of longitudinal rolls in the confined domain leads to transient turbulence, which eventually decays towards the laminar state before longitudinal rolls reemerge again. This process is repetitive, forming a cyclic process, which we refer to as the *thermally-assisted sustaining process (TASP)*. The TASP is subsequently further examined by varying Re and Ra . As Re decreases from $Re \approx 1000$ towards the intermittent roll regime (see figure 3.1), a simpler form of solutions emerges, such as stable periodic orbits, oscillating between the longitudinal roll and a laminar state. In contrast, as Re increases from it, shear-driven turbulence seems to become sustained indefinitely (or for a very long time), with the longitudinal rolls providing an intermediate route in the transition to turbulence from the laminar state. Our investigation of the role of unstable longitudinal rolls within confined domain have revealed three dynamical processes: the onset of (1)periodic orbits, (2) the TASP, and (3) providing an intermediate route towards turbulence. It was also shown that the stability of longitudinal rolls largely depends on Re and Ra , below which only stable longitudinal rolls are observed. Furthermore, the connection between the dynamical process identified here to the onset of wavy rolls warrants further investigation. We also acknowledge that more spatially subharmonic instabilities may arise as the domain size increases.

Finally, we assess the relevance of our findings in the confined domain and their connection to the large domain. We suggest that the breakdown towards the laminar state in the intermittent roll regime bears qualitative similarities to the periodic orbit between them in the confined domain.

Furthermore, transient turbulence that is sustained by longitudinal rolls is also evident in the large domain, where the flow transitions between transient turbulence, longitudinal rolls and the laminar state in figures 3.14(g,h). At $Re = 1050$, the turbulent-laminar bands dominate, weakly dependent on Ra , as suggested by figure A.2. It may be possible that these turbulent-laminar bands decay spontaneously towards the laminar state [Tuckerman et al., 2014, Gomé et al., 2020], and their lifetime statistics may depend on Ra , which warrants further investigation. However, if the TASP persists above a critical Ra providing a pathway to turbulence, then the turbulent-laminar bands could be sustained indefinitely. As Re approaches 2000, featureless turbulence emerges, with the first- and second-order statistics becoming independent of Re , indicating fully developed turbulence. It is likely that the range of $Ra \in [0, 10000]$ considered here is too low to significantly influence shear-driven turbulence at $Re = 2000$, suggested by the studies of turbulent RBP [Pirozzoli et al., 2017].

Chapter 4

The state space structure of Spiral Defect Chaos

The co-existence of ideal straight rolls (ISRs) and spiral-defect chaos (SDC) as bistable states in Rayleigh-Bénard convection above the onset of the linear instability is well established in extended spatial domains ($\Gamma \geq 40$ where Γ is the aspect ratio of the domain). However, multiple stable states have also been found independently, raising questions about the precise understanding of this observed bistability in extended domains. In this study, we isolate the localised structures of SDC by gradually reducing the spatial domain. By minimising the domain systematically to $\Gamma = 2\pi$, SDC appears transiently and eventually stabilises into new stable states referred to as elementary states. These elementary states are visibly and statistically similar to the spatially local patterns of SDC, indicative of invariant solutions underpinning the pattern formation in SDC.

To understand the state space structure further, we have examined the edge between ISRs and the elementary states, revealing multiple edge states, and conducted a series of numerical simulations along the unstable manifolds of unstable ISRs. The unstable ISRs near the Busse balloon are connected to stable ISRs and the base state through networks of heteroclinic orbits, forming a basin of attraction for each stable ISR. In contrast, the unstable ISRs further from the Busse balloon contain some unstable manifolds, along which the solution trajectory leads to SDC, suggesting that these unstable ISRs sit on the boundary between stable ISRs and SDC. Finally, we propose a state-space structure around the basic heat conduction state, stable/unstable ISRs, elementary states and transient SDC.

4.1 Objectives

The bistability between SDC and ISR is well established, but this also opens a question of how it is connected with the previous findings of multiple stable states (see §1.3). It is worth noting that a possible parameter in exploring this connection appears to be the domain size. Bistability has been reported in domains much larger ($\Gamma = 50$) than the multiple states found in small-to-moderate domains ($\Gamma \leq 10$) [Cakmur et al. \[1997a\]](#). Furthermore, giant rotating spirals have been found in domains comparable to the horizontal length scale of SDC [Plapp and Bodenschatz \[1996\]](#), [Plapp et al. \[1998\]](#). Under this premise, the scope of this study is to explore how SDC, ISRs and multiple states are

organised within a state space, where stable/unstable equilibria and their manifolds (or linear stability) could provide useful physical insights into the state transition dynamics.

Motivated by the observation that SDC consists of several localised structures that resemble multiple states (i.e. travelling waves, spirals, asymmetric states), we first seek to isolate these states by minimising the domain systematically. Confined within the minimal domain, SDC is found to appear only transiently and does not sustain for a long time. The transient SDC state eventually stabilises into a large number of stable multiple states, which will be referred to as the ‘elementary’ states of SDC, and they are subsequently found within the minimal domain. As we shall see later, these elementary states remarkably resemble local structures of SDC observed in wide computational domains, indicating that they possibly underpin the formation of SDC. Next, the state-space boundaries between SDC and ISRs are explored by employing the edge-tracking technique [Skufca et al. \[2006\]](#), [Schneider et al. \[2007\]](#), unveiling the existence of multiple edge states sitting on the boundaries. Finally, to understand the role of the unstable ISRs outside the Busse balloon, we perform a series of numerical experiments, in which a small perturbation is added along the unstable manifolds of several (unstable) ISRs outside of the Busse balloon. We shall see that some of their unstable manifolds are connected to stable ISRs within the Busse balloon, while the others are linked to transient SDC, which is subsequently stabilised into an elementary state. This suggests that some of the unstable ISRs act as signposts for the state-space boundary between stable ISRs and SDC (and/or elementary states).

The main contributions of the present chapter can be briefly summarised as follows,

1. Discovery of a number of stable invariant solutions which underpin the localised structures of SDC by minimising the computational domain for SDC (section [4.3](#));
2. Computation of some of multiple ‘edge states’ sitting on the separatrix between SDC and ISRs (section [4.4](#));
3. Several heteroclinic orbits connecting unstable ISRs and stable ISRs near the boundaries of the Busse balloon (section [4.5.1](#));
4. The role of unstable ISRs far from the Busse balloon acting as a signpost between ISRs and SDC (section [4.5.2](#)).

4.2 Problem formulation

4.2.1 Rayleigh-Benard convection (RBC)

The motion of fluid flow in an RBC system (see [§1.1](#)), is governed by the non-dimensionalised Navier-Stokes equations with Boussinesq approximation,

$$\frac{\partial \mathbf{u}}{\partial t} + (\mathbf{u} \cdot \nabla) \mathbf{u} = -\nabla p + Pr \nabla^2 \mathbf{u} + Ra Pr \theta \mathbf{j}, \quad (4.1a)$$

$$\frac{\partial \theta}{\partial t} + (\mathbf{u} \cdot \nabla) \theta = \nabla^2 \theta, \quad (4.1b)$$

$$\nabla \cdot \mathbf{u} = 0, \quad (4.1c)$$

with the following boundary conditions at the wall,

$$\mathbf{u}|_{y=0,1} = 0, \quad \theta|_{y=0} = 1, \quad \theta|_{y=1} = 0, \quad (4.2a)$$

and the periodic boundary condition in the horizontal direction. Here, t denotes the time scaled by the vertical thermal diffusion time, d^2/κ , and $\mathbf{x} (= (x, y, z))$ is the spatial coordinates non-dimensionalised by d , where x and z are two orthogonal horizontal directions and y is the vertical direction. $\mathbf{u} (= (u, v, w))$ is the velocity vector scaled with κ/d , p the pressure scaled with $\rho\kappa^2/d^2$, $\theta (\equiv (T - T_U)/\Delta T)$ the non-dimensional temperature with T being the absolute temperature, and \mathbf{j} denotes the unit vector in y -direction. The Rayleigh number and the Prandtl numbers are defined as in §1.1: $Ra = \alpha g d^3 \Delta T / \nu \kappa$, Prandtl number $Pr = \nu/\kappa$. Throughout this study, $Pr = 1$ is set.

4.2.2 Numerical method

The governing equations are solved numerically using Nektar++, an open-source spectral/ hp -element method framework [Cantwell et al. \[2015\]](#), [Moxey et al. \[2020\]](#). An initial computational mesh, composed of quadrilateral elements, in the x - y plane is generated using Gmsh [Geuzaine and Remacle \[2009\]](#) and then refined by Nekmesh, the mesh generator available in Nektar++. Several computational domains of different sizes are prepared: $(L_x, L_y, L_z) = (32\pi, 1, 32\pi), (16\pi, 1, 16\pi), (8\pi, 1, 8\pi), (4\pi, 1, 4\pi)$. The spatial domain is discretised using a quasi-3D approach with spectral/ hp elements in x - y domain and Fourier expansions in z -direction. The discretised equations are subsequently solved using a velocity-correction method based on a second-order implicit-explicit temporal scheme (see §2.4.1). Since different computational domain sizes were considered, the spatial distribution of spectral/ hp elements in the x - y plane and Fourier expansions along z was kept constant. A spatial resolution of $(\Delta x, \Delta y|_{y=0,d}, \Delta y|_{y=d/2}, \Delta z) = (0.1\pi, 0.0549, 0.367, 0.25\pi)$ with polynomial order $P = 4$, and temporal resolution of $\Delta t = 0.0125$ was sufficient to establish numerical independence – for example, the Nusselt number, $Nu (= -\int_{x,z} \frac{\partial \theta}{\partial y}|_{y=0} dx dz)$, varies less than 10^{-5} when P was increased to $P = 5$.

4.2.3 Linear stability analysis of ISRs

As discussed in §4.1, we will perform a set of numerical experiments, in which a small perturbation about several unstable ISRs is added along their unstable manifolds. To obtain the direction of the unstable manifolds (i.e. linear instability eigenfunctions), we consider a small perturbation about the ISR (base) state:

$$\mathbf{u}(\mathbf{x}, t) = \mathbf{u}_{ISR,q}(\mathbf{x}) + \mathbf{u}'(\mathbf{x}, t), \quad (4.3a)$$

$$\theta(\mathbf{x}, t) = \theta_{ISR,q}(\mathbf{x}) + \theta'(\mathbf{x}, t), \quad (4.3b)$$

$$p(\mathbf{x}, t) = p_{ISR,q}(\mathbf{x}) + p'(\mathbf{x}, t), \quad (4.3c)$$

where $\mathbf{s} = [\mathbf{u}, \theta, p]^T$, $\mathbf{s}_{ISR,q} = [\mathbf{u}_{ISR,q}, \theta_{ISR,q}, p_{ISR,q}]^T$ and $\mathbf{s}' = [\mathbf{u}', \theta', p']^T$ refers to solution vector, the ISR (base) state of a given wavenumber, q , and the perturbation respectively. The theoretical background of this section is discussed earlier in §1.2, and its numerical technique is presented in §2.5.1. Substitution of (4.3) into (4.1) leads to the following linearised equations:

$$\frac{\partial \mathbf{s}'}{\partial t} = \mathcal{A}(\mathbf{s}_{ISR,q}; Ra, Pr)\mathbf{s}', \quad (4.4a)$$

where

$$\mathcal{A}(\mathbf{s}_{ISR,q}; Ra, Pr) = \begin{pmatrix} -(\mathbf{U} \cdot \nabla) - (\nabla \mathbf{U} \cdot) + Pr\nabla^2 & RaPr\hat{\mathbf{j}} & -\nabla \\ -(\nabla \Theta \cdot) & -(\mathbf{U} \cdot \nabla) + \nabla^2 & 0 \\ \nabla \cdot & 0 & 0 \end{pmatrix}. \quad (4.4b)$$

For the sake of simplicity here, we will only consider the ISRs invariant along z -direction. Since the ISRs are also assumed periodic in x -direction, the following form of normal-mode solution can be considered:

$$\mathbf{s}'(\mathbf{x}, t) = \check{\mathbf{s}}(x, y)e^{i(\alpha x + \beta z) + \lambda t} + \text{c.c}, \quad (4.5)$$

where λ , α and β are the complex frequency, the streamwise wavenumber (or the Floquet exponent), and the spanwise wavenumber, respectively. Using the periodic nature of $\check{\mathbf{s}}(x, y)$ in x -direction, (4.5) can also be written as

$$\mathbf{s}'(\mathbf{x}, t) = \left[\sum_{n=-\infty}^{\infty} \check{\mathbf{s}}_n(y) e^{i\frac{2\pi}{L_x}(n+\epsilon)x} \right] e^{i\beta z + \lambda t} + \text{c.c}, \quad (4.6)$$

where $\epsilon (= \alpha L_x / (2\pi))$ is the Floquet detuning parameter with $0 \leq \epsilon \leq 1/2$. Since the stability analysis here will be limited to the identification of unstable manifolds of ISRs in a fixed computational domain, $\epsilon = 0$ (fundamental mode) is considered only - note that the modes associated with $\epsilon \neq 0$ are only observed in the x domains greater than L_x .

Substituting (4.6) into (4.4) leads to a discretised eigenvalue problem in terms of the eigenvalue λ , where the wavenumber in the z -direction must be restricted to be $\beta = 2\pi m / L_z$, and m is a positive integer, for the given computational domain. The resulting eigenvalue problems are solved using a time-stepper-based iterative Arnoldi algorithm (see 2.5.1). The eigenvalues of primary instabilities of RBC computed in Nektar++ are also verified against those obtained with a Chebyshev-collocation method in Appendix A.7.

4.3 Transient SDC and elementary states in minimal domain

In this section, we seek to capture localised structures of SDC using a minimal domain by systematically reducing the domain by half in the homogeneous (x - z) directions. A random noise, characterised by

Gaussian white noise (0 mean and 1 variance), generated with a total energy of

$$\delta = \frac{1}{\bar{V}} \int_{\Omega} \tilde{\mathbf{u}}(\mathbf{x})^T \tilde{\mathbf{u}}(\mathbf{x}) + RaPr\tilde{\theta}(\mathbf{x})^2 d\Omega \approx O(10^{-3}), \quad (4.7)$$

where $\tilde{\mathbf{u}}(\mathbf{x})$ and $\tilde{\theta}(\mathbf{x})$ refer to the perturbation velocity and temperature about the base state $\mathbf{U}(\mathbf{x}) = \mathbf{0}$ and $\Theta(y) = 1 - y$, is introduced as an initial condition to the system. Here, we note that the first term of the integrand in (4.7) is the kinetic energy of the perturbation velocity and the second one measures the potential energy from the perturbation temperature.

The system is time integrated for 300 units of vertical thermal diffusion time $t (= d^2/\kappa)$. The resulting mid-plane temperature snapshots $\theta(x, z)|_{y=d/2}$ at $t = 300$ exhibit features of spiral defect chaos, as shown in figure 4.1. When the domain size is large, for instance, $\Gamma = 8\pi$ shown in figure 4.1(a), features of SDC consist of many repeating localised spirals, defects and dislocations. Reducing the domain in half to $\Gamma = 4\pi$, shown in figure 4.1(b), led to a spatially less extensive chaotic state, revealing a single spiral, with some defects and dislocations. Surprisingly, a further reduction of the domain in half, $\Gamma = 2\pi$, does not lead to sustained SDC, but rather, a transient SDC state before settling into stable ‘elementary’ states. These elementary states are identified as *pacman* (PM), *spiral-defect* (SD), *hooked* (HK), and *peanut* (PN) states in figure 4.1 (c-f), which resemble the localised features of SDC (see the coloured bounding boxes in figures 4.1(a,b)). These states represent stable invariant solutions of (4.1). Specifically, PM state represents a steady equilibrium, SD and HK states are characterised by relative periodic orbits, and the PN state is a periodic orbit.

An example of a transient SDC state is shown in figure 4.2(a), where spirals, a typical feature of SDC ?, form spontaneously with a chaotic transient (figures 4.2(c-e)), before stabilising into SD state with a period of $T \approx 73$ (figures 4.2(f,g)). In addition to the elementary states presented in figures 4.1(c-f), we have identified ten additional elementary states, each independently preceded by a transient SDC state, and fourteen stable ISRs of varying wavenumbers (see Appendix ??). In total, we have identified 28 states with $\Gamma = 2\pi$. Minimising the domain further to $\Gamma = \pi$ only led to stable ISRs at least for the random initial conditions we have examined in this study. We therefore consider $\Gamma = 2\pi$ as the minimal domain, in which both transient SDC and elementary states exist. It is worth mentioning that solutions to multiple states were obtained in smaller domains with $\Gamma = 2$, but in a cylindrical domain [Ma et al., 2006, Borońska and Tuckerman, 2010a,b].

To show whether SDC and elementary states are related, we compare their state space trajectories, and the averaged wall-normal temperature profiles. Figure 4.3 presents the two chaotic trajectories of SDC from $\Gamma = 8\pi, 4\pi$, four of fourteen transient SDC trajectories obtained and fourteen stable fixed-points of ISRs from $\Gamma = 2\pi$ on a two-dimensional state portrait based on the volume ($\bar{V} = L_x L_y L_z$) normalised L2-norms of velocity ($\|\frac{1}{\bar{V}}\tilde{\mathbf{u}}\|_2$) and temperature ($\|\frac{1}{\bar{V}}RaPr\tilde{\theta}\|_2$) perturbations. The trajectories begin from $t = 3$, as those for $t < 3$ contain artificial transients and are omitted for clarity. The state space trajectories of SDC ($\Gamma = 8\pi, 4\pi$) and the transient SDC states for $\Gamma = 2\pi$ are visibly attracted toward a region, where $\|\frac{1}{\bar{V}}\tilde{\mathbf{u}}\|_2 \approx 6.3$ and $\|\frac{1}{\bar{V}}RaPr\tilde{\theta}\|_2 \approx 8.6$, as shown in figure 4.3(b). This suggests that they are presumably the same type of SDC emerging in different domains. The closely packed chaotic trajectories are in contrast to the ISRs populating sparsely.

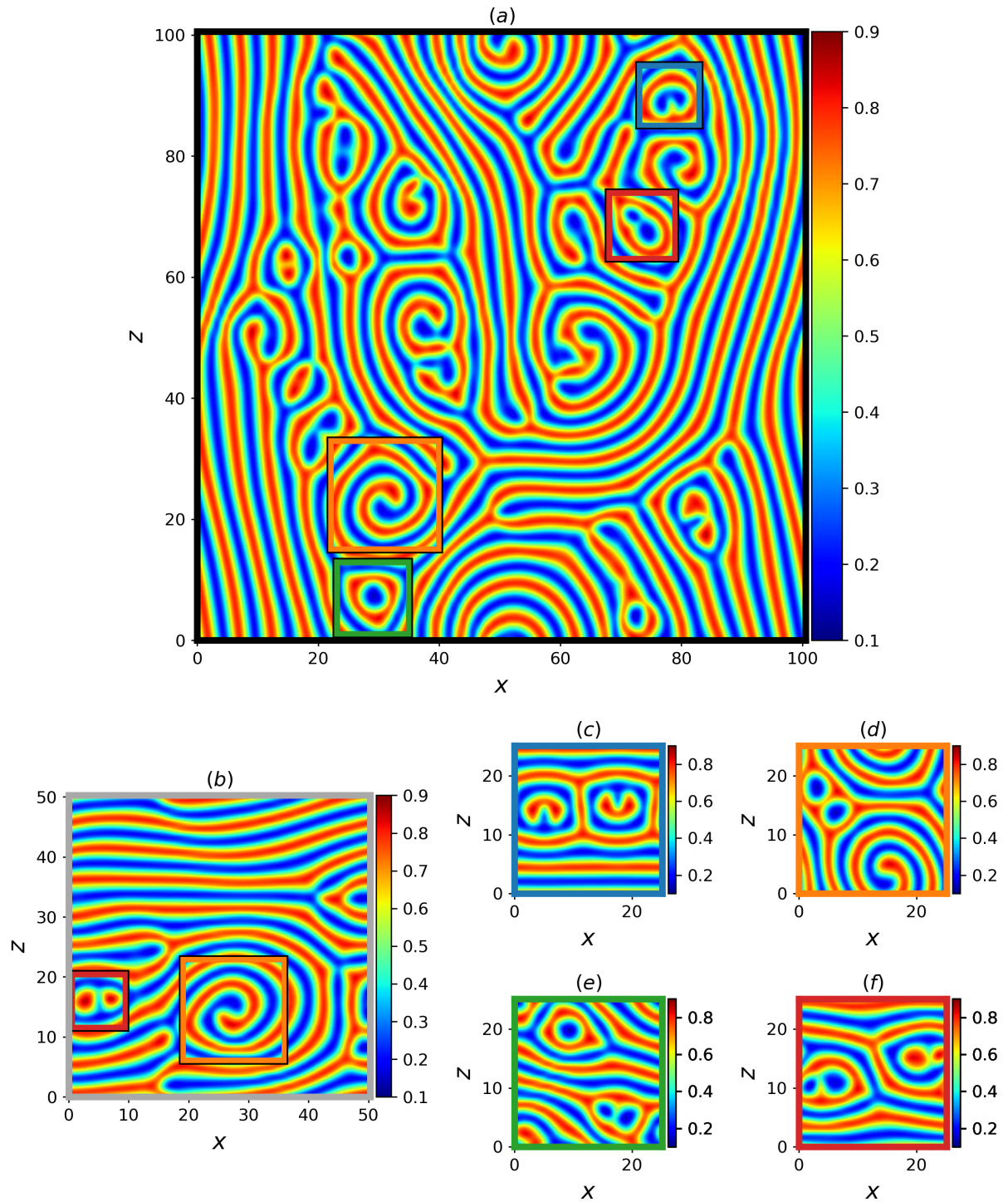


Figure 4.1: Midplane temperature snapshots, $\theta(x, z)|_{y=d/2}$, of spiral defect chaos (SDC) for a domain aspect ratio of (a) $\Gamma = 8\pi$ and (b) 4π . Elementary states of SDC captured when $\Gamma = 2\pi$: (c) steady *pacman* (PM), (d) relative periodic orbit *spiral-defect* (SD), (e) relative periodic orbit *hooked* (HK), and (f) periodic *peanut* (PN) elementary state. Note that the localised structures indicated by bounding boxes in (a,b) resemble structures in (c-f).

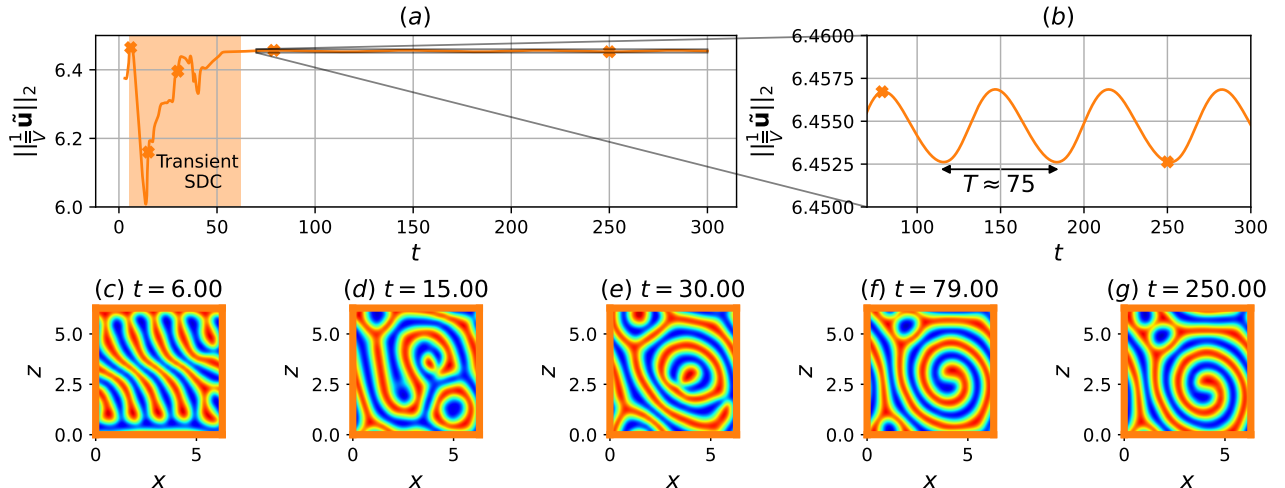


Figure 4.2: (a,b) Time history of the volume ($\bar{V} = L_x L_y L_z$) normalised L2-norm of velocity perturbations from a random initial condition with $\delta = 0.001$ and (c-g) Mid-plane temperature snapshots at $t = 6, 15, 30, 79, 250$. Here, transient chaotic SDC lasts up to $t \approx 70$, before stabilising into an SD state, emerging as a relative periodic orbit with the time period $T \approx 73$ propagating diagonally in the negative x - and z -directions.

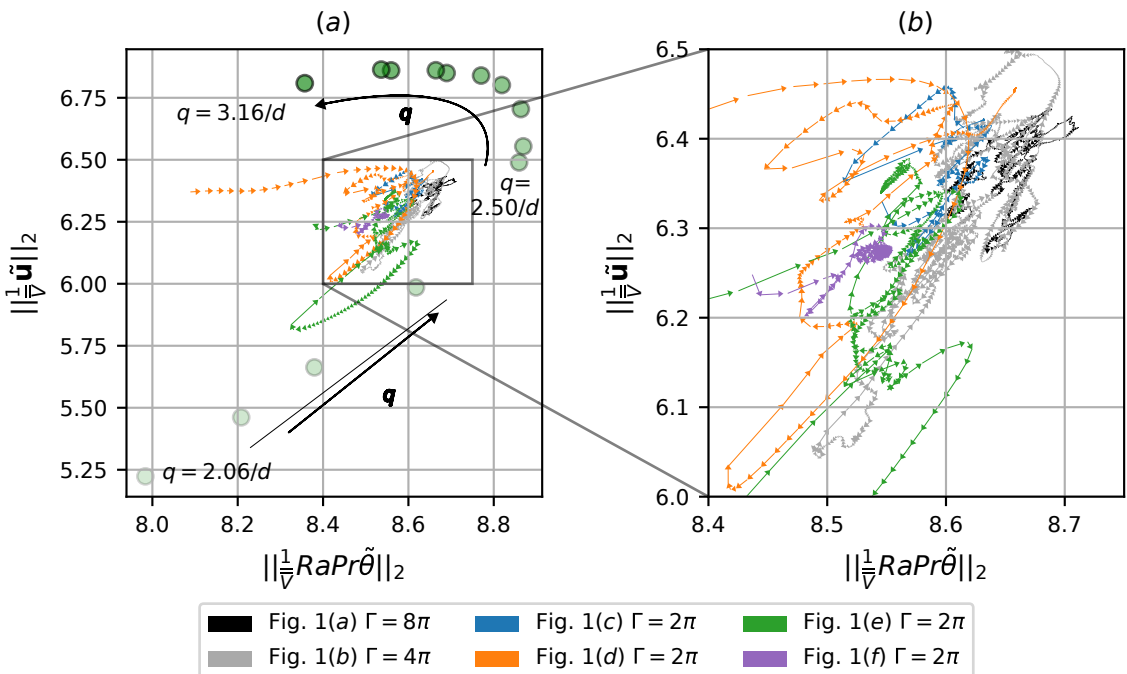


Figure 4.3: (a) State-space portrait in the plane of $||\frac{1}{\bar{V}}\tilde{u}||_2$ and $||\frac{1}{\bar{V}}RaPr\tilde{\theta}||_2$ for SDC from $\Gamma = 8\pi, 4\pi$ (figures 4.1(a,b)), four transient SDC state proceeding to stable elementary states (figures 4.1(c-f), A.6), and fourteen stable stationary ISRs of wavenumbers $2.0 \leq qd \leq 3.35$. Here, the magnitude of q is denoted by the opacity of the filled symbol (●), increasing from the bottom left and turning toward the top left shown as arrows; (b) Zoomed-in view of (a). The legend refers to the figures for respective trajectories preceding snapshots in figure 4.1.

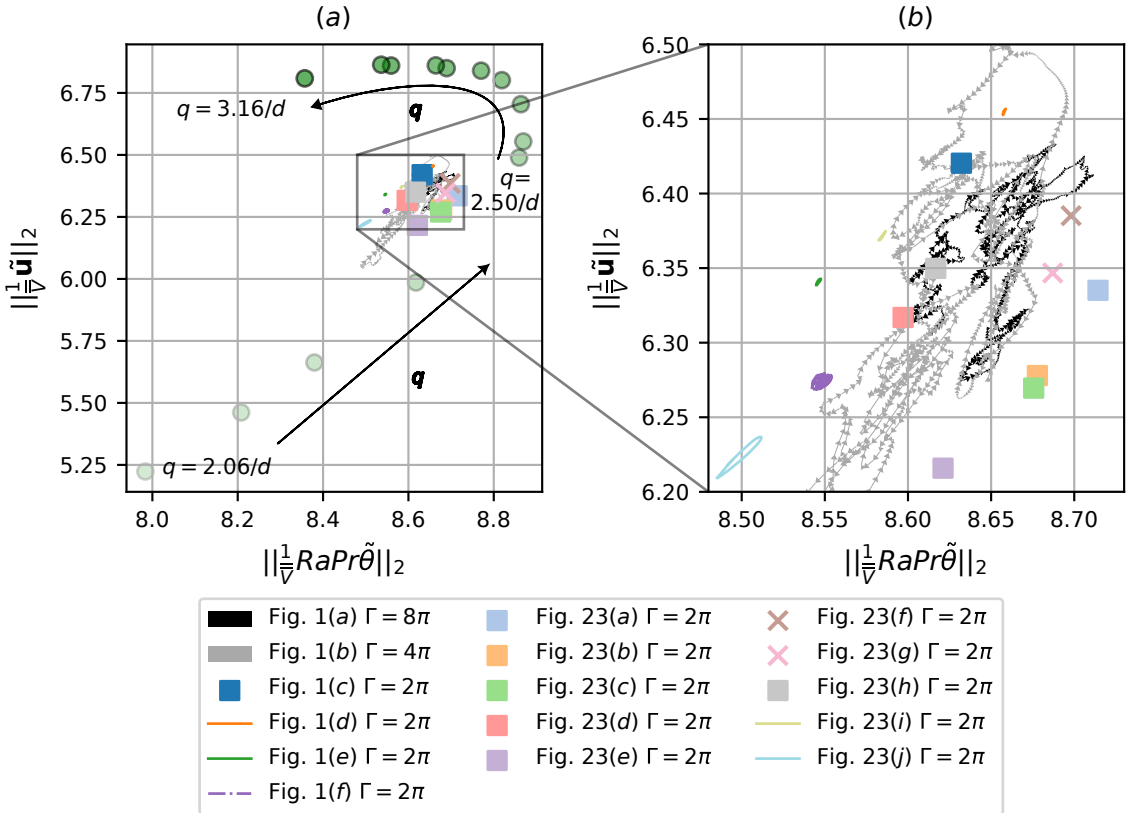


Figure 4.4: (a) State-space portrait (from figure 3) highlighting the transient SDC states for $\Gamma = 2\pi$ proceeding toward stable elementary states (see figures 4.1(c-f), A.6): steady states (■), travelling waves (×), periodic orbit (dash-dotted line) and relative periodic orbits (solid lines). Here, ISRs are denoted by the varying opacity of the filled symbol (●) increasing from the bottom left and turning toward the top left shown as arrows; (b) Zoomed-in view of (a).

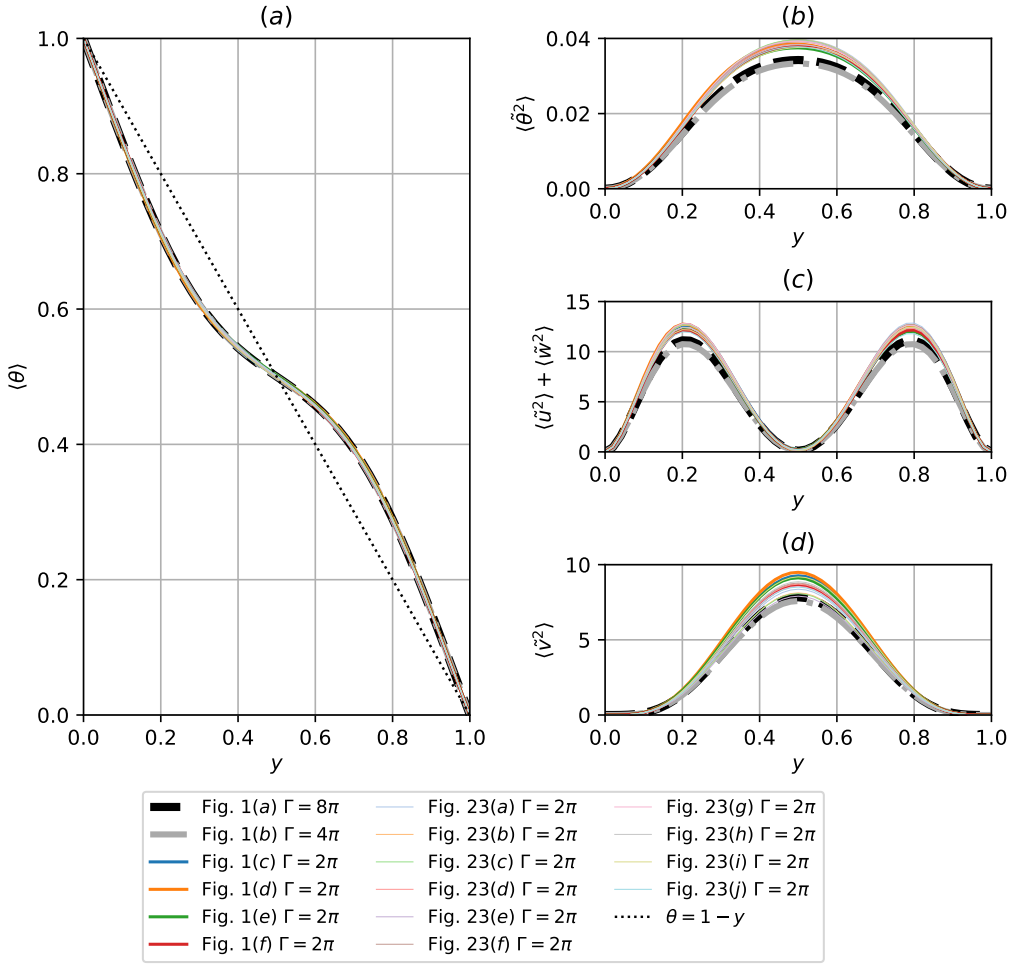


Figure 4.5: Profiles of (a) averaged temperature, (b) root-mean-squared temperature fluctuation, (c) sum of root-mean-squared x - z velocity fluctuations and (d) root-mean-squared wall-normal velocity fluctuations for the SDC and elementary states shown in figures 4.1(a-f) and in Appendix ???. Note that $\langle \cdot \rangle = \frac{1}{T L_x L_z} \int_{t,x,z} dt dx dz$ refers to the time and plane averaged operator, where T was chosen to be sufficiently long to ensure temporal convergence.

The transient SDC trajectories eventually stabilise into fourteen elementary states in figure 4.4, where the transient SDC trajectories from figure 4.3 are now omitted. Obscured by the transient SDC trajectories initially, the elementary states in figure 4.4(b) emerge as seven steady states (■), two travelling waves (×), one periodic orbit (dash-dotted line) and four relative periodic orbits (solid line). All the SDC trajectories for $\Gamma = 8\pi, 4\pi, 2\pi$ are organised around the fourteen elementary states (figure 4.4(b)). Notably, the state space trajectories of SDC and the elementary states are in close vicinity to the ISR of wavenumbers $q = 2.5/d$ (see figures 4.3 and 4.4), which corroborates with the averaged wavenumber of SDC, $q_{avg} \approx 2.5/d$ [Decker et al., 1994, Morris et al., 1993].

The comparison between the time-averaged mean temperature profile, mean-squared temperature fluctuations, and mean-squared velocity fluctuations of SDC (figures 4.1(a,b)) and elementary states (figures 4.1(c-f) and figure A.6) are presented in figure 4.5. In figure 4.5(c), we present the sum of mean-squared x - and z -velocity fluctuations due to horizontal isotropy. The mean temperature profiles of the elementary states closely match those of SDC (figure 4.5(a)). Notably, the mean-squared temperature and velocity fluctuations between SDC states (grey and black dashed curves) of figures

4.5(b-d) are similar. The mean-squared temperature and velocity fluctuations profiles of elementary states are comparable to those of SDC but are in general, slightly larger in magnitudes.

The spatial-temporal complexity of SDC reduces when the domain size is reduced from $\Gamma = 8\pi$ to $\Gamma = 4\pi$, i.e. less disordered spatial features. Reducing the domain from $\Gamma = 4\pi$ to $\Gamma = 2\pi$ led to transient SDC before stabilising into many elementary states. From the conventional view, especially made in the context of shear flow turbulence, this is unexpected as the chaotic state (i.e. turbulence) is commonly described as solution trajectories wandering around unstable invariant solutions ?????. However, in this particular case observed in RBC, the chaotic state (i.e. SDC) is instead stabilised into stable invariant solutions (elementary states). Despite this distinguished feature of the state space, each of the elementary states is still seen to emerge in a spatially localised manner of SDC in an extended domain (figure 4.1), and their spatially-averaged statistics are remarkably similar to those of SDC in extended domains (figure 4.5). Therefore, we consider the elementary states in the minimal domain to be the ‘building blocks’ structure of SDC.

4.4 Multiplicity of edge states

The stable nature of many ISRs and elementary states underpinning SDC implies the existence of state-space boundaries between them (i.e. edge). In this section, we perform the edge tracking between the stable manifolds of ISRs and elementary states to compute the attractors on the edge (i.e edge states). For the edge tracking, we use the bisection method (see §??), with an initial condition given by

$$\mathbf{s}_0(\mathbf{x}, t=0) = \chi \mathbf{s}_{ISR,q} + (1 - \chi) \mathbf{s}_{elementary}, \quad (4.8)$$

where $\mathbf{s}_0(= [\mathbf{u}_0, \theta_0, p_0]^T)$ refers to an initial condition consisting of a weighted sum, $\chi \in [0, 1]$, between a stable ISR state, $\mathbf{s}_{ISR,q}$ of a wavenumber q , and an elementary state, $\mathbf{s}_{elementary}$ where the subscript refers to its names in figures 4.1(c-f).

Given the large number of stable ISRs and elementary states, we shall focus on the computation of the edge states considering three of the stable ISRs and two of the elementary states. However, in principle, the edge tracking is technically possible with other stable ISRs and elementary states. As such, in general, multiple edge states are expected. The three ISRs are related to three different wavenumbers, denoted by $\mathbf{s}_{ISR,q=2.06/d}, \mathbf{s}_{ISR,q=2.24/d}, \mathbf{s}_{ISR,q=3.16/d}$ (figures A.7(b,d,j)) respectively, and the two elementary states are SD state, $\mathbf{s}_{spiral-defect}$ (figure 4.1(c)), and PM state, \mathbf{s}_{pacman} (figure 4.1(d)). Using this set of stable ISRs and elementary states, we aim to track the edge near $\mathbf{s}_{ISR,q}$ in the direction of $\mathbf{s}_{elementary}$ by bisecting the initial condition with χ in (4.8), whereby one of the two trajectories across the edge decays toward $\mathbf{s}_{ISR,q}$ and the other is attracted toward transient chaotic state (i.e. SDC), referred to as the ‘lower’ and ‘upper’ trajectories respectively. The bisection of the initial condition is carried out by monitoring the difference in two trajectories with Nu (i.e. ΔNu). When the two trajectories reach a certain time at which $\Delta Nu > 0.0007$, the bisection of the initial condition is repeated using the flow fields from the two different trajectories by replacing $\mathbf{s}_{ISR,q}$ and $\mathbf{s}_{elementary}$ in (4.8) with them. This process is repeated until the edge trajectory reaches an attractor (i.e. an edge state).

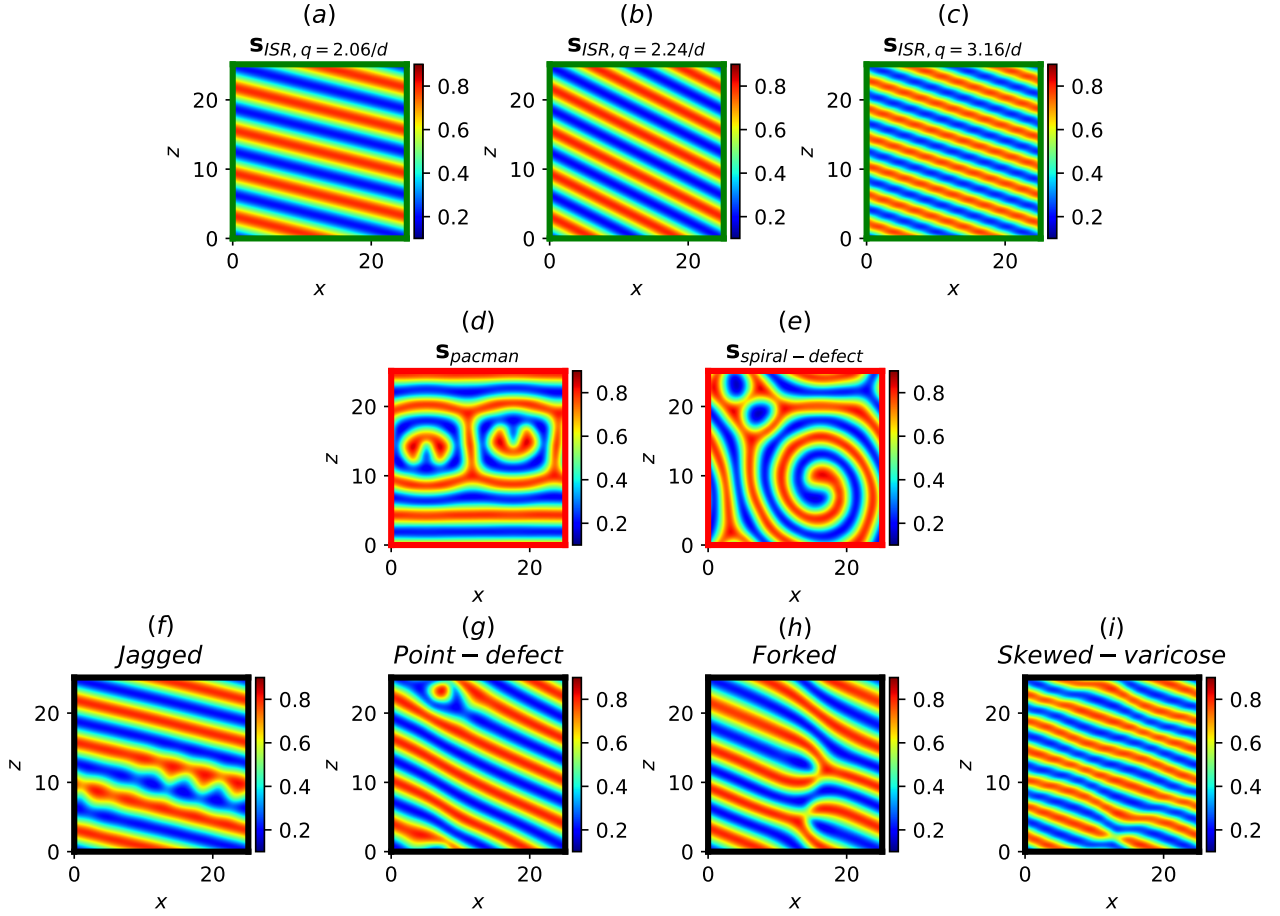


Figure 4.6: Mid-plane temperature fields of ISRs and elementary states used in Eq. (4.8), and the resulting edge states. Here, ISRs (green borders): (a) $s_{ISR,q}=2.06/d$, (b) $s_{ISR,q}=2.24/d$, (c) $s_{ISR,q}=3.16/d$; elementary states: (d) s_{pacman} , (e) $s_{spiral-defect}$; edge states (black borders): (f) *jagged*, (g) *point-defect*, (h) *forked* and (i) *skewed-varicose* edge state.

$s_{ISR,q}$	$s_{elementary}$	Edge state	State transitioned
$s_{ISR,q}=2.06/d$	$s_{spiral-defect}$	<i>Jagged</i> (Stationary)	Transient Chaos
$s_{ISR,q}=2.06/d$	s_{pacman}	<i>Jagged</i> (Stationary)	Transient Chaos
$s_{ISR,q}=2.24/d$	$s_{spiral-defect}$	<i>Point-defect</i> (Travelling wave)	$s_{bubble-defect}$
$s_{ISR,q}=2.24/d$	s_{pacman}	<i>Forked</i> (Relative Periodic Orbit)	Transient Chaos
$s_{ISR,q}=3.16/d$	$s_{spiral-defect}$	<i>Skewed-varicose</i> (Stationary)	Transient Chaos
$s_{ISR,q}=3.16/d$	s_{pacman}	<i>Skewed-varicose</i> (Stationary)	Transient Chaos

Table 4.1: A summary of the edge states computed. The first two columns denote the pair of initial conditions considered for edge tracking in Eq. (4.8). The names and classification of the edge states are described in the third column. The last column describes the state transitioned from $s_{ISR,q}$ for sufficiently large χ in Eq. (4.8).

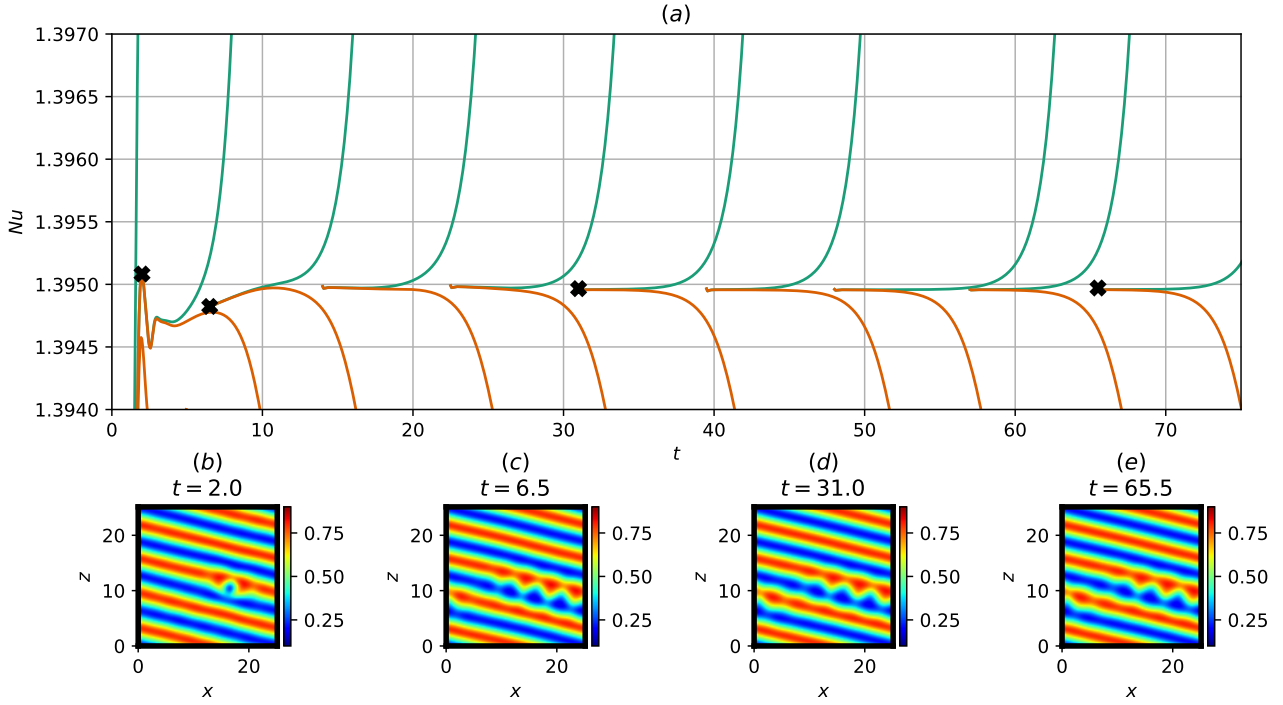


Figure 4.7: (a) Time history of Nu and (b-e) the corresponding mid-plane temperature field snapshots at $t = 2.0, 6.5, 31.0, 65.5$ along the edge trajectory obtained by bisecting $s_{ISR,q=2.06/d}$ and $s_{spiral-defect}$.

Table 4.1 summarises the edge states and their dynamical properties computed from six combinations of $s_{ISR,q}$ and $s_{elementary}$ states, and they are visualised with the mid-plane temperature field in figure 4.6. The convection patterns of edge states are often featured with mild spatial complexity compared to SDC and the elementary states. In particular, their patterns contain the underlying convection pattern of $s_{ISR,q}$ with spatially localised defects. We obtained four edge states: specifically, the *jagged* and *skewed-varicose* edge states are stationary, and the *point-defect* and *forked* edge states are travelling wave and a relative periodic orbit respectively. The *jagged*, *skewed-varicose* and *forked* edge states lie on the boundary, separating the basins of attraction of stable $s_{ISR,q}$ from transient SDC. In the case of the *point-defect* edge state, the solution trajectory is found to bypass the transient SDC state, directly settling into a stable elementary state characterised by bubble-like convection roll defects, $s_{bubble-defect}$. Since the *jagged*, *skewed-varicose*, *forked* edge states are similar in nature, acting as separatrices between $s_{ISR,q}$ states and transient SDC, we will focus our analysis on the *jagged* edge state only, alongside the *point-defect* edge state.

Using Nu as an observable, successive bisections between $s_{ISR,q=2.06/d}$ and $s_{spiral-defect}$ reveal the trajectory along the edge, as illustrated in figure 4.7. The trajectory along the edge spans from $t \approx 0 - 15$, and is initially characterised by a ‘speckled’ defect (figure 4.7(b)). The ‘speckled’ defect grows into a spatially localised jagged-like defect as the trajectory is attracted to the *jagged* stationary edge state from $t \approx 6.5$ onwards (figures 4.7(c-e)). We further examine the two trajectories in the opposite directions along the unstable manifold of the *jagged* edge state in figure 4.8, where the ‘upper’ trajectory evolves into a transient SDC and the ‘lower’ trajectory decays into the original stable $s_{ISR,q=2.06/d}$ state. Starting from the ‘upper’ trajectory (figure 4.8(a)), the spatially localised jagged

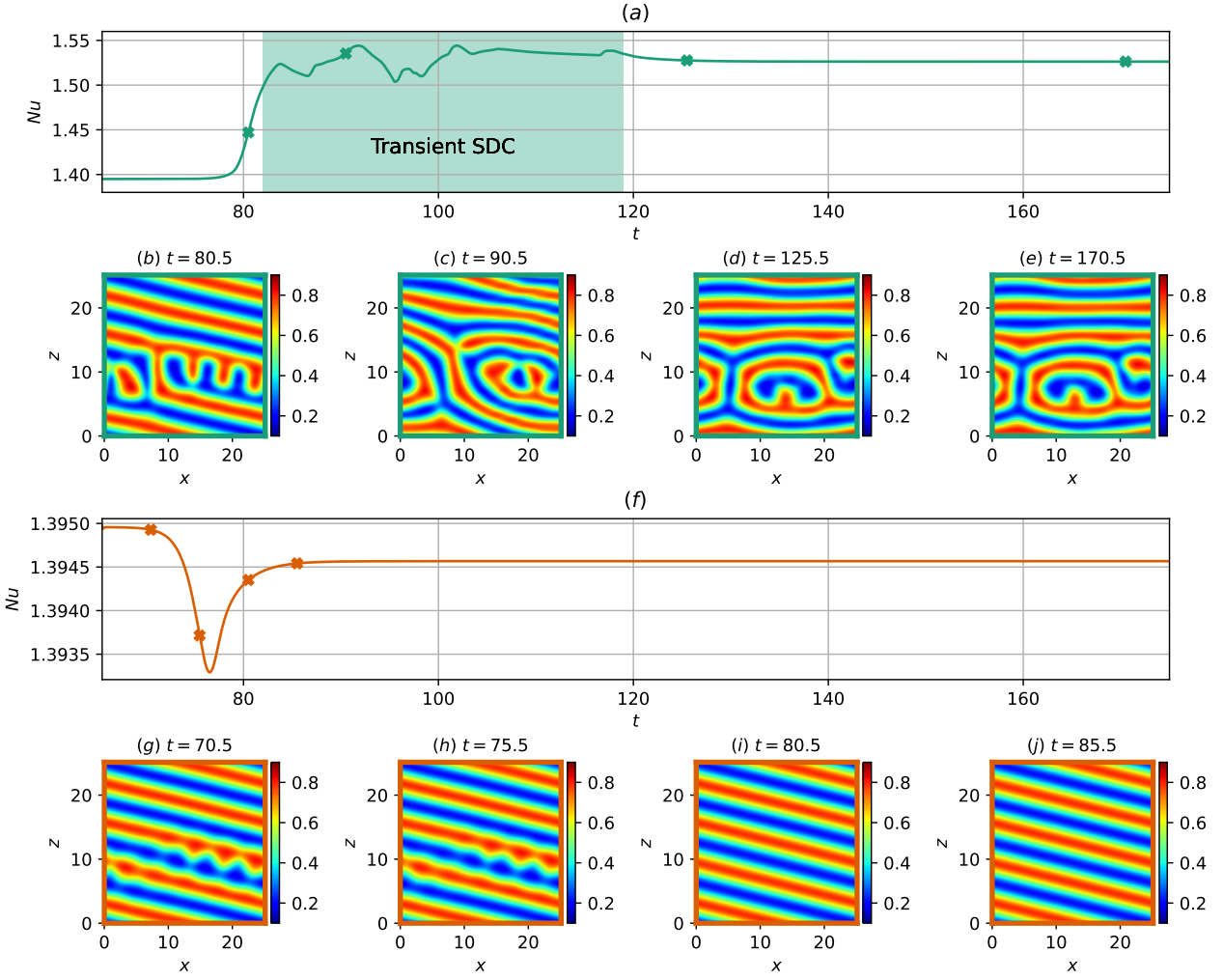


Figure 4.8: Time history of Nu along two opposite directions along the unstable manifold of the jagged edge state: (a) ‘upper’ trajectory leading to a transient SDC for $t \approx 85 – 120$ and subsequently to PM state for $t > 120$ and (f) ‘lower’ trajectory stabilising into $s_{ISR,q=2.06/d}$. Mid-plane temperature fields are visualised in (b-e) along the upper trajectory at $t = 80.5, 90.5, 125.5, 170.5$, and in (g-j) along the lower trajectory at $t = 70.5, 75.5, 80.5, 85.5$.

defect grew in the direction normal to the roll orientation at $t = 80.5$ (figure 4.8(b)), contaminating the adjacent roll structure and propagating through the domain where transient SDC emerges from $t > 80.5$, lasting up to $t \approx 120$ (a snapshot of transient chaotic SDC regime at $t = 90.5$ is shown in figure 4.8(c)). The trajectory subsequently stabilises into a travelling-wave PM elementary state described by ‘pac-man’ like patterns, propagating along the $-x$ direction from $t = 125.5$ to $t = 170.5$ (figures 4.8(d,e)). This is reminiscent of a secondary cross-roll instabilities experienced by low-wavenumber ISRs (such as $s_{ISR,q=2.06/d}$ considered here), where a defect propagates in the direction perpendicular to the rolls ?. Along the ‘lower’ trajectory (figure 4.8(f)), the jagged defects diffuse from $t = 70.5$ to $t = 75.5$, decaying into the stable $s_{ISR,q=2.06/d}$ state at $t = 80.5$ (figures 4.8(g-j)).

Next, we analyse the edge trajectory obtained bisecting between $s_{spiral-defect}$ and $s_{ISR,q=2.24}$ in figure 4.9. The trajectory along the edge from $t = 4$ (figure 4.9(b)) is described by time-dependent convection structures. The edge trajectory began to be stabilised into the *point-defect* edge state from

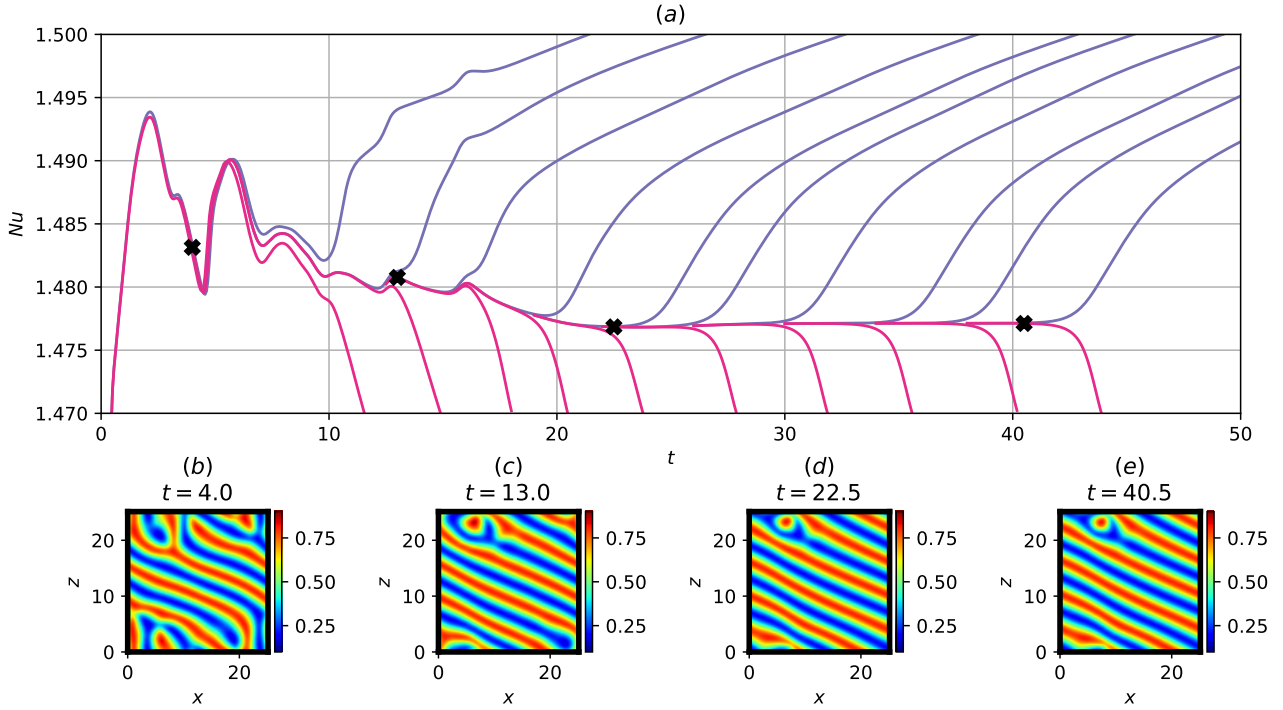


Figure 4.9: a) Time history of Nu and (b-e) the corresponding mid-plane temperature field snapshots at $t = 4, 13, 22.5, 40.5$ along the edge trajectory obtained by bisecting $s_{ISR,q=2.24}$ and $s_{spiral-defect}$.

$t = 13$ onwards (figure 4.9(c)), propagating along x direction from $t = 22.5$ (figures 4.9(d,e)). It is characterised by the convection structure of the $s_{ISR,q=2.24}$ state with a pointed defect structure, hence referred to as the *point-defect* edge state. The upper and lower trajectories through two opposite directions of the unstable manifold of the travelling wave *point-defect* edge state are subsequently examined in figure 4.10. Integrating along the upper trajectory (figure 4.10(a)), the spatially localised point-defect structure grew from $t = 43$ to $t = 83$ (figures 4.10(b-d)), saturating into a stationary elementary state at $t = 163$ (figure 4.10(e)) characterised by $s_{ISR,q=2.24}$ with a large bubble defect. Along the lower trajectory (figure 4.10(f)), the spatially localised point defect merged onto the adjacent convection roll from $t = 38$ to $t = 44.5$ (figures 4.10(g,h,i)), stabilising into the $s_{ISR,q=2.24/d}$ state at $t = 53$ (figure 4.10(j)). It is worth noting that, in this particular case, no chaotic transient in the form of SDC has been observed.

Finally, figure 4.11 depicts a state space portrait of stable ISRs, SDC and the edge/elementary states found here. As seen previously, SDC and elementary states are seen to be clustered around the region of $\|\frac{1}{V}\tilde{\mathbf{u}}\|_2 \approx 6.3$ and $\|\frac{1}{V}RaPr\tilde{\theta}\|_2 \approx 8.6$, whereas stable ISRs are distributed along a horseshoe-shaped band (green line). The edge states found in this study are located not far from the (green) horseshoe-shaped band of ISRs, as they presumably lie in a smaller (grey) horseshoe-shape band situated between ISRs and SDC or elementary states. While we have identified four edge states, we expect that there are more edge states, presumably distributed along the (grey) horseshoe-shaped band. It is also worth mentioning that the edge states we found here contain the underlying ISR structure ($s_{q=2.06/d, 2.24/d, 3.16/d}$) modified by spatially localised defects and ‘pinches’ between rolls, supporting its proximity with ISRs in the state space. This feature is also reminiscent of spatially

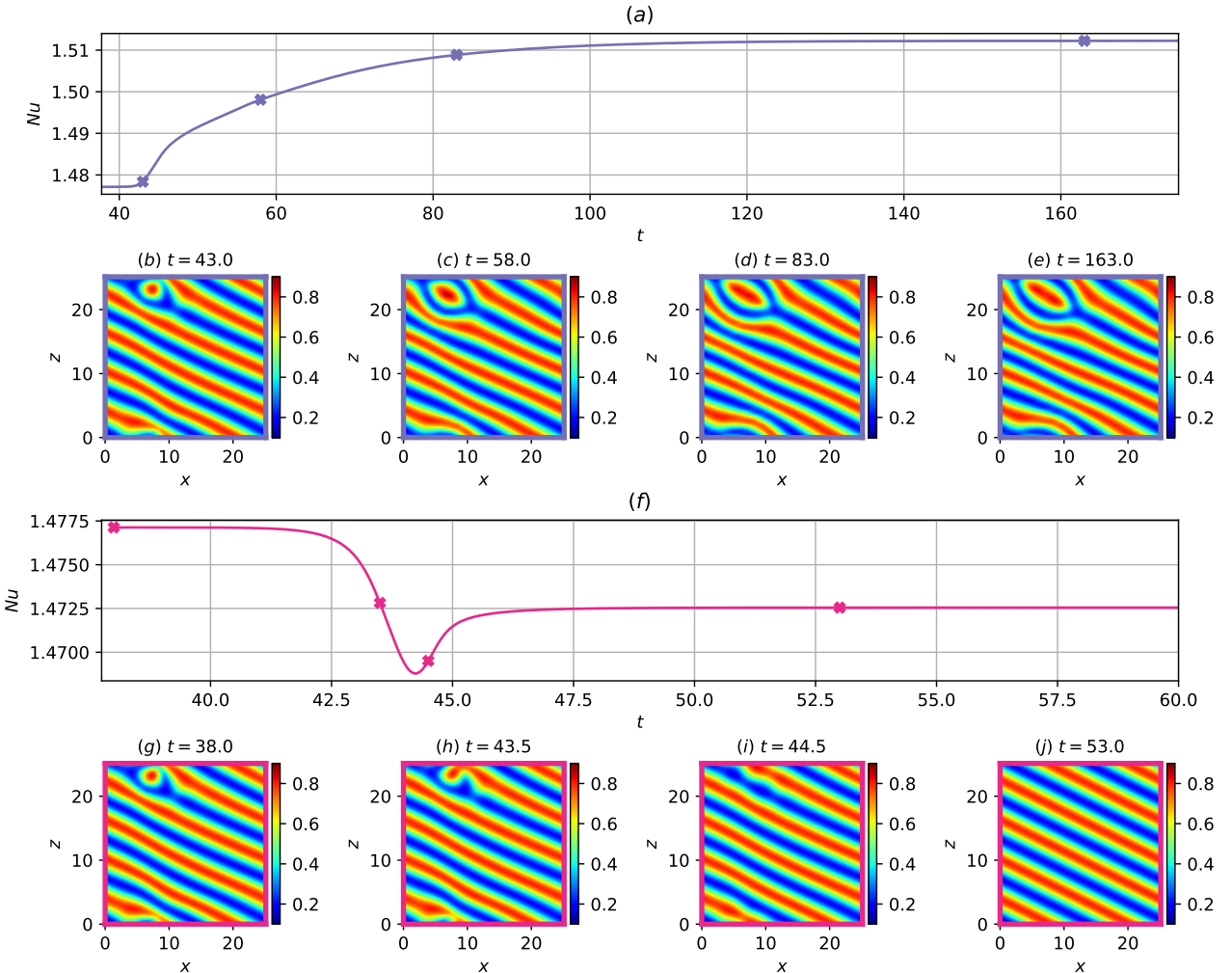


Figure 4.10: Time history of Nu along two opposite directions of the unstable manifold of the *point-defect* edge state: (a) ‘upper’ trajectory leading a stationary elementary state with bubble defect from $t \approx 43 - 163$ and (f) ‘lower’ trajectory decaying to the stable $s_{ISR,q=2.24}$ state. Mid-plane temperature fields are visualised in (b-e) along the upper trajectory at $t = 43.0, 58.0, 83.0, 163.0$, and in (g-j) along the lower trajectory at $t = 38.0, 43.5, 44.5, 53.0$.

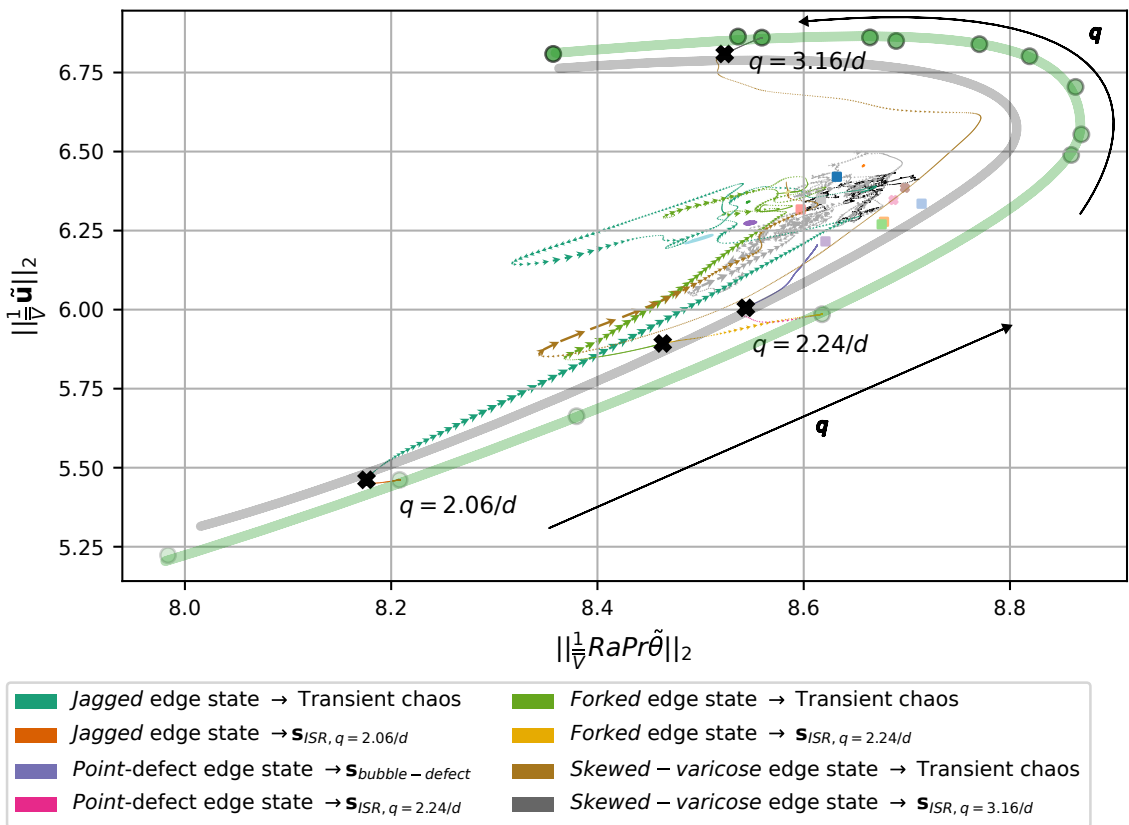


Figure 4.11: Phase portrait of the *jagged*, *point-defect*, *defect* and *skewed-varicose* edge states, along with stable ISRs, elementary states and transient SDC. Green and grey horseshoe lines are the regions, where stable ISRs and edge attractors are expected to be distributed when different sizes of the computational domain are considered.

Cases	$\beta = 0.25$	$\beta = 0.50$	$\beta = 0.75$	$\beta = 1.00$	$\beta = 1.25$	$\beta = 1.50$	$\beta = 1.75$
$q = 3.5/d$	ISR _{3.04}	(a) ISR _{2.50}	Stable	Stable	Stable	Stable	Stable
$q = 4.0/d$	ISR _{2.50}	(b) ISR _{3.16}	ISR _{3.00}	ISR _{2.83}	Stable	Stable	Stable
$q = 4.5/d$	ISR _{2.50}	ISR _{2.50}	(c) ISR _{3.00}	ISR _{3.20}	(d) Elementary	ISR _{2.50}	(e) Elementary

Table 4.2: Asymptotic state of secondary linear instabilities of $q = 3.5/d, 4.0/d, 4.5/d$. Subscripts in ISR refer to asymptotic wavenumber q , e.g., ISR_{2.5} refers to ideal straight rolls with wavenumber of $q = 2.5/d$. The asymptotic behaviours of (a-c) and (d,e) are discussed further in §4.5.1 and §4.5.2 respectively.

localised edge states identified in boundary layer flows ?. Lastly, we would like to emphasise that we have only considered initial conditions from the states between $s_{ISR,q}$ and $s_{elementary}$ and not strictly between $s_{ISR,q}$ and a transient SDC state. Nevertheless, three of the edge states are found to lie on the boundary separating the stable ISRs from transient SDC, supporting previous findings that the transient chaotic SDC are related to elementary states.

4.5 Unstable ideal straight rolls

Thus far, we have studied the edge and the edge states between some of the stable ISRs and elementary states. The dynamics associated with the unstable ISRs outside of the Busse balloon, however, remain unclear [Busse, 1981]. Given that the stable ISRs and SDC form a bistable system, it is expected that some of the unstable ISRs near the Busse balloon would asymptotically reach one of the stable ISRs as the difference between the stable and unstable ISRs would be sufficiently small [Steinberg and Ahlers, Croquette, 1989a]. On the other hand, the unstable ISRs, which exist far from the boundary of the Busse balloon, may well have a sufficiently large deviation from the stable ISRs, implying that they are possibly associated with a state-space route to the SDC. The purpose of this section is to test this hypothesis by examining the long-term behaviour of the linear instabilities of the unstable ISRs.

We consider the linear instabilities of 3 unstable ISRs on the right side of the Busse balloon, with increasing wavenumber of $q = 3.5/d, 4.0/d, 4.5/d$, as shown in figure 4.12(a). The identification of the linear instability mode (or unstable manifold) with the different spanwise wavenumbers β is considered (see (4.6)). Figure 4.12(b) presents the unstable eigenvalues as a function of β . There are 2, 4 and 7 unstable manifolds ($\Re(\lambda) > 0$) for unstable ISRs of $q = 3.5/d, 4.0/d, 4.5/d$ respectively, forming total 13 unstable manifolds. In general, the growth rate and the number of linear instability modes (i.e. the repelling strength and the number of unstable manifolds) increase as q increases. It is worth mentioning that the solutions of unstable ISRs of $s_{ISR,q}(x, y)$ (required for linear stability analysis) are obtained by restricting the computational domain to the 2D x - y plane which artificially suppresses 3D linear instabilities. We also note that the stability analysis of the unstable ISR, $q = 5.0/d$ was not considered as it quickly evolved into an unstable ISR of $q = 3.5/d$, which will be discussed in section §4.5.1.

To consider the long-term behavior in the direction of the unstable manifolds, an initial condition,

$$s_0(\mathbf{x}, t=0) = s_{ISR,q}(\mathbf{x}) + \hat{s}_\beta(x, y)e^{i\beta z}, \quad (4.9)$$

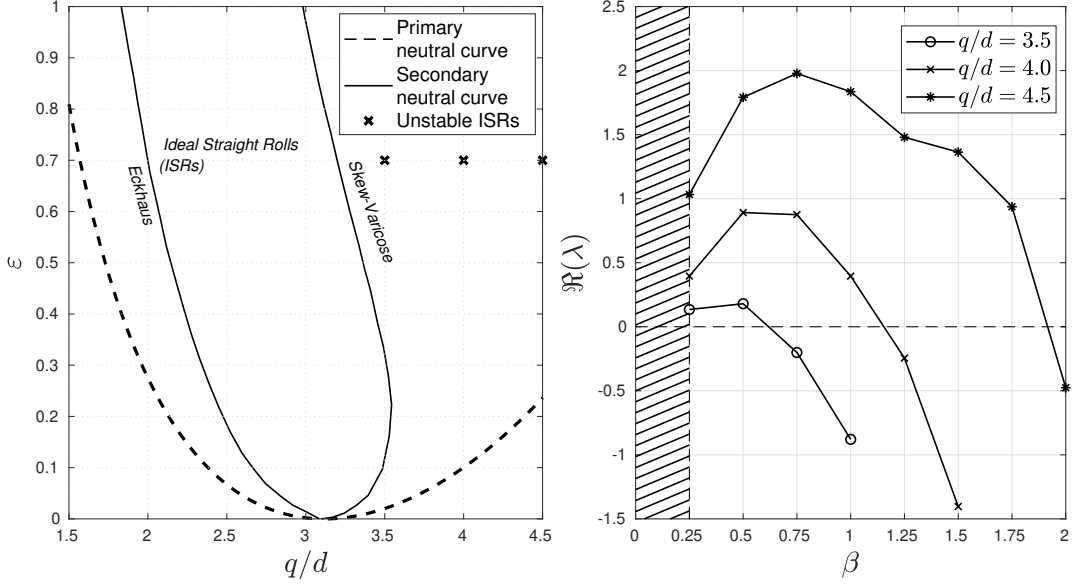


Figure 4.12: (a) Primary and secondary (Busse balloon from figure 1 ?) stability curves and unstable ISRs with $q = 3.5/d, 4.0/d, 4.5/d$; (b) Variation of the growth rate of instabilities of unstable ISRs as a function of spanwise wavenumber β . (Note that there are a total 13 unstable eigenmodes.)

is prescribed to equation (4.1). Here, $\hat{s}_\beta e^{i\beta z}$ is the unstable eigenmode, the amplitude of which was scaled such that its total energy (defined in (4.6)) of $\delta = 10^{-5}, 10^{-4}, 10^{-3}$ were considered. The total energy of the eigenmode, $\delta = 10^{-4}$ was found to be sufficiently small enough to ensure linear growth, while large enough to prevent other eigenmodes from being excited. Next, the initial condition is time integrated over an extended period until an asymptotic state is reached. Table 4.2 shows the asymptotic states of 13 linear instabilities, depicted in figure 4.12(b), of which 11 linear instabilities led to ISRs states, forming a network of heteroclinic orbits which will be discussed in §4.5.1. Only the remaining 2 instabilities led to a transient SDC state before settling into an elementary state discussed further in §4.5.2.

4.5.1 Pathways leading to ISRs - heteroclinic orbits

In this section, the asymptotic behaviour of the most unstable linear instabilities of ISRs (tab 4.2(a-c)) will be discussed. Figure 4.13 depicts the state space plot of volume normalised L2-norms of velocity and temperature. It reveals a number of heteroclinic orbits, connecting the base state (\bullet), stable ($\textcolor{green}{\bullet}$) and unstable ($\textcolor{red}{\bullet}$) ISRs. Figure 4.13(a) exhibits several solution trajectories linking the base state, stable and unstable ISRs: three orbits connecting the base state to all the stable and unstable ISRs shown, one from the ISR of $q = 3.5/d$ to that of $q = 2.5/d$, and one from the ISR of $q = 5.0/d$ to that of $q = 3.5/d$. Here, caution will need to be taken in interpreting each of the connections as a heteroclinic orbit, because there appears to be an invariant state at which the speed of the solution trajectory nearly vanishes (a sign of the existence of unstable invariant states or ghost states Strogatz [2018]): for example, see the solution trajectory between the ISR of $q = 3.5/d$ to that of $q = 2.5/d$

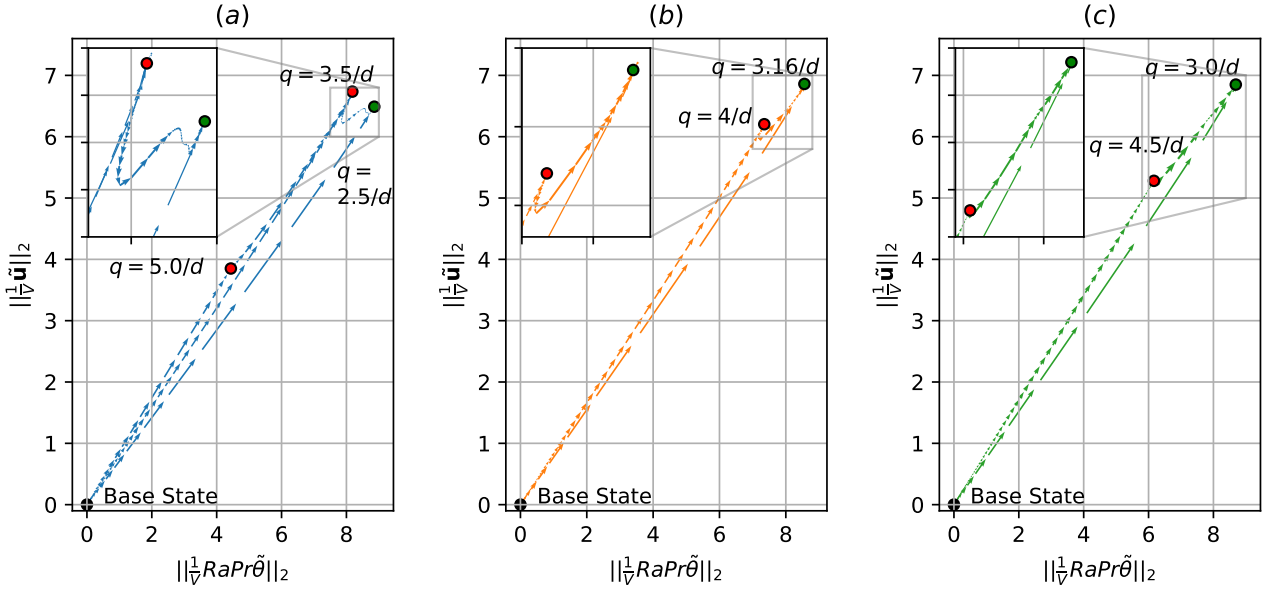


Figure 4.13: The phase-space solution trajectories connecting: (a) unstable base (conductive) state between 10 unstable rolls ($q = 5/d$), 7 unstable rolls ($q = 3.5/d$) and 5 stable rolls ($q = 2.5/d$); (b) unstable base (conductive) state between 8 unstable rolls ($q = 5/d$) and 6 stable rolls ($q = 3.16/d$); (c) unstable base (conductive) state between 9 unstable rolls ($q = 4.5/d$) and 6 stable rolls ($q = 3/d$). Here, the size of the arrows indicates the speed of the solution trajectory (or flow).

(in the inset of figure 4.13(a)), which will be discussed below with figure 4.14. Starting from the primary base state, the system saturates into an ISR of wavenumber $q = 5.0/d$. Since this ISR is linearly unstable, it evolves into another unstable ISR of $q = 3.5/d$, before ultimately stabilising into an ISR of $q = 2.5/d$. Next, figure 4.13(b) shows three solution trajectories connecting the base state, an unstable and stable ISR. Starting from the base state, the system transitions into an unstable ISR of $q = 4/d$ before stabilising into an ISR of $q = 3.16/d$. Lastly, figure 4.13(c) presents three solution trajectories connecting the base state, a stable and unstable ISR. Starting from the base state, it can evolve to an unstable ISR of $q = 4.5/d$ before settling into a stable ISR of $q = 3.0/d$. Figure 4.13 suggests that each of the stable ISRs within the Busse balloon has the basin of attraction, characterised by a web of heteroclinic orbits connecting some of the unstable ISRs outside of the Busse balloon. It is worth emphasising that the connections between the solutions presented here were obtained by time-integrating the dominant unstable manifolds of ISRs. In practice, there are many more unstable manifolds (see table 4.2) which have not been presented, potentially leading to more complex networks of heteroclinic orbits that form the basin of attraction for each stable ISR.

Figure 4.14 describes the asymptotic behaviour with the most unstable eigenmode for $q = 3.5/d$ (table 4.2(a)) in detail, corresponding to the connection between the unstable ISR of $q = 3.5/d$ and the stable ISR of $q = 2.5/d$ in figure 4.13(a). To observe the linear instability defined in Eq. (4.9), we report contribution of modal energy (figure 4.14(a)) as

$$E_k(t) = \frac{1}{2} \int_{\Omega} |\hat{u}_k(t)|^2 d\Omega, \quad (4.10)$$

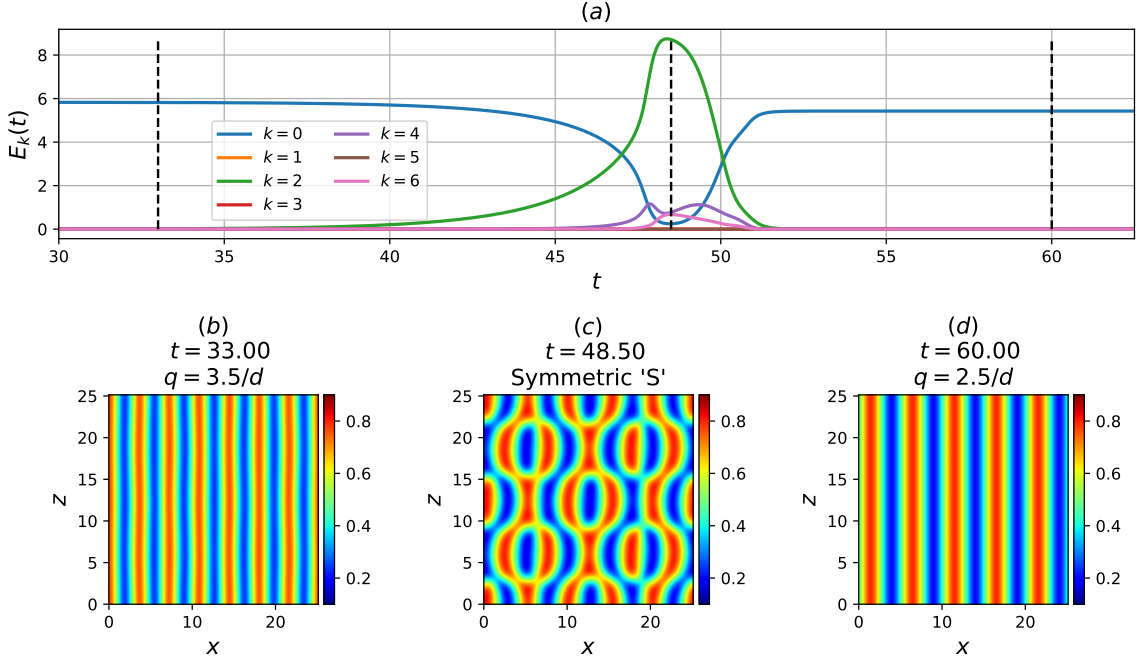


Figure 4.14: Asymptotic behaviour of the linear instability ($\hat{q}_{\beta=0.50}$) about unstable ISR $q = 3.5/d$. (a) Modal energy $E_k(t)$, and temperature snapshots, $\theta(x, z)|_{y=d/2}$ at (b) $t = 33$, (c) $t = 48.5$, (d) $t = 60$.

where $\hat{\mathbf{u}}_k$ refers to the k -th Fourier coefficient in z -direction. Initially, the simulation starts from the ISR state of 7 rolls ($t = 33$), corresponding to a roll-wavenumber of $q = 3.5/d$. The unstable eigenmode $\hat{s}_{\beta=0.50}$ grows exponentially before peaking at $t = 48.50$, forming an ‘S’-liked symmetric state (figure 4.14(c)). Note that, at this point, the time derivative of $E_k(t)$ nearly vanishes, indicating that the snapshot taken at $t = 48.50$ is potentially close to an unstable invariant state. Finally, the modal energy of $N_z = 2$ decays and the system settles into an ISR state of $q = 2.5/d$ (5 rolls aligned in the x -direction), which is within the Busse balloon.

Figure 4.15 illustrates the asymptotic behaviour with the most unstable eigenmode for $q = 4.0/d$ (table 4.2b), also depicted in the solution trajectory connecting the unstable ISR of $q = 4.0/d$ to the stable ISR of $q = 3.16/d$ in figure 4.13(b). Figure 4.15(a) shows the contribution of modal energy from each Fourier z component. From $t = 5 - 10$, the system experiences an exponential growth, guided by its dominant secondary eigenmode $\hat{s}_{\beta=0.50}$, where the 8 rolls ISRs ‘disintegrates’ into a convection pattern characterised by a symmetric ‘D’ convection pattern. Finally, the system stabilises into an ISR state with wavenumber $q = 3.16/d$.

Figure 4.16 presents the asymptotic behaviour with the most unstable eigenmode for $q = 4.5$ (table 4.2(c)), corresponding to the connection between the unstable ISR ($q = 4.5/d$) and the stable ISR ($q = 3/d$) in figure 4.13(c). Figure 4.16(a) shows the contribution of modal energy from each Fourier z component. Initially, the system begins as an ISR state of 9 rolls ($t = 1.25$). Next, the secondary eigenmode $\hat{s}_{\beta=0.75}$ grows exponentially and peaks at $t = 4.50$, leading to an intermediate state characterised by a symmetric ‘O’ convection rolls with small $dE_k(t)/dt$ (fig 4.16(c)). Finally, the system evolved into an ISR state of $q = 3/d$ as an asymptotic state.

All three cases examined here show that the transition from an unstable ISR to a stable ISR involves

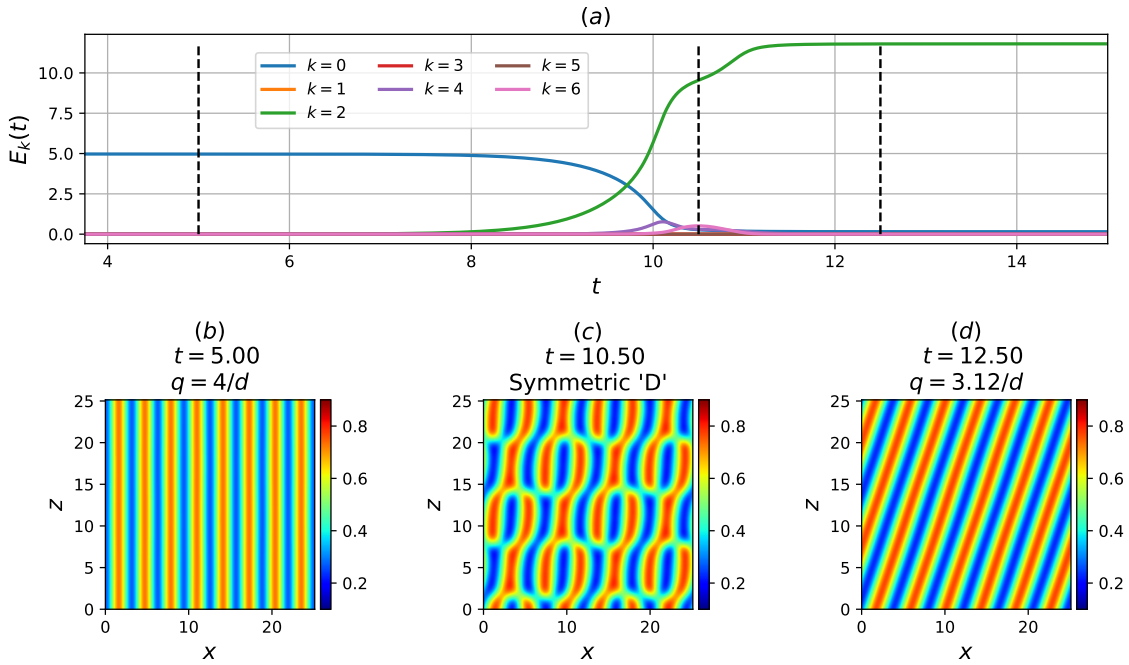


Figure 4.15: Asymptotic behaviour along the linear instability $\hat{s}_{\beta=0.50}$ about unstable ISR $q = 4.0/d$. (a) Modal energy $E_k(t)$, and temperature snapshots, $\theta(x, z)|_{y=d/2}$ at (b) $t = 5$, (c) $t = 10.5$, (d) $t = 12.5$.

an intermediate state, at which $dE_k(t)/dt$ is seen to be relatively small. In the transition pathway from the unstable to stable ISR, it is presumably that there exists an unstable equilibrium (i.e. fixed point/travelling-waves etc.) in the form of the original unstable ISR with its nonlinearly saturated instability, or ghost states [Strogatz \[2018\]](#). The existence of such a stationary solution can probably be computed with a typical Newton iteration or variational methods [[Viswanath, 2007](#), [Parker and Schneider, 2022](#)], beyond the scope of the present study. In any case, the numerical experiments here suggest that each of the stable ISR has a basin of attraction composed of a network of heteroclinic orbits involving connections between the base state and unstable ISRs.

4.5.2 Pathways leading to elementary states

Now, we discuss the asymptotic behaviour with linear instabilities of $\hat{s}_{\beta=1.25}$ and $\hat{s}_{\beta=1.75}$ about the unstable ISR of $q = 4.5/d$ (tab 4.2(d,e)). Contrary to the transitions presented in the previous section, the asymptotic states did not result in ISRs, but transient SDC before settling into an elementary state for case (e) (table 4.2(e)), and an elementary directly for case (d) (table 4.2(d)). The asymptotic behavior with $\hat{s}_{\beta=1.25}$ for unstable ISR $q = 4.5/d$ (table 4.2(d)) is presented in figure 4.17. At $t = 1.25$, the unstable ISR state ($q = 4.5/d$) is characterised by 9 rolls aligned along x direction. Subsequently, the state experiences the linear instability triggered ($t = 5$, figure 4.17(c)), shown as an exponential growth of the brown curve figure 4.17(a)), corresponding to the fifth Fourier modal energy (or $\beta = 1.25$). At $t = 6.75$, the system transitions into a saturated state temporarily (albeit unstable), characterised by square-like alternating convection patterns (figure 4.17(d)), and saturates briefly at $t = 8.75$, forming ‘S’-like convection patterns in figure 4.17(e). Finally, it settles into an

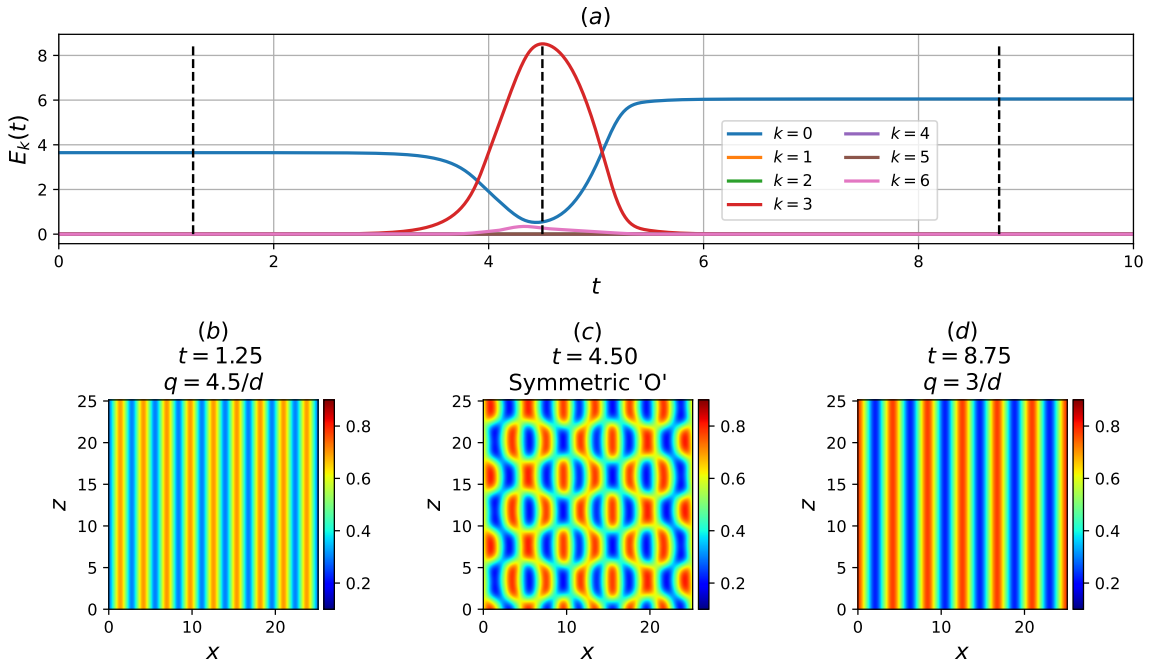


Figure 4.16: Asymptotic behaviour along the linear instability of $\hat{s}_{\beta=0.75}$ about unstable ISR of $q = 4.5/d$. (a) Modal energy $E_k(t)$, and temperature snapshots, $\theta(x, z)|_{y=d/2}$ at (b) $t = 1.25$, (c) $t = 4.50$, (d) $t = 8.75$.

oscillatory elementary state (i.e. stable periodic orbit) with an oscillation period of $T \approx 3.25$ (figures 4.17(f,g)).

The asymptotic behavior with $\hat{s}_{\beta=1.75}$ of unstable ISR $q = 4.5/d$ (table 4.2(e)) is presented in figure 4.18. Starting from $t = 1.25$, the unstable ISR state is characterised by 9 convection rolls aligned along the x -axis. The state experiences the linear instability imposed from $t = 1.25$ to $t = 7$, corresponding to an exponential growth in the grey curve ($E_7(t)$ in figure 4.18(a)), marked by cross-convection rolls in figure 4.18(c). Subsequently, the state exhibits a transient SDC behaviour from $t \approx 7$ to $t \approx 80$, characterised by an ‘O’-ring and ‘pac-man’ liked convection pattern illustrated in figure 4.18(d). Following this, the system stabilises into a short-period ($T \approx 1.8$) oscillatory behaviour between $t = 90$ and $t = 110$ (figure 4.18(e)), before transitioning into a long-period time-periodic state from $t = 110$ to $t = 201.75$ (figure 4.18(a) *cont.*), with a period of $T = 51.75$. The convection pattern appears to be travelling diagonally in the negative x - z directions (compare figures 4.18(f,g)), indicating that this state is a relative periodic orbit.

Figure 4.19 presents the state space trajectories of two pathways discussed above, represented by the volume-normalised L2-norms of velocity perturbations, temperature perturbations and Nusselt number. These trajectories are superimposed upon the state space trajectories of SDC (figures 4.1(a,b)), elementary states (figures 4.1(c-f)) and the fixed-point attractors of ISRs (figure 4.4). The purple trajectory represents the one along the linear instability direction (i.e. the unstable manifold) of $q = 4.5/d$ with $\beta = 1.25$. Originating from the unstable ISR ($q = 4.5/d$), briefly saturates at $\|\frac{1}{V}\tilde{\mathbf{u}}\| \approx 6.25$ and $\|\frac{1}{V}RaPr\tilde{\theta}\|_2 \approx 8$, before stabilising into a periodic orbit near the *spiral-defect* elementary state (see figure 4.1, represented by the orange trajectory in figure 4.4). The case of $q = 4.5/d$ along the linear instability direction for $\beta = 1.75$ is represented by the brown trajectory.

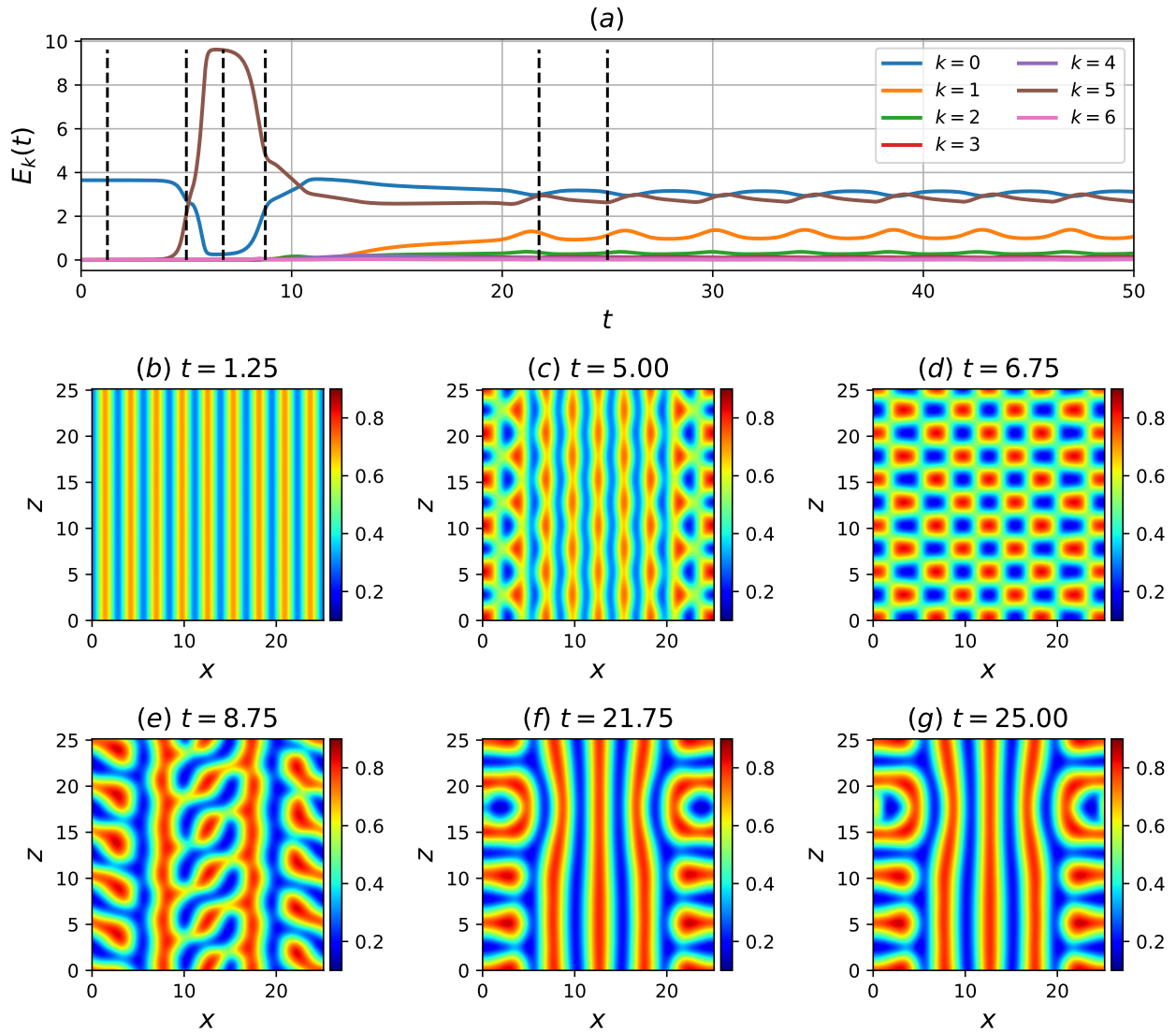


Figure 4.17: Asymptotic behaviour along the unstable manifold of $q = 4.5/d$, $\beta = 1.25$. (a) Modal energy $E_k(t)$ plot, and temperature snapshots $\theta(x, z)|_{y=d/2}$ at (b) $t = 1.25$, (c) $t = 5$, (d) $t = 6.75$, (e) $t = 8.75$, (f) $t = 21.75$ and (g) $t = 25$

Emanating from the unstable ISR ($q = 4.5/d$), the trajectory experiences a period of transient SDC behaviour in the vicinity of elementary states before converging onto a relative periodic orbit, as expected from figure 4.18. It is evident that the two trajectories arising from linear instabilities about the unstable ISR ($q = 4.5/d$) lie within the vicinity of SDC.

4.5.3 A pathway to SDC in an extended domain $\Gamma = 4\pi$

In §4.5.2, we have identified two distinct pathways to elementary states along some unstable manifolds from an unstable ISR. In particular, one of the trajectories evolved into transient SDC before stabilising into an elementary state. This is reminiscent of a chaotic saddle, but with a considerably short lifetime. The transient SDC behaviour observed within the minimal domain implies that if the same initial condition is added in an extended computational domain, it would trigger a chaotic state at least with a longer lifetime. This chaotic state is expected to be SDC in an extended domain, given the analysis in §4.5.2. To examine this hypothesis, we conduct a numerical simulation with an initial condition from the case of table 4.2(e) (i.e. the unstable ISR $q = 4.5/d$ with the instability mode of $\hat{s}_{\beta=1.75}$) in a domain twice larger than each horizontal direction ($\Gamma = 12.58$).

The solution trajectory along the unstable manifold, $s_{\beta=1.75}$, of ISR $q = 4.5/d$ in an extended domain ($\Gamma = 4\pi$) is presented in figure 4.20. The state, characterised by 18 convection rolls (figure 4.20(b)), experiences the linear instability from $t = 1.25$ to $t = 7$, marked by cross-convection rolls shown in figure 4.20(c). Subsequently, the state exhibits a prolonged period of chaotic behaviour, starting from $t = 7$ and lasting beyond $t = 200$. This is in stark contrast to the transient SDC behaviour observed in the minimal domain (figure 4.18), confirming the hypothesis above. Finally, it is interesting to note that the convection patterns of figures 4.20(f,g) contain localised structures that bear resemblance with the stationary *pac-man* (figure 4.1(c)) and oscillatory *peanut* (figure 4.1(f)) elementary states.

4.6 Concluding remarks

SDC has been considered one of the bistable states within a large spatial domain in Rayleigh-Bénard convection. However, existing studies have also shown the presence of multiple stable states in small and large domains, puzzling one's understanding of the bistable system in an extended spatial domain. Starting with numerical simulation in an extended domain ($\Gamma = 8\pi$), we have systematically reduced the computational domain, such that the fundamental patterns of SDC can be isolated. Through numerical experiments confined within a minimal domain of $\Gamma = 2\pi$, we have identified transient SDC before stabilising into a stable elementary states of SDC, and 14 different elementary states have been found in this way. From the conventional view of turbulence in shear flow, chaotic trajectories (representing turbulence) are expected to visit a set of unstable invariant solutions before eventually decaying to the base (laminar) state. However, in contrast to this expectation, the solution trajectory, once tangled into SDC stabilises into a non-trivial elementary state instead of returning to the base (ISR) state. This finding is new and challenges the understanding of transition from a dynamical system viewpoint. Despite this, the elementary states are still situated around the chaotic trajectories

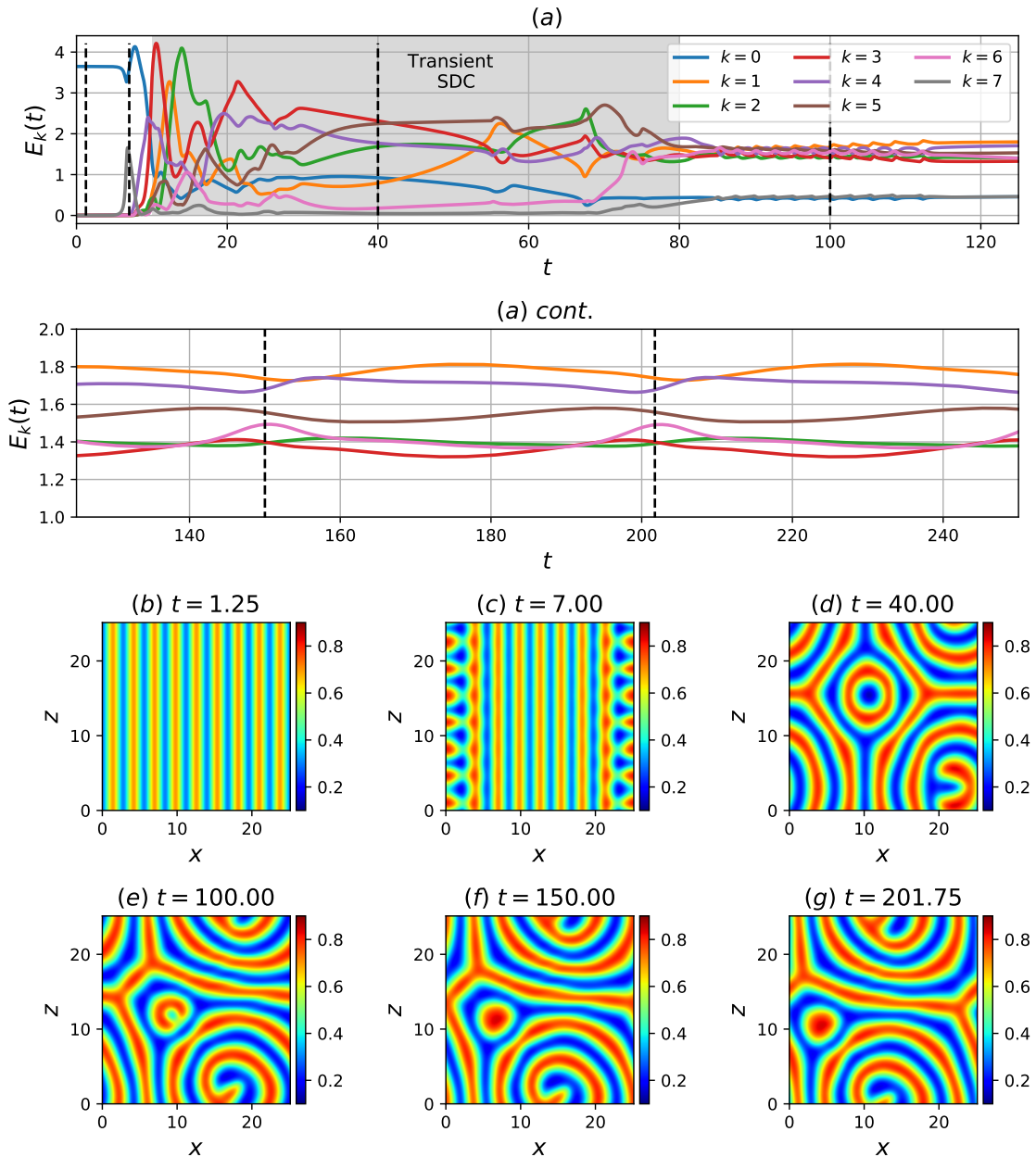


Figure 4.18: Asymptotic behaviour along the linear instability of $\hat{s}_{\beta=1.75}$ about unstable ISR $q = 4.5/d$. (a) Modal energy $E_k(t)$, and temperature snapshots $\theta(x, z)|_{y=d/2}$ at the onset of secondary instability at (b) $t = 1.25$, (c) $t = 7$, following a transient SDC behaviour at (d) $t = 40$, and settling into a elementary state at (e) $t = 100$, (f) $t = 150$ and (g) $t = 201.75$.

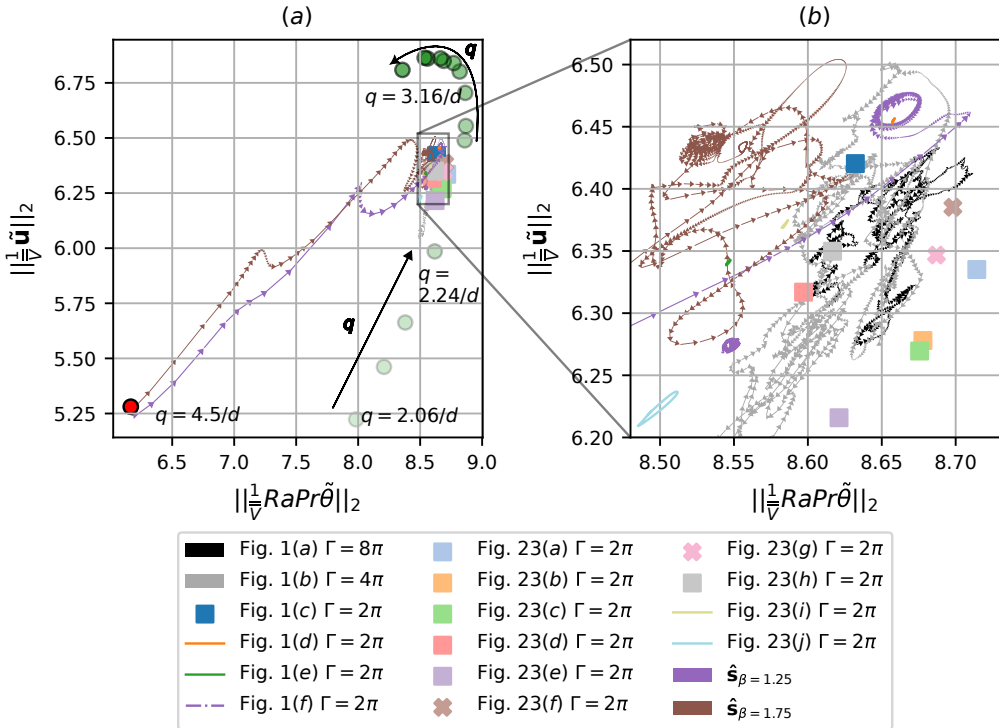


Figure 4.19: State space visualisations using (a) $\|\frac{1}{V}\tilde{\mathbf{u}}\|_2$ and $\|\frac{1}{V}RaPr\tilde{\theta}\|_2$, for SDC shown in figure 4.1(a,b), 4 elementary states shown in figures 4.1(c-f), linear instabilities (purple) $\hat{s}_{\beta=1.25}$, (brown) $\hat{s}_{\beta=1.75}$ about an unstable ISR $q = 4.5/d$ (figures 4.17, 4.18), and stable fixed-points of ISRs for wavenumber $q \in (2.0/d, 3.35/d)$ with the magnitude of q is depicted by the opacity of the filled symbol (●), with arrows denoting direction of increasing q . Figure (b) is a magnified plot of (a).

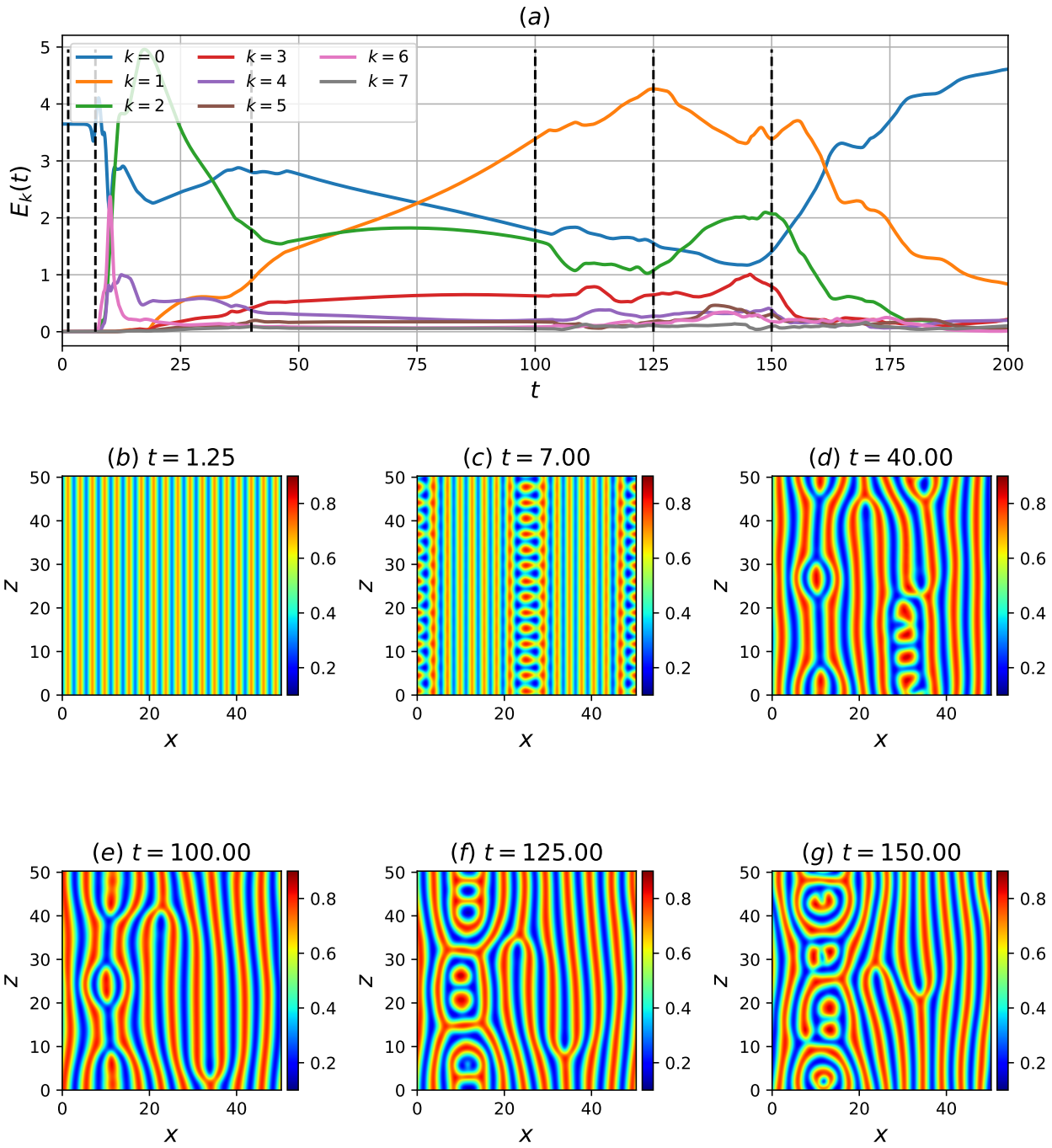


Figure 4.20: Asymptotic behaviour along the linear instability $\hat{s}_{\beta=1.75}$ about unstable ISR $q = 4.50/d$, in an extended domain $\Gamma = 4\pi$. (a) Modal energy $E_k(t)$, and temperature snapshots $\theta(x, z)|_{y=d/2}$, at (b) $t = 1.25$, (c) $t = 7$, (d) $t = 40$, (e) $t = 100$, (f) $t = 125$, (g) $t = 150$.

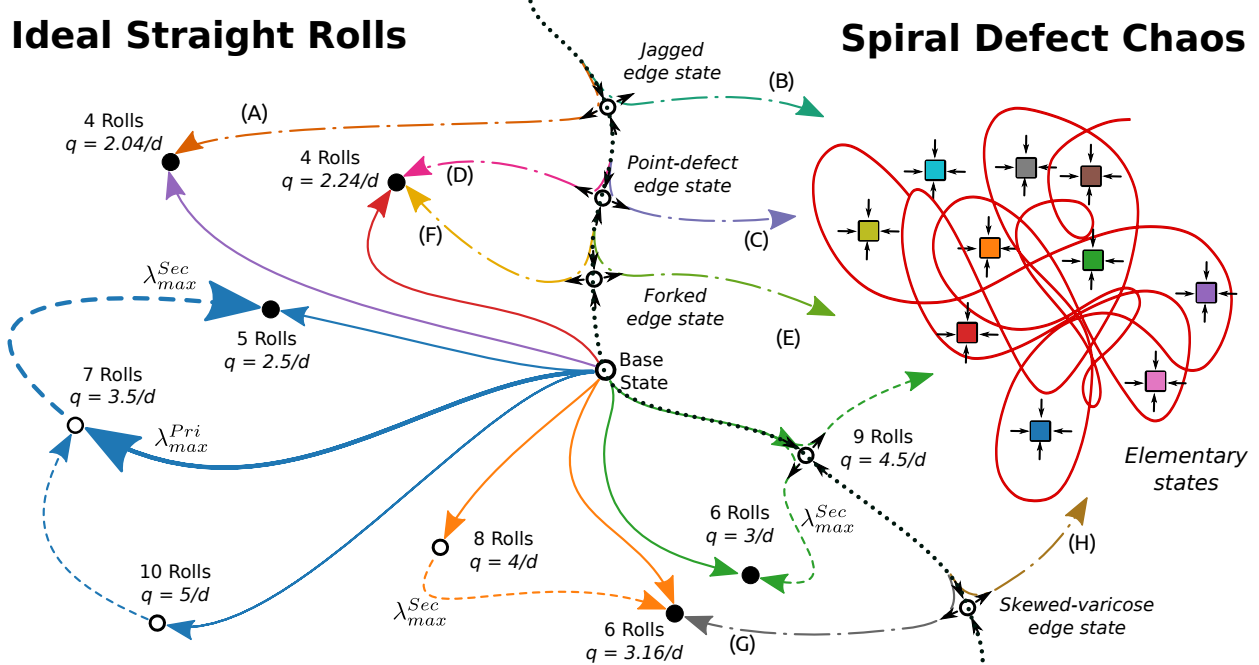


Figure 4.21: State space sketch containing the base, stable and unstable ISRs, edge, elementary states and SDC in a confined domain. Open circles, (\circ) and filled circles/squares (\bullet , \blacksquare) refer to unstable and stable states. Solid $(-)$ and dashed lines $(--)$ are the solution trajectories along the primary and secondary instabilities respectively, $\lambda_{max}^{Pri,Sec}$ refers to the most unstable primary and secondary linear instability manifolds. Blue, orange and green trajectories denote heteroclinic connections leading toward stable ISRs (trajectories labelled (A-G) and colors adapted from figure 4.13). Dashed-dotted trajectories $(-\cdot-)$ refer to solution trajectories emerging from the edge states (color-coded from figure 4.11). The dotted line (\cdots) represents the boundary between ISRs and SDC, consisting of many stable elementary states.

of SDC in the state space (figure 4.4), and their statistical properties (figure 4.5) are remarkably similar to those of SDC. This suggests that the computed elementary states may serve as ‘building block’ structures of SDC that interact with each other to form SDC in an extended domain.

To further understand the state space structure of SDC, ISRs and possible gateways toward SDC, we furnish a state space sketch of the solution trajectories connecting the base, stable and unstable ISRs, edge, elementary states and SDC, shown in figure 4.21. Starting from the base state, time-integrating along the unstable manifold guided by primary instabilities leads to either stable or unstable ISRs, denoted by solid trajectories. Notably, the most unstable primary instability leads to a 7 roll ISR ($q = 3.5/d$), before saturating into a stable 5 roll ISR ($q = 2.5/d$), following the most unstable secondary instability, depicted by dashed trajectories. These solution trajectories form a network of heteroclinic orbits, connecting the base state with stable ($q = 2.5/d$) and unstable ($q = 3.5/d, 5/d$) ISRs, represented in blue. Further from the boundaries of the Busse balloon, we have identified two more heteroclinic orbits that form a basin of attractor between the base state, and stable, unstable ISRs, labelled as a group of orange and green trajectories. These heteroclinic orbits are expected in experimental settings where initial conditions and background noise can be controlled precisely. In practice, where precise controls are inaccessible, it is more likely to observe SDC ($\Gamma = 4\pi, 8\pi$) or stable elementary states ($\Gamma = 2\pi$), which are embedded in the chaotic trajectories of SDC (see coloured ■), supporting the notion that SDC is underpinned by elementary states presumably interacting with each other. By examining the edge states between stable ISRs and elementary states, we have identified 4 edge states that lie on the boundary between stable ISRs and transient SDC, where the upper and lower trajectories emerging from their unstable manifold are represented by dash-dotted trajectories. Further from the Busse balloon, we have identified an unstable manifold of a 9 roll ($q = 4.5/d$) ISR, leading to the onset of SDC. Consequently, the unstable base state is also expected to lie on the boundary, as a controlled initial condition could guide the system toward the unstable 9-roll ISR, and subsequently the onset of SDC. Finally, the dotted line represents the boundary between ISRs and SDC, consisting of the base state, edge states and unstable 9 roll ISR ($q = 4.5/d$), illustrating four possible routes toward SDC. Although we have considered the unstable manifolds of ISRs for $\Gamma = 2\pi$, we acknowledge that the dimension of such manifolds depends on the domain size and that the presence of spatially subharmonic instabilities may arise as the domain size increases. Additionally, there may well be other unstable ISRs and edge states along the boundary. However, the investigation into the existence of such states is challenging due to the daunting computational efforts required. Recent advances, such as the framework proposed in [?], may help to accelerate linear stability analysis and facilitate further investigations.

Appendix A

Appendices

A.1 Non-dimensionalisation

The non-dimensionalised incompressible Navier-Stokes equations with Boussinesq approximations for buoyancy describe the motion of a fluid of RBP. where $\nabla^* = (\partial/\partial x^*, \partial/\partial y^*, \partial/\partial z^*)$ and t^* refer to the differential operators and time with dimensions in per unit space, m^{-1} , and time, s . $\mathbf{u}^*(\mathbf{x}^*), T(\mathbf{x}^*), p^*(\mathbf{x}^*)$ refers to the three-dimensional fluid velocity, temperature, pressure fields, in dimensional form, while T_0, \mathbf{f}_b refers to a reference temperature and body-forcing terms. To reduce the number of control parameters, we can suitably nondimensionalise the primitive variables by a velocity scale u_c , length scale, L_x , and time scale u_c/L_x , where u_c refers to the centreline velocity of a laminar flow and L_x refers to the streamwise length of the domain.

$\rho, \nu, \kappa, g, \gamma$ refers the fluid's density, kinematic viscosity and thermal diffusivity, gravity, thermal expansion coefficient, properties specific to a given a fluid. We note that that for a given pressure gradient, ΔP^* , a laminar centerline velocity forms as $w^*(y^*) = W_{lam}^*(1 - y^2/h^2)$. Here, we have a total of nine dimensional quantities $W_{lam}^*, \Delta T, h, \kappa, \nu, \rho, \gamma, g$ that describes the behaviour of the fluid motion. However, utilise the buckingham pi theorem where we can reduce the equations to less dependenc

A.2 Governing equations for Rayleigh-Bénard convection

The governing equations for Rayleigh-Bénard convection are the non-dimensionalised equations with the Boussinesq approximation for buoyancy-driven flow, given by

$$\frac{\partial \mathbf{u}}{\partial t} + (\mathbf{u} \cdot \nabla) \mathbf{u} = -\nabla p + Pr \nabla^2 \mathbf{u} + \frac{Ra Pr}{8} \theta \mathbf{j}, \quad (\text{A.1a})$$

$$\frac{\partial \theta}{\partial t} + (\mathbf{u} \cdot \nabla) \theta = \nabla^2 \theta, \quad (\text{A.1b})$$

$$\nabla \cdot \mathbf{u} = 0, \quad (\text{A.1c})$$

subjected to the following boundary conditions at the walls,

$$\mathbf{u}|_{y=\pm h} = 0, \quad \theta|_{y=-h} = 1, \quad \theta|_{y=h} = 0, \quad (\text{A.2a})$$

and the periodic boundary conditions imposed in the planar x and z directions. Here, t denotes the time scaled by the vertical thermal diffusion time, d^2/κ , and $\mathbf{x} (= (x, y, z))$ represents the spatial coordinates non-dimensionalised by depth, d . The horizontal directions are x and z , while y is the vertical direction. The velocity vector is given by $\mathbf{u} (= (u, v, w))$ and is scaled by thermal velocity, κ/d , p . The pressure is scaled by $\rho\kappa^2/d^2$, while $\theta (\equiv (T - T_U)/\Delta T)$ refers to the non-dimensional temperature with T being the absolute temperature, and \mathbf{j} denotes the unit vector in y -direction. The Rayleigh number Ra , and the Prandtl number, Pr , are defined as in §???. In this study, we set $Pr = 1$.

A.3 Projection methods for Navier-Stokes equations

In this section, we describe the projection methods for solving the incompressible Navier Stokes equations. The projection methods belong to a general class of splitting methods, where the solution step for obtaining the velocity and pressure from the incompressible Navier Stokes are uncoupled. The premise for being able to do this is because the pressure terms act as a Lagrange multiplier which enforces the incompressibility constraint. Suppose we want to find the function u that minimises the functional,

$$\min_{\mathbf{u} \neq 0} \frac{\nu}{2} (\nabla \mathbf{u}, \nabla \mathbf{u}) - (f, \mathbf{u}), \quad \text{s.t. } \nabla \cdot \mathbf{u} = 0 \quad (\text{A.3})$$

where $(\mathbf{x}, \mathbf{y}) = \int_{\Omega} \mathbf{x}^T \mathbf{y} d\Omega$ refers to a suitable inner product. To solve this optimisation problem, we use the method of Lagrange multipliers which handles the constrain, by converting the equation above into an unconstrained optimisation problem defined by the Lagrangian

$$\mathcal{L} = \frac{\nu}{2} (\nabla \mathbf{u}, \nabla \mathbf{u}) - (f, \mathbf{u}) - (p, \nabla \cdot \mathbf{u}) \quad (\text{A.4})$$

Taking the variation $\delta\mathcal{L}$, with respect $\delta\mathbf{u}$, we get

$$\frac{\delta\mathcal{L}}{\delta\mathbf{u}} = \nu(\nabla \mathbf{u}, \nabla \delta\mathbf{u}) - (f, \delta\mathbf{u}) - (p, \nabla \cdot \delta\mathbf{u}), \quad (\text{A.5})$$

$$= -\nu(\nabla^2 \mathbf{u}, \delta\mathbf{u}) - (f, \delta\mathbf{u}) + (\nabla p, \delta\mathbf{u}) \quad (\text{A.6})$$

$$= (-\nu\nabla^2 \mathbf{u} - f + \nabla p, \delta\mathbf{u}). \quad (\text{A.7})$$

and with respect to δp , we get,

$$-\frac{\delta\mathcal{L}}{\delta p} = (\delta p, \nabla \cdot \mathbf{u}). \quad (\text{A.8})$$

The optimal condition is defined by vanishing variations, hence, we recover the Stokes equations,

$$\nu\nabla^2 \mathbf{u} + \nabla p = -f \quad (\text{A.9a})$$

$$\nabla \cdot \mathbf{u} = 0 \quad (\text{A.9b})$$

In other words, the role of pressure is to serve as a constrain to enforce incompressibility, where we can consider a velocity field that is not divergence free, which is then corrected by pressure later - the splitting method. To witness this in action, we consider the basic approach of Chorin's projection which is a two step method,

$$\frac{\mathbf{u}^* - \mathbf{u}^n}{\Delta t} = -(\mathbf{u}^n \cdot \nabla) \mathbf{u}^n + \nu \nabla^2 \mathbf{u}^n \quad (\text{A.10a})$$

then,

$$\mathbf{u}^{n+1} = \mathbf{u}^* + \Delta t \nabla p^{n+1}. \quad (\text{A.10b})$$

The idea of projection stems of taking the weak formulation of the second equation with $\mathbf{v} \in \mathbf{V} := \mathbf{v} \in H_0^1(\Omega) : \nabla \cdot \mathbf{v} = 0$,

$$(\mathbf{u}^*, \mathbf{v}) = (\mathbf{u}^{n+1}, \mathbf{v}) + (\nabla p^{n+1}, \mathbf{v}) \quad (\text{A.11})$$

Taking integration by parts we get,

$$(\mathbf{u}^*, \mathbf{v}) = (\mathbf{u}^{n+1}, \mathbf{v}) - \underbrace{(\nabla p^{n+1}, \nabla \cdot \mathbf{v})}_{=0}, \quad (\text{A.12})$$

Hence,

$$(\mathbf{u}^*, \mathbf{v}) = (\mathbf{u}^{n+1}, \mathbf{v}) \quad (\text{A.13})$$

A.4 Simulation parameters for Ra - Re sweep

The spectral/ hp quadrilateral element width, heights and polynomial order are kept constant for all simulations, $(\Delta x, \Delta y|_{y=\pm h}, \Delta y|_{y=0}, P) = (0.1\pi, 0.0549, 0.367, 4)$. To resolve the high gradients, the quadrilateral element heights are bunched near the wall, $\Delta y|_{y=\pm h}$, and expanded in the channel center, $\Delta y|_{y=0}$. The basis type employed here consists of the modified Jacobi polynomials, known as the *modified* basis [?]. Table A.1 describes the number of Fourier expansions, N_z , and temporal resolution of 52 numerical experiments at $Re = 0, 0.1, 1, 10, 100, 500, 750, 1000, 1050, 2000$, and $Ra = 0, 2000, 3000, 5000, 8000, 10000$ with $Pr = 1$ and a large aspect ratio, $\Gamma = 4\pi$. The initial conditions of all numerical experiments were sampled from a statistically stationary solution based on the time history of the Nusselt number and shear. The laminar solution obtained for $Ra = 0$, $Re \leq 1000$ has been omitted in table A.1.

Ra	Re	N_z	dt	T	$\frac{d}{\kappa}$
0	1050	64	0.1	8000	-
0	2000	128	0.02	3000	-
2000	0	64	0.05	50	25
2000	0.1	64	0.005	5	25
2000	1	64	0.01	50	25
2000	10	64	0.05	50	2.5
2000	100	64	0.1	50	0.25
2000	500	64	0.1	50	0.05
2000	750	64	0.1	50	0.033
2000	1000	64	0.1	50	0.025
2000	1050	64	0.1	8000	3.81
2000	2000	128	0.02	2800	0.75
3000	0	64	0.05	3000	1500
3000	0.1	64	0.005	300	1500
3000	1	64	0.05	100	50
3000	10	64	0.05	50	2.5
3000	100	64	0.1	10000	50
3000	500	64	0.1	50	0.05
3000	750	64	0.1	50	0.033
3000	1000	64	0.1	50	0.025
3000	1050	64	0.1	8000	3.81
3000	2000	128	0.02	2800	0.75
5000	0	64	0.005	1200	600
5000	0.1	64	0.001	800	4000
5000	1	64	0.01	2500	1250
5000	10	64	0.05	500	25
5000	100	64	0.1	1000	5
5000	500	64	0.05	8000	8
5000	750	64	0.05	8000	5.33
5000	1000	64	0.02	8000	4
5000	1050	64	0.02	8000	3.81
5000	2000	128	0.02	2800	0.75
8000	0	64	0.0025	600	300
8000	0.1	64	0.0005	600	3000
8000	1	64	0.005	600	300
8000	10	64	0.05	500	25
8000	100	64	0.1	5000	25
8000	500	64	0.05	10000	10
8000	750	64	0.05	8000	5.33
8000	1000	64	0.02	8000	4
8000	1050	64	0.02	8000	3.81
8000	2000	128	0.02	2800	0.75
10000	0	64	0.0025	1000	500
10000	0.1	64	0.00025	800	4000
10000	1	64	0.0025	600	300
10000	10	64	0.05	12000	600
10000	100	64	0.1	8000	40
10000	500	64	0.05	8000	8
10000	750	64	0.05	8000	5.33
10000	1000	64	0.02	8000	4
10000	1050	64	0.02	8000	3.81
10000	2000	128	0.02	2800	0.75

Table A.1: The summary of the spatial and temporal resolution for a given Re , Ra . N_z denotes the number of Fourier expansions in the z -direction. $dt, T, d/\kappa$ denotes the timestep, final time and the final time scaled by the thermal timescale.

A.5 First- and second-order statistics of the buoyancy- and shear-driven regime

A.5.1 Buoyancy-driven regime

We present the first- and second-order statistics of the buoyancy-dominated regime (shaded in red), consisting of the (1) SDC & ISRs, and (2) ISRs states in figure A.1, illustrating its temporal and plane-averaged streamwise velocity, $\langle w \rangle_{x,z,t}$, temperature, $\langle \theta \rangle_{x,z,t}$, fluctuating wall-normal velocity squared normalised by thermal velocity scale, $\langle \tilde{v}\tilde{v} \rangle_{x,z,t}/u_\kappa^2$, fluctuating temperature squared, $\langle \tilde{\theta}\tilde{\theta} \rangle_{x,z,t}$ and fluctuating span- and streamwise velocities squared normalised by thermal velocity scale, $\langle \tilde{u}\tilde{u} + \tilde{w}\tilde{w} \rangle_{x,z,t}/u_\kappa^2$. We note that the fluctuating components are defined about a temporal-planar averaged quantity, i.e $\tilde{\mathbf{u}} = \mathbf{u} - \langle \mathbf{u} \rangle_{x,z,t}$. The mean temperature profiles (figure A.1(b)), and the fluctuating span- and streamwise velocities (figure A.1(f)) are visually similar for the same Ra , and are nearly independent of Re . However, we observe the dependence on Re at $Ra = 3000$ in the fluctuating temperature squared (figure A.1(d)), and fluctuating wall-normal velocities (figure A.1(c)), likely due to variations in convection structures, particularly in the convection roll wavenumbers. A detailed analysis of how the statistical properties vary with roll wavenumber is beyond the scope of this work. We propose that the underlying flow structure, consisting of convection rolls, describes the buoyancy-driven regime, shaded in red in figure 3.1. In this regime, the strength of the convection is primarily controlled by Ra , akin to RBC, and remains independent of Re .

A.5.2 Shear-driven regime

As Re falls within the range of $1050 \leq Re \leq 2000$, shear-driven turbulence dominates, where the impact of Ra on the first- and second-order statistics is weakly dependent on Ra in figure A.2. Figure A.2 describes the temporal and plane-averaged streamwise velocity, $\langle w \rangle_{x,z,t}$, temperature, $\langle \theta \rangle_{x,z,t}$, fluctuating streamwise velocity squared, $\langle \tilde{w}\tilde{w} \rangle_{x,z,t}$, fluctuating wall-normal velocity squared, $\langle \tilde{v}\tilde{v} \rangle_{x,z,t}$, fluctuating spanwise velocities squared, $\langle \tilde{u}\tilde{u} \rangle_{x,z,t}$, fluctuating Reynolds stresses $\langle \tilde{v}\tilde{w} \rangle_{x,z,t}$, and fluctuating temperature squared, $\langle \tilde{\theta}\tilde{\theta} \rangle_{x,z,t}$ at $Re = 2000, 1050$ for $Ra \in [0, 10000]$. The flow structures appear as uniform, featureless turbulence [?] at $Re = 2000$, independent of Ra . The spacetime figure of near-wall ($y^+ = 15$), wall-normal and spanwise perturbation kinetic energy, $\mathcal{E}_{u'+v'}$, at $Re = 2000$, $t \in [0, 2800]$, illustrating spatially uniform featureless turbulence, visually distinguishable with $Ra \in [0, 10000]$, corroborating with their Ra -independent first- and second-order statistics in figure A.2. In other words, the dominant physical mechanism is shear-driven turbulence at $Re = 2000$, independent of Ra .

As Re approaches $Re = 1050$, the midplane temperature in figure 3.1 shows regions of spatially localised structures, indicating the presence of turbulent-laminar bands, described in figure 3.3 and 3.4 later. The mean streamwise velocity and temperature gradients at both ends of the wall, and second-order statistics, are enhanced slightly from $Ra = 0$ to $Ra = 10000$. This enhancement could be due to the coexistence of longitudinal rolls with turbulent bands at $Ra = 10000$, discussed in §??. Notably, we have also included the statistics for a subcritical case ($Ra < Ra_{\parallel}$) at $Ra = 1000$,

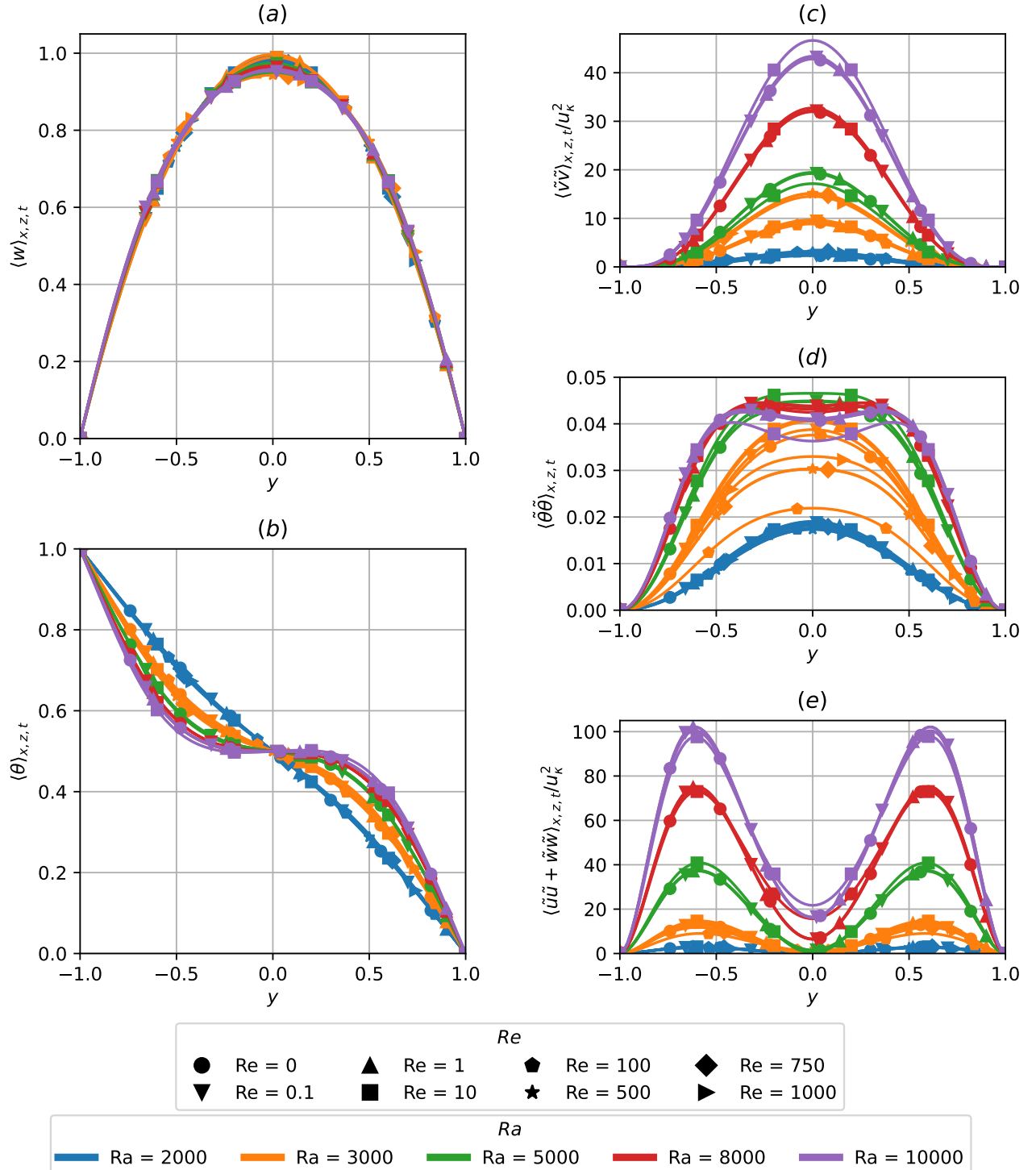


Figure A.1: The wall-normal distribution of temporal and plane- averaged (a) streamwise velocity, (b) temperature, (c) fluctuating wall-normal velocity squared normalised by thermal velocity scale, (d) fluctuating temperature squared and (e) fluctuating span- and streamwise velocities squared normalised by thermal velocity scale of buoyancy-driven regime shaded in red in figure 3.1.

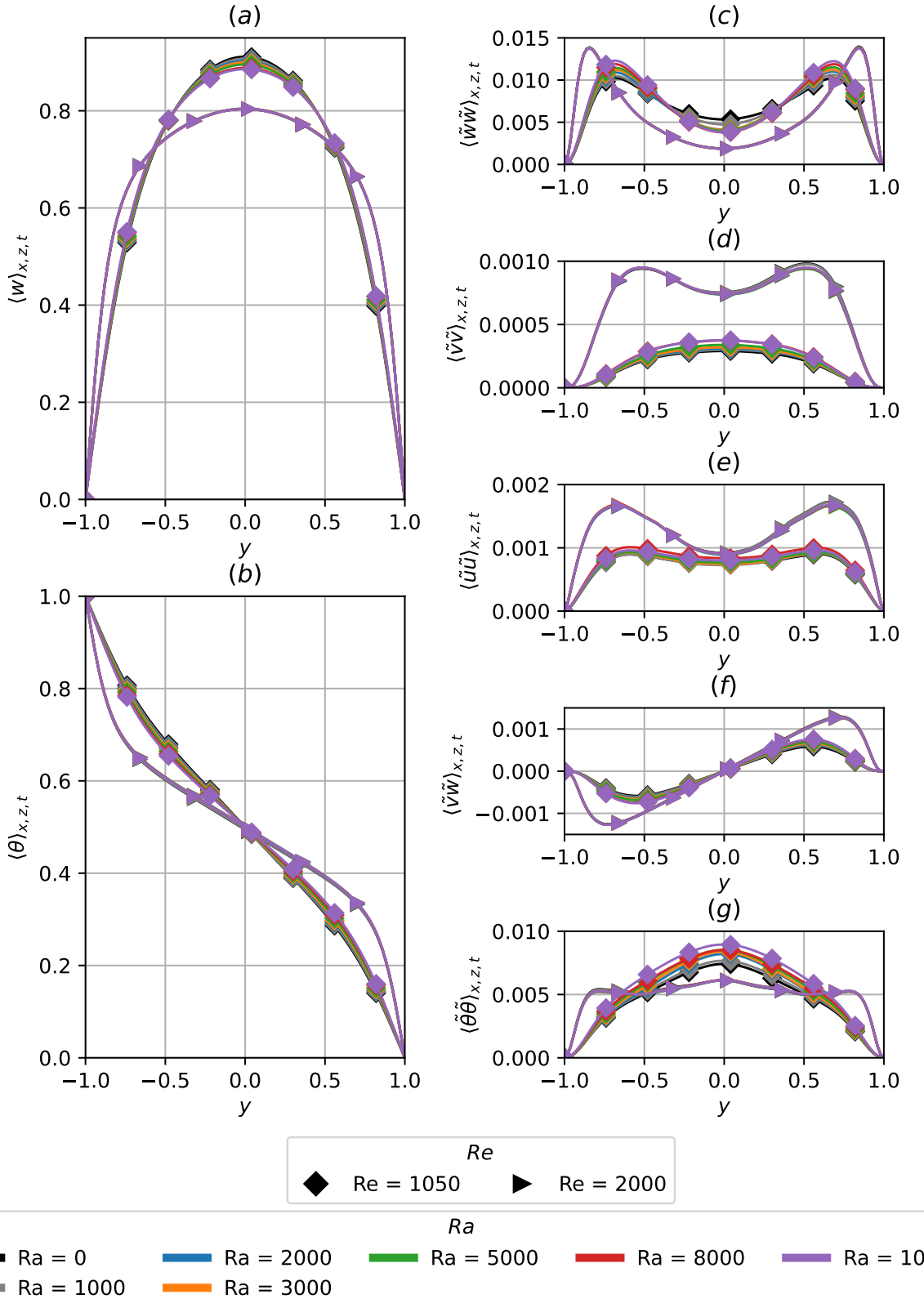


Figure A.2: The wall-normal distribution of temporal and plane- averaged (a) streamwise velocity, (b) temperature, (c) fluctuating streamwise velocity squared, (d) fluctuating wall-normal velocity squared, (e) fluctuating spanwise velocities squared, (f) fluctuating Reynolds stresses and (g) fluctuating temperature squared in the shear-driven regime shaded in blue in figure 3.1.

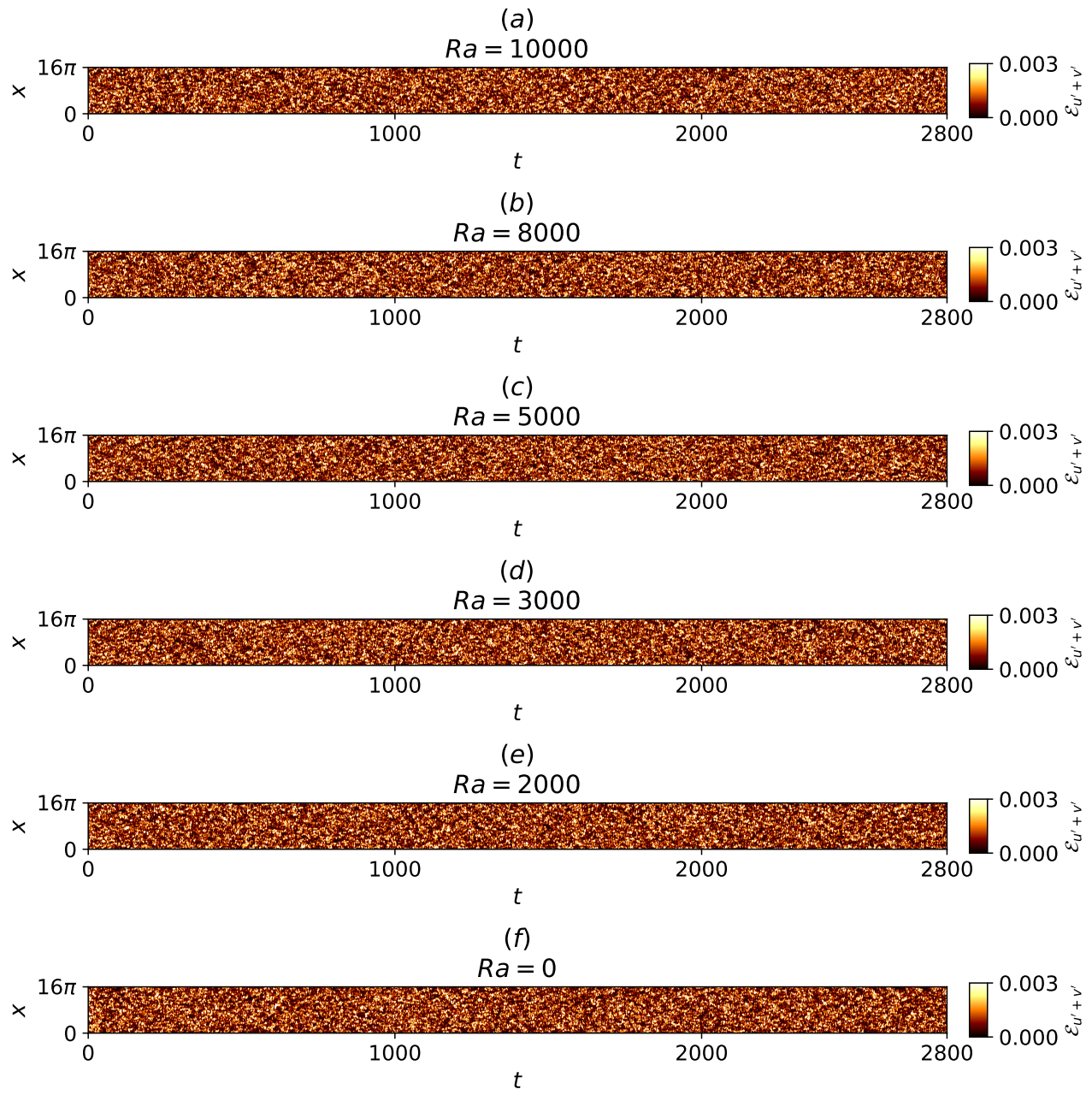


Figure A.3: Spacetime plots of near-wall, wall-normal and spanwise perturbation kinetic energy for $Re = 2000$, $t \in [0, 2800]$, $\Gamma = 4\pi$ at (a) $Ra = 10000$, (b) $Ra = 8000$, (c) $Ra = 5000$, (d) $Ra = 3000$, (e) $Ra = 2000$, (f) $Ra = 0$.

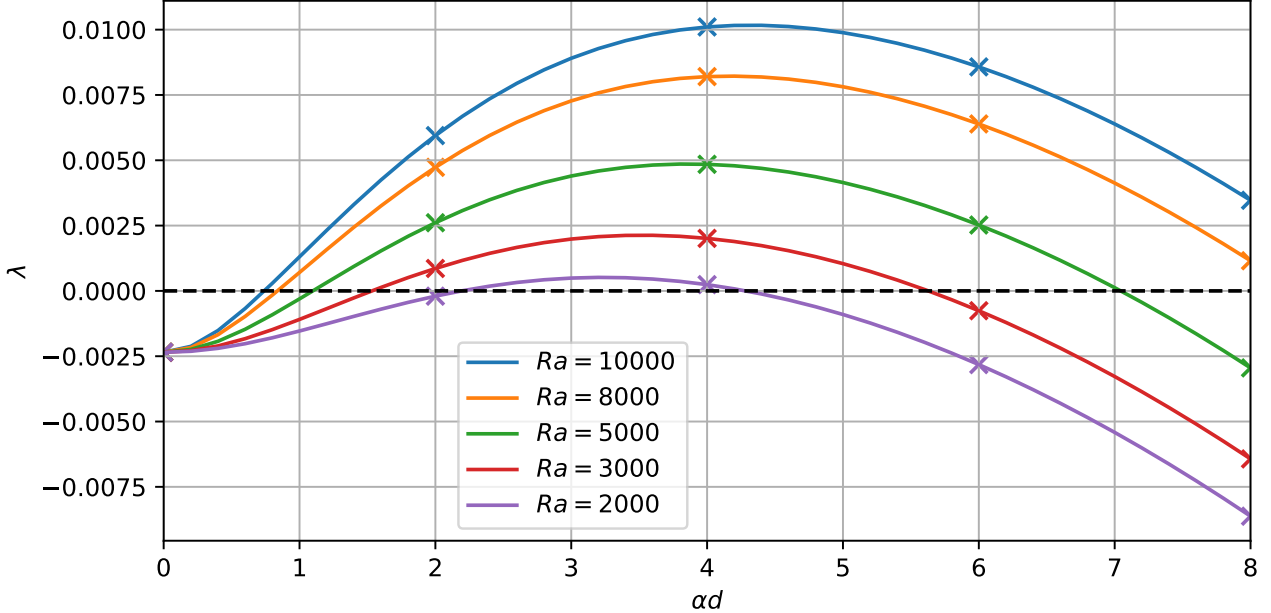


Figure A.4: Growth rates of primary instabilities at $Ra = 10000, 8000, 5000, 3000, 2000$ leading to the onset of longitudinal rolls against spanwise wavenumber of αd at $Re = 1050$.

indicating the presence of subcritical effects as the statistics are slightly enhanced from $Ra = 0$ to $Ra = 1000$, reported by ?. Nonetheless, there is a distinct change of state between $Re = 1000$ to 1050 (see figure 3.1), marked by the transition from the longitudinal/intermittent roll regime to shear-driven turbulence at $Re \geq 1050$, thus, shaded in blue in figure 3.1.

A.6 Growth rates of primary instabilities

Figure A.4 shows the eigenvalues of the primary instabilities as a function of its spanwise wavenumber αd , leading to the onset of longitudinal rolls at $Re = 1050$. The results are obtained using a Chebyshev-collocation method discretised by 51 Chebyshev polynomials [?]. The crosses denote the spanwise wavenumbers admissible within the domain $\Gamma = \pi/2$, where $\alpha d = 4$ corresponds to the dominant eigenmode.

A.7 Verification of linear stability analysis

Figure A.5 shows the eigenvalues as a function of spanwise wavenumber β of RBC at $\varepsilon = 0.7$. The results are obtained using Nektar++ and compared against a Chebyshev-collocation method discretised by 101 Chebyshev polynomials ?.

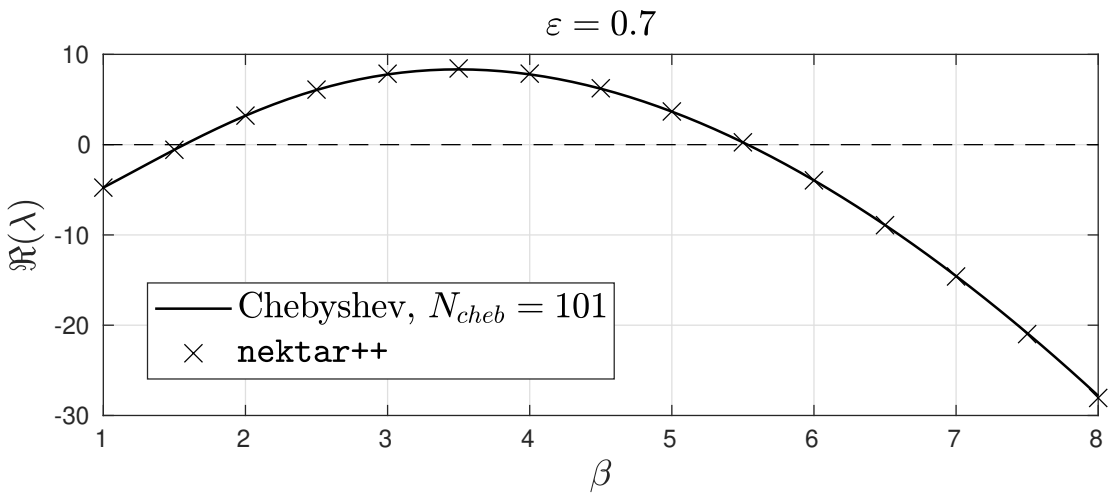


Figure A.5: Eigenvalues of primary instabilities of RBC at $\varepsilon = 0.7$ computed in Nektar++ compared against a Chebyshev-collocation method with 101 Chebyshev expansions.

A.8 Other elementary states and ISRs

Figure A.6 presents snapshots of temperature slices ($\theta(x, z)|_{d/2}$), depicting ten distinct elementary states. These states are obtained within a minimal domain $\Gamma = 2\pi$, consisting of eight stationary states (figures A.6(a-h)) and two travelling-wave states (figures A.6(i,j)). Figure A.7 features a snapshot of fourteen ideal straight rolls (ISRs), and they satisfy rotational symmetry about the y -axis and mirror symmetries about the x - and z -axes due to the horizontal isotropy of the present system. These ISRs represent stable fixed-points in the state space of figures 4.3, 4.4, 4.11, 4.19.

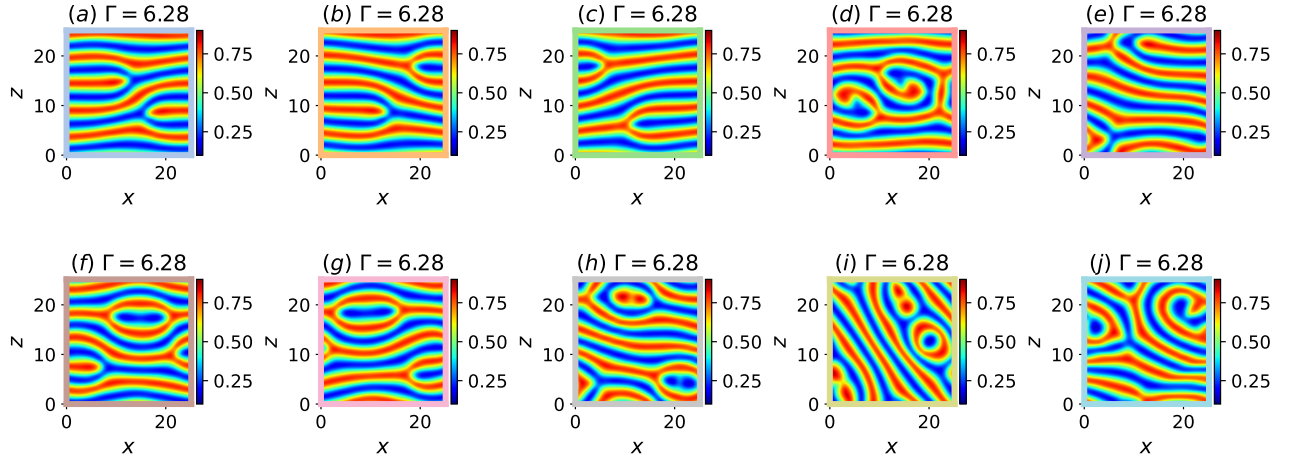


Figure A.6: Temperature snapshots, $\theta(x, z)|_{y=d/2}$, of 10 elementary states confined within a minimal domain $\Gamma = 2\pi$: (a) steady ‘forked-A’ state, (b) steady ‘forked-B’ state, (c) steady ‘forked-c’ state, (d) steady ‘twin-armed’ state, (e) steady ‘tri-rolls’ state, (f) travelling-wave ‘O-a’ state, (g) travelling-wave ‘O-b’ state, (h) steady ‘keyhole’ state, (i) relative periodic orbit ‘eye’ state, (j) relative periodic orbit ‘S’ state

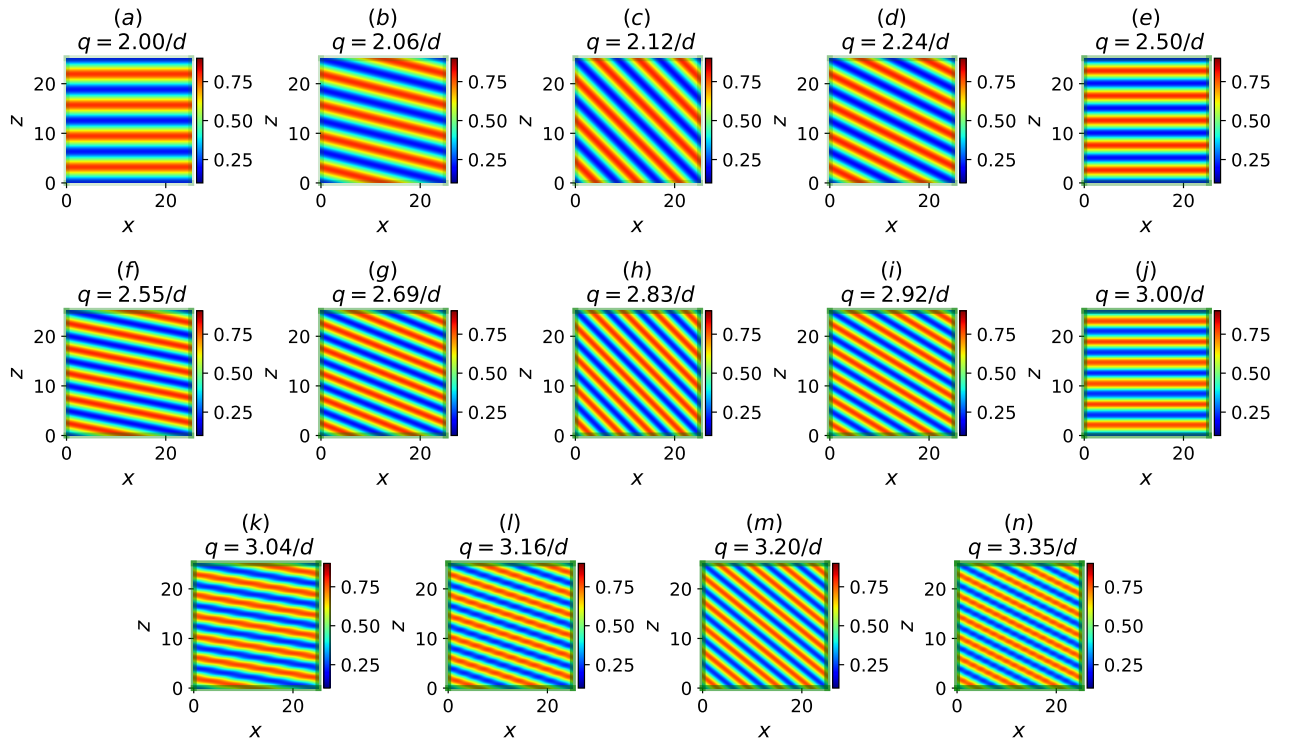


Figure A.7: Temperature snapshots, $\theta(x, z)|_{y=d/2}$, of 14 stable ideal straight rolls (ISRs) confined within a minimal domain, $\Gamma = 6.28$. Plots (a-n) are ordered in increasing wavenumbers, $q \in (2/d, 3.35/d)$.

Bibliography

H. Affan and R. Friedrich. Spiral defect chaos in an advection-reaction-diffusion system. *Physical Review E*, 89(6):062920, June 2014. ISSN 1539-3755, 1550-2376. doi: 10.1103/PhysRevE.89.062920. URL <https://link.aps.org/doi/10.1103/PhysRevE.89.062920>.

Guenter Ahlers. Experiments on spatio-temporal chaos.

Mitsunobu Akiyama, Guang-Jyh Hwang, and KC Cheng. Experiments on the onset of longitudinal vortices in laminar forced convection between horizontal plates. 1971. ISSN 0022-1481.

Edward Anderson, Zhaojun Bai, Christian Bischof, L Susan Blackford, James Demmel, Jack Dongarra, Jeremy Du Croz, Anne Greenbaum, Sven Hammarling, and Alan McKenney. *LAPACK users' guide*. SIAM, 1999. ISBN 0-89871-447-8.

Walter Edwin Arnoldi. The principle of minimized iterations in the solution of the matrix eigenvalue problem. *Quarterly of applied mathematics*, 9(1):17–29, 1951. ISSN 0033-569X.

Kerstin Avila, David Moxey, Alberto De Lozar, Marc Avila, Dwight Barkley, and Björn Hof. The Onset of Turbulence in Pipe Flow. *Science*, 333(6039):192–196, July 2011. ISSN 0036-8075, 1095-9203. doi: 10.1126/science.1203223. URL <https://www.science.org/doi/10.1126/science.1203223>.

Marc Avila, Ashley P. Willis, and Björn Hof. On the transient nature of localized pipe flow turbulence. *Journal of Fluid Mechanics*, 646:127–136, March 2010. ISSN 0022-1120, 1469-7645. doi: 10.1017/S0022112009993296. URL https://www.cambridge.org/core/product/identifier/S0022112009993296/type/journal_article.

Marc Avila, Dwight Barkley, and Björn Hof. Transition to Turbulence in Pipe Flow. *Annual Review of Fluid Mechanics*, 55(1):575–602, January 2023. ISSN 0066-4189, 1545-4479. doi: 10.1146/annurev-fluid-120720-025957. URL <https://www.annualreviews.org/doi/10.1146/annurev-fluid-120720-025957>.

Kapil M. S. Bajaj, David S. Cannell, and Guenter Ahlers. Competition between spiral-defect chaos and rolls in Rayleigh-Bénard convection. *Physical Review E*, 55(5):R4869–R4872, May 1997. ISSN 1063-651X, 1095-3787. doi: 10.1103/PhysRevE.55.R4869. URL <https://link.aps.org/doi/10.1103/PhysRevE.55.R4869>.

D. Barkley, H. M. Blackburn, and S. J. Sherwin. Direct optimal growth analysis for timesteppers. *International Journal for Numerical Methods in Fluids*, 57(9):1435–1458, July 2008. ISSN 0271-2091, 1097-0363. doi: 10.1002/fld.1824. URL <https://onlinelibrary.wiley.com/doi/10.1002/fld.1824>.

Dwight Barkley and Laurette S. Tuckerman. Computational Study of Turbulent Laminar Patterns in Couette Flow. *Physical Review Letters*, 94(1):014502, January 2005. doi: 10.1103/PhysRevLett.94.014502. URL <https://link.aps.org/doi/10.1103/PhysRevLett.94.014502>. Publisher: American Physical Society.

Dwight Barkley and Laurette S Tuckerman. Mean flow of turbulent–laminar patterns in plane Couette flow. *Journal of Fluid Mechanics*, 576:109–137, 2007. ISSN 1469-7645. Publisher: Cambridge University Press.

Myron J. Block. Surface Tension as the Cause of Bénard Cells and Surface Deformation in a Liquid Film. *Nature*, 178(4534):650–651, September 1956. ISSN 0028-0836, 1476-4687. doi: 10.1038/178650a0. URL <https://www.nature.com/articles/178650a0>.

Eberhard Bodenschatz, David S. Cannell, John R. De Bruyn, Robert Ecke, Yu-Chou Hu, Kristina Lerman, and Guenter Ahlers. Experiments on three systems with non-variational aspects. *Physica D: Nonlinear Phenomena*, 61(1-4):77–93, December 1992. ISSN 01672789. doi: 10.1016/0167-2789(92)90150-L. URL <https://linkinghub.elsevier.com/retrieve/pii/016727899290150L>.

Eberhard Bodenschatz, Werner Pesch, and Guenter Ahlers. Recent Developments in Rayleigh-Bénard Convection. *Annual Review of Fluid Mechanics*, 32(1):709–778, January 2000. ISSN 0066-4189, 1545-4479. doi: 10.1146/annurev.fluid.32.1.709. URL <https://www.annualreviews.org/doi/10.1146/annurev.fluid.32.1.709>.

Katarzyna Borońska and Laurette S. Tuckerman. Extreme multiplicity in cylindrical Rayleigh-Bénard convection. I. Time dependence and oscillations. *Physical Review E*, 81(3):036320, March 2010a. ISSN 1539-3755, 1550-2376. doi: 10.1103/PhysRevE.81.036320. URL <https://link.aps.org/doi/10.1103/PhysRevE.81.036320>.

Katarzyna Borońska and Laurette S. Tuckerman. Extreme multiplicity in cylindrical Rayleigh-Bénard convection. II. Bifurcation diagram and symmetry classification. *Physical Review E*, 81(3):036321, March 2010b. ISSN 1539-3755, 1550-2376. doi: 10.1103/PhysRevE.81.036321. URL <https://link.aps.org/doi/10.1103/PhysRevE.81.036321>.

S Bottin, F Daviaud, P Manneville, and O Dauchot. Discontinuous transition to spatiotemporal intermittency in plane Couette flow. *Europhysics Letters (EPL)*, 43(2):171–176, July 1998. ISSN 0295-5075, 1286-4854. doi: 10.1209/epl/i1998-00336-3. URL <https://iopscience.iop.org/article/10.1209/epl/i1998-00336-3>.

N. Boullé, V. Dallas, and P. E. Farrell. Bifurcation analysis of two-dimensional Rayleigh-Bénard convection using deflation. *Physical Review E*, 105(5):055106, May 2022. ISSN 2470-0045, 2470-0053. doi: 10.1103/PhysRevE.105.055106. URL <https://link.aps.org/doi/10.1103/PhysRevE.105.055106>.

F. H. Busse. The oscillatory instability of convection rolls in a low Prandtl number fluid. *Journal of Fluid Mechanics*, 52(1):97–112, March 1972. ISSN 0022-1120, 1469-7645. doi: 10.1017/S0022112072002988. URL https://www.cambridge.org/core/product/identifier/S0022112072002988/type/journal_article.

F H Busse. Non-linear properties of thermal convection. *Reports on Progress in Physics*, 41(12):1929–1967, December 1978. ISSN 0034-4885, 1361-6633. doi: 10.1088/0034-4885/41/12/003. URL <https://iopscience.iop.org/article/10.1088/0034-4885/41/12/003>.

F. H. Busse. Transition to turbulence in Rayleigh-Beénard convection. In Harry L. Swinney and Jerry P. Gollub, editors, *Hydrodynamic Instabilities and the Transition to Turbulence*, volume 45, pages 97–137. Springer Berlin Heidelberg, Berlin, Heidelberg, 1981. ISBN 978-3-540-13319-3 978-3-540-38449-6. doi: 10.1007/3-540-13319-4_15. URL http://link.springer.com/10.1007/3-540-13319-4_15. Series Title: Topics in Applied Physics.

F. H. Busse and J. A. Whitehead. Instabilities of convection rolls in a high Prandtl number fluid. *Journal of Fluid Mechanics*, 47(2):305–320, May 1971. ISSN 0022-1120, 1469-7645. doi: 10.1017/S0022112071001071. URL https://www.cambridge.org/core/product/identifier/S0022112071001071/type/journal_article.

Kathryn M. Butler and Brian F. Farrell. Three-dimensional optimal perturbations in viscous shear flow. *Physics of Fluids A: Fluid Dynamics*, 4(8):1637–1650, August 1992. ISSN 0899-8213. doi: 10.1063/1.858386. URL <https://pubs.aip.org/pof/article/4/8/1637/402702/Three-dimensional-optimal-perturbations-in-viscous>.

Henri Bénard. Les tourbillons cellulaires dans une nappe liquide. - Méthodes optiques d’observation et d’enregistrement. *Journal de Physique Théorique et Appliquée*, 10(1):254–266, 1901. ISSN 0368-3893. doi: 10.1051/jphystap:0190100100025400. URL <http://www.edpsciences.org/10.1051/jphystap:0190100100025400>.

Reha V. Cakmur, David A. Egolf, Brendan B. Plapp, and Eberhard Bodenschatz. Bistability and Competition of Spatiotemporal Chaotic and Fixed Point Attractors in Rayleigh-Bénard Convection. *Physical Review Letters*, 79(10):1853–1856, September 1997a. ISSN 0031-9007, 1079-7114. doi: 10.1103/PhysRevLett.79.1853. URL <https://link.aps.org/doi/10.1103/PhysRevLett.79.1853>.

Reha V. Cakmur, David A. Egolf, Brendan B. Plapp, and Eberhard Bodenschatz. Transition from Spatiotemporal Chaos to Ideal Straight Rolls in Rayleigh-Benard Convection, February 1997b. URL <http://arxiv.org/abs/patt-sol/9702003>. arXiv:patt-sol/9702003.

C.D. Cantwell, D. Moxey, A. Comerford, A. Bolis, G. Rocco, G. Mengaldo, D. De Grazia, S. Yakovlev, J.-E. Lombard, D. Ekelschot, B. Jordi, H. Xu, Y. Mohamied, C. Eskilsson, B. Nelson, P. Vos, C. Biotto, R.M. Kirby, and S.J. Sherwin. Nektar++: An open-source spectral/ h p element framework. *Computer Physics Communications*, 192:205–219, July 2015. ISSN 00104655. doi: 10.1016/j.cpc.2015.02.008. URL <https://linkinghub.elsevier.com/retrieve/pii/S0010465515000533>.

Philippe Carrière and Peter A. Monkewitz. Convective versus absolute instability in mixed Rayleigh–Bénard–Poiseuille convection. *Journal of Fluid Mechanics*, 384:243–262, April 1999. ISSN 0022-1120, 1469-7645. doi: 10.1017/S0022112098004145. URL https://www.cambridge.org/core/product/identifier/S0022112098004145/type/journal_article.

Subrahmanyan Chandrasekhar. The stability of spiral flow between rotating cylinders. *Philosophical Transactions of the Royal Society of London. Series A, Mathematical and Physical Sciences*, 263 (1135):57–91, May 1968. ISSN 0080-4614, 2054-0272. doi: 10.1098/rsta.1968.0006. URL <https://royalsocietypublishing.org/doi/10.1098/rsta.1968.0006>.

K.-H. Chiam, M. R. Paul, M. C. Cross, and H. S. Greenside. Mean flow and spiral defect chaos in Rayleigh-Bénard convection. *Physical Review E*, 67(5):056206, May 2003. ISSN 1063-651X, 1095-3787. doi: 10.1103/PhysRevE.67.056206. URL <https://link.aps.org/doi/10.1103/PhysRevE.67.056206>.

Alexandre Joel Chorin. A numerical method for solving incompressible viscous flow problems. *Journal of Computational Physics*, 2(1):12–26, August 1967. ISSN 00219991. doi: 10.1016/0021-9991(67)90037-X. URL <https://linkinghub.elsevier.com/retrieve/pii/002199916790037X>.

Douglas C. Chu and George Em Karniadakis. A direct numerical simulation of laminar and turbulent flow over riblet-mounted surfaces. *Journal of Fluid Mechanics*, 250:1–42, May 1993. ISSN 0022-1120, 1469-7645. doi: 10.1017/S0022112093001363. URL https://www.cambridge.org/core/product/identifier/S0022112093001363/type/journal_article.

R. M. Clever and F. H. Busse. Transition to time-dependent convection. *Journal of Fluid Mechanics*, 65(4):625–645, October 1974. ISSN 0022-1120, 1469-7645. doi: 10.1017/S0022112074001571. URL https://www.cambridge.org/core/product/identifier/S0022112074001571/type/journal_article.

R. M. Clever and F. H. Busse. Instabilities of longitudinal rolls in the presence of Poiseuille flow. *Journal of Fluid Mechanics*, 229(-1):517, August 1991. ISSN 0022-1120, 1469-7645. doi: 10.1017/S0022112091003142. URL http://www.journals.cambridge.org/abstract_S0022112091003142.

A. Cloot and G. Lebon. A nonlinear stability analysis of the Bénard–Marangoni problem. *Journal of Fluid Mechanics*, 145(-1):447, August 1984. ISSN 0022-1120, 1469-7645.

doi: 10.1017/S0022112084003013. URL http://www.journals.cambridge.org/abstract_S0022112084003013.

Vincent Croquette. Convective pattern dynamics at low Prandtl number: Part I. *Contemporary Physics*, 30(2):113–133, March 1989a. ISSN 0010-7514, 1366-5812. doi: 10.1080/00107518908225511. URL <http://www.tandfonline.com/doi/abs/10.1080/00107518908225511>.

Vincent Croquette. Convective pattern dynamics at low Prandtl number: Part II. *Contemporary Physics*, 30(3):153–171, May 1989b. ISSN 0010-7514, 1366-5812. doi: 10.1080/00107518908222594. URL <http://www.tandfonline.com/doi/abs/10.1080/00107518908222594>.

P Cvitanović and J F Gibson. Geometry of the turbulence in wall-bounded shear flows: periodic orbits. *Physica Scripta*, T142:014007, December 2010. ISSN 0031-8949, 1402-4896. doi: 10.1088/0031-8949/2010/T142/014007. URL <https://iopscience.iop.org/article/10.1088/0031-8949/2010/T142/014007>.

S. J. Davies and C. M. White. An experimental study of the flow of water in pipes of rectangular section. *Proceedings of the Royal Society of London. Series A, Containing Papers of a Mathematical and Physical Character*, 119(781):92–107, May 1928. ISSN 0950-1207, 2053-9150. doi: 10.1098/rspa.1928.0086. URL <https://royalsocietypublishing.org/doi/10.1098/rspa.1928.0086>.

R. B. Dean. Reynolds Number Dependence of Skin Friction and Other Bulk Flow Variables in Two-Dimensional Rectangular Duct Flow. *Journal of Fluids Engineering*, 100(2):215–223, June 1978. ISSN 0098-2202, 1528-901X. doi: 10.1115/1.3448633. URL <https://asmedigitalcollection.asme.org/fluidsengineering/article/100/2/215/409704/Reynolds-Number-Dependence-of-Skin-Friction-and>.

W. Decker, W. Pesch, and A. Weber. Spiral defect chaos in Rayleigh-Bénard convection. *Physical Review Letters*, 73(5):648–651, August 1994. ISSN 0031-9007. doi: 10.1103/PhysRevLett.73.648. URL <https://link.aps.org/doi/10.1103/PhysRevLett.73.648>.

Juan C. Del Álamo and Javier Jiménez. Linear energy amplification in turbulent channels. *Journal of Fluid Mechanics*, 559:205, July 2006. ISSN 0022-1120, 1469-7645. doi: 10.1017/S0022112006000607. URL http://www.journals.cambridge.org/abstract_S0022112006000607.

Lifang Dong, Fucheng Liu, Shuhua Liu, Yafeng He, and Weili Fan. Observation of spiral pattern and spiral defect chaos in dielectric barrier discharge in argon/air at atmospheric pressure. *Physical Review E*, 72(4):046215, October 2005. ISSN 1539-3755, 1550-2376. doi: 10.1103/PhysRevE.72.046215. URL <https://link.aps.org/doi/10.1103/PhysRevE.72.046215>.

Y. Duguet, A. P. Willis, and R. R. Kerswell. Transition in pipe flow: the saddle structure on the boundary of turbulence. *Journal of Fluid Mechanics*, 613:255–274, October 2008. ISSN 0022-

1120, 1469-7645. doi: 10.1017/S0022112008003248. URL https://www.cambridge.org/core/product/identifier/S0022112008003248/type/journal_article.

Y. Duguet, P. Schlatter, and D. S. Henningson. Formation of turbulent patterns near the onset of transition in plane Couette flow. *Journal of Fluid Mechanics*, 650:119–129, May 2010. ISSN 0022-1120, 1469-7645. doi: 10.1017/S0022112010000297. URL https://www.cambridge.org/core/product/identifier/S0022112010000297/type/journal_article.

Robert E. Ecke, Yuchou Hu, Ronnie Mainieri, and Guenter Ahlers. Excitation of Spirals and Chiral Symmetry Breaking in Rayleigh-Bénard Convection. *Science*, 269(5231):1704–1707, September 1995. ISSN 0036-8075, 1095-9203. doi: 10.1126/science.269.5231.1704. URL <https://www.science.org/doi/10.1126/science.269.5231.1704>.

Wiktor Eckhaus. *Studies in Non-Linear Stability Theory*, volume 6 of *Springer Tracts in Natural Philosophy*. Springer Berlin Heidelberg, Berlin, Heidelberg, 1965. ISBN 978-3-642-88319-4 978-3-642-88317-0. doi: 10.1007/978-3-642-88317-0. URL <http://link.springer.com/10.1007/978-3-642-88317-0>.

David A. Egolf, Ilarion V. Melnikov, and Eberhard Bodenschatz. Importance of Local Pattern Properties in Spiral Defect Chaos. *Physical Review Letters*, 80(15):3228–3231, April 1998. ISSN 0031-9007, 1079-7114. doi: 10.1103/PhysRevLett.80.3228. URL <https://link.aps.org/doi/10.1103/PhysRevLett.80.3228>.

David A. Egolf, Ilarion V. Melnikov, Werner Pesch, and Robert E. Ecke. Mechanisms of extensive spatiotemporal chaos in Rayleigh–Bénard convection. *Nature*, 404(6779):733–736, April 2000. ISSN 0028-0836, 1476-4687. doi: 10.1038/35008013. URL <https://www.nature.com/articles/35008013>.

T. Ellingsen and E. Palm. Stability of linear flow. *The Physics of Fluids*, 18(4):487–488, April 1975. ISSN 0031-9171. doi: 10.1063/1.861156. URL <https://pubs.aip.org/pfl/article/18/4/487/459138/Stability-of-linear-flow>.

Greg Evans and Ralph Greif. Unsteady three-dimensional mixed convection in a heated horizontal channel with applications to chemical vapor deposition. *International Journal of Heat and Mass Transfer*, 34(8):2039–2051, August 1991. ISSN 00179310. doi: 10.1016/0017-9310(91)90215-Z. URL <https://linkinghub.elsevier.com/retrieve/pii/001793109190215Z>.

Holger Faisst and Bruno Eckhardt. Traveling Waves in Pipe Flow. *Physical Review Letters*, 91(22):224502, November 2003. ISSN 0031-9007, 1079-7114. doi: 10.1103/PhysRevLett.91.224502. URL <https://link.aps.org/doi/10.1103/PhysRevLett.91.224502>.

Holger Faisst and Bruno Eckhardt. Sensitive dependence on initial conditions in transition to turbulence in pipe flow. *Journal of Fluid Mechanics*, 504:343–352, April 2004. ISSN 0022-1120, 1469-7645. doi: 10.1017/S0022112004008134. URL http://www.journals.cambridge.org/abstract_S0022112004008134.

Brian F. Farrell. Optimal excitation of perturbations in viscous shear flow. *The Physics of Fluids*, 31(8):2093–2102, August 1988. ISSN 0031-9171. doi: 10.1063/1.866609. URL <https://pubs.aip.org/pfl/article/31/8/2093/966463/Optimal-excitation-of-perturbations-in-viscous>.

Mitchell J Feigenbaum. The universal metric properties of nonlinear transformations. *Journal of Statistical Physics*, 21:669–706, 1979. ISSN 0022-4715. Publisher: Springer.

Ciprian Foias, George R Sell, and Roger Temam. Inertial manifolds for nonlinear evolutionary equations. *Journal of Differential Equations*, 73(2):309–353, June 1988. ISSN 00220396. doi: 10.1016/0022-0396(88)90110-6. URL <https://linkinghub.elsevier.com/retrieve/pii/0022039688901106>.

Keisuke Fukui, Masamoto Nakajima, and Hiromasa Ueda. The longitudinal vortex and its effects on the transport processes in combined free and forced laminar convection between horizontal and inclined parallel plates. *International Journal of Heat and Mass Transfer*, 26(1):109–120, January 1983. ISSN 00179310. doi: 10.1016/S0017-9310(83)80013-1. URL <https://linkinghub.elsevier.com/retrieve/pii/S0017931083800131>.

K. S. Gage and W. H. Reid. The stability of thermally stratified plane Poiseuille flow. *Journal of Fluid Mechanics*, 33(1):21–32, July 1968. ISSN 0022-1120, 1469-7645. doi: 10.1017/S0022112068002326. URL https://www.cambridge.org/core/product/identifier/S0022112068002326/type/journal_article.

Christophe Geuzaine and Jean-François Remacle. Gmsh: A 3-D finite element mesh generator with built-in pre- and post-processing facilities. *International Journal for Numerical Methods in Engineering*, 79(11):1309–1331, September 2009. ISSN 0029-5981, 1097-0207. doi: 10.1002/nme.2579. URL <https://onlinelibrary.wiley.com/doi/10.1002/nme.2579>.

J. F. Gibson, J. Halcrow, and P. Cvitanović. Visualizing the geometry of state space in plane Couette flow. *Journal of Fluid Mechanics*, 611:107–130, September 2008. ISSN 0022-1120, 1469-7645. doi: 10.1017/S002211200800267X. URL https://www.cambridge.org/core/product/identifier/S002211200800267X/type/journal_article.

J. F. Gibson, J. Halcrow, and P. Cvitanović. Equilibrium and travelling-wave solutions of plane Couette flow. *Journal of Fluid Mechanics*, 638:243–266, November 2009. ISSN 0022-1120, 1469-7645. doi: 10.1017/S0022112009990863. URL https://www.cambridge.org/core/product/identifier/S0022112009990863/type/journal_article.

J. P. Gollub and Harry L. Swinney. Onset of Turbulence in a Rotating Fluid. *Physical Review Letters*, 35(14):927–930, October 1975. ISSN 0031-9007. doi: 10.1103/PhysRevLett.35.927. URL <https://link.aps.org/doi/10.1103/PhysRevLett.35.927>.

Gene H Golub and Charles F Van Loan. *Matrix computations*. JHU press, 2013. ISBN 1-4214-0859-7.

Sébastien Gomé, Laurette S. Tuckerman, and Dwight Barkley. Statistical transition to turbulence in plane channel flow. *Physical Review Fluids*, 5(8):083905, August 2020. ISSN 2469-990X. doi: 10.1103/PhysRevFluids.5.083905. URL <https://link.aps.org/doi/10.1103/PhysRevFluids.5.083905>.

Michael D. Graham and Daniel Floryan. Exact Coherent States and the Nonlinear Dynamics of Wall-Bounded Turbulent Flows. *Annual Review of Fluid Mechanics*, 53(1):227–253, January 2021. ISSN 0066-4189, 1545-4479. doi: 10.1146/annurev-fluid-051820-020223. URL <https://www.annualreviews.org/doi/10.1146/annurev-fluid-051820-020223>.

M.D. Green, K.S. Kirilov, M. Turner, J. Marcon, J. Eichstädt, E. Laughton, C.D. Cantwell, S.J. Sherwin, J. Peiró, and D. Moxey. NekMesh: An open-source high-order mesh generation framework. *Computer Physics Communications*, 298:109089, May 2024. ISSN 00104655. doi: 10.1016/j.cpc.2024.109089. URL <https://linkinghub.elsevier.com/retrieve/pii/S0010465524000122>.

J. Halcrow, J. F. Gibson, P. Cvitanović, and D. Viswanath. Heteroclinic connections in plane Couette flow. *Journal of Fluid Mechanics*, 621:365–376, February 2009. ISSN 0022-1120, 1469-7645. doi: 10.1017/S0022112008005065. URL https://www.cambridge.org/core/product/identifier/S0022112008005065/type/journal_article.

James M. Hamilton, John Kim, and Fabian Waleffe. Regeneration mechanisms of near-wall turbulence structures. *Journal of Fluid Mechanics*, 287:317–348, March 1995. ISSN 0022-1120, 1469-7645. doi: 10.1017/S0022112095000978. URL https://www.cambridge.org/core/product/identifier/S0022112095000978/type/journal_article.

Ronald D. Henderson and Dwight Barkley. Secondary instability in the wake of a circular cylinder. *Physics of Fluids*, 8(6):1683–1685, June 1996. ISSN 1070-6631, 1089-7666. doi: 10.1063/1.868939. URL <https://pubs.aip.org/pof/article/8/6/1683/260183/Secondary-instability-in-the-wake-of-a-circular>.

Thorwald Herbert. PARABOLIZED STABILITY EQUATIONS. *Annual Review of Fluid Mechanics*, 29(1):245–283, January 1997. ISSN 0066-4189, 1545-4479. doi: 10.1146/annurev.fluid.29.1.245. URL <https://www.annualreviews.org/doi/10.1146/annurev.fluid.29.1.245>.

C.Q Hoard, C.R Robertson, and A Acrivos. Experiments on the cellular structure in bénard convection. *International Journal of Heat and Mass Transfer*, 13(5):849–856, May 1970. ISSN 00179310. doi: 10.1016/0017-9310(70)90130-4. URL <https://linkinghub.elsevier.com/retrieve/pii/0017931070901304>.

B. Hof, P. G. J. Lucas, and T. Mullin. Flow state multiplicity in convection. *Physics of Fluids*, 11(10):2815–2817, October 1999. ISSN 1070-6631, 1089-7666. doi: 10.1063/1.870178. URL <https://pubs.aip.org/pof/article/11/10/2815/254396/Flow-state-multiplicity-in-convection>.

Björn Hof, Jerry Westerweel, Tobias M. Schneider, and Bruno Eckhardt. Finite lifetime of turbulence in shear flows. *Nature*, 443(7107):59–62, September 2006. ISSN 0028-0836, 1476-4687. doi: 10.1038/nature05089. URL <https://www.nature.com/articles/nature05089>.

Eberhard Hopf. A mathematical example displaying features of turbulence. *Communications on Pure and Applied Mathematics*, 1(4):303–322, December 1948. ISSN 0010-3640, 1097-0312. doi: 10.1002/cpa.3160010401. URL <https://onlinelibrary.wiley.com/doi/10.1002/cpa.3160010401>.

M. Z. Hossain and J. M. Floryan. Drag reduction in a thermally modulated channel. *Journal of Fluid Mechanics*, 791:122–153, March 2016. ISSN 0022-1120, 1469-7645. doi: 10.1017/jfm.2016.42. URL https://www.cambridge.org/core/product/identifier/S0022112016000422/type/journal_article.

M. Z. Hossain and J. M. Floryan. On the role of surface grooves in the reduction of pressure losses in heated channels. *Physics of Fluids*, 32(8):083610, August 2020. ISSN 1070-6631, 1089-7666. doi: 10.1063/5.0018416. URL <https://pubs.aip.org/pof/article/32/8/083610/1060903/On-the-role-of-surface-grooves-in-the-reduction-of>.

M. Z. Hossain, D. Floryan, and J. M. Floryan. Drag reduction due to spatial thermal modulations. *Journal of Fluid Mechanics*, 713:398–419, December 2012. ISSN 0022-1120, 1469-7645. doi: 10.1017/jfm.2012.465. URL https://www.cambridge.org/core/product/identifier/S002211201200465X/type/journal_article.

Yuchou Hu, Robert Ecke, and Guenter Ahlers. Convection near threshold for Prandtl numbers near 1. *Physical Review E*, 48(6):4399–4413, December 1993. ISSN 1063-651X, 1095-3787. doi: 10.1103/PhysRevE.48.4399. URL <https://link.aps.org/doi/10.1103/PhysRevE.48.4399>.

Yuchou Hu, Robert Ecke, and Guenter Ahlers. Convection for Prandtl numbers near 1: Dynamics of textured patterns. *Physical Review E*, 51(4):3263–3279, April 1995. ISSN 1063-651X, 1095-3787. doi: 10.1103/PhysRevE.51.3263. URL <https://link.aps.org/doi/10.1103/PhysRevE.51.3263>.

Yuchou Hu, Robert E. Ecke, and Guenter Ahlers. Convection under rotation for Prandtl numbers near 1: Linear stability, wave-number selection, and pattern dynamics. *Physical Review E*, 55(6):6928–6949, June 1997. ISSN 1063-651X, 1095-3787. doi: 10.1103/PhysRevE.55.6928. URL <https://link.aps.org/doi/10.1103/PhysRevE.55.6928>.

Patrick Huerre and Peter A Monkewitz. Local and global instabilities in spatially developing flows. *Annual review of fluid mechanics*, 22(1):473–537, 1990. ISSN 0066-4189.

Yongyun Hwang and Carlo Cossu. Linear non-normal energy amplification of harmonic and stochastic forcing in the turbulent channel flow. *Journal of Fluid Mechanics*, 664:51–73, December 2010. ISSN 0022-1120, 1469-7645. doi: 10.1017/S0022112010003629. URL https://www.cambridge.org/core/product/identifier/S0022112010003629/type/journal_article.

O. Iida and Y. Nagano. The Relaminarization Mechanisms of Turbulent Channel Flow at Low Reynolds Numbers. *Flow, Turbulence and Combustion*, 60(2):193–213, 1998. ISSN 13866184. doi: 10.1023/A:1009999606355. URL <http://link.springer.com/10.1023/A:1009999606355>.

Harold Jeffreys. Some cases of instability in fluid motion. *Proceedings of the Royal Society of London. Series A, Containing Papers of a Mathematical and Physical Character*, 118(779):195–208, March 1928. ISSN 0950-1207, 2053-9150. doi: 10.1098/rspa.1928.0045. URL <https://royalsocietypublishing.org/doi/10.1098/rspa.1928.0045>.

Klavs F. Jensen, Erik O. Einset, and Dimitrios I. Fotiadis. Flow Phenomena in Chemical Vapor Deposition of Thin Films. *Annual Review of Fluid Mechanics*, 23(1):197–232, January 1991. ISSN 0066-4189, 1545-4479. doi: 10.1146/annurev.fl.23.010191.001213. URL <https://www.annualreviews.org/doi/10.1146/annurev.fl.23.010191.001213>.

Argyris John, Faust Gunter, and Haase Maria. Routes to chaos and turbulence. A computational introduction. *Philosophical Transactions of the Royal Society of London. Series A: Physical and Engineering Sciences*, 344(1671):207–234, August 1993. ISSN 0962-8428, 2054-0299. doi: 10.1098/rsta.1993.0088. URL <https://royalsocietypublishing.org/doi/10.1098/rsta.1993.0088>.

J. John Soundar Jerome, Jean-Marc Chomaz, and Patrick Huerre. Transient growth in Rayleigh-Bénard-Poiseuille/Couette convection. *Physics of Fluids*, 24(4):044103, April 2012. ISSN 1070-6631, 1089-7666. doi: 10.1063/1.4704642. URL <https://pubs.aip.org/pof/article/24/4/044103/257562/Transient-growth-in-Rayleigh-Benard-Poiseuille>.

A. Karimi, Zhi-Feng Huang, and M. R. Paul. Exploring spiral defect chaos in generalized Swift-Hohenberg models with mean flow. *Physical Review E*, 84(4):046215, October 2011. ISSN 1539-3755, 1550-2376. doi: 10.1103/PhysRevE.84.046215. URL <https://link.aps.org/doi/10.1103/PhysRevE.84.046215>.

George Karniadakis and Spencer J Sherwin. *Spectral/hp element methods for computational fluid dynamics*. Oxford University Press, 2005. ISBN 0-19-852869-8.

George Em Karniadakis, Moshe Israeli, and Steven A Orszag. High-order splitting methods for the incompressible Navier-Stokes equations. *Journal of Computational Physics*, 97(2):414–443, December 1991. ISSN 00219991. doi: 10.1016/0021-9991(91)90007-8. URL <https://linkinghub.elsevier.com/retrieve/pii/0021999191900078>.

Pavan V. Kashyap, Yohann Duguet, and Olivier Dauchot. Linear Instability of Turbulent Channel Flow. *Physical Review Letters*, 129(24):244501, December 2022. ISSN 0031-9007, 1079-7114. doi: 10.1103/PhysRevLett.129.244501. URL <https://link.aps.org/doi/10.1103/PhysRevLett.129.244501>.

Genta Kawahara and Shigeo Kida. Periodic motion embedded in plane Couette turbulence: regeneration cycle and burst. *Journal of Fluid Mechanics*, 449:291–300, December 2001. ISSN 0022-1120,

1469-7645. doi: 10.1017/S0022112001006243. URL https://www.cambridge.org/core/product/identifier/S0022112001006243/type/journal_article.

R.E. Kelly. The Onset and Development of Thermal Convection in Fully Developed Shear Flows. In *Advances in Applied Mechanics*, volume 31, pages 35–112. Elsevier, 1994. ISBN 978-0-12-002031-7. doi: 10.1016/S0065-2156(08)70255-2. URL <https://linkinghub.elsevier.com/retrieve/pii/S0065215608702552>.

K.J. Kennedy and A. Zebib. Combined free and forced convection between horizontal parallel planes: some case studies. *International Journal of Heat and Mass Transfer*, 26(3):471–474, March 1983. ISSN 00179310. doi: 10.1016/0017-9310(83)90052-2. URL <https://linkinghub.elsevier.com/retrieve/pii/0017931083900522>.

R. R. Kerswell and O. R. Tutty. Recurrence of travelling waves in transitional pipe flow. *Journal of Fluid Mechanics*, 584:69–102, August 2007. ISSN 0022-1120, 1469-7645. doi: 10.1017/S0022112007006301. URL https://www.cambridge.org/core/product/identifier/S0022112007006301/type/journal_article.

T. Khapko, T. Kreilos, P. Schlatter, Y. Duguet, B. Eckhardt, and D. S. Henningson. Edge states as mediators of bypass transition in boundary-layer flows. *Journal of Fluid Mechanics*, 801:R2, August 2016. ISSN 0022-1120, 1469-7645. doi: 10.1017/jfm.2016.434. URL https://www.cambridge.org/core/product/identifier/S0022112016004341/type/journal_article.

John Kim, Parviz Moin, and Robert Moser. Turbulence statistics in fully developed channel flow at low Reynolds number. *Journal of Fluid Mechanics*, 177:133–166, April 1987. ISSN 0022-1120, 1469-7645. doi: 10.1017/S0022112087000892. URL https://www.cambridge.org/core/product/identifier/S0022112087000892/type/journal_article.

S. J. Kline, W. C. Reynolds, F. A. Schraub, and P. W. Runstadler. The structure of turbulent boundary layers. *Journal of Fluid Mechanics*, 30(4):741–773, December 1967. ISSN 0022-1120, 1469-7645. doi: 10.1017/S0022112067001740. URL https://www.cambridge.org/core/product/identifier/S0022112067001740/type/journal_article.

E.L. Koschmieder and S.G. Pallas. Heat transfer through a shallow, horizontal convecting fluid layer. *International Journal of Heat and Mass Transfer*, 17(9):991–1002, September 1974. ISSN 00179310. doi: 10.1016/0017-9310(74)90181-1. URL <https://linkinghub.elsevier.com/retrieve/pii/0017931074901811>.

Tobias Kreilos and Bruno Eckhardt. Periodic orbits near onset of chaos in plane Couette flow. *Chaos: An Interdisciplinary Journal of Nonlinear Science*, 22(4):047505, December 2012. ISSN 1054-1500, 1089-7682. doi: 10.1063/1.4757227. URL <https://pubs.aip.org/cha/article/22/4/047505/341745/Periodic-orbits-near-onset-of-chaos-in-plane>.

Ying-Cheng Lai and Tamás Tél. *Transient Chaos*, volume 173 of *Applied Mathematical Sciences*. Springer New York, New York, NY, 2011. ISBN 978-1-4419-6986-6 978-1-4419-6987-3. doi: 10.1007/978-1-4419-6987-3. URL <http://link.springer.com/10.1007/978-1-4419-6987-3>.

Lev D Landau. On the problem of turbulence. volume 44, page 311, 1944.

P. D. Lax and A. N. Milgram. IX. Parabolic Equations. In *Contributions to the Theory of Partial Differential Equations. (AM-33)*, pages 167–190. Princeton University Press, December 1955. ISBN 978-1-4008-8218-2. doi: 10.1515/9781400882182-010. URL <https://www.degruyter.com/document/doi/10.1515/9781400882182-010/html>.

P. Le Gal, A. Pocheau, and V. Croquette. Square versus Roll Pattern at Convective Threshold. *Physical Review Letters*, 54(23):2501–2504, June 1985. ISSN 0031-9007. doi: 10.1103/PhysRevLett.54.2501. URL <https://link.aps.org/doi/10.1103/PhysRevLett.54.2501>.

Richard B Lehoucq, Danny C Sorensen, and Chao Yang. *ARPACK users' guide: solution of large-scale eigenvalue problems with implicitly restarted Arnoldi methods*. SIAM, 1998. ISBN 0-89871-407-9.

Jun Liu and Guenter Ahlers. Spiral-Defect Chaos in Rayleigh-Bénard Convection with Small Prandtl Numbers. *PHYSICAL REVIEW LETTERS*, 77(15), 1996.

Mary Lowe and J. P. Gollub. Pattern Selection near the Onset of Convection: The Eckhaus Instability. *Physical Review Letters*, 55(23):2575–2578, December 1985. ISSN 0031-9007. doi: 10.1103/PhysRevLett.55.2575. URL <https://link.aps.org/doi/10.1103/PhysRevLett.55.2575>.

J-M Luijkx, Jean Karl Platten, and J Cl Legros. On the existence of thermoconvective rolls, transverse to a superimposed mean Poiseuille flow. *International Journal of Heat and Mass Transfer*, 24(7):1287–1291, 1981. ISSN 0017-9310. Publisher: Elsevier.

Dong-Jun Ma, De-Jun Sun, and Xie-Yuan Yin. Multiplicity of steady states in cylindrical Rayleigh-Bénard convection. *Physical Review E*, 74(3):037302, September 2006. ISSN 1539-3755, 1550-2376. doi: 10.1103/PhysRevE.74.037302. URL <https://link.aps.org/doi/10.1103/PhysRevE.74.037302>.

Paul Manneville and Yves Pomeau. Intermittency and the Lorenz model. *Physics Letters A*, 75(1-2):1–2, 1979. ISSN 0375-9601. Publisher: North-Holland.

Á. Meseguer and L.N. Trefethen. Linearized pipe flow to Reynolds number 107. *Journal of Computational Physics*, 186(1):178–197, March 2003. ISSN 00219991. doi: 10.1016/S0021-9991(03)00299-9. URL <https://linkinghub.elsevier.com/retrieve/pii/S0021999103000299>.

Stephen W. Morris, Eberhard Bodenschatz, David S. Cannell, and Guenter Ahlers. Spiral defect chaos in large aspect ratio Rayleigh-Bénard convection. *Physical Review Letters*, 71(13):2026–2029, September 1993. ISSN 0031-9007. doi: 10.1103/PhysRevLett.71.2026. URL <https://link.aps.org/doi/10.1103/PhysRevLett.71.2026>.

Stephen W. Morris, Eberhard Bodenschatz, David S. Cannell, and Guenter Ahlers. The spatio-temporal structure of spiral-defect chaos. *Physica D: Nonlinear Phenomena*, 97(1-3):164–179, October 1996. ISSN 01672789. doi: 10.1016/0167-2789(96)00096-6. URL <https://linkinghub.elsevier.com/retrieve/pii/0167278996000966>.

David Moxey, Chris D. Cantwell, Yan Bao, Andrea Cassinelli, Giacomo Castiglioni, Sehun Chun, Emilia Juda, Ehsan Kazemi, Kilian Lackhove, Julian Marcon, Gianmarco Mengaldo, Douglas Serfon, Michael Turner, Hui Xu, Joaquim Peiró, Robert M. Kirby, and Spencer J. Sherwin. Nektar++: Enhancing the capability and application of high-fidelity spectral/ h p element methods. *Computer Physics Communications*, 249:107110, April 2020. ISSN 00104655. doi: 10.1016/j.cpc.2019.107110. URL <https://linkinghub.elsevier.com/retrieve/pii/S0010465519304175>.

H. W. Müller, M. Lücke, and M. Kamps. Transversal convection patterns in horizontal shear flow. *Physical Review A*, 45(6):3714–3726, March 1992. ISSN 1050-2947, 1094-1622. doi: 10.1103/PhysRevA.45.3714. URL <https://link.aps.org/doi/10.1103/PhysRevA.45.3714>.

M. Nagata. Three-dimensional finite-amplitude solutions in plane Couette flow: bifurcation from infinity. *Journal of Fluid Mechanics*, 217:519–527, August 1990. ISSN 0022-1120, 1469-7645. doi: 10.1017/S0022112090000829. URL https://www.cambridge.org/core/product/identifier/S0022112090000829/type/journal_article.

M. Nagata. Three-dimensional traveling-wave solutions in plane Couette flow. *Physical Review E*, 55(2):2023–2025, February 1997. ISSN 1063-651X, 1095-3787. doi: 10.1103/PhysRevE.55.2023. URL <https://link.aps.org/doi/10.1103/PhysRevE.55.2023>.

X. Nicolas, A. Mojtabi, and J. K. Platten. Two-dimensional numerical analysis of the Poiseuille–Bénard flow in a rectangular channel heated from below. *Physics of Fluids*, 9(2):337–348, February 1997. ISSN 1070-6631, 1089-7666. doi: 10.1063/1.869235. URL <https://pubs.aip.org/pof/article/9/2/337/259822/Two-dimensional-numerical-analysis-of-the>.

X. Nicolas, J.-M. Luijkx, and J.-K. Platten. Linear stability of mixed convection flows in horizontal rectangular channels of finite transversal extension heated from below. *International Journal of Heat and Mass Transfer*, 43(4):589–610, February 2000. ISSN 00179310. doi: 10.1016/S0017-9310(99)00099-X. URL <https://linkinghub.elsevier.com/retrieve/pii/S001793109900099X>.

Xavier Nicolas. Revue bibliographique sur les écoulements de Poiseuille–Rayleigh–Bénard : écoulements de convection mixte en conduites rectangulaires horizontales chauffées par le bas. *International Journal of Thermal Sciences*, 41(10):961–1016, October 2002. ISSN 12900729. doi: 10.1016/S1290-0729(02)01374-1. URL <https://linkinghub.elsevier.com/retrieve/pii/S1290072902013741>.

Xavier Nicolas, Shihe Xin, and Noussaiba Zoueidi. Characterisation of a Wavy Convective Instability in Poiseuille-Rayleigh-Be’nard Flows: Linear Stability Analysis and Non Linear Numerical Simulations Under Random Excitations. In *2010 14th International Heat Transfer Conference, Volume*

7, pages 203–208, Washington, DC, USA, January 2010. ASMEDC. ISBN 978-0-7918-4942-2 978-0-7918-3879-2. doi: 10.1115/IHTC14-22256. URL <https://asmedigitalcollection.asme.org/IHTC/proceedings/IHTC14/49422/203/360332>.

Xavier Nicolas, Noussaiba Zoueidi, and Shihe Xin. Influence of a white noise at channel inlet on the parallel and wavy convective instabilities of Poiseuille-Rayleigh-Bénard flows. *Physics of Fluids*, 24(8):084101, August 2012. ISSN 1070-6631, 1089-7666. doi: 10.1063/1.4737652. URL <https://pubs.aip.org/pof/article/24/8/084101/258132/Influence-of-a-white-noise-at-channel-inlet-on-the>.

William M'F. Orr. The Stability or Instability of the Steady Motions of a Perfect Liquid and of a Viscous Liquid. Part II: A Viscous Liquid. *Proceedings of the Royal Irish Academy. Section A: Mathematical and Physical Sciences*, 27:69–138, 1907. ISSN 00358975. URL <http://www.jstor.org/stable/20490591>. Publisher: Royal Irish Academy.

Steven A. Orszag. Accurate solution of the Orr-Sommerfeld stability equation. *Journal of Fluid Mechanics*, 50(4):689–703, December 1971. ISSN 0022-1120, 1469-7645. doi: 10.1017/S0022112071002842. URL https://www.cambridge.org/core/product/identifier/S0022112071002842/type/journal_article.

Steven A. Orszag and Anthony T. Patera. Secondary instability of wall-bounded shear flows. *Journal of Fluid Mechanics*, 128(-1):347, March 1983. ISSN 0022-1120, 1469-7645. doi: 10.1017/S0022112083000518. URL http://www.journals.cambridge.org/abstract_S0022112083000518.

Steven A. Orszag, Moshe Israeli, and Michel O. Deville. Boundary conditions for incompressible flows. *Journal of Scientific Computing*, 1(1):75–111, 1986. ISSN 0885-7474, 1573-7691. doi: 10.1007/BF01061454. URL <http://link.springer.com/10.1007/BF01061454>.

S. Ostrach and Y. Kamotani. Heat Transfer Augmentation in Laminar Fully Developed Channel Flow by Means of Heating From Below. *Journal of Heat Transfer*, 97(2):220–225, May 1975. ISSN 0022-1481, 1528-8943. doi: 10.1115/1.3450344. URL <https://asmedigitalcollection.asme.org/heattransfer/article/97/2/220/416581/Heat-Transfer-Augmentation-in-Laminar-Fully>.

MT Ouazzani, Jean-Paul Caltagirone, Gilles Meyer, and Abdelkader Mojtabi. Etude numerique et expérimentale de la convection mixte entre deux plans horizontaux à températures différentes. *International journal of heat and mass transfer*, 32(2):261–269, 1989. ISSN 0017-9310. Publisher: Elsevier.

MT Ouazzani, Jean Karl Platten, and Abdelkader Mojtabi. Etude expérimentale de la convection mixte entre deux plans horizontaux à températures différentes—II. *International journal of heat and mass transfer*, 33(7):1417–1427, 1990. ISSN 0017-9310. Publisher: Elsevier.

Hervé Pabiou, Xavier Nicolas, Shihe Xin, and Sophie Mergui. Observations d'une instabilité convective apparaissant sous la forme de rouleaux sinueux dans un écoulement de Poiseuille–Rayleigh–Bénard. *Mécanique & industries*, 4(5):537–543, 2003. ISSN 1296-2139. Publisher: Elsevier.

Hervé Pabiou, Sophie Mergui, and Christine Bénard. Wavy secondary instability of longitudinal rolls in RayleighPoiseuille flows. *Journal of Fluid Mechanics*, 542(-1):175, October 2005. ISSN 0022-1120, 1469-7645. doi: 10.1017/S0022112005006154. URL http://www.journals.cambridge.org/abstract_S0022112005006154.

Chaitanya S Paranjape. Onset of turbulence in plane Poiseuille flow. 2019. Publisher: IST Austria Klosterneuburg, Austria.

Chaitanya S. Paranjape, Yohann Duguet, and Björn Hof. Oblique stripe solutions of channel flow. *Journal of Fluid Mechanics*, 897:A7, August 2020. ISSN 0022-1120, 1469-7645. doi: 10.1017/jfm.2020.322. URL https://www.cambridge.org/core/product/identifier/S0022112020003225/type/journal_article.

Chaitanya S. Paranjape, Gökhan Yalnız, Yohann Duguet, Nazmi Burak Budanur, and Björn Hof. Direct Path from Turbulence to Time-Periodic Solutions. *Physical Review Letters*, 131(3):034002, July 2023. ISSN 0031-9007, 1079-7114. doi: 10.1103/PhysRevLett.131.034002. URL <https://link.aps.org/doi/10.1103/PhysRevLett.131.034002>.

J.P. Parker and T.M. Schneider. Variational methods for finding periodic orbits in the incompressible Navier–Stokes equations. *Journal of Fluid Mechanics*, 941:A17, June 2022. ISSN 0022-1120, 1469-7645. doi: 10.1017/jfm.2022.299. URL https://www.cambridge.org/core/product/identifier/S0022112022002993/type/journal_article.

V. C. Patel and M. R. Head. Some observations on skin friction and velocity profiles in fully developed pipe and channel flows. *Journal of Fluid Mechanics*, 38(1):181–201, August 1969. ISSN 0022-1120, 1469-7645. doi: 10.1017/S0022112069000115. URL https://www.cambridge.org/core/product/identifier/S0022112069000115/type/journal_article.

Anthony T Patera. A spectral element method for fluid dynamics: Laminar flow in a channel expansion. *Journal of Computational Physics*, 54(3):468–488, June 1984. ISSN 00219991. doi: 10.1016/0021-9991(84)90128-1. URL <https://linkinghub.elsevier.com/retrieve/pii/0021999184901281>.

M. R. Paul, M. I. Einarsson, P. F. Fischer, and M. C. Cross. Extensive chaos in Rayleigh–Bénard convection. *Physical Review E*, 75(4):045203, April 2007. ISSN 1539-3755, 1550-2376. doi: 10.1103/PhysRevE.75.045203. URL <https://link.aps.org/doi/10.1103/PhysRevE.75.045203>.

M.R. Paul, K.-H. Chiam, M.C. Cross, P.F. Fischer, and H.S. Greenside. Pattern formation and dynamics in Rayleigh–Bénard convection: numerical simulations of experimentally realistic geometries. *Physica D: Nonlinear Phenomena*, 184(1-4):114–126, October 2003. ISSN 01672789. doi: 10.

1016/S0167-2789(03)00216-1. URL <https://linkinghub.elsevier.com/retrieve/pii/S0167278903002161>.

Anne Pellew and Richard Vynne Southwell. On maintained convective motion in a fluid heated from below. *Proceedings of the Royal Society of London. Series A. Mathematical and Physical Sciences*, 176(966):312–343, November 1940. ISSN 0080-4630, 2053-9169. doi: 10.1098/rspa.1940.0092. URL <https://royalsocietypublishing.org/doi/10.1098/rspa.1940.0092>.

Sergio Pirozzoli, Matteo Bernardini, Roberto Verzicco, and Paolo Orlandi. Mixed convection in turbulent channels with unstable stratification. *Journal of Fluid Mechanics*, 821:482–516, June 2017. ISSN 0022-1120, 1469-7645. doi: 10.1017/jfm.2017.216. URL https://www.cambridge.org/core/product/identifier/S0022112017002166/type/journal_article.

Brendan B Plapp and Eberhard Bodenschatz. Core dynamics of multi-armed spirals in Rayleigh-Bénard convection. *Physica Scripta*, T67:111–116, January 1996. ISSN 0031-8949, 1402-4896. doi: 10.1088/0031-8949/1996/T67/022. URL <https://iopscience.iop.org/article/10.1088/0031-8949/1996/T67/022>.

Brendan B. Plapp, David A. Egolf, Eberhard Bodenschatz, and Werner Pesch. Dynamics and Selection of Giant Spirals in Rayleigh-Bénard Convection. *Physical Review Letters*, 81(24):5334–5337, December 1998. ISSN 0031-9007, 1079-7114. doi: 10.1103/PhysRevLett.81.5334. URL <https://link.aps.org/doi/10.1103/PhysRevLett.81.5334>.

Brendan Bryce Plapp. Spiral pattern formation in Rayleigh-Benard convection. *Ph.D. Thesis*, page 3118, December 1997. URL <https://ui.adsabs.harvard.edu/abs/1997PhDT.....105P>.

A. Prigent and O. Dauchot. "Barber pole turbulence" in large aspect ratio Taylor-Couette flow. *Physical Review Letters*, 89(1):014501, June 2002. ISSN 0031-9007, 1079-7114. doi: 10.1103/PhysRevLett.89.014501. URL <http://arxiv.org/abs/cond-mat/0009241>. arXiv:cond-mat/0009241.

Arnaud Prigent, Guillaume Grégoire, Hugues Chaté, and Olivier Dauchot. Long-wavelength modulation of turbulent shear flows. *Physica D: Nonlinear Phenomena*, 174(1-4):100–113, January 2003. ISSN 01672789. doi: 10.1016/S0167-2789(02)00685-1. URL <https://linkinghub.elsevier.com/retrieve/pii/S0167278902006851>.

Chris C.T Pringle, Yohann Duguet, and Rich R Kerswell. Highly symmetric travelling waves in pipe flow. *Philosophical Transactions of the Royal Society A: Mathematical, Physical and Engineering Sciences*, 367(1888):457–472, February 2009. ISSN 1364-503X, 1471-2962. doi: 10.1098/rsta.2008.0236. URL <https://royalsocietypublishing.org/doi/10.1098/rsta.2008.0236>.

Gregory Pujals, Manuel García-Villalba, Carlo Cossu, and Sébastien Depardon. A note on optimal transient growth in turbulent channel flows. *Physics of Fluids*, 21(1):015109, January 2009. ISSN 1070-6631, 1089-7666. doi: 10.1063/1.3068760. URL <https://pubs.aip.org/pof/article/21/1/015109/256743/A-note-on-optimal-transient-growth-in-turbulent>.

Subhashis Ray and J. Srinivasan. Analysis of conjugate laminar mixed convection cooling in a shrouded array of electronic components. *International Journal of Heat and Mass Transfer*, 35(4):815–822, April 1992. ISSN 00179310. doi: 10.1016/0017-9310(92)90249-R. URL <https://linkinghub.elsevier.com/retrieve/pii/001793109290249R>.

Lord Rayleigh. LIX. *On convection currents in a horizontal layer of fluid, when the higher temperature is on the under side.* *The London, Edinburgh, and Dublin Philosophical Magazine and Journal of Science*, 32(192):529–546, December 1916. ISSN 1941-5982, 1941-5990. doi: 10.1080/14786441608635602. URL <https://www.tandfonline.com/doi/full/10.1080/14786441608635602>.

Satish C. Reddy and Dan S. Henningson. Energy growth in viscous channel flows. *Journal of Fluid Mechanics*, 252:209–238, July 1993. ISSN 0022-1120, 1469-7645. doi: 10.1017/S0022112093003738. URL https://www.cambridge.org/core/product/identifier/S0022112093003738/type/journal_article.

Satish C. Reddy, Peter J. Schmid, and Dan S. Henningson. Pseudospectra of the Orr–Sommerfeld Operator. *SIAM Journal on Applied Mathematics*, 53(1):15–47, February 1993. ISSN 0036-1399, 1095-712X. doi: 10.1137/0153002. URL <http://pubs.siam.org/doi/10.1137/0153002>.

Florian Reetz and Tobias M. Schneider. Invariant states in inclined layer convection. Part 1. Temporal transitions along dynamical connections between invariant states. *Journal of Fluid Mechanics*, 898:A22, September 2020. ISSN 0022-1120, 1469-7645. doi: 10.1017/jfm.2020.317. URL https://www.cambridge.org/core/product/identifier/S0022112020003171/type/journal_article.

Florian Reetz, Tobias Kreilos, and Tobias M. Schneider. Exact invariant solution reveals the origin of self-organized oblique turbulent-laminar stripes. *Nature Communications*, 10(1):2277, May 2019. ISSN 2041-1723. doi: 10.1038/s41467-019-10208-x. URL <https://doi.org/10.1038/s41467-019-10208-x>.

Florian Reetz, Priya Subramanian, and Tobias M. Schneider. Invariant states in inclined layer convection. Part 2. Bifurcations and connections between branches of invariant states. *Journal of Fluid Mechanics*, 898:A23, September 2020. ISSN 0022-1120, 1469-7645. doi: 10.1017/jfm.2020.318. URL https://www.cambridge.org/core/product/identifier/S0022112020003183/type/journal_article.

Osborne Reynolds. XXIX. An experimental investigation of the circumstances which determine whether the motion of water shall be direct or sinuous, and of the law of resistance in parallel channels. *Philosophical Transactions of the Royal Society of London*, 174:935–982, December 1883. ISSN 0261-0523, 2053-9223. doi: 10.1098/rstl.1883.0029. URL <https://royalsocietypublishing.org/doi/10.1098/rstl.1883.0029>.

Osborne Reynolds. IV. On the dynamical theory of incompressible viscous fluids and the determination of the criterion. *Philosophical Transactions of the Royal Society of London. (A.)*, 186:123–164,

December 1895. ISSN 0264-3820, 2053-9231. doi: 10.1098/rsta.1895.0004. URL <https://royalsocietypublishing.org/doi/10.1098/rsta.1895.0004>.

Gabriele Rocco. Advanced Instability Methods using Spectral/hp Discretisations and their Applications to Complex Geometries. 2014.

H. T. Rossby. A study of Bénard convection with and without rotation. *Journal of Fluid Mechanics*, 36(2):309–335, April 1969. ISSN 0022-1120, 1469-7645. doi: 10.1017/S0022112069001674. URL https://www.cambridge.org/core/product/identifier/S0022112069001674/type/journal_article.

David Ruelle and Floris Takens. On the nature of turbulence. *Communications in Mathematical Physics*, 20(3):167–192, September 1971. ISSN 0010-3616, 1432-0916. doi: 10.1007/BF01646553. URL <http://link.springer.com/10.1007/BF01646553>.

Sten Rüdiger and Fred Feudel. Pattern formation in Rayleigh-Bénard convection in a cylindrical container. *Physical Review E*, 62(4):4927–4931, October 2000. ISSN 1063-651X, 1095-3787. doi: 10.1103/PhysRevE.62.4927. URL <https://link.aps.org/doi/10.1103/PhysRevE.62.4927>.

A. Scagliarini, H. Einarsson, Á. Gylfason, and F. Toschi. Law of the wall in an unstably stratified turbulent channel flow. *Journal of Fluid Mechanics*, 781:R5, October 2015. ISSN 0022-1120, 1469-7645. doi: 10.1017/jfm.2015.498. URL https://www.cambridge.org/core/product/identifier/S002211201500498X/type/journal_article.

Andrea Scagliarini, Armann Gylfason, and Federico Toschi. Heat flux scaling in turbulent Rayleigh-Bénard convection with an imposed longitudinal wind. *Physical Review E*, 89(4):043012, April 2014. ISSN 1539-3755, 1550-2376. doi: 10.1103/PhysRevE.89.043012. URL <http://arxiv.org/abs/1311.4598>. arXiv:1311.4598 [physics].

H. Schlichting. Zur Entstehung der Turbulenz bei der Plattenströmung. *Nachrichten von der Gesellschaft der Wissenschaften zu Göttingen, Mathematisch-Physikalische Klasse*, 1933:181–208, 1933. URL <http://eudml.org/doc/59420>.

Hermann Schlichting and Klaus Gersten. Onset of Turbulence (Stability Theory). In *Boundary-Layer Theory*, pages 415–496. Springer Berlin Heidelberg, Berlin, Heidelberg, 2017. ISBN 978-3-662-52917-1 978-3-662-52919-5. doi: 10.1007/978-3-662-52919-5_15. URL http://link.springer.com/10.1007/978-3-662-52919-5_15.

A. Schlüter, D. Lortz, and F. Busse. On the stability of steady finite amplitude convection. *Journal of Fluid Mechanics*, 23(01):129, September 1965. ISSN 0022-1120, 1469-7645. doi: 10.1017/S0022112065001271. URL http://www.journals.cambridge.org/abstract_S0022112065001271.

Peter J. Schmid. Nonmodal Stability Theory. *Annual Review of Fluid Mechanics*, 39(1):129–162, January 2007. ISSN 0066-4189, 1545-4479. doi: 10.1146/annurev.fluid.38.050304.092139. URL <https://www.annualreviews.org/doi/10.1146/annurev.fluid.38.050304.092139>.

Peter J. Schmid and Dan S. Henningson. *Stability and Transition in Shear Flows*, volume 142 of *Applied Mathematical Sciences*. Springer New York, New York, NY, 2001. ISBN 978-1-4612-6564-1 978-1-4613-0185-1. doi: 10.1007/978-1-4613-0185-1. URL <http://link.springer.com/10.1007/978-1-4613-0185-1>.

Rainer Schmitz, Werner Pesch, and Walter Zimmermann. Spiral-defect chaos: Swift-Hohenberg model versus Boussinesq equations. *Physical Review E*, 65(3):037302, March 2002. ISSN 1063-651X, 1095-3787. doi: 10.1103/PhysRevE.65.037302. URL <https://link.aps.org/doi/10.1103/PhysRevE.65.037302>.

Tobias M Schneider and Bruno Eckhardt. Edge states intermediate between laminar and turbulent dynamics in pipe flow. *Philosophical Transactions of the Royal Society A: Mathematical, Physical and Engineering Sciences*, 367(1888):577–587, February 2009. ISSN 1364-503X, 1471-2962. doi: 10.1098/rsta.2008.0216. URL <https://royalsocietypublishing.org/doi/10.1098/rsta.2008.0216>.

Tobias M. Schneider, Bruno Eckhardt, and James A. Yorke. Turbulence transition and the edge of chaos in pipe flow. *Physical Review Letters*, 99(3):034502, July 2007. ISSN 0031-9007, 1079-7114. doi: 10.1103/PhysRevLett.99.034502. URL <http://arxiv.org/abs/nlin/0703067>. arXiv:nlin/0703067.

Masaki Shimizu and Paul Manneville. Bifurcations to turbulence in transitional channel flow. *Physical Review Fluids*, 4(11):113903, November 2019. doi: 10.1103/PhysRevFluids.4.113903. URL <https://link.aps.org/doi/10.1103/PhysRevFluids.4.113903>. Publisher: American Physical Society.

Jennifer H. Siggins. Dynamics of target patterns in low-Prandtl-number convection. *Journal of Fluid Mechanics*, 475:357–375, January 2003. ISSN 0022-1120, 1469-7645. doi: 10.1017/S0022112002002896. URL https://www.cambridge.org/core/product/identifier/S0022112002002896/type/journal_article.

Joseph D. Skufca, James A. Yorke, and Bruno Eckhardt. Edge of Chaos in a Parallel Shear Flow. *Physical Review Letters*, 96(17):174101, May 2006. ISSN 0031-9007, 1079-7114. doi: 10.1103/PhysRevLett.96.174101. URL <https://link.aps.org/doi/10.1103/PhysRevLett.96.174101>.

C. R. Smith and S. P. Metzler. The characteristics of low-speed streaks in the near-wall region of a turbulent boundary layer. *Journal of Fluid Mechanics*, 129(-1):27, April 1983. ISSN 0022-1120, 1469-7645. doi: 10.1017/S0022112083000634. URL http://www.journals.cambridge.org/abstract_S0022112083000634.

Arnold Sommerfeld. *Ein Beitrag zur hydrodynamischen Erklärung der turbulenten Flüssigkeitsbewegungen*. 1909.

Baofang Song, Dwight Barkley, Björn Hof, and Marc Avila. Speed and structure of turbulent fronts in pipe flow. *Journal of Fluid Mechanics*, 813:1045–1059, February 2017. ISSN 0022-1120, 1469-7645. doi: 10.1017/jfm.2017.14. URL https://www.cambridge.org/core/product/identifier/S0022112017000143/type/journal_article.

Herbert Brian Squire. On the stability for three-dimensional disturbances of viscous fluid flow between parallel walls. *Proceedings of the Royal Society of London. Series A, Containing Papers of a Mathematical and Physical Character*, 142(847):621–628, November 1933. ISSN 0950-1207, 2053-9150. doi: 10.1098/rspa.1933.0193. URL <https://royalsocietypublishing.org/doi/10.1098/rspa.1933.0193>.

V Steinberg and Guenter Ahlers. Pattern Formation and Wave- Number Selection by Rayleigh-Benard Convection in a Cylindrical Container. *Physica Scripta T*.

Steven H. Strogatz. *Nonlinear Dynamics and Chaos*. CRC Press, 0 edition, May 2018. ISBN 978-0-429-96111-3. doi: 10.1201/9780429492563. URL <https://www.taylorfrancis.com/books/9780429961113>.

J. Swift and P. C. Hohenberg. Hydrodynamic fluctuations at the convective instability. *Physical Review A*, 15(1):319–328, January 1977. ISSN 0556-2791. doi: 10.1103/PhysRevA.15.319. URL <https://link.aps.org/doi/10.1103/PhysRevA.15.319>.

Harry L Swinney and Jerry P Gollub. The transition to turbulence. *Physics today*, 31(8):41–49, 1978. ISSN 0031-9228. Publisher: American Institute of Physics.

J. J. Tao, Bruno Eckhardt, and X. M. Xiong. Extended localized structures and the onset of turbulence in channel flow. *Physical Review Fluids*, 3(1):011902, January 2018. doi: 10.1103/PhysRevFluids.3.011902. URL <https://link.aps.org/doi/10.1103/PhysRevFluids.3.011902>. Publisher: American Physical Society.

Vassilios Theofilis. Advances in global linear instability analysis of nonparallel and three-dimensional flows. *Progress in Aerospace Sciences*, 39(4):249–315, May 2003. ISSN 03760421. doi: 10.1016/S0376-0421(02)00030-1. URL <https://linkinghub.elsevier.com/retrieve/pii/S0376042102000301>.

Sadayoshi Toh and Tomoaki Itano. A periodic-like solution in channel flow. *Journal of Fluid Mechanics*, 481:67–76, April 2003. ISSN 00221120, 14697645. doi: 10.1017/S0022112003003768. URL http://www.journals.cambridge.org/abstract_S0022112003003768.

W. Tollmien. Über die Entstehung der Turbulenz. 1. Mitteilung. *Nachrichten von der Gesellschaft der Wissenschaften zu Göttingen, Mathematisch-Physikalische Klasse*, 1929:21–44, 1928. URL <http://eudml.org/doc/59276>.

Lloyd N. Trefethen. Pseudospectra of Linear Operators. *SIAM Review*, 39(3):383–406, January 1997. ISSN 0036-1445, 1095-7200. doi: 10.1137/S0036144595295284. URL <http://pubs.siam.org/doi/10.1137/S0036144595295284>.

Takahiro Tsukahara, Kaoru Iwamoto, Hiroshi Kawamura, and Tetsuaki Takeda. DNS of heat transfer in a transitional channel flow accompanied by a turbulent puff-like structure, September 2014a. URL <http://arxiv.org/abs/1406.0586>. arXiv:1406.0586 [physics].

Takahiro Tsukahara, Yasuo Kawaguchi, and Hiroshi Kawamura. An experimental study on turbulent-stripe structure in transitional channel flow, 2014b. URL <https://arxiv.org/abs/1406.1378>. Version Number: 2.

Takahiro Tsukahara, Yohji Seki, Hiroshi Kawamura, and Daisuke Tochio. DNS of turbulent channel flow at very low Reynolds numbers, September 2014c. URL <http://arxiv.org/abs/1406.0248>. arXiv:1406.0248 [physics].

Laurette S. Tuckerman and Dwight Barkley. Global Bifurcation to Traveling Waves in Axisymmetric Convection. *Physical Review Letters*, 61(4):408–411, July 1988. ISSN 0031-9007. doi: 10.1103/PhysRevLett.61.408. URL <https://link.aps.org/doi/10.1103/PhysRevLett.61.408>.

Laurette S. Tuckerman and Dwight Barkley. Bifurcation Analysis for Timesteppers. In *Numerical Methods for Bifurcation Problems and Large-Scale Dynamical Systems*, volume 119, pages 453–466. Springer New York, New York, NY, 2000. ISBN 978-1-4612-7044-7 978-1-4612-1208-9. doi: 10.1007/978-1-4612-1208-9_20. URL http://link.springer.com/10.1007/978-1-4612-1208-9_20. Series Title: The IMA Volumes in Mathematics and its Applications.

Laurette S Tuckerman and Dwight Barkley. Patterns and dynamics in transitional plane Couette flow. *Physics of Fluids*, 23(4), 2011. ISSN 1070-6631. Publisher: AIP Publishing.

Laurette S. Tuckerman, Tobias Kreilos, Hecke Schröbsdorff, Tobias M. Schneider, and John F. Gibson. Turbulent-laminar patterns in plane Poiseuille flow. *Physics of Fluids*, 26(11):114103, November 2014. ISSN 1070-6631, 1089-7666. doi: 10.1063/1.4900874. URL <https://pubs.aip.org/pof/article/26/11/114103/315350/Turbulent-laminar-patterns-in-plane-Poiseuille>.

R. Temam. Sur l’approximation de la solution des équations de Navier-Stokes par la méthode des pas fractionnaires (II). *Archive for Rational Mechanics and Analysis*, 33(5):377–385, January 1969. ISSN 0003-9527, 1432-0673. doi: 10.1007/BF00247696. URL <http://link.springer.com/10.1007/BF00247696>.

Geoffrey K. Vallis, Douglas J. Parker, and Steven M. Tobias. A simple system for moist convection: the Rainy–Bénard model. *Journal of Fluid Mechanics*, 862:162–199, March 2019. ISSN 0022-1120, 1469-7645. doi: 10.1017/jfm.2018.954. URL https://www.cambridge.org/core/product/identifier/S0022112018009540/type/journal_article.

Milton Van Dyke and Milton Van Dyke. *An album of fluid motion*, volume 176. Parabolic Press Stanford, 1982.

D. Viswanath. Recurrent motions within plane Couette turbulence. *Journal of Fluid Mechanics*, 580:339–358, June 2007. ISSN 0022-1120, 1469-7645. doi: 10.1017/S0022112007005459. URL https://www.cambridge.org/core/product/identifier/S0022112007005459/type/journal_article.

Eduardo Vitral, Saikat Mukherjee, Perry H. Leo, Jorge Viñals, Mark R. Paul, and Zhi-Feng Huang. Spiral defect chaos in Rayleigh-Bénard convection: Asymptotic and numerical studies of azimuthal flows induced by rotating spirals. *Physical Review Fluids*, 5(9):093501, September 2020. ISSN 2469-990X. doi: 10.1103/PhysRevFluids.5.093501. URL <https://link.aps.org/doi/10.1103/PhysRevFluids.5.093501>.

Fabian Waleffe. Exact coherent structures in channel flow. *Journal of Fluid Mechanics*, 435:93–102, May 2001. ISSN 0022-1120, 1469-7645. doi: 10.1017/S0022112001004189. URL https://www.cambridge.org/core/product/identifier/S0022112001004189/type/journal_article.

Fabian Waleffe. Homotopy of exact coherent structures in plane shear flows. *Physics of Fluids*, 15(6):1517–1534, June 2003. ISSN 1070-6631, 1089-7666. doi: 10.1063/1.1566753. URL <https://pubs.aip.org/pof/article/15/6/1517/448391/Homotopy-of-exact-coherent-structures-in-plane>.

James M. Wallace, Helmut Eckelmann, and Robert S. Brodkey. The wall region in turbulent shear flow. *Journal of Fluid Mechanics*, 54(1):39–48, July 1972. ISSN 0022-1120, 1469-7645. doi: 10.1017/S0022112072000515. URL https://www.cambridge.org/core/product/identifier/S0022112072000515/type/journal_article.

Jue Wang, John Gibson, and Fabian Waleffe. Lower Branch Coherent States in Shear Flows: Transition and Control. *Physical Review Letters*, 98(20):204501, May 2007. ISSN 0031-9007, 1079-7114. doi: 10.1103/PhysRevLett.98.204501. URL <https://link.aps.org/doi/10.1103/PhysRevLett.98.204501>.

H. Wedin and R. R. Kerswell. Exact coherent structures in pipe flow: travelling wave solutions. *Journal of Fluid Mechanics*, 508:333–371, June 2004. ISSN 0022-1120, 1469-7645. doi: 10.1017/S0022112004009346. URL http://www.journals.cambridge.org/abstract_S0022112004009346.

José Eduardo Wesfreid. Henri Bénard: Thermal convection and vortex shedding. *Comptes Rendus. Mécanique*, 345(7):446–466, June 2017. ISSN 1873-7234. doi: 10.1016/j.crme.2017.06.006. URL <https://comptes-rendus.academie-sciences.fr/mecanique/articles/10.1016/j.crme.2017.06.006/>.

G. E. Willis and J. W. Deardorff. The oscillatory motions of Rayleigh convection. *Journal of Fluid Mechanics*, 44(04):661, December 1970. ISSN 0022-1120, 1469-7645. doi: 10.1017/S0022112070002070. URL http://www.journals.cambridge.org/abstract_S0022112070002070.

W. W. Willmarth and S. S. Lu. Structure of the Reynolds stress near the wall. *Journal of Fluid Mechanics*, 55(1):65–92, September 1972. ISSN 0022-1120, 1469-7645. doi: 10.1017/S002211207200165X. URL https://www.cambridge.org/core/product/identifier/S002211207200165X/type/journal_article.

Hao-wen Xi, J. D. Gunton, and Jorge Viñals. Spiral defect chaos in a model of Rayleigh-Bénard convection. *Physical Review Letters*, 71(13):2030–2033, September 1993. ISSN 0031-9007. doi: 10.1103/PhysRevLett.71.2030. URL <https://link.aps.org/doi/10.1103/PhysRevLett.71.2030>.

Haowen Xi and J. D. Gunton. Spatiotemporal chaos in a model of Rayleigh-Bénard convection. *Physical Review E*, 52(5):4963–4975, November 1995. ISSN 1063-651X, 1095-3787. doi: 10.1103/PhysRevE.52.4963. URL <https://link.aps.org/doi/10.1103/PhysRevE.52.4963>.

Xiangkai Xiao and Baofang Song. The growth mechanism of turbulent bands in channel flow at low Reynolds numbers. *Journal of Fluid Mechanics*, 883:R1, January 2020. ISSN 0022-1120, 1469-7645. doi: 10.1017/jfm.2019.899. URL https://www.cambridge.org/core/product/identifier/S0022112019008991/type/journal_article.

Shihe Xin, Xavier Nicolas, and Patrick Le Quéré. Stability analyses of Longitudinal Rolls of Poiseuille-Rayleigh-Bénard Flows in Air-Filled Channels of Finite Transversal Extension. *Numerical Heat Transfer, Part A: Applications*, 50(5):467–490, July 2006. ISSN 1040-7782, 1521-0634. doi: 10.1080/10407780600620079. URL <http://www.tandfonline.com/doi/abs/10.1080/10407780600620079>.

Xiangming Xiong, Jianjun Tao, Shiyi Chen, and Luca Brandt. Turbulent bands in plane-Poiseuille flow at moderate Reynolds numbers. *Physics of Fluids*, 27(4):041702, April 2015. ISSN 1070-6631, 1089-7666. doi: 10.1063/1.4917173. URL <https://pubs.aip.org/pof/article/27/4/041702/1019208/Turbulent-bands-in-plane-Poiseuille-flow-at>.

Stefan Zammert and Bruno Eckhardt. Crisis bifurcations in plane Poiseuille flow. *Physical Review E*, 91(4):041003, April 2015. ISSN 1539-3755, 1550-2376. doi: 10.1103/PhysRevE.91.041003. URL <https://link.aps.org/doi/10.1103/PhysRevE.91.041003>.